Re-Os Chronology and Systematics of Graphite

By

Jonathan Alan Scott Toma

A thesis submitted in partial fulfillment of the requirements for the degree of

Doctor of Philosophy

Department of Earth and Atmospheric Sciences
University of Alberta

Abstract

Graphite-forming events occurred throughout Earth history and extend up to solar and pre-solar contexts. However, a comprehensive understanding of the timeline of these events has been hindered by a lack of chronological information for graphite. Here we explore the geochronological potential of natural graphite using the Re-Os decay system and investigate its application thereafter in terrestrial systems.

Graphite Re and Os concentrations and isotopic ratios are shown here to be highly variable (Re = 0.2-1520 ppb; Os = 89-19,577 ppt; $^{187}Re/^{188}O$ = 10.8-4101; $^{187}Os/^{188}Os$ = 0.57-42.18) but analogous to those observed in terrestrial sulfides, organic-rich sedimentary rocks, and hydrocarbons. The variability in graphite Re contents is ostensibly controlled by graphite crystallinity (d_{002} and $L_{c(002)}$) with Re contents exhibiting an inverse relationship with graphite crystallinities.

High-precision (<1%) graphite Re-Os isochron dating is established here using hydrothermal graphite formed in mid-crustal shear zones (1731 ± 7 Ma [2σ; MSWD = 1]; Saskatchewan, Canada) and tanzanite-tsavorite gemstone deposits (587 ± 2 Ma [2σ; MSWD = 1]; Merelani Hills, Tanzania) and metamorphic graphite-pyrite formed in the Franciscan subduction zone (161 ± 2 Ma [2σ; MSWD = 0.2]; California, USA).

Graphite Re-Os dating is then coupled with additional geochronological (pyrite Re-Os dating and monazite/zircon U-Pb dating), isotopic tracer ($^{187}Os/^{188}Os$ and $^{13}C/^{12}C$) and XRD/Raman thermometry data to constrain the timing of large-scale carbon cycling in Paleoproterozoic graphitic shear zones associated with Nuna assembly, tanzanite-tsavorite

gemstone mineralization in the Mozambique belt, and Os cycling associated with subduction-

zone metamorphism in the Franciscan subduction system.

Preface

Chapter 1 through 4 of this thesis is an original work by the author and any reference to such work can be made with the following citation: Toma, J. Re-Os systematics and chronology of graphite and pyrite. Doctoral Thesis, University of Alberta (2023).

Chapter 2 of this thesis is published in the journal *Geochimica et Cosmochimica Acta* with the title of "Re-Os systematics and chronology of graphite" and an author/coauthor list that includes Jonathan Toma, Robert A. Creaser, Colin Card, Richard A. Stern, Thomas Chacko, and Mathew Steele-MacInnis. The full citation of this publication is as follows: Toma, J., Creaser, R.A., Card, C., Stern, R.A., Chacko, T., & Steele-MacInnis, M. Re-Os systematics and chronology of graphite. *Gechim. Cosmochim. Acta* **323**, 164-182 (2022). Author contributions: *J. Toma*: Conceptualization, Investigation, Methodology, Visualization, Writing – original draft, Writing – review and editing. *R.A. Creaser*: Conceptualization, Methodology, Supervision, Writing – review and editing. *C. Card*: Assisted with sample collection and Writing – review and editing. *R.A. Stern*: Assisted with SIMS C isotope analysis and Writing -review and editing. *T. Chacko*: Writing – review and editing. *M. Steele-MacInnis*: Assisted with Raman analysis. In accordance with thesis formatting, minor modifications have been made to the original publication. These include figure/table naming and reference citations.

Chapter 3 of this thesis is in review at the journal *Geology* with the title of "Did subducted graphite fertilize the Franciscan mantle wedge with radiogenic Os?" and an author/coauthor list that includes Jonathan Toma and Robert A. Creaser. Author contributions: *J. Toma*: Conceptualization, Investigation, Methodology, Visualization, Writing – original draft, Writing – review and editing. *R.A. Creaser*: Conceptualization, Methodology, Supervision, Writing – review and editing. In accordance with thesis formatting, minor modifications have been made to the original publication. These figure/table naming and reference citations.

A modified version of Chapter 4 of this thesis will be submitted to the journal *Nature Geoscience* with the title of "Carbon cycling in Paleoproterozoic shear zones linked to Nuna assembly" and an author/coauthor list that includes Jonathan Toma, Robert A. Creaser, Colin

Acknowledgments

Table of Contents

List of Tables

List of Figures

List of Abbreviations

$(CH_3)_2CO$	Acetone
α	Alpha
Å	Angstrom
Ap	Apatite
AB	Alberta
Alt	Altered
~	Approximately
Ar	Argon
avg	Average
BSE	Backscattered electron imaging
$Ba(OH)_2$	Barium Hydroxide
$Ba(NO_3)_2$	Barium Nitrate
Bl	Beaverlodge Domain
Bt	Biotite
BR	Brazil
CA	California
C	Carbon
CO_2	Carbon dioxide
CM	Carbonaceous Material/Matter
°C	Celsius
cm	Centimeters
Ce	Cerium
Cpy	Chalcopyrite

$CHCl_3$	Chloroform
Cr	Chromium
CrO_3	Chromium trioxide
Cw	Clearwater Domain
ca.	Circa
CRO	Coast Range Ophiolite
Co	Cobalt
R^2	Coefficient of determination (R squared)
$L_{c(002)}$	Crystallite size
λ	Lambda or decay constant
Dee	Deerite
δ	Delta notation
Dio	Diopside
De	Dodge Domain
EM	Electromagnetic
ENG	England
FT	Fission track dating
FSS	Franciscan Subduction System
Ga	Giga-annum; Billion years
GPa	Gigapascals
Au	Gold
g	Gram
Gr	Graphite
HCl	Hydrochloric acid

h	Hour
HF	Hydrofluoric acid
H	Hydrogen
H_2O_2	Hydrogen peroxide
HT	Hydrothermal
$d_{(002)}$	Interplanar spacing
Fe	Iron
kb	Kilobar
keV	Kiloelectronvolt
kg	Kilogram
km	Kilometer
kV	Kilovolts
KIS	Kivalliq Igneous Suite
LA-ICPMS	Laser-ablation inductively coupled plasma spectrometry
Pb	Lead
MSWD	Mean squared weighted deviation
Ma	Mega-annum; Million years
MH	Merelani Hills
M	Metamorphic
Mc	Meteoritic
CH_4	Methane
MI	Methylene iodide
Mi	Michigan
μm	Micron

MORB	Mid-ocean ridge basalt
mA	Milliamps
mg	Milligram
mL	Milliliter
mm	Millimeter
Myr	Million years
MQ	Milli-Q Water
Mo	Molybdenum
$(Ce)PO_4$	Monazite
Mnz	Monazite
Mk	Mudjatik Domain
nA	Nanoamps
nm	Nanometers
Nd	Neodymium
NH	New Hampshire
NY	New York
Ni	Nickle
HNO_3	Nitric acid
N	Nitrogen
NE	Northeast
NW	Northwest
NO	Norway
OAE	Ocean anoxic event
Ω	Ohm

ORS	Organic-rich sedimentary rocks
Os	Osmium
ppb	parts-per-billion
ppt	parts-per-trillion
PLc	Patterson Lake Corridor
%	Percent
‰	Parts per thousand or per mille
pg	Picrogram
K	Potassium
Py	Pyrite
P	Pressure
Qtz	Quartz
RCMS	Raman Carbonaceous Material Spectrometry
Re	Rhenium
Sm	Samarium
SK	Saskatchewan
SEM	Scanning electron microscope
SCT	Scotland
SIMS	Secondary Ionization Mass Spectrometry
σ	Sigma or one standard deviation of the mean
SiO	Silicates
STz	Snowbird Tectonic Zone
NaOH	Sodium hydroxide
SPT	Sodium polytungstate

SE	Southeast
Sp	Sphalerite
H_2SO_4	Sulfuric acid
SO_2	Sulfur dioxide
LK	Sri Lanka
Stlp	Stilpnomelane
To	Tantato Domain
TZ	Tanzania
Tzn	Tanzanite
T	Temperature
TIMS	Thermal Ionization Mass Spectrometry
Th	Thorium
TOC	Total organic carbon
THO	Trans-Hudson Orogen
Tsv	Tsavorite
UK	United Kingdom
USA	United States of America
U	Uranium
V	Vanadium
Vc	Vein core
Vr	Vein rim
VPDB	Vienna Pee Dee Belemnite
H_2O	Water
WDS	Wavelength dispersive spectrometers

Wt.%	Weight percent
Wn	Wollaston Domain
WMTZ	Wollaston-Mudjatik Transition Zone
XRD	X-ray Diffraction
yr	Year
Y	Yttrium
Zr	Zircon
$ZrSiO_4$	Zircon

1| Introduction

1.1. INTRODUCTION

Graphite (native hexagonal carbon) is one among a dozen or so minerals within in the mineral kingdom (5600+ minerals) that forms in 12 or more different formation conditions that include pre-solar, solar, and planetary settings (Hazen and Morrison, 2022). This diversity of paragenetic modes means that graphite is prevalent across a wide array of extraterrestrial (pre-solar grains, solar condensates, uralites, IAB irons) and terrestrial (metamorphic and hydrothermal) materials (Luque et al., 2013; Croat et al., 2014; Buseck and Beyssac, 2014; Rumble, 2014; Rubin and Ma, 2017).

Research into natural graphite has primarily been concerned with understanding graphite's origin through carbon isotope, fluid inclusion, and Raman/X-Ray Diffraction methods, which have provided key insights into the source (biological or abiological) and crystallization temperature (300℃ to 600℃) of graphitic carbon (Wada et al., 1994; Beyssac et al., 2002; Luque et al., 2012). However, a lack of direct age-dating techniques has hindered progress related to the timing of graphite-forming events. Building genetic models of ore formation at the deposit and district-scale, for example, requires a robust and precise chronology of graphite formation that has hitherto been lacking. These age-related deficits also hamper attempts at understanding the rates of graphite mineralization during metamorphic and hydrothermal events. Teasing apart such multi-generational events has, instead, relied on indirect age dating of mineral phases (i.e., zircon, monazite, and biotite) in adjoining host-rock materials that may or may not be synchronous with graphite formation (Silva, 1987; Ortega et al., 2010; Zang et al., 2014).

Developing a method to radiometrically date graphite is, therefore, instrumental for overcoming these shortcomings and building realistic models for graphite formation in terrestrial or extraterrestrial contexts. The research conducted herein (2019-2023) aims to overcome this technical hurdle by developing graphite into a viable geochronometer using the

Re-Os decay system and applying this novel dating technique to a series of case studies to test and then apply the method for resolving geological problems. The primary research questions herein, therefore, relate to whether (1) graphite can be reliably radiometrically dated using the Re-Os decay system and (2) graphite Re-Os dating can inform us about important geological processes related to graphite formation, such as ore mineralization, subduction metamorphism, and carbon cycling during mountain building events.

This approach is supplemented with other radiometric dating methods to ascertain a more robust chronology of graphite formation. Graphite formed from regional metamorphism, for example, may crystallize during multiple stages of the prograde to retrograde metamorphic cycle. Anchoring graphite Re-Os dates to a particular part of the cycle, therefore, requires additional geochronological tools, such as in-situ U-Pb monazite and zircon dating, to help constrain the various stages of mountain building (Regis et al., 2016; Schulz 2021 and references therein). Integrating U-Pb monazite/zircon dating with Re-Os graphite dating allows us to deconvolve prograde (metamorphic) graphite from retrograde (fluid-deposited) graphite. This approach is particularly relevant to one of our study sites, namely graphitic-pyritic shear zones beneath the Athabasca Basin in Saskatchewan, Canada, since these pre-Athabasca Supergroup structures record a complex interplay between polyphase metamorphism, hydrothermal alteration, and diagenetic overprinting (Jefferson et al., 2007; Mercadier et al., 2010).

Similarly, pyrite, which forms alongside graphite in many environments - shear zones included, is employed as a Re-Os geochronometer, and be used in parallel with Re-Os graphite dating to help corroborate the timing of high-temperature fluid events associated with retrograde metamorphism, high-pressure events association with subduction metamorphism, and fluid-flow events association with gemstone mineralization. Rhenium-osmium graphite dating could, then, provide a definitive account of carbonic fluid flow in shear zones interior and exterior to the Athabasca Basin, subduction zone graphitization, and graphite associated with gem formation. Together, these three approaches (U-Pb monazite/zircon, Re-Os pyrite,

and Re-Os graphite dating) provide a powerful trifecta of methods for delineating crustal graphite formation events.

Graphite Re-Os dating will also be paired with XRD/Raman crystallinity data to constrain the temperature of graphite formation and ^{13}C/^{12}C isotopes to constrain the source (organic vs inorganic) of graphitic carbon that collectively provide a more robust picture of graphite crystallization in the Earth's crust.

1.2. METHODS

1.2.1. Crustal Re-Os geochronology

Rhenium-osmium isotopes are utilized to obtain age information from graphite and pyrite by exploiting the natural radioactive decay of ^{187}Re into ^{187}Os in combination with the isochron method. The Re-Os isochron method for crustal sulfides and shales routinely yields radiometric dates with age uncertainties (<1% to 5%) sufficient to discriminate between multiple graphite/pyrite-forming events. Radiogenic Os incorporated into graphite/pyrite during crystallization (common Os) can in turn be used for Os source tracing purposes. Crust-mantle ^{187}Os/^{188}Os heterogeneities arise from Re being more incompatible than Os during mantle melting. As a result, the continental crust (^{187}Os/^{188}Os = 1.4) is markedly more enriched in radiogenic Os than the mantle (^{187}Os/^{188}Os = 0.13) (Peucker-Ehrenbrink and Ravizza, 2000; Meisel et al., 2001). By leveraging this fact, we can use the Os isotope composition of graphite and pyrite to distinguish between crust and mantle sources.

Graphites formed in-situ and/or allochthonous from sedimentary organic carbon can also provide maximum depositional age information for the sedimentary organic carbon protolith following graphitization/graphite deposition by rearranging the Re-Os isochron equation (Eq. 1) to solve for time (Eq. 2):

$$\text{Equation (1): } ^{187}\text{Os}/^{188}\text{Os}_{\text{IG}} = {}^{187}\text{Os}/^{188}\text{Os}_{\text{IP}} + {}^{187}\text{Re}/^{188}\text{Os}_{\text{IP}}(e^{\lambda t_d} - 1)$$

$$\text{Equation (2): } t_d = \frac{\ln(\dfrac{^{187}\text{Os}/^{188}\text{Os}_{\text{IG}} - {}^{187}\text{Os}/^{188}\text{Os}_{\text{IP}}}{^{187}\text{Re}/^{188}\text{Os}_{\text{IP}}} + 1)}{\lambda}$$

where $^{187}Os/^{188}Os_{IG}$ = initial $^{187}Os/^{188}Os$ ratio of graphite, $^{187}Os/^{188}Os_{IP}$ = initial $^{187}Os/^{188}Os$ ratio of sedimentary protolith inferred from mantle $^{187}Os/^{188}Os$ vales (>0.13) or greater, $^{187}Re/^{188}Os_{IP}$ = initial $^{187}Re/^{188}Os$ of sedimentary protolith inferred from a median $^{187}Re/^{188}Os$ shale value of 517 (Dubin and Peucker-Ehrenbrink, 2015), λ = ^{187}Re decay constant of 1.666 · 10^{-11} .a-1 (Smoliar et al., 1996), and t_d = time of sedimentary protolith deposition (yrs).

1.2.2. U-Pb geochronology

Uranium-lead isotopes are used here to obtain age information from monazite ((Ce,La, Th)PO$_4$) and zircon (ZrSiO$_4$) present in igneous and metamorphic rocks. Monazite and zircon are light rare earth element (LREE)-enriched phosphate and zirconium silicate minerals, respectively, with ppm-to wt.%-level U concentrations and negligible initial lead concentrations (Montel et al., 1996; Jackson and Montenari, 2019). This latter characteristic allows monazite and zircon U-Pb dates ($^{206}Pb/^{238}U$ and $^{207}Pb/^{235}U$) to be obtained from single crystals that are subsequently plotted on a Concordia diagram in $^{207}Pb/^{235}U$ –$^{206}Pb/^{238}U$ space.

1.2.3. $^{13}C/^{12}C$ isotopes

Carbon isotopes were employed here to trace graphitic carbon to biogenic (sedimentary organic carbon) or abiogenic (mantle vs. sedimentary inorganic carbon) sources by taking advantage of the C isotopic differences inherent to inorganic ($\delta^{13}C_{mantle}$ = -5.0 to -10.0 ‰, $\delta^{13}C_{carbonate}$ = +5.0 to -5.0 ‰,) verus organic ($\delta^{13}C_{organic\ carbon}$ = -15.0 to -40.0 ‰) carbon (Amari et al., 1990; Luque et al., 2012). By examining the C isotope compositions of fluid-deposited graphite, we can validate prior results that constrain the $\delta^{13}C$ values of certain studied graphites and evaluate the relationship between $^{187}Re/^{188}Os$ isotopic fractionation and C isotopic sources. Similarly, limited C isotope data on graphites associated with the pre-Athabasca shear zones imply biogenic carbon sources (Martz et al., 2017). By expanding on this current dataset, we can establish if there are any major C isotope variations that would imply mixing of multiple carbon sources.

1.2.4. Raman spectrometry and XRD crystallinity

Raman spectrometry and XRD crystallinity are used here to constrain the crystallization temperature of graphite. Graphitization (i.e., the conversion of sedimentary carbonaceous matter into well-crystallized hexagonal carbon) is primarily a temperature-driven process (Tagiri and Oba, 1986; Wada et al., 1994; Beyssac et al., 2002). We can thus estimate the temperature of graphite formation by analyzing graphite crystallinities using Raman spectrometry and XRD crystallinity data. Similarly, XRD crystallinity parameters, such as interplanar spacing and crystallite size, can be used in tandem with graphite trace element concentrations to understand trace element, Re and Os, occupancy in graphite.

1.2.5. Samples

Project samples were acquired from external collaborators (government and industry partners) and online mineral dealers. Graphitic-pyritic shear-hosted samples from the Athabasca area (northern Saskatchewan) were sourced from government core facilities in Alberta and Saskatchewan and industry collaborators with the remaining graphite samples sourced from online mineral distributors. Further details relating to sample selection and the analytical methods can be found in Chapters 2-4.

1.2. SCOPE AND OBJECTIVES

The main objects of this dissertation are tied to the development and application of graphite Re-Os dating to crustal systems and are described as follows:

1. **Develop graphite into a geochronometer using the Re-Os decay system**

   Characterize (i) the natural variation of Re in graphite, (ii) Re residency in graphite and (iii) establish graphite as a viable Re-Os geochronometer using the Re-Os decay system.

2. **Elucidate the role of graphite in Os cycling in subduction zones**

   Characterize the age of graphitization in the Franciscan subduction zone (Jurassic aged) of California and explore graphite as a potential mineralogical source of Os cycling in subduction zones.

3. **Characterize carbon cycling associated with Nuna assembly**

   Investigate large-scale carbon cycling in pre-Athabasca Supergroup shear zones (Alberta-Saskatchewan) associated with Paleoproterozoic mountain building events via Re-Os pyrite/graphite and U-Pb monazite/zircon dating.

2|Re-Os systematics and chronology of graphite

Abstract

Natural graphite forms in a range of metamorphic and hydrothermal environments across timelines spanning from the birth of the solar system, to the evolution of early Precambrian life, and the development of contemporary geotectonic cycles. A precise timeline of these and other graphite-forming events, however, has hitherto been obscured by a lack of radiometric ages and as such, chronologies are inferred from host-rock or hydrothermal mineral ages. Herein we examine the Re-Os systematics and chronology of graphite formed in a suite of terrestrial and extraterrestrial environments (n = 17) with the principal aim of establishing the viability of Re-Os geochronology of natural graphite.

Graphite Re and Os contents and isotopic ratios exhibit a wide range of values that extend up to 1520 ppb Re, 19,577 ppt Os, and 4101 and 42.18 for ^{187}Re/^{188}Os and ^{187}Os/^{188}Os ratios, respectively. These values are broadly comparable to those reported for crustal sulfides, organic-rich sedimentary rocks, and hydrocarbons. X-ray diffraction crystallinity data reveals that graphite Re abundances show a broadly inverse correlation with graphite formation temperature and crystallinity (d_{002} and $L_{c(002)}$) with interplanar spacing (d_{002}) having the strongest anti-correlation with graphite Re contents.

The viability of graphite Re-Os geochronology is demonstrated with two independent case studies (Wollaston-Mudjatik Transition shear zones, Saskatchewan, Canada and Merelani Hills, Tanzania) yielding precise (<1%) Re-Os isochron dates of 1731.52 ± 7.43 Ma (2σ; MSWD = 1.3) and 586.89 ± 2.39 Ma (2r; MSWD = 1.2) that are consistent, within uncertainty, to their mineralization ages constrained by other radiometric methods. These data confirm that graphite mineralization was synchronous with Trans-Hudsonian exhumation and tsavorite-tanzanite gemstone mineralization, respectively. Method accuracy, however, appears contingent on the analytical protocols used to isolate graphite, e.g. handpicking vs. heavy

liquids (SPT) and water, with the latter perturbing graphite Re-Os systematics by as much as 20%. We, therefore, recommend handpicking paired with magnetic separation and grain mount examination.

Our Re-Os age results are then coupled with new SIMS carbon isotope data (Wollaston-Mudjatik Transition graphite: $\delta^{13}C$ = -21.64 to -15.28‰; Merelani Hills graphite: $\delta^{13}C$ = -25.90 to -24.36 ‰) and $^{187}Os/^{188}Os_i$ isotope data (Wollaston-Mudjatik Transition graphite = 0.3119 ± 0.0037; Merelani Hills graphite = 1.680 ± 0.038) to constrain graphitic carbon to sedimentary carbonate/organic (Wollaston-Mudjatik Transition graphite) and organic (Merelani Hills graphite) carbon sources. This unique pairing of isotope systems in graphite provides the first detailed chronology of localized carbon mobility in the Earth's crust.

Re-Os graphite geochronology likely has wide applications in ore-deposit and metamorphic geology with the potential to reshape our understanding of carbon cycling in the crust-mantle system, and for graphite exploration initiatives that are critical for a global transition to a green economy.

2.1. INTRODUCTION

Graphite is an allotrope of carbon found extra- terrestrially in pre-solar grains (Amari et al., 1990; Croat et al., 2014) and IAB meteorites (Brett and Higgins, 1969; Rubin and Ma, 2017) and terrestrially in rocks formed by hydrothermal (Luque et al., 2013; Rumble, 2014) and metamorphic processes (Buseck and Beyssac, 2014). The physio- chemical processes that lead to graphite mineralization can vary from fluid mixing, to changes in P-T conditions, fluid-rock interactions, and changes in oxygen fugacity (Rumble, 2014), and result in morphologically diverse cubic, flaky, rosette, spherulitic, colloform and amorphous (cryptocrystalline) varieties (Brett and Higgins, 1969; Barraenechea et al., 2009). Graphite is also part of Earth's carbon cycle and a critical component of modern Li-ion battery technology upon which much energy storage relies (Jara et al., 2019). As such, exploration for commercially viable deposits of graphite is strategically important for accommodating society's increased demand for critical elements (Jara et al., 2019).

Although the origins of graphitic carbon have been studied in detail through carbon isotope analyses (Luque et al., 2012), the inability to directly date graphitic carbon has been a longstanding problem and has required researchers to infer the age of graphite mineralization from other sources (Silva, 1987; Ortega et al., 2010; Zhang et al. 2014). Rumble (2014) notes that ''Accurate understanding of the dynamics of hydrothermal graphite deposition is currently curtailed by a conspicuous lack of information on the chronology of graphite deposits." However, some of the impurities present in natural graphite include parts per million (ppm) levels of redox sensitive metals such as Fe, Ni, Cr, Co, V, and Mo (Watanabe and Narukawa, 2000; Ambrosi et al., 2012) suggesting that geochemically similar elements such as Re may also be present among this cohort of impurity metals. If so, then application of the ^{187}Re-^{187}Os decay system could provide an innovative solution to the graphite dating problem. Indeed, laboratory experiments have revealed that Re oxides/chlorides form Graphite Intercalation Compounds that provide support for this possibility (Scharff et al., 1991; Fröba et al., 1995), and recent measurements of Re-Os in natural graphite have yielded imprecise age data (Sun et al., 2021). However, the wider applicability and robustness of these prior Re-Os graphite measurements remain unconstrained.

Here we examine meteoritic (n = 1), hydrothermal (n = 12) and metamorphic (n = 4) graphite for Re and Os concentrations, isotopic ratios and XRD crystallinity, and show that graphite can contain Re and Os abundances that significantly exceed average upper continental crust levels (Chen et al., 2016). Further, we demonstrate using two independent case studies, from Canada and Tanzania, that precise (<1% 2σ) Re-Os age information can be obtained from crustal graphite. We then discuss these results with source tracer data for graphite (Secondary Ionization Mass Spectrometry (SIMS) C isotopes and ^{187}Os/^{188}Os$_i$ ratios) and thermometry data (XRD crystallinity and Raman spectroscopy) and speculate on the larger implications of Re-Os graphite dating on the geosciences.

2.2. GEOLOGICAL SETTINGS AND MATERIALS

To assess graphite Re concentrations, we initially surveyed a range of graphite localities (n = 17) in North and South America, Africa, Europe, and Asia (Fig. 2.1 and Fig. 2.2; Tables A1

and A4). Graphite specimens were either acquired from online mineral distributors or sampled directly from core facilities (e.g. Saskatchewan, CA) and include graphite formed via regional metamorphism of carbonaceous sediments in sedimentary basins (e.g. Merelani Hills, Tanzania) and subduction zone environments (e.g. Laytonville, California, USA) (Fig. 2.1), allochthonous fluid (abiotic and biotic) deposition in lower-mid crustal (e.g. Khatagaha Mine, Sri Lanka), magmatic (e.g., Borrowdale, England), and fault-controlled environments (e.g. Wollaston-Mudjatik Transition (WMT) shear zones, Canada) (Fig. 2.1), and nebular condensation (e.g. Canyon Diablo, USA; Fig. 2.1) [see Tables A1 and A4 for a comprehensive list]. A subset of these graphites (WMT, Canada and Merelani Hills, Tanzania) was then selected for Re-Os geochronology and SIMS $^{13}C/^{12}C$ isotope analysis based on existing age constraints for mineralization in the graphite host rocks, Re content of graphite, and ease of graphite separation from the bulk rock (refer to Appendix A for detailed hand sample and petrographic analysis).
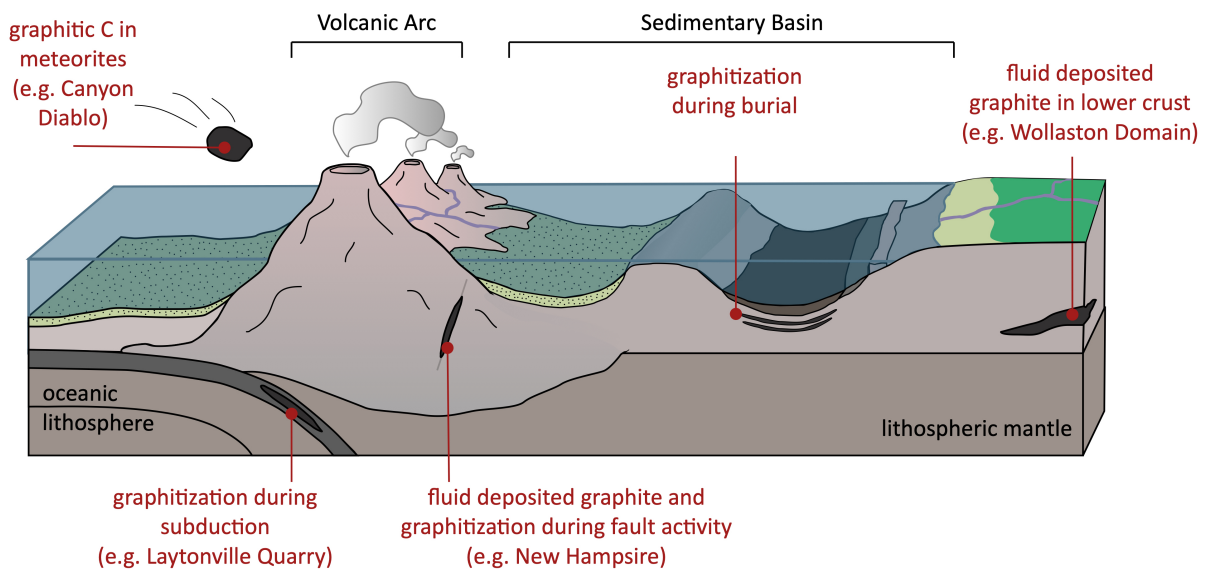
Figure 2.1. Typical graphite occurrences in the Earth's crust.

2.2.1. Wollaston-Mudjatik Transition graphitic shear zones, Saskatchewan, CA

Wollaston-Mudjatik Transition (WMT) graphite (northern Saskatchewan, Canada) occurs in metamorphosed Paleoproterozoic supracrustal rocks and shear zones underlying Paleo- to Mesoproterozoic (ca. 1710– 1540 Ma) Athabasca Supergroup sedimentary rocks with the latter (shear zones) being the foci for many late- forming (ca. 1550–1400 Ma) Athabasca uranium deposits (Jefferson et al., 2007; Jeanneret et al., 2017). Graphitization was purportedly initiated when carbonaceous metapelites ($\delta^{13}C$ = -28.6 to -20.2‰) were subjected to prograde (650℃) metamorphism during the Trans-Hudson orogeny (THO = 1840–1810 Ma). This graphitic carbon (±carbon in marbles) was subsequently redistributed by meteoric water and deposited as vein graphite ($\delta^{13}C$ = 29.5 to 22.7‰) in reactivated shear zones (this study's focus) as the THO entered its retrograde (450℃) uplift and unroofing stage (ca. 1775–1720 Ma) (Martz et al., 2017). An alternative, and/or compounding, driver for sedimentary (± mantle) carbon redistribution is a high-heat flow (fluid) event associated with the Kivalliq Igneous Suite (KIS = 1777–1720 Ma; Peterson et al., 2015; Adlakha and Hattori, 2021).

2.2.2. Merelani Hills Graphite, Arusha, Tanzania

Merelani Hills graphite (flaky) is associated with tsavorite (V-rich grossular) and tanzanite (V-rich zoisite) gemstone deposits in the Lelatema fold belt (Feneyrol et al., 2010). Metasedimentary sequences (Si-C-V-rich pelites, carbonates, and evaporites) in the region underwent upper amphibolite-facies metamorphism (650–750℃) during the East African Orogeny (ca. 650–605 Ma) (Feneyrol et al., 2013, 2017). Prograde metamorphism (ca. 600 Ma and >650℃) converted C-rich shales into graphitic ($\delta^{13}C$ = -25 to -24‰) ± pyritic gneisses and intercalated limestones-evaporites into calc-silicate tsavorite-bearing nodules (Olivier, 2006; Feneyrol et al., 2017). This event was followed by tanzanite (±quartz-tsavorite-graphite) veining and lensing related to rehydration during retrograde amphibolite-facies metamorphism (650 ± 50℃) (Olivier, 2006; Feneyrol et al., 2013). Carbon-bearing fluids (C-O-H(-N) system) precipitating this secondary graphite (and the subject of the study here) likely source endogenously from adjoining metapelites (Olivier, 2006; Feneyrol et al., 2017).

2.3. METHODS

2.3.1. Graphite mineral separation for Re-Os geochronology

Rock specimen JT20-MH from the Merelani Hills (Fig. A3a) was friable enough to be disaggregated by hand into its constituent mineral grains. Coarse-grained graphite (0.2–2.0 mm) was subsequently separated from the bulk aggregate by Frantz Isodynamic magnetic separation (1.74 A; tilt = 0˚). A similar methodology was employed for rock specimen JT20-05 (Fig. A2a) but graphite (±biotite and quartz) grains were crushed by ceramic mortar and pestle and sieved to 70–200 µm (1200 mg) and 200–325 µm grain sizes (150 mg) prior to Frantz Isodynamic magnetic separation. Coarse-grained (JT20-MH) and fine-grained (JT20-5) graphite were then split into five to seven 150– 400 mg aliquots according to their magnetic susceptibility (JT20-MH = 0.830–1.74 A and tilt = 0˚; JT20-05 = 0.27– 1.30 A and tilt = 25˚).

2.3.2. Grain mount preparation

Grain mounts and thin sections (Figs. A1-A5) were prepared at the University of Alberta's Thin Section Laboratory using standard polishing and abrading equipment. Six individual mineral separates (3- and 5-mm diameter discs) were allocated for each grain mount, which were epoxy sealed and polished for microanalysis. Mount preparation for SIMS carbon isotope analysis was carried out within the Canadian Centre for Isotopic Microanalysis (CCIM), University of Alberta. Mount M1648 comprised of small discs (~2.5- and 3.0-mm diameter) cored from polished thin-sections (JT20-5 and JT20-MH; Figs. A1-A3) and included CCIM vitreous carbon reference material (RM) S0233A for calibration. Mount M1648 was coated with 20 nm of Au prior to scanning electron microscopy (SEM) using a Zeiss EVO MA15 instrument, operating at 20 kV and 3 nA beam current, and then an additional 80 nm prior to SIMS analysis.

Figure 2.2. Rhenium concentrations of various graphite samples. Re_{UCC} = average Re content of the upper continental crust = 0.25 ± 0.12 pbb (Chen et al., 2016). Graphites >1-2 ppb Re are potentially dateable (see *section 2.6.4* for detail). Re_{SF}, Re_{ORS}, and Re_{moly} refers to median Re values for sulfides (8.34 ppb), organic-rich sediments (33.90 ppb), and molybdenites (86980 ppb). Plot is in log format.

2.3.3. Re-Os isotopes

Rhenium and osmium isotope geochemistry was conducted at the University of Alberta's Re-Os crustal geochronology laboratory. Graphite (16–80 mg) aliquots were digested in borosilicate glass Carius tubes using an 8 mL (1:1) mixture of 4 N H_2SO_4 and 4 N CrO_3-H_2SO_4 (0.5 g CrO3 per 1mL of 4 N H_2SO_4) and a known amount of ^{185}Re-^{190}Os mixed spike (UA3) over a

period of 72 h at 240˚C (see Section 2.4.2 and 2.5.2 and Figs. 2.4 and 2.5 for detailed digestion experiments). Samples were subsequently frozen in dry ice-ethanol baths and processed via standard chloroform extraction for Os (Toma et al., 2020) and acetone extraction for Re (Li et al., 2009) procedures. Rhenium and osmium were then purified by anion exchange chromatography (Toma et al., 2020) and microdistillation (Birck et al., 1997), respectively.

Aliquots of Re and Os were loaded onto Ni and Pt filaments and coated with $Ba(NO_3)_2$ and $Ba(OH)_2$ salts. Rhenium and osmium isotope measurements were subsequently performed on a Thermo Scientific Triton Thermal Ionization Mass Spectrometer in negative polarity mode (N-TIMS) using static Faraday collectors and secondary electron multipliers. Instrument performance was monitored over a 4-month period using in-house laboratory standard AB2, which yielded $^{187}Os/^{188}Os$ and $^{185}Re/^{187}Re$ ratios of 0.10680 ± 0.00018 and 0.59791 ± 0.0008 (1σ). Post-analysis data reduction included mass bias corrections, isobaric oxide corrections, blank corrections, and spike-sample unmixing (isotope dilution). Average Re and Os procedural blank concentrations were 11.4 ± 2.7 pg and 0.07 ± 0.04 pg, with a $^{187}Os/^{188}Os$ ratio of 0.25 ± 0.13. All ages were generated using IsoplotR (Vermeesch, 2018) and are reported as Model 1 ages (MSWD 1; probability of fit >0.15; ^{187}Re decay constant = 1.666e11.a-1 (±0.31%; Smoliar et al., 1996)).

2.3.4. In-situ carbon isotopes

Isotopes of carbon ($^{13}C/^{12}C$) were measured using the Cameca IMS-1280 multi-collector ion microprobe at CCIM. Analytical methods for C-isotopes follow those established for diamond (Stern et al., 2014). Primary beam conditions included the use of 20 keV $^{133}Cs^+$ ions focused to a diameter ~ 15 mm and beam currents of ~ 1.5 nA. The primary beam was rastered across a 20 x 20 μm area for 30 s prior to analysis, to clean the surface of Au and contaminants, and implant Cs. The normal incidence electron gun was not utilized. Negative secondary ions were extracted through 10 kV potential to the grounded secondary column (Transfer section). Automated tuning of the secondary ions in the Transfer section preceded each analysis. Secondary ion collection conditions for C-isotopes included an entrance slit width of 110 μm, field aperture of 5 x 5 mm, a field aperture-to-sample magnification of 100, and a fully-open

energy slit. Both ^{12}C and ^{13}C were analyzed simultaneously in Faraday cups (L'2 using $10^{10}\,\Omega$ amplifier, and FC2 with $10^{11}\,\Omega$) at mass resolutions of 2000 and 2900, respectively. Faraday cup baselines were determined once at the start of the session. Mean count rates for $^{12}C^-$ and $^{13}C^-$ were typically 1.0×10^9 and 1.1×10^7 counts/s, respectively, determined over a 60 s counting interval, with total analysis time of 210 s. The analytical sequence interspersed measurements of unknowns with the vitreous carbon RM S0233A, having $\delta^{13}C_{VPDB}$ = -21.6 ±0.5 ‰ in a 4:1 ratio. The standard deviation of the the $^{13}C^-/^{12}C$ values for S0233A was ± 0.06‰ after correction for systematic within-session drift of <0.5‰. Uncertainties of individual $\delta^{13}C_{VPDB}$ analyses average ±0.15 ‰ (2σ). Separate to this study, analyses of CCIM Bogola Mine graphite S0294 referenced to S0233A yield $\delta^{13}C_{VPDB}$ ~ -7.2 ±0.3 ‰ (1 standard deviation), consistent with the range of conventionally-determined values of -7.0‰ to -9.0‰ (Dobner et al., 1978). Carbon isotope data are reported here in delta notation normalized to Vienna Pee Dee Belemnite (VPDB) standard.

2.3.5. X-ray diffraction and Raman spectroscopy

X-ray diffraction and Raman spectroscopy analyses were conducted at the University of Alberta's X-ray Diffraction and Fluid Inclusion Laboratories, respectively.

X-ray diffraction was performed on a Rigaku Ultimate IV x-ray diffractometer fixed with a cobalt anode (38 kV and 38 mA) and D/Tex Ultra Scintillation detectors (Fe filter) arranged in Bragg-Brentano geometries. Powdered samples were mounted onto zero background plates using ethanol and scanned with $K\alpha_1(100)$ [1.54060 Å] wave- lengths. Peak information (i.e. height, area and full width at half maximum) was processed with JADE 9.6 software and phase identification was done using DIFFRAC.EVA software with the 2021 ICDD PDF 4+ and PDF 4+/ Organics databases. Graphite crystallite size and thermometry data was calculated according to Wada et al. (1994).

Raman spectra were acquired in backscattered geometry using a Horiba LabRAM HR Evolution Raman micro- scope, an excitation wavelength of 532 nm focused through a 100x objective lens, an 1800 grooves/mm grating, and a confocal hole of 50 mm. Spectra were

recorded over the first-order band range of carbonaceous material from 1100 to 1800 cm^1. Peak fitting was done using a PseudoVoigt function in the peak- and curve-fitting software Fityk (Wojdyr, 2010), which involved baseline corrections followed by peak fitting centered at ca. 1355 cm^{-1} (D1 band) and 1580 cm^{-1} (G band). Crystallization temperatures were estimated according to Beyssac et al. (2002).

2.4. EXPERIMENTAL

2.4.1. Re-Os graphite leaching experiments

Standardized workflows for Re-Os isotope analysis include physically separating host-analyte phases (e.g. sulfides) from rock aggregate according to their density and/or magnetic susceptibility prior to chemical treatment and mass spectrometric analysis (Stein, 2014; Saintilan et al., 2020). The most common density separation procedures either involve heavy liquids (e.g. sodium polytungstate (SPT) or methylene iodine or water to isolate the target mineral phase. These procedures have been in use for decades and show no evidence of disrupting the Re-Os systematics of sulfides (Hnatyshin et al., 2019), although Re has been shown to leach from bulk organic matter under laboratory conditions (Selby and Creaser, 2003), and the Re-Os systems in weathered shales have been shown to be disturbed (Georgiev et al., 2012). With this in mind, we have designed experiments using SPT and ultrapure deionized (18.2 MΩ) Milli-pore water to test the effects of liquid density separation on graphite Re- Os systematics.

Graphite separates JT20-MH-NM-1.74-SPT and JT20- 5-NM-1.40-SPT were treated with 250-mL of SPT (density = 2.3 g/cm^3) housed in individual separatory funnels that were manually rotated in a clockwise motion to fully immerse the graphite in SPT. After five-minutes, the suspension was decanted into another funnel where SPT was separated from graphite via gravity filtration. Graphite was subsequently rinsed with ethanol to remove any residual SPT and placed on a hot plate (T = 80℃) to dry.

Graphite separates JT20-MH-BULK-MQ1 and JT20-5- NM-0.4-MQ1/MQ2 were treated with 3-mL of ultrapure deionized (18.2 MΩ) Milli-pore water housed in a 22-mL glass vial that

was capped and left for 5 min (JT20-MH-NM-1.74-MQ1; T = 23.7°C), 24 hours (JT20-5-NM-0.4-MQ2; T = 87.5°C), and 5 days (JT20-5-NM-0.4-MQ1; T = 23.7°C). Graphite specimens were then separated from the water treatment solution using gravity filtration, followed by an ethanol rinse.
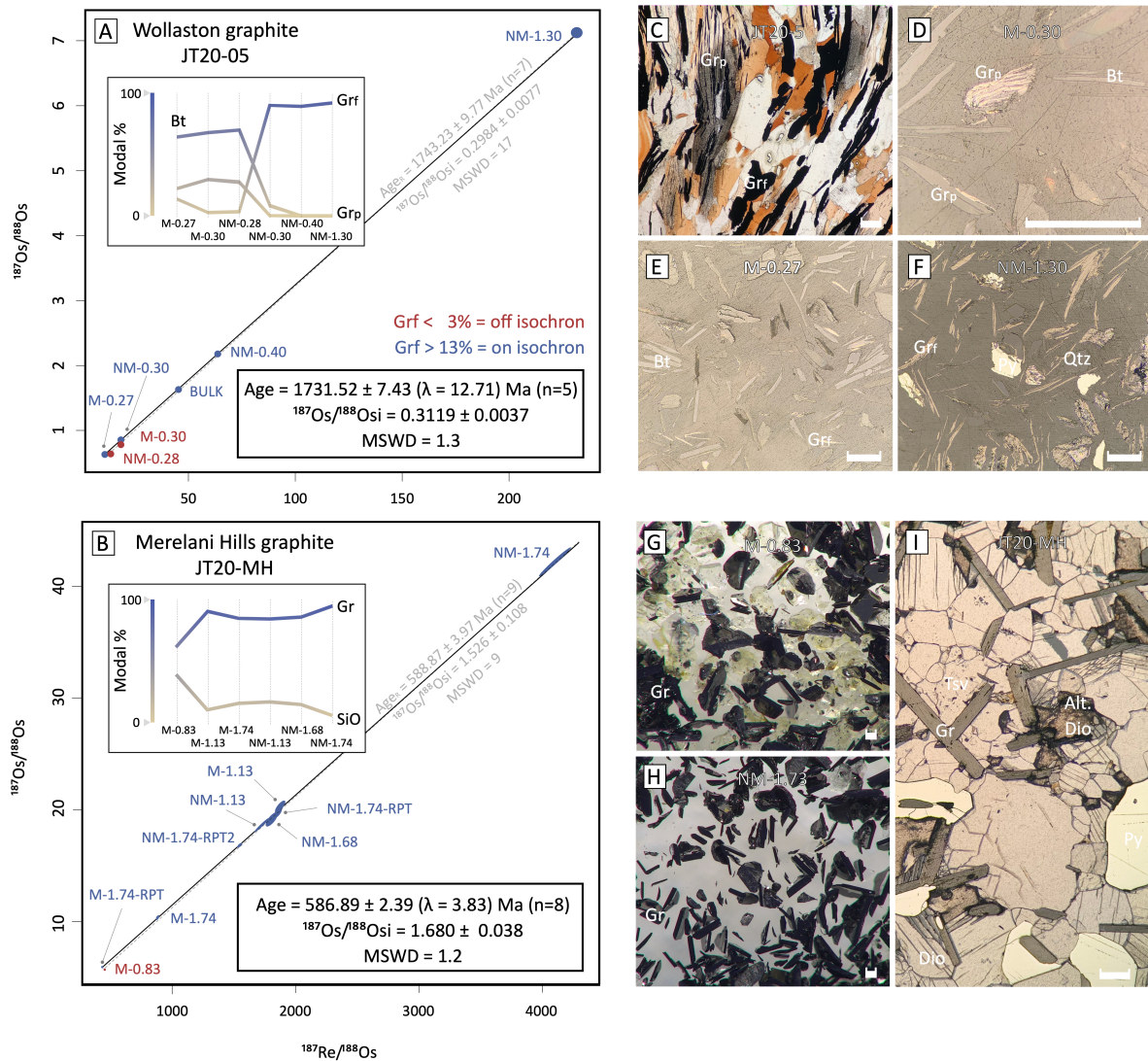
Figure 2.3. Re-Os graphite isochrons of (a) Wollaston-Mudjatik Transition (JT20-5) and (b) Merelani Hills (JT20-MH) graphite (IsoplotR; Vermeesch, 2018). Error ellipses are reported in 2σ notation but are smaller than the symbols in (a) and thus not shown. Re-Os isochron ages were calculated using the [187]Re decay constant of Smoliar et al. (1996) and include decay constant uncertainties (λ = 1.666·10⁻¹¹ ± 0.31%) in brackets. Graphical insert (a) depicts modal percent abundances for biotite (Bt) and fully (Gr$_f$) and partially (Gr$_p$) formed graphite for each mineral separate, whereas graphical insert (b) shows graphite (Gr) and silicate (SiO) abundances. Blue and red text in (a) and (b) refer to datapoints included or rejected from the accepted isochron age (black text) based on textural and modal percentage estimates (also see Table 2), whereas grey text/dashed line refers to rejected isochron ages (Age$_R$).

Transmitted (c) and reflected light (d-f) photomicrographs of JT20-5 show Gr_f and Gr_p and biotite (Bt) and quartz (Qtz) (d-f) and a progression from Gr_f-poor (d) to Gr_f-rich (f) in grain mounts M-0.30, M-0.27, and NM-1.30. Plane (g-h) and reflected light (i) photomicrographs of JT20-MH depict graphite-included in altered-silicates (g) and pure graphite (h) in grain mounts M-0.83 and NM-1.73 and tsavorite (Tsv), Gr, pyrite (Py) and altered (Alt. Dio) and non-altered diopside (Dio) in thin section. Scale bar is 200 μm.

2.4.2. Graphite digestion experiments

Graphite decomposition experiments were performed using an adaption of the Carius tube method (Shirey and Walker, 1995). Experimental parameters that were adjusted during the investigation include (1) the digestion medium/ volume of medium (inverse aqua regia-H_2O_2, CrO_3-H_2SO_4 mixture, and concentrated HNO_3-H_2SO_4) and (2) the digestion period (24- and 72-hour intervals), whereas the digestion temperature was held constant at 240°C for each experimental run. Inverse aqua regia-H_2O_2, and concentrated HNO_3-H_2SO_4 were selected for testing based on previous graphite decomposition literature (Watanabe and Narukawa, 2000; Sun et al., 2021).

Four 50–80 mg coarse-grained (0.2–2.0 mm) graphite aliquots (JT20-MH-A, -B, -C, and -D) were added to four individual borosilicate glass Carius tubes. Carius tubes labeled JT20-MH-A and -B were filled with 8 mL of inverse aqua regia (3:1 ratio of concentrated HNO3 and HCl) and 0.5 mL of 30% H_2O_2 and digested under closed-vessel conditions in a convection oven for 24- and 72-h intervals at 240°C, whereas Carius tubes labeled JT20-MH-C and JT20-MH-D were filled with a 1:1 8 mL mixture of 4 N H_2SO_4 and 4 N CrO_3-H_2SO_4 (0.5 g CrO_3 per 1mL of 4 N H_2SO_4) over analogous digestion periods and temperatures. An additional seven Carius tubes (JT20-MH-E, -F, -G, -H, -I, -J, and -K) housing comparable amounts of coarse-grained graphite (100 mg) were filled with 8 mL of (1) concentrated HNO_3 and H_2SO_4 at 7:1 (-E), 3:1 (-F), and 2:1 (-G) ratio mixtures and (2) 4 N H_2SO_4 and 4 N CrO_3-H_2SO_4 at 7:1 (-H), 3:1 (-I), 5:3 (-J), and 1:1 (-K) ratio mixtures, sealed with a blow torch, and digested in a convection oven for 72-h at 240 °C.

2.5. RESULTS

2.5.1. Descriptions of mineral separates

Mineral separates from the Wollaston-Mudjatik Transition shear zones (JT20-05) contain various mixtures of graphite, quartz, biotite, and pyrite (Table A2). Mineral separates have estimated modal proportions of graphite and pyrite ranging from 30 to 91% and 1 to 5%. The largest proportion of graphite (88–91%) is found in the least magnetic fractions (NM-0.30, NM-0.40 and NM-1.30) with the residual 9–11% comprising pyrite, biotite, and quartz (Fig. 2.3a graphical insert; Fig. A4). The remaining separates (M-0.27, M-0.30, NM-0.28) have varying amounts of graphite (30–35%), biotite (63–70%) and pyrite (0–1%) (Fig. 2.3a, d-f). Graphite in mineral separates M-0.27, M-0.30, and NM-0.28 is either fully (2–13%) or partially (22–29%) formed with the latter graphite exhibiting incomplete graphite-biotite replacement and/or being encased in biotite sheaths (Fig. 2.3c/d; see Appendix A for notes on nomenclature).

Mineral separates from Merelani Hills (JT20-MH) contain graphite, pyrite, quartz, diopside, and tsavorite (Table A2). Mineral separates have estimated modal proportions of graphite and pyrite ranging from 61% to 95% and 0 to 1% (Table A2 and Fig. 2.3b graphical insert, e/h; Fig. A5). The remaining 5 to 38% are silicate phases (quartz, diopside, and tsavorite). Diopside and tsavorite are concentrated in the most magnetic fractions (M-0.83 and M-1.13). Mineral separate M-0.83 is notable for containing the largest proportion of silicate phases at 38%, many of which contain graphite inclusions and show alteration along their periphery (Fig. 2.3g/i).

Wollaston-Mudjatik Transition and Merelani Hills graphite grains were also examined for micro- to nanometer-sized inclusions of pyrite or other sulfides via SEM imaging. However, the only visible inclusions observed at the 1-10 µm scale were silicates (WMT = biotite; Merelani Hills = diopside/quartz) rather than sulfides (see Fig. A6).
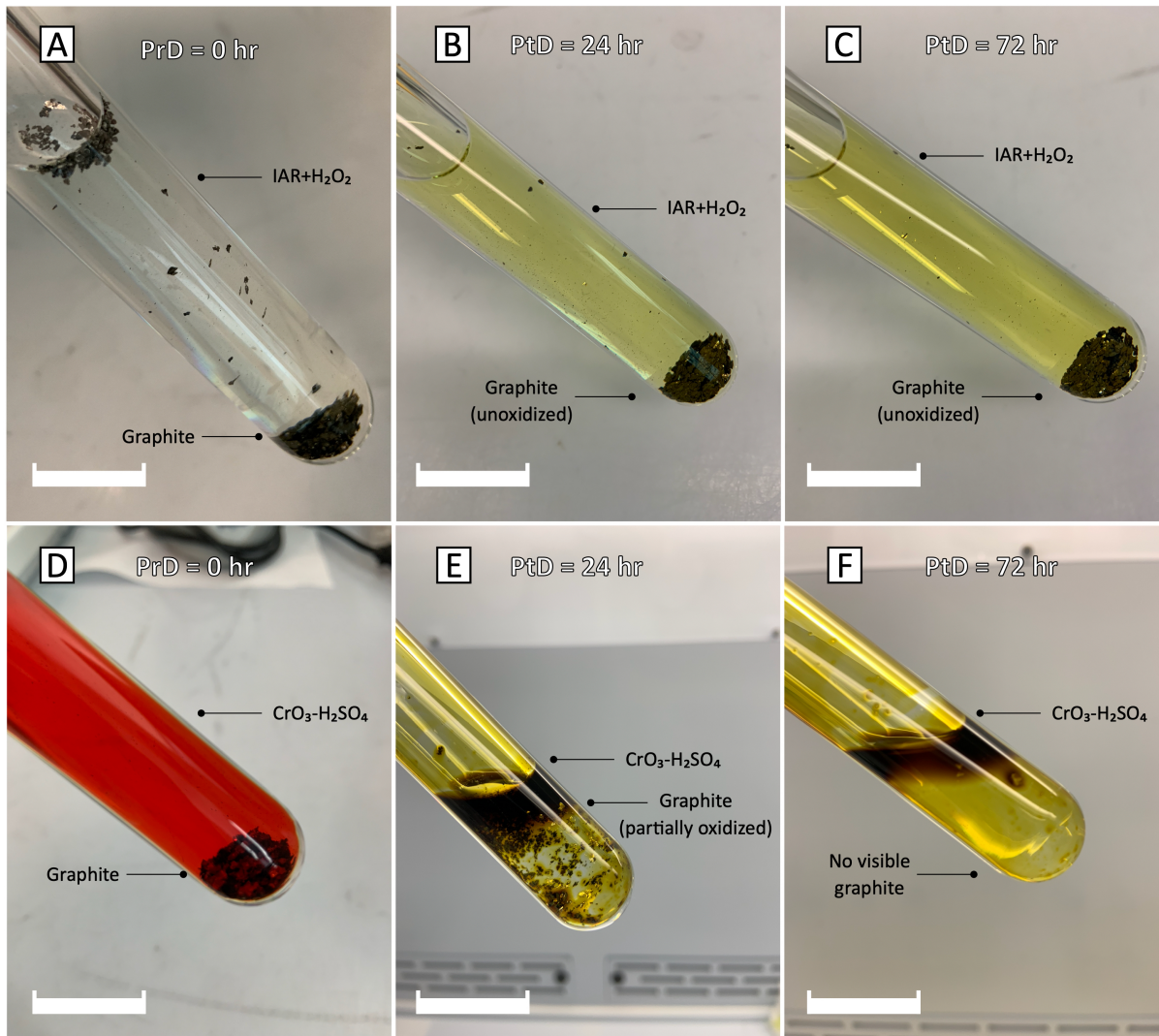
Figure 2.4. Photographs depicting pre- (a = inverse aqua regia-H_2O_2 mixture and d = CrO_3-H_2SO_4 mixture) and post-digested (b, c, e, and f) graphite samples. Unoxidized graphite after (b) 24-hour and (c) 72-hour digestion periods at 240˚C using 8 mL of inverse aqua regia (3:1 ratio of concentrated HNO_3 and HCl) and 0.5 mL of 30% H_2O_2 via the Carius tube method. Partially (e) and fully (f) oxidized graphite after 24-hour and 72-hour digestion periods at 240˚C using a 1:1 8 mL mixture of 4 N H_2SO_4 and 4 N CrO_3-H_2SO_4 (0.5 g CrO3 per 1mL of 4 N H_2SO_4) via the Carius tube method. Scale bar is 1.75 cm. Prd = Pre-digestion; PtD = Post-digestion; IAR = inverse aqua regia.

2.5.2. Graphite digestions

Carius tubes JT20-MH-A and -B contained equal proportions of unoxidized graphite irrespective of the digestion period (24- and 72-h intervals) (Fig. 2.4a-c). Comparably, graphite remained unoxidized in Carius tubes JT20-MH- E, -F, and -G after their respective digestion

periods (not shown). However, Carius tubes JT20-MH-C and -D exhibit partial to complete oxidization after 24-h and 72-h (Fig. 2.4d- f). From these observations we conclude that the inverse aqua regia-H_2O_2 mixture and concentrated HNO_3 and H_2SO_4 mixtures employed here are inadequate for decomposing graphite, whereas the CrO_3-H_2SO_4 mixture is sufficient at dissolving graphite after a 72-h, but not a 24-h, digestion period at 240˚C.

Carius tubes JT20-MH-H, -I, -J, and -K contained various amounts of unoxidized graphite following a digestion period of 72-h at 240˚C (Fig. 2.5). However, the amount of unoxidized graphite inversely correlated with the volume of 4 N CrO_3-H_2SO_4 housed in each sample Carius tube. For example, ca. 45/100, 14/100, 6/100, and 5/100 mg of unoxidized graphite remained in Carius tubes housing 1 mL (JT20-MH-H), 2 mL (JT20-MH-I), 3 mL (JT20-MH-J), and 4 mL (JT20-MH-K) of 4 N CrO_3-H_2SO_4 (Fig. 2.5a). Hexavalent (red) chromium was completely to near-completely reduced to trivalent (green-blue) chromium in Carius tubes JT20-MH-H and -I, but not -J and -K, implying full to near-full exhaustion of the Cr(VI) oxidant in the former two samples (Fig. 2.5b-e). Slow reaction kinetics likely inhibited complete oxidation of graphite in the latter two samples.
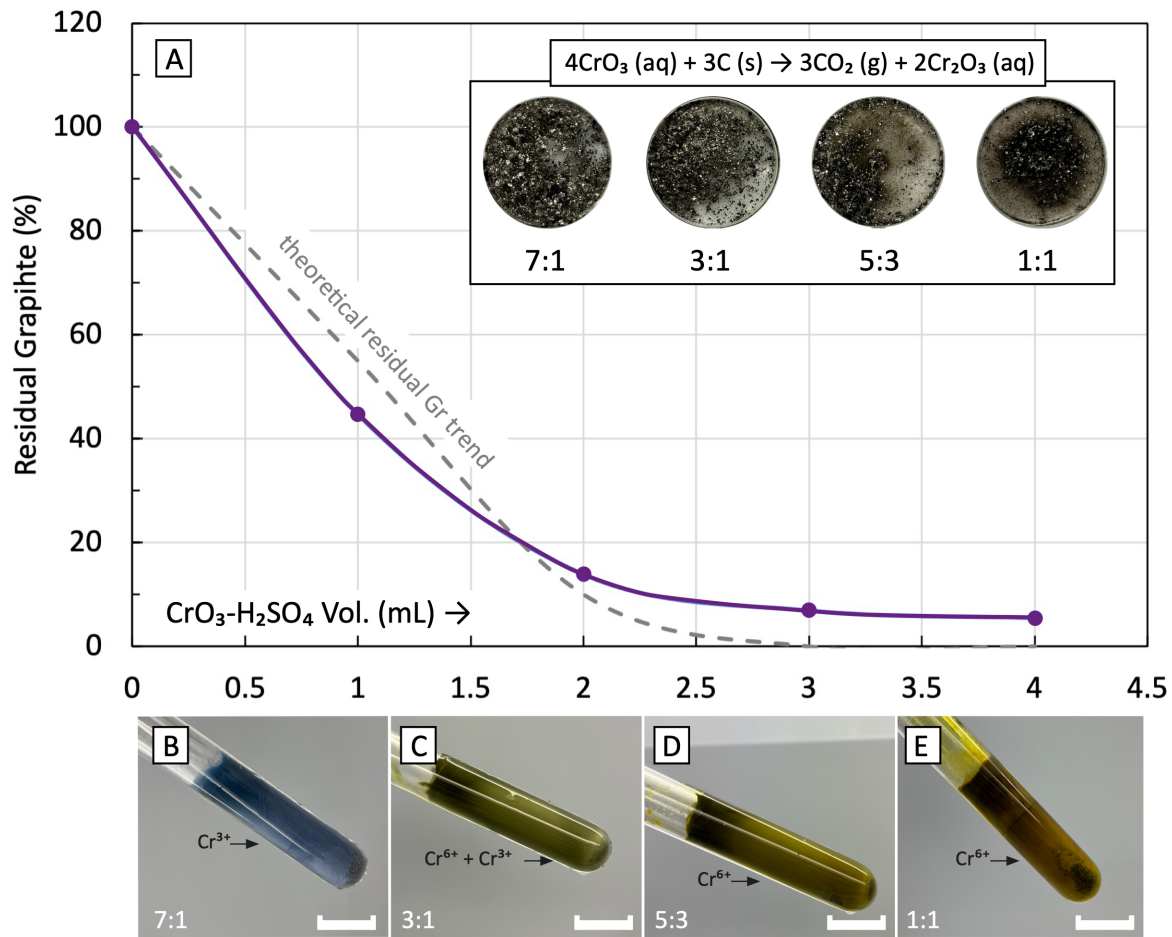
Figure 2.5. Graphite decomposition experiments involving 7:1, 3:1, 5:3, and 1:1 8 mL mixtures of 4 N H_2SO_4 and 4 N CrO_3-H_2SO_4 (0.5 g CrO3 per 1mL of 4 N H_2SO_4). Plot (a) depicts the relationship between volume of 4 N CrO_3-H_2SO_4 and residual (unoxidized) graphite post-digestion. Panel insert in plot (a) shows residual graphite recovered (diameter = 2.5 cm), whereas panels (b-e) show oxidation state of Cr in CrO_3-H_2SO_4 mixture post-digestion. Scale bar = 1.75 cm.

2.5.3. Re and Os graphite concentrations

The entire suite of bulk graphite Re concentrations (n = 17) range from 0.2 to 1520.2 ppb. Metamorphic graphite exhibits the highest Re concentrations (Re = 0.6–1520.2 ppb), followed by meteoritic graphite (Re = 87.2 pp b), and finally hydrothermal graphite (Re = 0.2–71.4 ppb) (Table A1; Fig. 2.2). A subset of the bulk graphite samples (n = 6) have Os concentrations that range from 89 to 19,577 ppt (Table A3).

Graphite processed via mineral separation (JT20-MH and JT20-5) exhibits Re and Os concentrations that range from 6.8 to 71.5 ppb and 171 to 7550 ppt. Measured Re and Os concentrations are highest in separates with the highest modal proportions of graphite (JT20-5-M-0.27/M- 0.30/NM-0.28; JT20-MH-M-0.83) and lowest in the samples with the lowest modal percent graphite. Both bulk graphite and mineral separate graphite ^{187}Re/^{188}Os and ^{187}Os/^{188}Os ratios (n = 25) range from 10.8 to 4100.9 and 0.5658 to 42.1781 and display no discernable pattern between graphite type and Re/Os fractionation (Table A3).

2.5.4. Re-Os geochronology

Graphite separates from Wollaston-Mudjatik Transition shear zones (JT20-5) and Merelani Hills (JT20-MH) yield Model 3 isochrons with Re-Os dates of 1743.23 ± 9.77 Ma (2σ; MSWD = 17; n = 7; Fig. 3.3a) and 588.87 ± 3.97 Ma (2σ; MSWD = 9.2; n = 9; Fig. 3.3b), respectively, and ^{187}Os/^{188}Os initial ratios of 0.2984 ± 0.0077 (2σ) and 1.526 ± 0.108 (2σ), respectively. However, rejecting mineral separates with the largest abundance of partially formed graphite (JT20-5-M-0.30/M-28; Fig. 3.3d) or graphite-included silicates (JT20-MH-M-0.83; Fig. 3.3g-i) yields Model 1 isochrons with Re-Os dates of 1731.52 ± 7.48 Ma (2σ; MSWD = 1.3; n = 5; Fig. 3.3a) and 586.89 ± 2.39 Ma (2σ; MSWD = 1.2; n = 8; Fig. 3.3b), respectively, and ^{187}Os/^{188}Os initial ratios of 0.3119 ± 0.0037 (2σ) and 1.680 ± 0.038 (2σ), respectively.

2.5.5. Re-Os leaching experiments

Graphite treated with ultrapure deionized (18.2 MΩ) Milli-pore water (T = 23.5°C) exhibits systematically lower ^{187}Re/^{188}Os ratios (JT20-5-NM-0.4-MQ1 = -4%; JT20-M H-BULK = -5%; JT20-5-NM-0.4-MQ2 = -10%) relative to the reference isochron for both samples (Fig. 2.6a/b; Table A3). This negative shift in ^{187}Re/^{188}Os isotope ratios yields predictably steeper isochron slopes, older absolute ages, and an overall increase in age uncertainties by a factor of 4 and implies Re was leached preferentially over Os (Fig. 2.6a/b). Negative ^{187}Re/^{188}Os fractionation (10%) also appears to scale with temperature (T = 87.5°C). In contrast, graphite treated with SPT (T = 23.5 °C) exhibits systematically higher ^{187}Re/^{188}Os ratios (JT20-MN-NM-1.74- SPT = 3%; JT20-5-NM-1.30-SPT = 18%) relative to each reference isochron (Fig. 2.6a/b;

Table A3). This positive shift in ^{187}Re/^{188}Os ratios in turn resulted in shallower isochron slopes, younger absolute ages, and both increases (JT20-5: 5%) and decreases (JT20-MH = 0.3%) in age uncertainties and suggests Os was leached preferentially over Re.
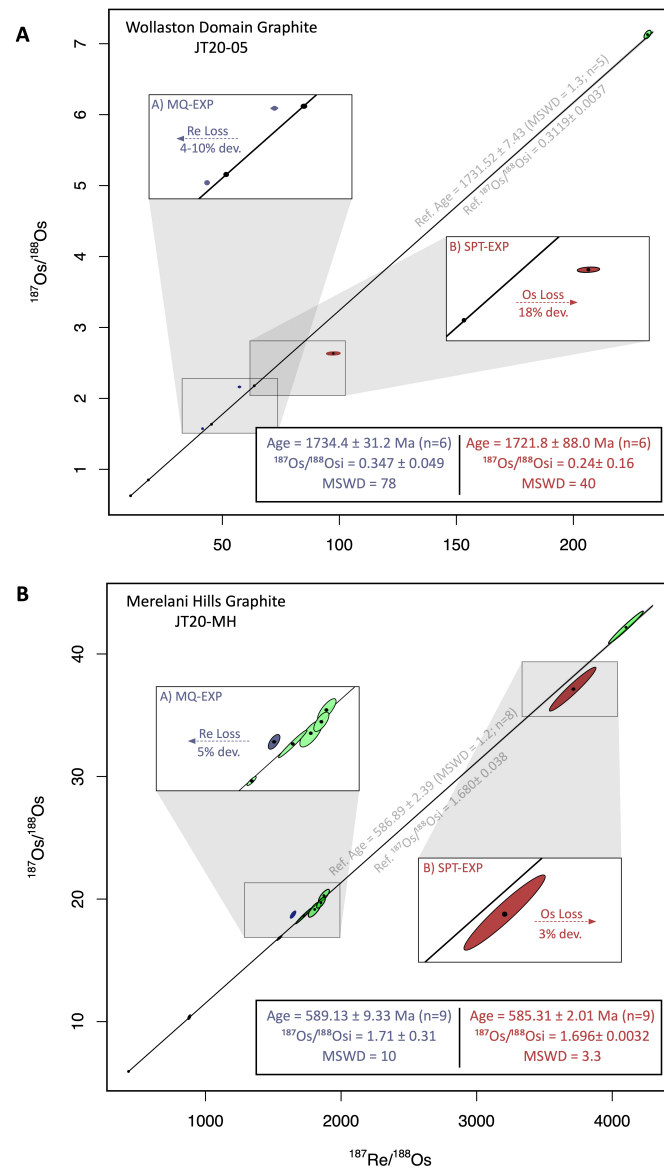
Figure 2.6. Rhenium-osmium water-treated (blue) and SPT-treated (red) graphite data plotted on each datasets reference Re/Os isochron (ref. Re/Os age and ^{187}Os/^{188}Os values shown in grey). Water-treated and SPT-treated graphite (plot (a) = Wollaston-Mudjatik Transition/JT20-5; plot (b) = Merelani Hills/JT20-MH) exhibit ^{187}Re/^{188}Os values that plot to left (Re loss) and to the right (Os loss) of each datasets reference Re/Os isochron and yield spurious Re-Os age and ^{187}Os/^{188}Os uncertainties and MSWD values.

2.5.6. SIMS $^{13}C/^{12}C$ isotopes

SIMS carbon isotope analysis of Merelani Hills (JT20- MH) and Wollaston-Mudjatik Transition shear zone (JT20-5) graphite yield $\delta^{13}C$ values that range from -25.90 to -24.35‰ ($\delta^{13}C_{avg}$ = -24.82 ± 0.72‰; 2σ; n = 113) and -21.64 to -15.28‰ ($\delta^{13}C_{avg}$ = -18.28 ± 2.19‰; 2σ; n = 65, respectively, which amounts to a < 1‰ and ca. 5‰ variation in $\delta^{13}C$ on an inter- and intra-grain scale (Fig. 2.7; Table A5).
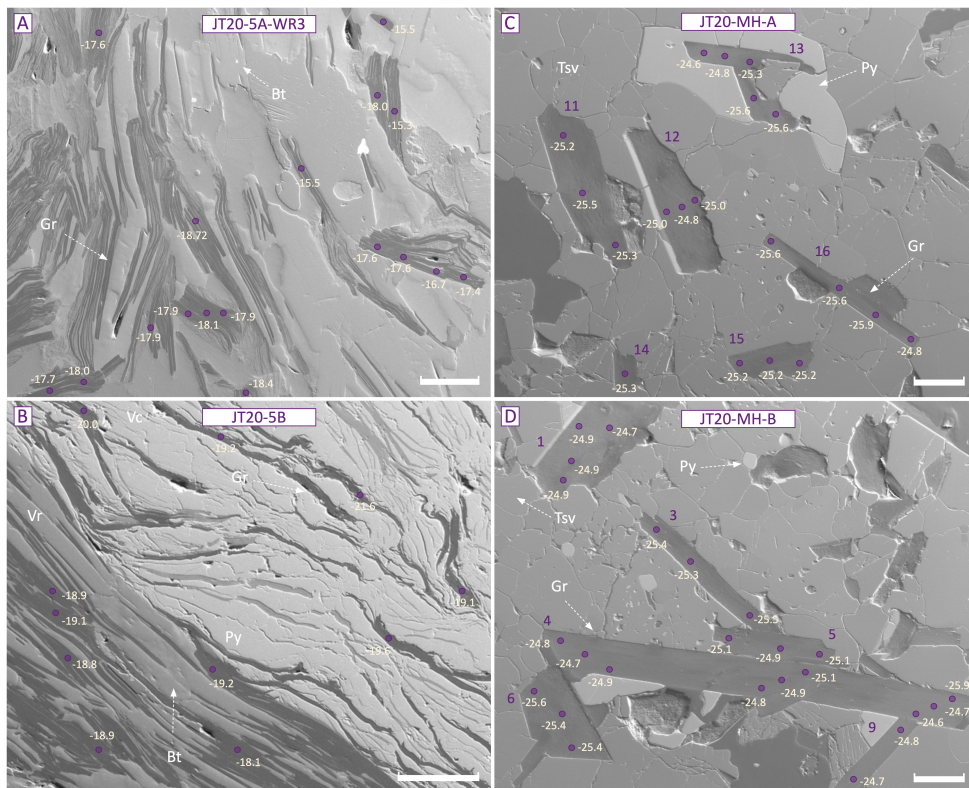
Figure 2.7. BSE images and SIMS $\delta^{13}C$ values of (a-b) Wollaston-Mudjatik Transition (JT20-5A/B) and (c-d) Merelani Hills (JT20-MH-A/B) graphite. (a) $\delta^{13}C$ values of graphite replacing biotite in wall rock (WR) distal to the pyrite-graphite-biotite vein (V) in JT20-5, (b) $\delta^{13}C$ values of graphite within the veins core (Vc) and rim (Vr) in JT20-5, and (c-d) inter- and intragrain $\delta^{13}C$ values of graphite in JT20-MH-A/B. Carbon isotopes are reported in delta (δ) notation normalized to standard VPDB and have uncertainties on the order of ± 0.08 to 0.18 (2σ). Scale bar is 200 μm.

2.5.7. Graphite crystallinity

The entire suite of graphite samples (n = 17) display diffraction angles and $d_{(002)}$ spacing of ca. 26° and 3.341-3.375 Å and yield corresponding crystallite sizes ($L_{c(002)}$) of 160–690 Å (Table A1; Fig. 2.8). Calculated crystallization temperatures for metamorphic graphite correlate broadly with metamorphic grade and range from 414 to 846°C, whereas temperatures for hydrothermal graphite range from 520 to 955°C (Tagiri and Oba, 1986; Wada et al., 1994) (Table A1).
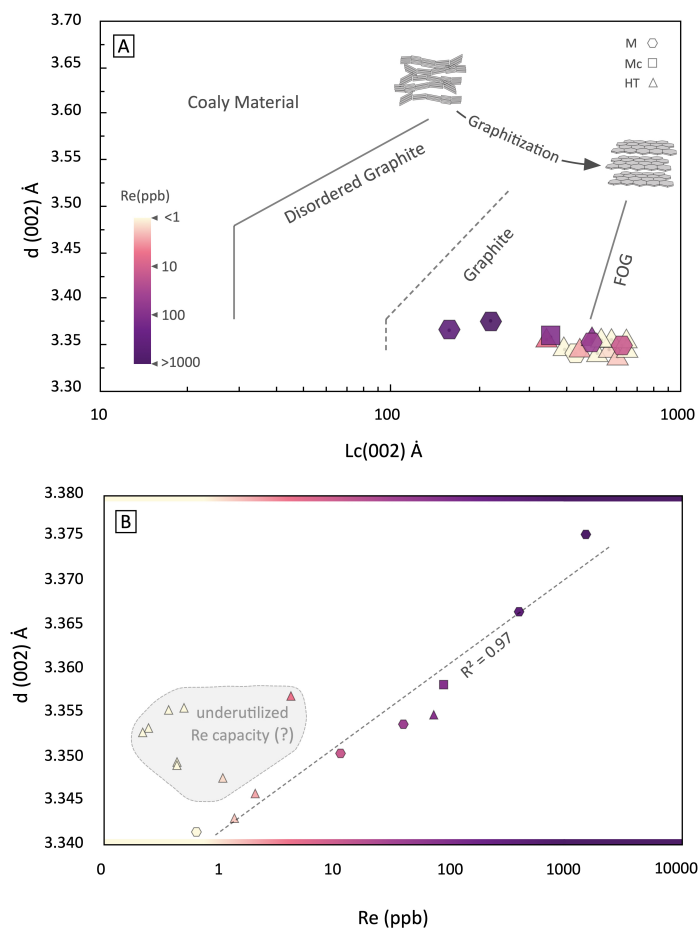
Figure 2.8. Plot (a) illustrates the relationship between Re concentration and crystallite size ($Lc_{(002)}$) and interplanar spacing ($d_{(002)}$) in metamorphic (M = hexagon symbol), meteoritic (Mc = square symbol), and hydrothermal (HT = triangle symbol) graphite. FOG = fully ordered graphite. Plot (a) modified after Tagiri and Oba (1986) and Buseck and Beyssac (2014). Plot (b) depicts the relationship between Re concentration and interplanar spacing in M, Mc, and HT graphite. Note: x- and y-axes are in logarithmic and linear notation, respectively.

Wollaston-Mudjatik Transition shear zone (JT20-5) graphite exhibits Raman spectra with prominent G bands at 1580 cm^{-1} and weak or absent D bands at 1355 cm^{-1} typical of well-crystallized graphite. Estimated crystallization temperatures for WMT graphite is 537-641℃ (Table A7 and Fig. A7).

2.6. DISCUSSION

2.6.1. Controls on graphite Re concentrations

Graphite reported here (n = 17) exhibits Re concentrations (Re = 0.2 to 1520.2 ppb) that commonly (n = 15/17) exceed upper continental crustal (UCC) Re values (Re = 0.25 ppb; Chen et al., 2016) by a factor of 4 or more, and are comparable to those present in terrestrial sulfides (Re$_{median}$ = = 8.3 ppb), hydrocarbons (Re$_{median}$ = 21.9 ppb), and organic-rich sediments (ORS; Re$_{median}$ = = 33.9 ppb) (Fig. 2.2). These observations are unsurprising considering graphite either forms as the direct end-member product following ORS carbonization (i.e. ORS → kerogen → coal → graphite) or precipitates under comparable physio-chemical conditions as hydrothermal and metamorphic sulfides (Buseck and Beyssac, 2014). This co-genetic relationship has, for example, been observed in numerous graphite localities formed throughout Precambrian and Phanerozoic time (Ferry, 1981; Jaszczak et al., 2009; Luque et al., 2013; Touret et al., 2019).

Graphite Re abundances are, however, quite variable on both an intra- and inter-group level (Fig. 2.2). For instance, Re concentrations average 482.1 (median = 203. 8) and 10.1 (median = 0.8) ppb in metamorphic (n = 4) and hydrothermal (n = 12) graphite with meteoritic (n = 1) graphite falling in between these two groups at 87.2 ppb Re. Conversely, within group Re values range from 0.6–1520.2 ppb and 0.2–71.4 ppb for metamorphic and hydrothermal graphite, respectively. In addition, within-group Re variation for metamorphic graphite trends with metamorphic temperature. For example, low-T graphitic slates (Bessie Mine, MI, USA [Re = 396.2 ppb]) and blueschist-facies rocks (Laytonville, CA, USA [Re = 1520.2 ppb]) contain more Re than their higher-T graphitic schist counterparts (Foss Mine, Scotland, UK [Re = 0.6 ppb];

Minas Gerais, Brazil [Re = 11.4 ppb]). This relationship between temperature (i.e. metamorphic grade) and Re concentration has an inverse correlation coefficient of 0.39 (not shown).

Carbonaceous material, when exposed to higher metamorphic temperatures, transforms progressively and irreversibly from a non-crystalline, disordered state into crystalline graphite (Landis, 1971; Grew, 1974; Wada et al., 1994). This manifests in crystallographic shortening of the interplanar spacing ($d_{(002)}$) between graphene sheets and ordering of carbon layers via increases in crystallite size ($L_{c(002)}$) until a fully-ordered state is achieved ($d_{(002)}$ = 3.35–3.36 Å; $L_C(002)$ = > 500) (Fig. 8a; Tagiri and Oba, 1986). According to this classification, the low-grade metamorphic graphite studied here is both more disordered than its higher-grade counterparts and more enriched in Re content (Fig. 2.8a). Hydrothermal graphite, however, may not obey this temperature-dependent relationship and instead precipitates preferentially as fully-ordered graphite irrespective of temperature (Luque et al., 2013, Rumble, 2014), and hence yields lower Re contents compared to metamorphic graphite (Fig. 2.2 and Fig. 2.8a).

Of the two crystallinity parameters, interplanar spacing is the strongest candidate for controlling graphite Re abundances since trace metal impurities, which commonly intercalate into graphitic layered structures, persist up to ppm-levels in high purity-high crystallinity graphite (Kiciń ́ski and Dyjak, 2020). Metamorphic graphite, for example, typically has lower crystallinities and higher impurities than vein graphite (Jara et al., 2019). It is therefore feasible that intercalation impurities are functionally constrained by variations in interplanar spacing, such that the $d_{(002)}$ spacing of ideal hexagonal graphite (3.35 Å) significantly impedes trace element occupancy along intercalation sites. This is supported by the positive correlation between $d_{(002)}$ and Re abundances (R^2 = 0.97) in metamorphic and meteoritic ± hydrothermal graphite (Fig. 2.8b) that is otherwise absent when comparing crystallite size (R^2 = 0.54; not shown) and implies that Re occupancy is limited to < 10 ppb at interplanar spacing scales of 3.35 Å (Fig. 2.8b). Hydrothermal graphite samples of low Re content that deviate from this trend line may signify precipitation from a Re-depleted fluid and thus have an underutilized Re intercalation capacity (Fig. 2.8b).

2.6.2. Chronology of carbonic fluid flow in Wollaston-Mudjatik Transition shear zones

Graphite deposition in WMT shear zones has previously been ascribed to retrograde metamorphism in the Trans- Hudson orogeny (THO) that is bracketed to ca. 1770– 1720 Ma (Martz et al., 2017) by cooling ages of Rb-Sr biotite and Ar-Ar muscovite. However, these ages have been interpreted by Peterson et al. (2015) to reflect a thermal event related to widespread Kivalliq igneous suite (KIS) emplacement (ca. 1770–1730 Ma) and affiliated metallogenic events. This resurgent heat (+fluid) flow presumably redistributed graphite and deposited hydrothermal quartz (Card, 2014) along fault systems that later became the foci of major uranium deposits (IAEA, 2018; Adlakha and Hattori, 2021).

Our Re-Os graphite date (1731.52 ± 7.43 [with decay constant uncertainty (λ) = 12.71] Ma; Fig. 2.9a) falls at the younger age range of thermotectonism in the region (^{40}Ar-^{39}Ar muscovite weighted mean age = 1731 ± 18 Ma [Alexandre et al., 2009]; reset U-Pb rutile age = 1732 ± 10 Ma [Adlakha and Hattori, 2021]) but provides the first precise age of aqueous-carbonic fluid flow in shear zones associated with uranium mineralization, at the Phoenix U deposit. Graphite deposition then either formed in response to post-THO exhumation and cooling (Martz et al., 2017) and/or a high heat flow event related to KIS emplacement (Adlakha and Hattori, 2021) as aqueous fluids redistributed carbon from adjacent wall rocks into semi-brittle to brittle- ductile shear zones.

Martz et al. (2017) concluded that this thermotectonic event was dominated by carbonic fluids of the C-O-H(-N) system and precipitated shear-bound graphite (δ^{13}C = -29 to -23 ‰) according to the reaction CO_2 + CH_4 → 2C + $2H_2O$. This fluid presumably acquired its C isotope composition through equilibration with metamorphic graphite (δ^{13}C = -28 to -20 ‰) and carbonate minerals, respectively, in the surrounding metapelites and marbles.
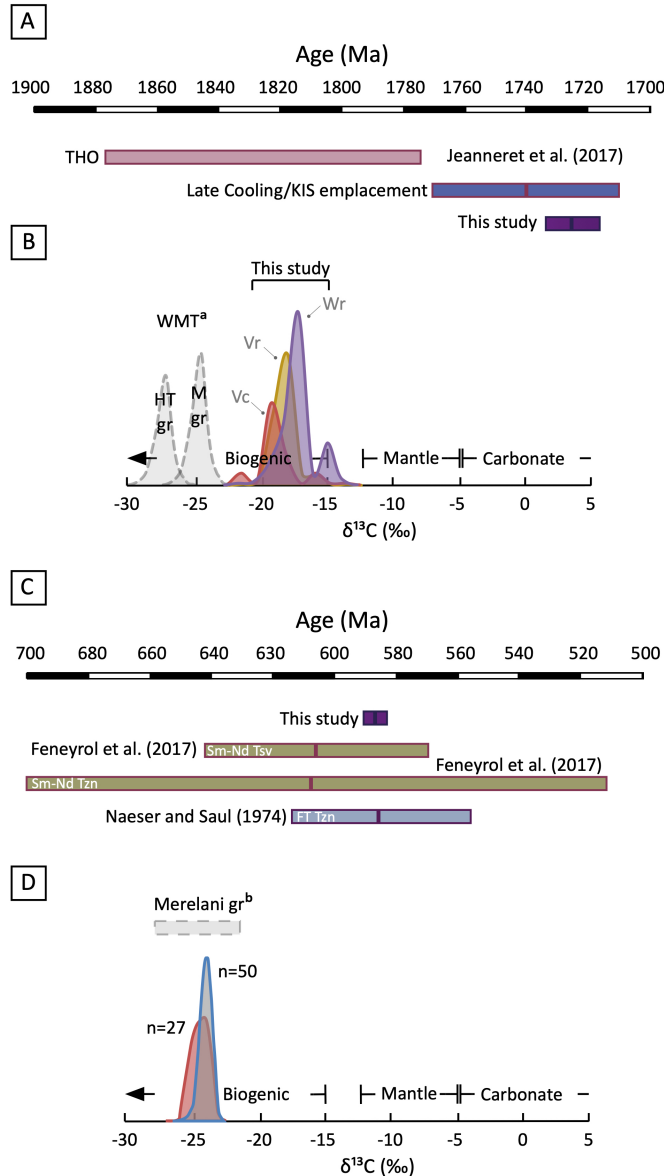
Figure 2.9. Plots comparing published literature ages and $\delta^{13}C$ values of graphite from the Wollaston-Mudjatik Transition (a-b) and Merelani Hills (c-d) with Re-Os graphite ages and SIMS $\delta^{13}C$ graphite values obtained in this study. Re-Os graphite ages in (a) and (c) overlap with THO late cooling ages and tsavorite-tanzanite formation ages, respectively. Plot (b) shows SIMS $\delta^{13}C$ graphite values in the vein core (Vc = red), vein rim (Vr = orange), and wall rock (Wr = purple) of JT20-5, whereas plot (d) shows SIMS $\delta^{13}C$ graphite values in JT20-MH-A (red) and JT20-MH-B (purple). WMT = Wollaston-Mudjatik Transition, THO = Trans-Hudson Orogeny, HT gr = hydrothermal graphite, M gr = metamorphic graphite, Tsv = tsavorite, Tzn = tanzanite, and FT = fission track dating. [a]Martz et al., 2017; [b]Olivier, 2006. Re-Os isochron ages (this study) include analytical and systematic uncertainties (^{187}Re decay constant of Smoliar et al., 1996).

Shear-hosted graphite studied here, however, has intermediate C isotope compositions (δ^{13}C = -21.64 to -15.28 ‰; Fig. 2.9b) consistent with derivation from a more ^{13}C-enriched fluid. Graphite in sample JT20-5 is crystallographically well-ordered and occurs as discrete flakes (Fig. A2) distinct from the poorly-ordered ''sooty'' hydrothermal graphite reported by Martz et al. (2017). If a crystallinity-temperature relationship is assumed, then the latter crystallized at a temperature that is 200°C cooler than the graphite reported here (T$_{XRD}$ = 648°C; T$_{Raman}$ = 641°C). A drop in the temperature of graphite precipitation plausibly accounts for the carbon isotope shifts observed within our vein (-21.64 to -16.91 ‰) and wall rock (-19.20 to -15.28 ‰) graphite (Fig. 2.7a/b; Fig. 2.9b) but is inadequate to explain the lighter C isotope values reported by Martz et al. (2017) (Luque et al., 2013). Instead, these C isotope differences either signal derivation from a heterogenous organic carbon source or variable mixing of organic and carbonate sedimentary sources.

Wollaston-Mudjatik Transition graphite, therefore, precipitated from a C-O-H(-N) fluid with carbon isotope signatures inherited from organic (± carbonate) carbon presumably sourced locally from Wollaston Supergroup graphitic pelites and marbles (Martz et al., 2017). The ^{187}Os/^{188}Os$_i$ signature (0.3119 ± 0.0037; Fig. 2.3a) of the graphite is then either derived from a single or mixed crustal Os source. The mass contributions of Re and Os from carbonates would likely be small in comparison to those from organic-rich sediments (Dubin and Peucker-Ehrenbrink, 2015) suggesting a carbonaceous sedimentary Os source for the precipitating graphite. Assuming this parental sediment had a Paleoproterozoic mantle ^{187}Os/^{188}Os (0.12) value and an average shale ^{187}Re/^{188}Os ratio of 517 (Dubin and Peucker-Ehrenbrink, 2015), we can calculate a maximum apparent depositional age of 1754 Ma. This age post-dates orogenic burial and is thus implausibly young. Instead, Wollaston carbonaceous sediment likely had an average crustal ^{187}Re/^{188}Os ratio between 20–71 (Ackerman et al., 2017; Chen et al., 2016), which leads to an apparent depositional age between 1892– 2304 Ma.

2.6.3. Graphite chronology in Merelani Hills (Lelatema Fold Belt)

Metamorphic and hydrothermal graphite formation in the Lelatema Fold Belt accompanied tsavorite and tanzanite gemstone mineralization in metasedimentary and calc-

silicate rocks subjected to prograde and retrograde amphibolite facies metamorphism during the East African Orogeny (Olivier, 2006; Feneyrol et al., 2013). A proxy timeline for both graphite mineralizing events in the Lelatema Fold Belt can be inferred from amphibolite facies (ca. 620–560 Ma) and tsavorite-tanzanite ages (Sm-Nd$_{tsavorite}$ = 606 ± 36 Ma; Sm-Nd$_{tanzanite}$ = 607 ± 95 Ma; fission track$_{tanzanite}$ = 585 ± 29 Ma) that *ipso facto* bracket graphite formation to a broad 55 Myr window in the late Neoproterozoic (Feneyrol et al., 2013, 2017) (Fig. 2.9c).

The Re-Os hydrothermal graphite age result (586.89 ± 2.39 [λ = 3.83] Ma; Fig. 2.9c) falls within the existing broad age bracket, but provides the first highly precise age of retrograde metamorphism in the region, relevant for tsavorite and tanzanite mineralization. X-ray diffraction thermometry data reported here (Table 1) also confirms that graphite crystallized (T = 645°C) at similar temperatures as tanzanite (650 ± 50°C) and further supports a graphite-tanzanite paragenetic relationship (Olivier, 2006).

The source of V in tsavorite and tanzanite has previously been attributed to organic-(V)-rich mudstones based primarily on biogenic C isotope (-25 to -22 ‰; Fig. 2.9d) and V-rich signatures present in graphite and mudstone geo- chemical (Sr and Ba) signatures preserved in graphitic gneisses (Olivier, 2006). SIMS ^{13}C/^{12}C isotope measurements reported here confirm a predominately organic graphitic C isotope signature (-25.9 to -24.4 ‰) that is homogenous within a ≤ 1‰ variation on an inter- and intragrain scale (Fig. 2.7c/d and Fig. 2.9d). A single (organic) C source can then be inferred from these homogenous C isotope compositions combined with prior quartz-hosted fluid inclusion data (Feneyrol et al., 2017). These data imply that the ^{187}Os/^{188}Os$_i$ (Fig. 2.3b) signature of fluid-deposited graphite in Merelani Hills was inherited from organic material in the parent mudstones, and thus represents an evolved sea-water ^{187}Os/^{188}Os signature. The highly radiogenic signature preserved in the graphite (^{187}Os/^{188}Os$_i$ = 1.680 vs. ^{187}Os/^{188}Os$_{mantle}$ = 0.126) then either evolved from a primitive (Archean?) sedimentary source (Olivier, 2006) or Neoproterozoic sediment with a dominantly continental ^{187}Os/^{188}Os seawater signature. Evaporate-carbonate successions in the Lelatema Fold Belt linked to sabkha-type basin conditions and presumed to be Neoproterozoic in age favor the latter hypothesis (Feneyrol et al., 2013). This conclusion is supported by an apparent

mudstone depositional age of 641–766 Ma inferred from an average shale ^{187}Re/^{188}Os ratio of 517 (Dubin and Peucker-Ehrenbrink, 2015) and a seawater ^{187}Os/^{188}Os ratio between 0.126 and 1.205 (Meisel et al., 2001; Chen et al., 2016).

2.6.4. Re-Os graphite workflow

Standardized workflows for Re/Os geochronology commonly employ water or SPT to isolate the desired mineral phase(s) prior to further geochronological investigation. However, applying analogous liquid density separation protocols for Re-Os graphite dating is problematic since water and/or SPT appear to non- stoichiometrically leach Re and Os from graphite that manifested in artificially higher or lower ^{187}Re/^{188}Os ratios (Fig. 2.6a/b). Consequently, water/SPT-treated graphite may produce Re/Os dates that are younger or older than their untreated counterparts and lead to incorrect Re/Os age assignments (Fig. 2.6a/b). Conversely, the age uncertainties may become inflated in such a way that the Re/ Os dates now overlap with multiple geologic events that are otherwise causally distinct. This blurring of causal relationships is exemplified in our SPT-treated dataset (JT20-5-NM-1.30-SPT) where the error envelope in our Re/Os date (1731.52 ± 7.43 Ma) ballooned to 88.00 Ma and now overlaps with the THO (ca. 1875–1775 Ma), post-orogenic cooling (ca. 1731 Ma) and Athabasca sediment deposition (ca. 1700–1690 Ma) (Jeanneret et al., 2017). These results similarly imply that graphite Re-Os systematics may be susceptible to post-depositional geological disturbance. It is therefore advised that Re-Os graphite dating workflows emphasize handpicking coarse-grained (fresh) graphite and/or crushing and sieving massive and/or high-volume (fresh) graphite samples followed by magnetic separation to concentrate the desired mineral analyte as described in Section 3.1. Mineral aliquots should then be apportioned towards grain mounts for textural and phase analysis and/or sent for XRD or micro- probe quantitative phase identification.

Graphite separates procured for Re-Os analysis by isotope dilution require digestion protocols that ensure spike-sample equilibration. Achieving this feat, however, is hindered by the fact that graphite resists decomposition by most mineral acids (HCl, HNO$_3$, HF, H$_2$SO$_4$). Indeed, experimental tests performed here show that oxidizing mixtures of HNO$_3$-HCl-H$_2$O$_2$ and

HNO_3-H_2SO_4 are wholly incapable of decomposing coarse-grained graphite after 72-h at 240 ℃ using standard Carius tube methods (Fig. 2.4a-c). These findings are important to highlight since a recent study by Sun et al. (2021) employed inverse aqua regia-H_2O_2 digestion protocols for Re-Os graphite analysis. A replicate test of Sun et al.'s (2021) digestion procedure (not shown) failed to decompose coarse-grained graphite studied here. Incomplete sample digestion can, however, be avoided by employing the CrO_3-H_2SO_4 method for decomposing graphite (Fig. 2.4d-f). The amount of graphite oxidized by this mixture (see *Section 2.3.3*) is stoichiometrically limited to 180 mg, but in a practical sense may be constrained to sub- 100 mg aliquots due to slow reaction kinetics inhibiting graphite decomposition over 72-h at 240 ℃ (Fig. 2.5) and may ultimately limit the method to graphites with >1–2 ppb Re. A recommended workflow for graphite Re-Os dating is provided in Appendix A (Fig. A10).

2.6.5. Implications for graphite research

Many of the graphite localities studied here exhibit ppb-level quantities of Re (Figs. 2.1 and 2.2) and, as such, are amenable for further geochronological investigation. Preliminary Model Age estimates of Minas Gerais, Bessie Mine, and Plumbago Mine graphite constrain the maximum age of graphite formation to 2394, 1420, and 596 Ma. Conversely, preliminary $^{187}Os/^{188}Os_i$ estimates of Minas Gerais (0.13), Laytonville Quarry (0.22), Bessie Mine (0.49), and Plumbago Mine (0.70) graphite have also provided speculative clues for the source of Os (mantle = 0.133 vs. continental = 1.40) - and perhaps graphitic C – that require more exhaustive follow-up enquiries (Table A3).

Future investigation of graphite, therefore, has the potential to help delineate rates of hydrothermal graphite deposition, challenge or confirm existing graphite formation models, expand our understanding of the mechanism of graphitization, and refine our view of the deep carbon cycle. The source tracing abilities afforded by the Re-Os graphite chronometer has the potential to expand our understanding of the formation, erosion, and transport of graphitic carbon across a wide-range of spatial- temporal scales, such as Cenozoic uplift of the Himalayas to carbon recycling in Phanerozoic subduction zones to large-scale carbon burial events in the Precambrian (Baker and Fallick, 1989; Galy et al., 2008). Beyond these examples, Re-Os graphite

chronometry could also be applied to more obscure graphite occurrences linked to the evolution of Archean life (Ohtomo et al., 2013) and early Solar System events (Matsuda et al., 2005) or be used, comparably to Re-Os sulfide dating, as a tool for enhancing greenfield exploration efforts for graphite by inferring ore-field relationships from the chronology of deposit-scale mineralizing events. This latter application is particularly relevant as world economies look to adopt green technologies (e.g. lithium-ion batteries and other storage devices) that rely on graphite to function, and thus increased demand of graphite, high grade or otherwise, will have to be supplemented with increased supply (Jara et al., 2019). Ultimately, this study suggests that graphite, like sulfide minerals, organic-rich sediments, and hydro-carbons (Stein and Hannah, 2015), is a viable Re-Os geochronometer and the method can contribute fundamental insights into the diverse processes of graphite mineralization.

2.7. CONCLUSIONS

Metamorphic, hydrothermal, and meteoritic graphite has Re and Os abundances ranging from 0.2 to 1520 ppb and 89 ppt to 19,577 ppt, respectively, similar to those in terrestrial sulfides, organic-rich sediments, and hydrocarbons, and significantly higher than average rocks of the upper continental crust.

Rhenium concentrations are highest in metamorphic graphite, and specifically low-grade (low T) graphite found in slates and schists. Graphite Re abundances also trend inversely with crystallinity, with high crystallinity hydrothermal graphite containing far less Re than low crystallinity metamorphic and meteoritic graphite. A positive correlation between interplanar spacing (d_{002}) and graphite Re concentrations ($R^2 = 0.97$) indicates that d_{002} spacing limits Re occupancy to 10 ppb or less at scales less than 3.35 Å.

Graphite Re-Os geochronology was investigated using hydrothermal graphite sampled from two localities – Wollaston-Mudjatik Transition shear zones, SK, CA and Merelani Hills, TZ, which yield precise (<1%) Re-Os isochron dates of 1731.52 ± 7.43 Ma (2σ; MSWD = 1.3) and 586.89 ± 2.39 Ma (2σ; MSWD = 1.2). Both ages overlap previously inferred ages for graphite formation in these areas but are more precise than existing age data. For the two studied localities, graphite

mineralization is confirmed to be coeval with Trans-Hudsonian exhumation and cooling and/or the Kivalliq igneous event and tsavorite- tanzanite gemstone mineralization. Accuracy of the method, however, may depend on the analytical protocols used to concentrate graphite (handpicking vs. heavy liquids (SPT) or water).

SIMS $^{13}C/^{12}C$ isotope (WMT graphite = = -21.64 to -15.28 ‰; Merelani Hills graphite = -25.90 to -24.35 ‰) and $^{187}Os/^{188}Os$ initial ratios (WMT graphite = 0.3119 ± 0.0037; Merelani Hills graphite = 1.680 ± 0.038) data broadly confirm prior literature findings. The $^{13}C/^{12}C$ and $^{187}Os/^{188}Os_i$ ratios in WMT graphite are consistent with derivation from a C-O-H-(N) fluid sourced locally from Wollaston Supergroup metapelites possibly with some additional contribution of carbon from basement marbles, whereas the $^{13}C/^{12}C$ ratios and evolved $^{187}Os/^{188}Os_i$ isotope signatures in Merelani Hills derived from CH_4-rich fluids expelled from neighbouring Neoproterozoic carbonaceous sedimentary rocks.

3|Did subducted graphite fertilize the Franciscan mantle wedge with radiogenic Os?

Abstract

New chronology for graphite formation related to subduction-zone metamorphism in Laytonville Quarry (California, USA) of the Franciscan Complex using the Re-Os decay system yields a precise graphite-pyrite Re-Os age of 161.39 ± 1.50 Ma (MSWD = 0.15; n = 5). Combined with Raman thermometry estimates (461-506°C) this age links graphitization to the early stages of Franciscan subduction, synchronous with deep (blueschist-eclogite) rather than shallow subduction processes. Initial ^{187}Os/^{188}Os (0.195) of Laytonville graphite suggests that radiogenic ^{187}Os/^{188}Os signatures (0.130-0.158) preserved in some Franciscan forearc mantle peridotites (ca. 160-150 Ma) were plausibly sourced from graphitic carbon in the subducted slab with graphitization being the primary mechanism for Os release. This conclusion implies that graphitic carbon is an important mineralogical host for Os recycling in subduction settings.

3.1. INTRODUCTION

Carbonaceous matter within the sedimentary cover of oceanic crust is progressively transformed into graphitic carbon during subduction zone metamorphism (Buseck and Beyssac, 2014). Graphitized carbon can be mobilized from the descending slab and degassed as CO_2 in volcanic arc settings (Plank and Manning, 2019; Tumiati et al., 2022) or recycled into the deep mantle and transformed to diamond at 155-200 km depths (Stachel and Luth, 2015). Recent investigations show that Re and Os are present in subducted graphite and hence can be redistributed in the mantle and/or arc magmas (Toma et al., 2022). Indeed, many arc magmas and arc-mantle xenoliths contain ^{187}Os/^{188}Os isotopic signatures (>0.13) consistent with recycling of crustal-derived Os (Brandon et al., 1996; Snortum et al., 2020). Such recycling shifts the ^{187}Os/^{188}Os of arc magmas (<0.13) towards crustal-like (1.4) values. However, the role of graphite in recycling of Re and Os is untested, as this requires an accurate timeline for graphitization that can be linked with crustal Os input into the arc mantle and magmas derived

therefrom. Recent developments in graphite Re-Os dating now allow for such linkages to be made (Toma et al., 2022).

Here we present the first graphite-pyrite date from subducted oceanic crust preserved in the Franciscan Complex of California, USA. The new age data are integrated with Raman Carbonaceous Material Spectrometry (RCMS) to constrain the conditions and timing of graphitization and propose a link between crustal Os recycling into the Franciscan forearc mantle from subducted graphite.

3.2. GEOLOGICAL SETTING

The Franciscan Complex is part of the larger Franciscan Subduction System (FSS) that includes the Coast Range Ophiolite (CRO), Sierra Nevada magmatic arc, and Great Valley Group fore arc basin, exposed in continuous outcrop in western California and southern Oregon, USA (Fig. 3.1a). This relict subduction system formed via eastward subduction of the Farallon Oceanic Plate beneath the western margin of the North American Plate, which began in the Early Jurassic (ca. 176 Ma) and continued through a non-accretionary phase until the Early Cretaceous (ca. 130 Ma) (Ernst, 1970; Dumitru et al., 2010; Mulcahy et al., 2018). During this interval, oceanic crust of the CRO was formed (ca. 170-161 and 150 Ma) in the forearc (Rutte et al., 2020 and references therein) coincident with middle-stage arc plutonic emplacement (ca. 185-143 Ma) of the Sierra Nevada Batholiths to the east (Paterson and Ducea, 2015). Forearc basin sediments of the Great Valley Group were deposited above the CRO as early as the Late Jurassic (ca. 153-135 Ma, Orme and Surpless, 2019). Subducted oceanic crust and metasediment was subsequently exhumed from the mantle wedge by ca. 150 Ma (Rutte et al., 2020) and later accreted (ca. 123-73 Ma) with trench sediment to form the Franciscan Complex (Dumitru et al., 2010).

The Franciscan Complex (Fig. 3.1a) is an ensemble of coherent and mélange terranes subdivided by metamorphic grade and age into the Coast (Early Tertiary zeolite-facies blocks), Central (Jurassic blueschist- and amphibolite-eclogite-facies blocks), and Eastern (Early Cretaceous blueschist-facies blocks) Belts (Raymond, 2018). The Central Belt hosts, in part,

exotic blocks of the Laytonville mélange sequence (Mendocino Co., California, USA) (Wood, 1982). The Laytonville Quarry exotic block is a collection of deep-sea (± organic-rich) sediments, primarily metapelites, deposited above mid-ocean ridge basalts of the East Pacific Rise, that underwent blueschist-facies metamorphism during subduction (Wood, 1982). This exotic block underwent three stages of metamorphism starting with aegirine and garnet formation, followed by high-P/low-T deerite and zussmanite growth, and ending in low-P/low-T howieite, riebeckite, and stilpnomelane replacement (Wood, 1982). A subpopulation of these metapelites underwent graphitization and pyritization at some point during their metamorphic history (Wood, 1982). Specimen *SPXX-m6424*, which was sampled from this graphite-rich subpopulation and is also deerite- and stipnomelane-bearing (Fig. B1-B5 of Appendix B), is the subject of this study.
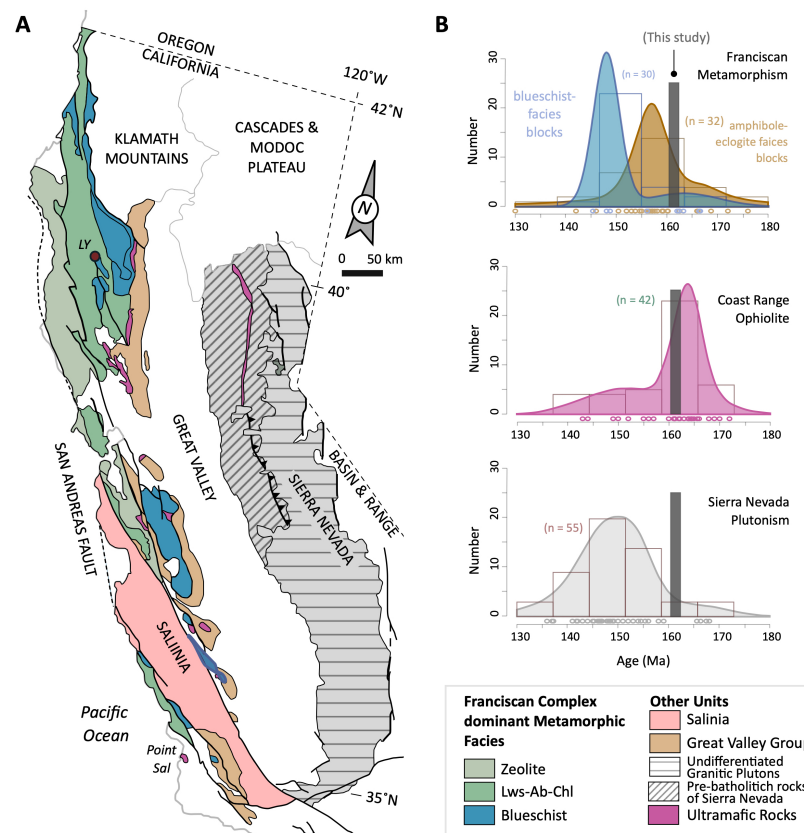
Figure 3.1. Map (A) and chronology (B) of the Franciscan Subduction System. Red dot in (a) denotes Laytonville (LY) Quarry sampling location. Map and probability density plot data modified from Mulcahy et al. (2018).

3.3. RESULTS

Laytonville whole rock (n = 1), graphite (n = 5), and pyrite (n = 2) Re and Os values range from 116-2412 ppb and 5-86 ppb with graphite hosting the highest Re and Os concentrations at 2410 ppb and 86 ppb (Table B1; Appendix B). Whole-rock, graphite, and pyrite $^{187}Re/^{188}Os$ and $^{187}Os/^{188}Os$ ratios range from 129-197 and 0.55- 0.72, respectively, with pyrite being the most radiogenic at 0.72 followed by graphite at 0.65 and whole rock at 0.55 (Table B1; Appendix B). Plotting all graphite and pyrite Re/Os isotopic ratios (n = 7) in isochron space yields a Model 3 age of 164.63 ± 12.31 Ma (2σ; MSWD = 140) and an $^{187}Os/^{188}Os_i$ ratio of 0.191 ± 0.031 (Fig. 3.2). However, eliminating impure graphite separates (M-0.11 and NM-0.49) containing late-forming mineral phases (stilpnomelane) and/or graphite-included silicates (see Fig. 3.2 and Appendix B) yields a Model 1 Re-Os isochron age of 161.39 ± 1.50 (2σ; MSWD = 0.15) and an $^{187}Os/^{188}Os_i$ ratio of 0.1953 ± 0.0037 (Fig. 3.2). Concordant $^{187}Os/^{188}Os_i$ ratios (0.19) coupled with evidence of syntectonic of pyrite-graphite growth (see Fig. 2AI-II and Fig. B2b-d of Appendix B) argues that the two minerals formed concurrently.

Laytonville graphite exhibits Raman spectra with well-defined graphite (G) and disordered (D1) bands at 1569-1580 cm^{-1} and 1342-1347 cm^{-1}, respectively, typical of more disordered forms of carbonaceous material. Laytonville graphite yields crystallization temperatures of 461-506± 50 ℃ (Fig.B7; Table A3; Appendix B), slightly higher than temperature estimates (439℃) obtained using XRD crystallinity geothermometry (Toma et al., 2022). Raman spectra is assumed here to vary with temperature (Beyssac et al. 2002) but the presence of heteroatoms (i.e., O and H) and sp3 hybridization may also play a role (Toffolo et al., 2023).
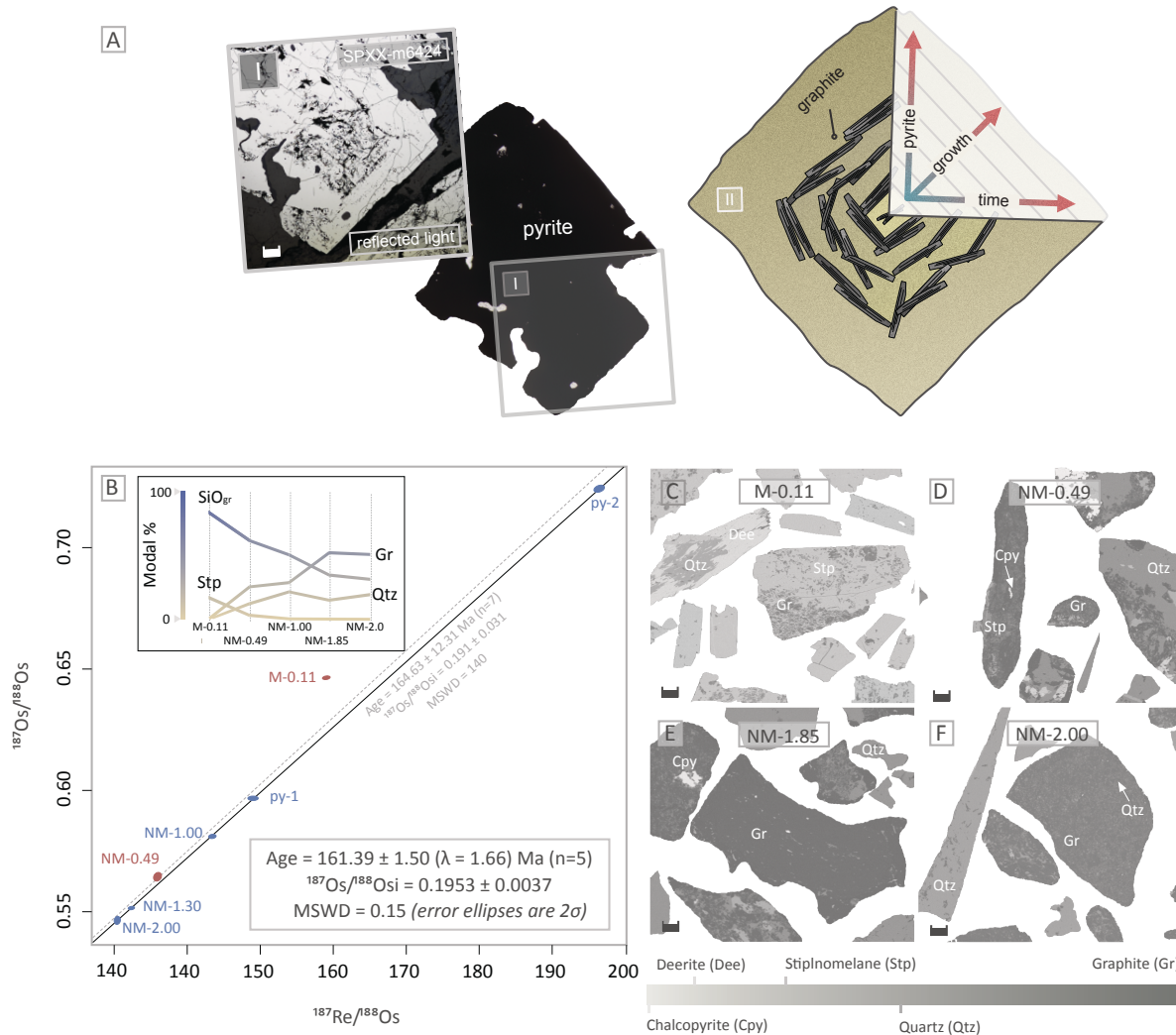
Figure 3.2. (AI) Pyrite overgrowing and displacing graphitic fabric into orientations that (AII) mimic successive stages of crystal growth. (B) Graphite-pyrite Re-Os isochron (IsoplotR; Vermeesch, 2018). Uncertainties with ^{187}Re decay constant ($\lambda = 1.666 \cdot 10^{-11} \pm 0.31\%$) of Smoliar et al. (1996) shown in brackets. Graphical inset in (B) shows the modal percentages of graphite (Gr), silicates with Gr inclusions (SiO$_{gr}$), quartz (qtz), and stilpnomelane (stp) in each separate. Datapoints that fall off the isochron have the highest proportion of SiO$_{gr}$ and Stp grains, which is illustrated further with representative BSE images (C-F). Scale bar = 20 μm.

3.4. DISCUSSION

3.4.1. Linking graphitization to Franciscan subduction

The pressure-temperatures conditions experienced by the Laytonville exotic block reflect the broader metamorphic histories of the Central Belt of the Franciscan Complex. Meta-ironstones and glaucophane schists, for example, host relict garnets partially replaced by

chlorite and amphibole that formed during early prograde metamorphism (Wood, 1982; McDowell et al., 1984). Similar garnets preserved elsewhere in the Central Belt further attest to a high P-T (P = up to 25 kb and T = 400-600 ℃) event bracketed to ca. 157-170 Ma (Fig. 3.1b) (Rutte et al., 2020) with the earliest dates signaling subduction initiation (Mulcahy et al., 2018). Whole-rock K-Ar dates (158 ± 6 Ma and 168 ± 18 Ma; Fig. 3.1b) from garnet-bearing blueschists in Laytonville may also reflect this older event as they predate later-forming phengite grains (K-Ar = 151-156 ± 4 Ma) (McDowell et al., 1984). The phengite K-Ar dates fall within the age bracket of blueschist-facies exhumation in the region (Fig. 3.1b) (ca. 143.4-156.4 Ma), but likely post-date earlier retrograde amphibolite-facies events at 157-168 Ma (Rutte et al., 2020).

Our graphite-pyrite Re-Os date (161.39 ± 1.50 Ma, including decay constant uncertainty ± 1.66 Ma) is older than Laytonville phengite K-Ar ages and falls within the established age range for amphibolite-eclogite-facies metamorphism in the Franciscan Complex (Fig. 3.1b/3.2). Graphite crystallization temperatures (461-506 ± 50℃) are also >150 ℃ or more above known lawsonite blueschist-facies temperatures (150-250 ℃/ ~80-120 Ma) in the Franciscan but overlap with the upper (300-400 ℃) and lower (400-500 ℃) temperature range of epidote blueschist- (120-154 Ma) and eclogite- (157-168 Ma) facies metamorphism, respectively (Wakabayashi and Dumitru, 2007; Cooper et al., 2011; Rutte et al., 2020). Graphitization is an irreversible process, so crystallinity estimates reflect peak crystallization temperatures (Buseck and Beyssac, 2014). The graphitic metapelite studied here, therefore, was metamorphosed at temperatures no greater than 500 ± 50 ℃. We interpret the age and temperature of graphitization and pyritization to reflect early prograde (blueschist-eclogite facies) metamorphism associated with deep (P = up to 2.5 GPa; T = 400-600 ℃), rather than shallow (P = 0.3-0.8 GPa; T = < 300 ℃), Franciscan subduction processes (Raymond, 2018).

Between the time of sediment deposition and graphitization, the Laytonville Quarry rocks acquired a more radiogenic Os isotopic signature by ingrowth of [187]Os. This time interval can be estimated by assuming an initial mantle [187]Os/[188]Os ratio (0.129) and an average shale [187]Re/[188]Os ratio (517) (Dubin and Peucker-Ehrenbrink, 2015) that yields a 6.2-9.2 Myr interval between sediment deposition (168.49-171.47 Ma) and graphitization (161.39 ± 1.50 Ma,

^{187}Os/^{188}Os = 0.1953). If the whole-rock ^{187}Re/^{188}Os value of our graphitic schist is used (131.3), then this interval becomes 29-32 Myr. In either case, sediments of Jurassic age are implicated as protoliths, a time of major organic carbon burial on the planet (Kemp et al., 2022). Subducted Jurassic organic-rich sediments are also inferred as a Re source in modern volcanic fumaroles in arcs through recycling (Tessalina et al., 2008; Liao et al., 2019).

3.4.2. Graphite fertilizing the mantle with radiogenic Os

Osmium is released from oceanic crust and recycled into the mantle wedge during slab dehydration and/or melting as evidenced from forearc and sub-arc mantle xenoliths (Brandon et al., 1996; Day et al., 2009). Indeed, forearc peridotites of the CRO record evidence of metasomatism by slab-derived, Os-bearing, fluids (Snortum and Day, 2020). However, the nature of minerals involved in Os release during subduction metamorphism is poorly known. Sulfides are stable at depths beyond the blueschist-eclogite transition zone and thus may be a poor source of labile Os in the absence of slab melting and/or supercritical fluid interaction (van Acken et al. 2014; Liu et al., 2018). The graphitic samples studied here are highly reduced and in the absence of an oxidizing medium, Os is immobile (Xiong and Wood, 2000), and hence Os would be retained within the descending slab until sufficient depths are reached to destabilize Os-bearing phases (Liu et al., 2018). During slab descent, graphite breakdown may occur from devolatilization reactions (2 C + 2 H$_2$O → CO$_2$ + CH$_4$) induced by prograde metamorphism (Pattison, 2005; Plank and Manning, 2019). Although these reactions may be insufficient to affect the Mo budget of metasedimentary rocks (Stepanov, 2021), this does not appear to be the case for Re and Os (Toma et al., 2022). Late-forming hydration reactions, such as those introduced by slab exhumation, may also induce graphite decomposition. However, these late-stage hydration reactions have only mildly perturbed the Re-Os systematics of graphite in contact with secondary phases, such as stilpnomelane, as seen here (Fig. 3.2).

The primary mechanism driving Re+Os partitioning from graphite into slab-derived fluids therefore may derive from the process of graphitization whereby carbonaceous matter devolatilizes and recrystallizes into graphite. Prograde metamorphism progressively and

irreversibly rearranges amorphous carbon atoms into ordered crystalline lattices that systematically expel impurity elements from its structure. This process is mainly driven by increases in temperature and begins after the coalification stage of sedimentary organic matter at around 300 ℃ and continues until hexagonal graphite is formed above 600 ℃ (Beyssac et al., 2002). This end-member product is defined by interplanar spacing ($d_{(002)}$) scales and crystallite sizes ($Lc_{(002)}$) of <3.35 Å and >500 Å, respectively (Tagiri and Oba, 1986). However, if graphitization is incomplete, then the carbonaceous matter will have varying degrees of crystallinities and impurities, such as the semi-ordered ($d_{(002)}$ = 3.375 Å and $Lc_{(002)}$ = 223 Å) graphitic carbon studied here with ppm-level Re and up to 85 ppb Os (Toma et al., 2022). This contrasts to the ppb-level Re and ppt-level Os found in well-ordered graphite that are capped at < 10 ppb Re at $d_{(002)}$ scales of < 3.35 Å (Toma et al., 2022). This relationship implies that any carbonaceous material that has reached complete graphitization (>600 ℃) will have expelled any Os and Re exceeding this minimum threshold. For Laytonville Quarry graphite, this would amount to >99% loss of its current Re and Os contents when subjected to Franciscan subduction depths (80-100 km) where the temperature exceeds 600 ℃.
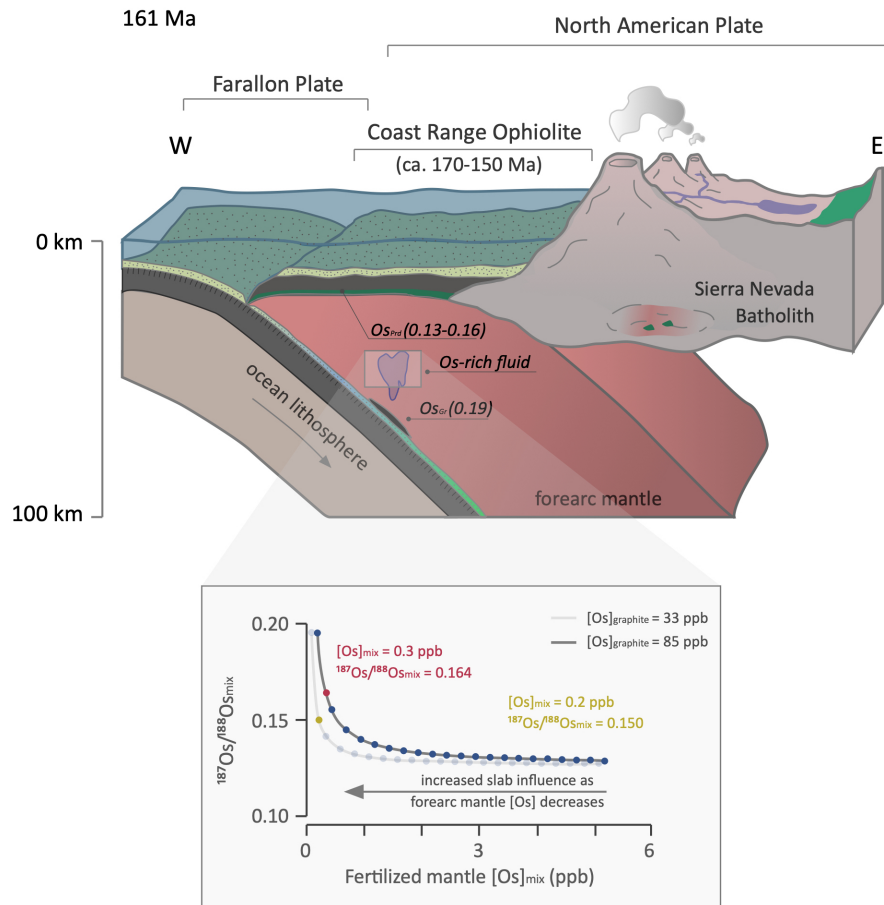
Figure 3.3. Upper figure depicts hypothetical scenario for Os cycling in the Franciscan Subduction System. The lower figure depicts results of mass balance modelling fo Os released from a graphitic crustal block ($2.8 \cdot 10^7$ g with 24 wt.% C) that is mixed with a forearc mantle block ($3.2 \cdot 10^9$ g) with variable Os concentrations (0-5 ppb) yielding a fertilized mantle mix of Os concentrations (ppb) and $^{187}Os/^{188}Os$ ratios (see Appendix B for details). Blue dots = 0.25 decrease in original forearc mantle Os. Red/orange circle/text = forearc mantle with 0.15 ppb Os fertilized by Os released from modeled graphitic crustal block with 85 (light grey line) and 33 (dark grey line) ppb Os. Os_{Prd} = $^{187}Os/^{188}Os$ ratio of forearc peridotite, Os_{Gr} = $^{187}Os/^{188}Os$ ratio of graphite.

Graphitization offers a plausible explanation for CRO peridotites (formed at ca. 160-150 Ma) in the FSS (Fig. 3.1b) with elevated $^{187}Os/^{188}Os$ ratios (0.130-0.158) relative to mantle values ($^{187}Os/^{188}Os$ = 0.129) (Fig. 3.3). These radiogenic CRO samples have lower Os concentrations (0.15 ppb) relative to other CRO samples (2 ppb) with mantle-like $^{187}Os/^{188}Os$ values (0.129) and likely indicate infiltration by slab-derived fluids with moderately radiogenic $^{187}Os/^{188}Os$ values (0.2-0.3) and low (0.01-0.1 ppb) Os contents (Snortum and Day, 2020). These $^{187}Os/^{188}Os$ estimates are consistent with the $^{187}Os/^{188}Os$ initial values (0.195) present in

Laytonville Quarry graphite (Fig. 3.2) at ca. 160 Ma and implicate Franciscan graphite as a viable source for radiogenic Os in CRO peridotites. The combination of extremely high Os abundance coupled with radiogenic Os make graphite a major influence in subduction zone Os recycling mass balance. For example, a block of Laytonville Quarry crust of 1 km x 1 km x 10 m would release up to 0.58g of Os during complete graphitization with $^{187}Os/^{188}Os$ of 0.1953 (see Appendix B). This amount of Os is enough to alter the $^{187}Os/^{188}Os$ of a 1 km^3 block of peridotite having 0.15 ppb Os, from 0.129 to 0.164. Although this shift to more radiogenic Os values is less where forearc peridotites contain higher Os concentrations (Fig. 3.3), a >2% mass ^{187}Os slab contribution is enough to shift the $^{187}Os/^{188}Os$ signatures of forearc peridotites above PUM values. We suggest that Os and Re expulsion during graphitization of carbonaceous material is a viable process for Os and Re element cycling in subduction zones where organic matter is involved.

We can estimate the global Os flux (229 kg/yr) entering subduction zones from organic carbon (11 Mt/yr) using a shale with a median TOC and Os concentration of 2.69 wt.% and 586 ppt, respectively (see Appendix B). Assuming this organic carbon inherited a modern seawater $^{187}Os/^{188}Os$ signature (~1.0) at the time of sediment deposition means that ~30 kg of ^{187}Os fertilizes the mantle wedge each year in a 100% recycling scenario where the organic matter is either completely graphitized and/or devolatilized through fluid-rock interactions. By comparison, the global Os flux (~554 kg/yr) from subducted oceanic crust (estimated at $6.93 \cdot 10^{16}$ g/yr with an average Os concentration and $^{187}Os/^{188}Os$ value of 8 ppt and 0.133, respectively) supplies only ~9.8 kg/yr of ^{187}Os (see Appendix B). This estimate implies, in relative terms, that sedimentary organic carbon contributes 75% of the total radiogenic Os budget subducted annually.

4|Carbon cycling in Paleoproterozoic shear zones in Northern Saskatchewan linked to Nuna assembly

Abstract

A peak in organic carbon burial ca. 2.1-1.8 billion years ago (Ga) led to the prolific growth of graphite-rich orogens internal to the supercontinent Nuna. The temporal history of graphitic carbon found in such orogens, however, is poorly understood, which in turn limits attempts at understanding the timescales of carbon cycling during orogenesis. Here we examine the graphitic roots of Paleoproterozoic orogens (Taltson-Snowbird orogeny = ca. 1.94-1.89 Ga and Trans-Hudson orogeny = ca. 1.84-1.72 Ga) in North America associated with Nuna assembly and show using a coupled Re-Os and U-Pb dating approach, that the studied graphite, hosted in shear zones, predominantly reflects biogenic carbon that was hydrothermally remobilized during the final, exhumation, stages of orogenesis at ca. 1.92-1.67 Ga. Our results demonstrate that graphite deposition occurred with a periodicity of ca. 29 Myr and likely involved carbon cycling on the scale of a million tons or more over a 200 Myr interval. These findings imply that the mass movement of graphitic carbon is an endemic feature of the orogenic cycle. Given the late-orogenic, fluid-mediated timing of graphitization, we speculate on the possibility that Taltson-Snowbird and Trans-Hudson graphitic shear zones have a metallogenic heritage linked to ancient orogenic gold deposits.

4.1. INTRODUCTION

Archean-Paleoproterozoic cratonic nuclei were assembled into the supercontinent Nuna at ca. 2.1-1.8 Ga through a series of global orogenic events (Fig. 4.1) that were preceded by a global period of peak biomass burial (e.g., the Lumagundi-Jatuli and Shunga Event; Condie et al., 2001). This carbonaceous matter has been invoked as key to providing the necessary competency contrasts for widespread thrusting, folding, and shearing to occur (Parnell and

Brolly, 2021). Consequently, organic (± inorganic) carbon became graphitized and concentrated along shear surfaces through fault-slip activity, as a common feature of Paleoproterozoic orogen development (Parnell and Brolly, 2021; Parnell et al., 2021), but the timing and extent of these later, shear-zone, graphite concentration events remain poorly documented relative to the broader orogenic cycles.

Remnants of such Paleoproterozoic mountain belts (Taltson-Snowbird and Trans-Hudson orogen) are located, in part, beneath the Athabasca Basin (Alberta and Saskatchewan, Canada) where a network of graphitic-pyritic shear zones underlie the highest-grade unconformity uranium deposits in the world (Jefferson et al., 2007). These shear zones are distributed among a handful of Archean-Paleoproterozoic lithotectonic blocks of the Rae and Hearne Cratons (Fig. 4.2) (Card et al., 2007; Paná et al., 2007) and have the potential to provide key insights into graphitization and carbon cycling within mountain belts associated with Nuna supercontinent assembly.

Shear formation was initiated diachronously from ca. 1.95 to 1.75 Ga across the Rae and Hearne cratons via collisional tectonics involving the Slave-Rae (Taltson Orogen), Rae-Hearne (Snowbird Orogen), and Hearne-Superior (Trans-Hudson Orogen) cratons as the core of Laurentia assembled (Hoffman, 1988, 2014; Corrigan et al., 2009). Mountain building initiated the first stage of graphitization via the prograde metamorphism of carbonaceous sedimentary rocks, which was followed by successive, retrograde fluid-deposited, graphite events in shear zones (Martz et al., 2017; Toma et al., 2022).

Herein, we utilize graphite-pyrite Re-Os dating (Toma et al., 2022) to document the temporal variation in graphite formation across shear zones representing the assembly of the Nuna supercontinent in North America (Fig. 4.1). We complement this work with U-Pb monazite geochronology to constrain prograde-retrograde metamorphic conditions during supercontinent amalgamation. We show that formation of hydrothermal graphite and pyrite in shear zones is a late-tectonic feature in the sequential assembly of Nuna from NW (older) to SE (younger) and may carry important broader metallogenic implications.

Nuna (1.79-1.73 Ga)
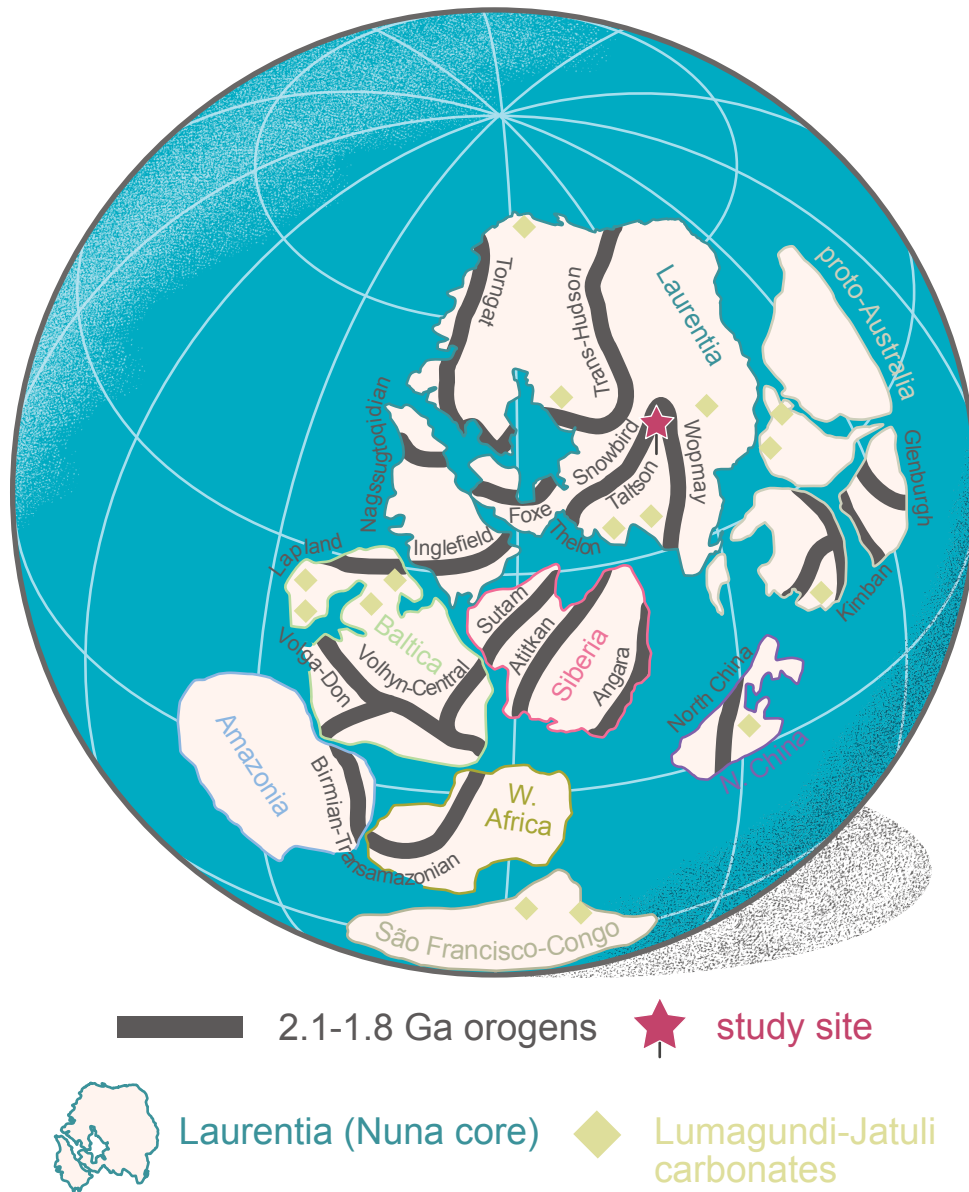
Figure 4.1. Paleoproterozoic collisional orogens distributed throughout Nuna (ca. 1.79-1.73 Ga) that contain the world's richest graphite deposits (8-30 wt.% C). Locations of Lumagundi-Jatuli Excursion-bearing successions ($\delta^{13}C_{carb}$ > 5‰) shown as yellow diamonds. Compiled after Condie (2013), Martin et al. (2013), and Gong et al. (2021).

4.2. METHODS

4.2.1. Mineral separation for Re-Os geochronology

Rock specimens were crush into 1-5 mm-sized rock chips using a hammer and anvil lined with duct tape and plastic to minimize metal contamination. Rock fragments were then pulverized using a zirconium disc mill and sieved to 70–200 μm sizes. Pyrite was isolated from the bulk rock via methylene iodine (MI) heavy liquid density separation, whereas graphite was concentrated using Frantz Isodynamic magnetic separation (current = 2.00 A and tilt = 15°). Concentrated pyrite and graphite were then split into magnetically distinct 100-500 mg aliquots via Frantz Isodynamic magnetic separation (current = 0.05 to 2.00 A and tilt = -5° to 15°).

4.2.2. Thin section and grain mount preparation

Thin section and grain mount preparation was carried out at the University of Alberta's Thin Section Laboratory using standard abrading and polishing equipment. Mineral separates used for Re-Os geochronology were mounted on to 3-5 mm diameter discs that were epoxy sealed and polished for petrographic and micro-analysis.

4.2.3. Electron Microprobe X-ray Mapping

X-ray mapping was performed at the University of Alberta's Electron Microprobe Laboratory using a JEOL JXA-8900R electron microprobe equipped with five wavelength dispersive spectrometers (WDS). Thin sections (Fig. C1b-C5b) were carbon-coated prior to backscattered electron (BSE) imaging and X-ray mapping. Maps of the intensities of Ce Lα, Th Mα, U Mα, Y Lα, and Zr Lα X-rays were acquired by rastering a fully focused electron beam using a beam current of 20 nA, accelerating voltage of 20 keV, and count time of 20 msec per pixel over an area of 500 by 500 pixels; the magnification used for any given set of maps depended on the grain size.

4.2.4. Re-Os Geochronology

Rhenium-osmium geochemistry was performed in a class-100 clean room at the University of Alberta's Re-Os Crustal Geochronology Laboratory. Aliquots of graphite (10-100 mg) and pyrite (30-100 mg) mineral separates (*see Appendix C2*) were transferred to individual borosilicate glass Carius tubes along with a known amount of ^{185}Re-^{190}Os tracer solution (UA3) and an 8 mL 1:1 mixture of 4 N H_2SO_4 and 4 N CrO_3-H_2SO_4 (0.5 g CrO3 per 1mL of 4 N H_2SO_4) and a 3:1 mixture of concentrated purged-distilled nitric acid and concentrated TMG hydrochloric acid (inverse aqua regia), respectively. This was immediately followed by cryogenic freezing (-116 ˚C) via ethanol-dry ice bath. Carius tubes housing graphite and pyrite were then sealed with a blow torch and spike-sample equilibrated at 240˚C for 72 hours and 220 ˚C for 24 hours, respectively.

Post-digested sample Carius tubes were frozen prior to opening and then processed via chloroform solvent extraction (Toma et al., 2020) and microdistillation (Birck et al., 1997) to isolate and purify Os, respectively. Chromic-sulfuric solutions were then processed via acetone solvent extraction and anion exchange chromatography to separate and purify Re (Toma et al., 2020), respectively, while aqua regia solutions were process using anion exchange chromatography and anion exchange single bead to separate and purify Re, respectively (Hnatyshin et al., 2016).

Purified Re and Os was loaded onto Ni and Pt filaments, respectively, and coated with Ba(NO$_3$)$_2$ and Ba(OH)$_2$ salts. Rhenium and osmium isotope measurements were made on a Thermo Scientific Triton Thermal Mass Spectrometer in negative polarity mode (N-TIMS) using static Faraday collectors and secondary electron multipliers. Instrument performance was monitored over a two-month period using in-house laboratory standard AB2, which yielded ^{187}Os/^{188}Os and ^{185}Re/^{187}Re ratios of 0.10680 ± 0.00018 and 0.59791 ± 0.0008 (1σ). Post-analysis data reduction included mass bias corrections, isobaric oxide corrections, blank corrections, and spike-sample unmixing (isotope dilution). Average Re and Os procedural blank concentrations were 11.4 ± 2.7 pg and 0.07 ± 0.04 pg, with a ^{187}Os/^{188}Os ratio of 0.25 ± 0.13, respectively. All ages were generated using IsoplotR (Vermeesch, 2018) and are reported as Model 1 (MSWD ≤

2) or Model 3 (MSWD ≥ 2) ages (probability of fit > 0.15; ^{187}Re decay constant = 1.666e11.a-1 ± 0.31%; Smoliar et al., 1996).

4.2.5. In-situ U-Pb Geochronology

Uranium-lead geochronology was performed on a Nu Plasma 1 Multi-Collector Inductively Coupled Plasma Mass Spectrometer (MC-ICP-MS) interfaced with a 213 nm New Wave laser ablation workstation (4Hz; 2.20 J/cm^3; 10-12 µm [monazite] and 15-25 µm [zircon] diameter spot-size) housed at the University of Alberta CCIM, following procedures modified from Simonetti et al (2005). Monazite (20-100 µm diameter) and zircon (30-100 µm diameter) targets within polished thin section were pre-characterized using BSE imaging and/or X-ray mapping prior to microanalysis. In house laboratory standards, Western Australia (monazite, Simonetti et al., 2006; Heaman unpublished data) and LH9415 (zircon, Simonetti et al., 2005), were analyzed pre- and post-sample runs (30/1s integrations) to monitor instrument performance and U/Pb fractionation. Data reduction included standard-sample bracketing and error propagation but precluded common Pb corrections due to the difficulty of accurately and precisely resolving the Hg isobar on mass 204. Secondary standards of monazite (TG09 and 44069, Aleinikoff et al., 2006) and zircon (OG1, Stern et al., 2019 and FC1, Paces and Miller, 1993) were analyzed for additional data-quality assurances. All reference standards yielded a <5% (2σ) reproducibility for ^{207}Pb/^{206}Pb and ^{206}Pb/^{238}U. Secondary reference materials TG09. 44069, OG1 and FC1 produced weighted-mean ^{207}Pb/^{206}Pb dates of 2551.87 ± 1.76 Ma (2σ; MSWD = 0.29; n = 23), 448.59 ± 3.42 Ma (2σ; MSWD = 0.54; n = 15), 3469.71 ± 3.79 Ma (2σ; MSWD = 0.26; n = 6) and 1095.41 ± 3.79 Ma (2σ; MSWD = 1.94; n = 25), respectively. All U-Pb ages were generated using IsoplotR (Vermeesch, 2018).

4.2.6. Bulk carbon isotopes

Carbon isotopes (^{13}C/^{12}C) were measured using a Thermo Delta V Plus isotope ratio mass spectrometer housed at the University of Alberta's Stable Isotope Laboratory. Decarbonated graphite powders were loaded into a quartz tube together with CuO reagent. The sample tube was then sealed under high vacuum and combusted in a muffle furnace at 1000 °C overnight. The resultant CO_2 gas was cryogenically purified and measured for C

isotopes at dual-inlet mode. Carbon isotope compositions are reported in delta (δ) notation normalized to Vienna Pee Dee Belemnite (VPDB) standard. Individual graphites had a $\delta^{13}C$ reproducibility better than 0.2‰ when reported at the 95% (2σ) confidence level.

4.3. RESULTS

Graphite occurrences are primarily concentrated (1% to 20%) within high-strain (brittle to ductile) zones and/or disseminated in adjacent basement lithologies as semi- (sooty) to fully-ordered (flaky) graphite varieties (Card, 2012; Pascal et al., 2016; Martz et al., 2017; Hillacre et al., 2021; Toma et al., 2022) with carbon isotopic signatures indicating a mainly biogenic origin (-30 to -15 ‰) (Kyser et al., 1988; Pană et al., 2007; Martz et al., 2017; Toma et al., 2022).

Shear-bounded graphite is hosted in shear planes, faults, and cataclasites of metamorphic (schists and gneiss) and igneous (pegmatites) protoliths and occurs as disseminated and/or anastomosing vein networks (μm- to m-scale) that are aligned both parallel to and across foliation (Card, 2012; Martz et al., 2017; Toma et al., 2022). In many cases, this graphite exhibits replacive textures with and/or interleave with phyllosilicate minerals (biotite, chlorite, sericite) or are intergrown with hydrothermal quartz and pyrite (± other sulfides) (Fig. 4.2).

The geochronology results of the present study comprise nine Re-Os isochron graphite/pyrite ages and ten in-situ U-Pb monazite/zircon ages (supplementary information of Appendix C) that yield formation ages between 1.94 Ga and 1.68 Ga and provide a direct link between graphitic-pyritic fluid flow in Pre-Athabasca shear zones and Paleoproterozoic mountain building during the nascent assembly of Nuna. All Re-Os and U-Pb age uncertainties are reported at the 2σ-level and include decay constant uncertainties.
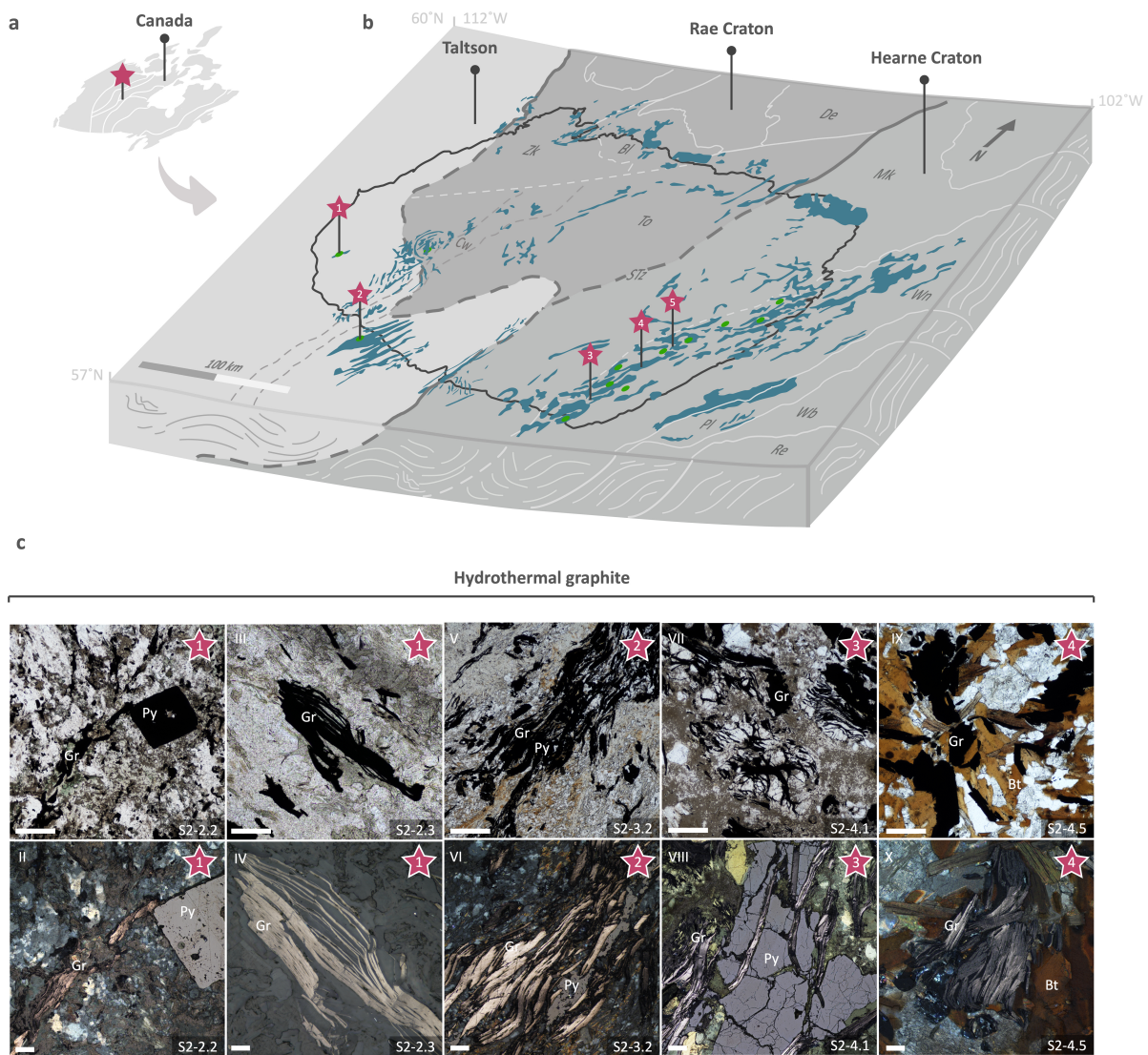
Figure 4.2. (a-b) Locations for drill core (red star) sampled from subsurface Precambrian basement rock in northern Alberta and Saskatchewan, Canada. (a) Sampling location relative to major lithotectonic blocks (white outlines) in Canada. (b) Graphitic-pyritic shear zones sampled (red star) in Taltson (1 = Maybelle River; 2 = Patterson Lake South) and Hearne Craton (3 = Key Lake; 4 = Christie Lake; 5 = Phoenix Deposit) basement. Blue areas = graphitic-pyritic zones inferred from EM conductors/drill core; orange dots = major U-deposits; black line = perimeter of the Athabasca Basin; dotted lines = inferred tectonic boundaries. (c) Transmitted light (top row) and reflected light (bottom row) photomicrographs depicting metamorphic (I-II) and hydrothermal (III-X) graphite and pyrite. Scale bar = 50 μm. Abbreviations: Cw = Clearwater; Zk = Zemlak, Bl = Beaverlodge, De = Dodge, To = Tantato, Mk = Mudjatik, Wn = Wollaston, STz = Snowbird Tectonic Zone; py = pyrite, gr = graphite, bt = biotite. See Appendix C for drill core depth locations.

4.3.1. Correlations with the Taltson-Snowbird Orogen – NW Nuna

The Taltson-Snowbird orogeny (ca. 1.94-1.90 Ga) was preceded by a period of accretion and partial melting along the margin of southern Rae craton that led to the formation of the Taltson basement complex (ca. 2.4-2.1 Ga) (Card et al., 2014). Continental-arc plutonism from easterly subduction generated diorite and tonalite melts shortly thereafter (ca. 2.01-1.97 Ga; Fig. 4.3)(Stern et al., 2003; Card et al., 2014; Powell et al., 2018). Granitoid emplacement was followed by prograde burial of metasedimentary rocks, thrust-sense deformation, and anatectic melting effected by east-west collision of the Slave-Rae cratons (Bethune et al., 2013). Monazite and zircon U-Pb dates recovered from high-strain zones and syn- to post-tectonic granitoids in northern Alberta and Saskatchewan bracket this prograde (M1) metamorphic event to ca. 1.94-1.92 Ga (Card et al., 2014; Card et al., 2018; Powell et al., 2018; Stern et al., 2003) (Fig. 4.3). Traces of this event are further recorded in mylonites studied here (monazite weighted-mean $^{207}Pb/^{206}Pb$ date = 1925 ± 7 Ma; Appendix C2-2.3) recovered from the Maybelle River shear zone in northern Alberta (Fig. 4.2 and Fig. 4.3). Coeval with this granulite-facies event is the first occurrence of shear-zone pyritization (Re-Os Model 3 isochron date = 1940 ± 19 Ma; Appendix C2-3.1) within metapelites of the Patterson Lake Corridor (PLc) of the southeastern Taltson Domain, Saskatchewan (Fig. 4.2 and Fig. 4.3).

Taltson and the neighboring southern Rae Province entered the terminal stage of orogenesis by ca. 1.91-1.89 Ga as the Rae-Hearne provinces collided (Ashton et al., 2009; Bethune et al., 2013; Johnstone et al., 2021). Retrograde cooling (M2) occurred as Taltson and Rae crust was exhumed to mid-crustal levels. This retrograde event is expressed mineralogically in high-strain zones by the overprinting of high-grade mineral assemblages by lower-grade (amphibolite to greenschist facies) assemblages (Panǎ et al., 2007). Monazite, zircon, and hornblende-biotite radiometric dates recovered from shear zones in northern Alberta and Saskatchewan provide direct constraints on the timing of compressional and extensional deformation events (Morrissey et al., 2022 and references therein). Recrystallized zircons and metamorphic monazite recovered from mylonitic pelites in the PLc and Maybelle River shear zones provide additional constraints on this extensional shearing event (zircon weighted-mean

^{207}Pb/^{206}Pb date = 1903 ± 8 Ma; Appendix C2-3.2 and 1908 ± 11 Ma; Appendix C2-2.3; monazite weighted-mean ^{207}Pb/^{206}Pb date = 1897 ± 8 Ma; Appendix C2-2.2) (Fig. 4.3). Synchronous with amphibolite-facies metamorphism was pyritization-graphitization of Maybelle River shear zones (Re-Os Model 3 isochron date = 1918 ± 18 Ma; Appendix C2-2.2 and Re-Os Model 1 isochron date = 1906 ± 11 Ma; Appendix C2-2.1) (Fig. 4.3). Statistically unresolvable with graphitization-pyritization of Maybelle shear zones, was the fluid deposition of pyrite-graphite in mylonitic pelites in Patterson Lake (PLc) shear zones (Re-Os Model 3 isochron date = 1883 ± 14 Ma; Supplementary Section S2-3.2) (Fig. 4.3). Together, these Re-Os dates provide a regional link between metamorphic and hydrothermal pyritization and graphitization of shear zones across Taltson-aged rocks in northern Alberta and Saskatchewan at 1890-1920 Ma, late in the Taltson orogenic cycle.

Taltson shear zones in NE Alberta and NW Saskatchewan were structurally reactivated at ca. 1.82 Ga during either protracted cooling following peak metamorphism or emplacement of Clearwater Domain granites (ca. 1.84 Ga) (Stern et al., 2003; Powell et al., 2022). Shear zones in NE Alberta proximal to Maybelle River shear zone record sericite ^{40}Ar-^{39}Ar ages of 1846.5-1813.4 Ma and may be associated with far-field Trans-Hudson tectonism (Pană et al., 2010). This reactivation event is coeval with the remobilization of pyrite (Re-Os Model 1 isochron = 1808 ± 18 Ma; Appendix C2-2.1) and graphite (Re-Os Model 1 isochron = 1783 ± 18 Ma; Appendix C2-2.1) in the Maybelle River shear zone proximal to this location and places a minimum estimate on when younger graphitization-pyritization occurred in Taltson shear zones (Fig. 4.3).
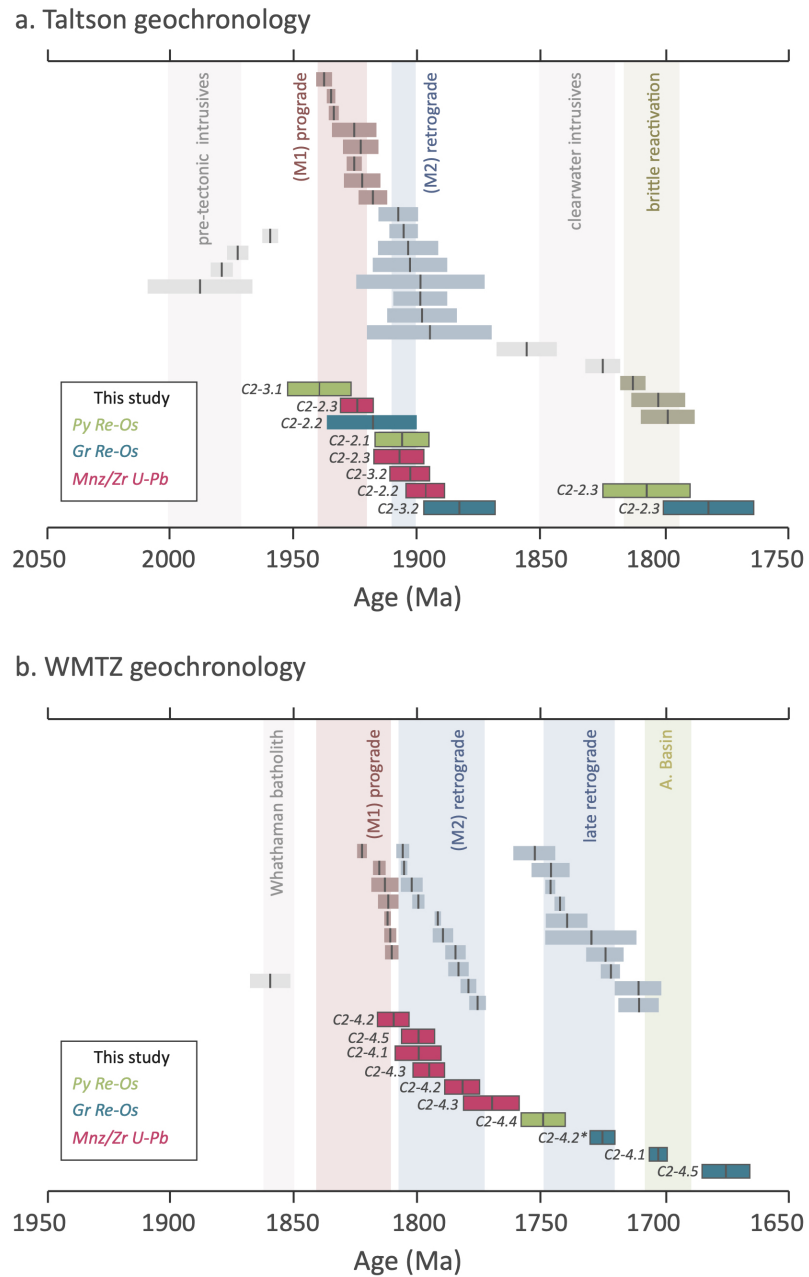
Figure 4.3. Pyrite (Py)/graphite (Gr) Re-Os isochron and monazite (Mnz)/zircon (Zrn) weighted-mean $^{207}Pb/^{206}Pb$ dates plotted alongside (a) Taltson and (b) Wollaston-Mudjatik Transition Zone (WMTZ) geochronology. See Sections *C2-2.1* to C*S2-4.5* of Appendix C for sample information. *Re-Os age from Toma et al. (2022)

4.3.2. Correlations with the Trans-Hudson Orogen – SE Nuna

The Wollaston-Mudjatik Transition Zone (WMTZ) is a high-strain corridor located within the southern Hearne Province in northern Saskatchewan that preserves the evolution of the

Trans-Hudson Orogeny from the incipient stages of prograde metamorphism initiated by Hearne-Superior collision (ca. 1.84 Ga) to the terminal stages of orogenic collapse (ca. 1.72 Ga) (Jeanneret et al., 2017). Orogenesis began with the southward thrusting of the thinned Hearne margin during Hearne-Sask collision and subsequent burial and prograde metamorphism of Wollaston Supergroup (deposited at ca. 2050-1860 Ma; Yeo et al., 2007) sedimentary rocks into graphite-bearing metapelites (Jeanneret et al., 2017) and emplacement of grey granites (ca. 1.84 Ga) formed from crustal melts during crustal thickening. Contemporaneous with this event was the development of garnet-bearing assemblages, localized partial melting of metapelites of the Wollaston Supergroup, the development of east-west-trending S1 foliation, and emplacement of tholeiitic to calc-alkaline intrusions (ca. 1.84-1.82 Ga) (Harper et al., 2006; Jeanneret et al. 2017). Monazite U-Pb dates recovered from Hearne lithologies in the WMTZ constrain peak metamorphism (750-825 ℃ and 6-9 kbar) and D1 phase of deformation to ca. 1813 Ma (Annesley et al., 2005; Mckechnie et al., 2012; Jeanneret et al., 2017).

Retrograde metamorphism and sinistral transpressive deformation followed this M1-D1 event as the southern Hearne margin was exhumed and isothermally decompressed to mid-crustal levels (2-6 kbar and 450-825 ℃) (Annesley et al., 2005; Martz et al., 2017). This M2-D2 event led to the development of NE-trending foliation, upright F2 folding of the S1 foliation, steeply-dipping S2 foliation, and shear zone development across the WMTZ (Jeanneret et al., 2016). Monazite U-Pb dates from paragneisses and zircon U-Pb dates recovered from pegmatites in the area constrain peak thermotectonism of M2-D2 to ca. 1.77 ± 0.01 Ga, whereas the broader M2-D2 event is bracketed to ca. 1.81-1.77 Ga. Monazite U-Pb dates (weighted-mean $^{207}Pb/^{206}Pb$ date = 1784 ± 10 Ma, Appendix C2-4.1; 1812 ± 7 Ma and 1780 ± 7 Ma, Appendix C2-4.2; 1794 ± 7 and 1763 ± 12 Ma, Appendix C2-4.3; 1800 ± 7 Ma, Appendix C2-4.5) recovered from retrogressed shear zones in the WMTZ fall precisely within this window of M2-D2 tectono-metamorphism (Fig. 4.3).

Regional orogenic cooling began at the terminus of this M2-D2 event (ca. 1.77 Ga) and continued until ca. 1.72 Ga (Jeanerret et al., 2016). This event led to retrogressive breakdown of cordierite into phyllosilicates, chloritization of biotite, sulfide and graphite remobilization and

precipitation, quartz flooding, and dissolution/reprecipitation of monazite and zircon (Card 2012, 2013; Card and Noll, 2016). Biotite ^{40}Ar/^{39}Ar dates from the Wollaston Domain constrain this event to ca. 1.74-1.72 Ga (Schneider et al., 2007), which is consistent within uncertainty to recrystallized monazite U-Pb (1718 ± 12 Ma) and biotite Rb-Sr (1711 ± 8 Ma) dates in the region (Worden et al., 1985; Jeanneret et al., 2016). Hydrothermal graphite (Re-Os Model 1 isochron date = 1732 ± 13 Ma, Toma et al., 2022) and pyrite (Re-Os Model 3 isochron date = 1749 ± 18 Ma, Appendix C2-4.4) recovered from shear zones in the WMTZ further confirms the synchroneity of this major fluid-flow event (Toma et al., 2022) (Fig. 4.3). However, graphite remobilization appears to be stretched out over 40-50 Myr interval (Re-Os Model age = 1703 ± 9 Ma, Appendix C2-4.1; Re-Os Model 3 isochron date =1681 ± 24 Ma, Appendix C2-4.5) possibly extending up until and/or after the basal sediments of Athabasca Basin were deposited (ca. 1.71-1.68 Ga) (Fig. 4.3).

4.4. CARBON CYCLING AND NUNA ASSEMBLY

The Assembly of Nuna (ca. 2.00-1.60 Ga) was spurred by the contraction of intercontinental seaways and convergence of numerous cratonic nuclei (Baltica, Laurentia, and Siberia) that culminated in a sequence of global thermotectonic and magmatic events (Fig. 4.1; Evans and Mitchell, 2011). The closure of the Snowbird and Manikewan oceans (ca. 2.0-1.8 Ga) in the northern hemisphere, for example, initiated formation of the Laurentian microcontinent (Slave, Rae, Hearne, and Superior) that produced the Taltson-Snowbird and Trans-Hudson orogens internal to the Nuna supercontinent (Pehrsson et al., 2016) (Fig. 4.1 and 4.4). Our new Re-Os and U-Pb datasets reveal that these mountain belts became graphitized-pyritized over several generations (ca. 1.94-1.68 Ga) with a periodicity of ca. 29 Myrs as orogenesis progressed eastward across proto-Laurentia (Fig. 4.4) from NW to SE.
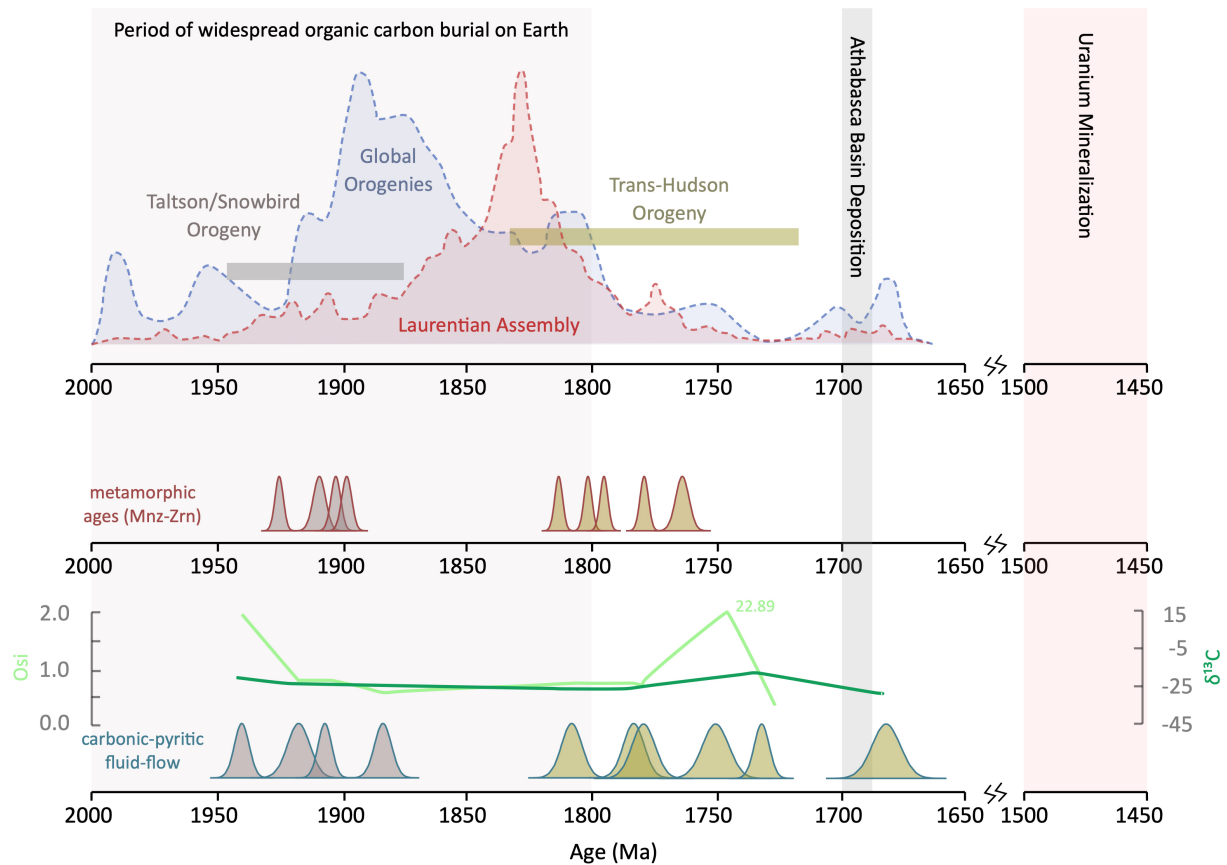
Figure 4.4. Re-Os pyrite/graphite and U-Pb zircon/monazite ages plotted alongside literature ages for the Taltson/Snowbird and Trans-Hudson orogenies and carbon isotope values and $^{187}Os/^{188}Os$ initial ratios for our studied graphite. Blue (global orogenies) and red (Laurentian Assembly) histograms modified after Pehrsson et al. (2016).

Much of this graphite, however, is structurally controlled and derives from organic (± inorganic) carbon mobilized from adjacent metapelites (± marbles) and redeposited in the brittle-ductile regime. For instance, the isotopically light carbon signatures ($\delta^{13}C$ = -28.30 ‰ to -20.90 ‰; Fig. 4.4) preserved in our studied graphite imply a predominantly biological rather than abiological origin (see Appendix C) and was likely precipitated during cooling of the C-O-H(-N) system by the reaction: CO_2 + CH_4 → $2C$ + $2H_2O$ (Martz et al., 2017; Toma et al., 2022). This interpretation is supported by the absence of mantle-like osmium ($^{187}Os/^{188}Os_{mantle}$ = 0.12) in shear-zone hosted graphite ($^{187}Os/^{188}Os_i$ = 0.33 to 0.77; Fig. 4.4).

The timing of this carbon cycling event coincides precisely with the onset of uplift and unroofing of Taltson-Snowbird and Trans-Hudson orogens (Fig. 4.3). Carbonaceous metapelites of the Murmac Bay Group, Waugh Lake Group, Virgin Schist Group, and Wollaston Supergroup are probable organic carbon-rich source rocks (McDonough et al., 1997; Yeo et al., 2007; Ashton et al., 2013; Card et al., 2020). These precursor sediments were likely deposited along continental margins and interiors (> ca. 1.84 Ga) prior to being deformed during Laurentian assembly. Extensional reactivation provided a conduit for hydrothermal fluids to concentrate 2-20 wt.% C in shears zones over 150 m vertical distances (Card and Heath, 2015).

This carbon cycling event necessitates the redistribution of upwards of 10% of the total carbon present in a 5 km x 0.5 km x 0.5 km supracrustal block hosting 4 wt.% C to produce a graphitized shear zone with > 5 wt.% C extending over a 75 m depth interval. Generalizing this scenario across entire structural corridors, such as the WMTZ and PLc, suggests that >20 million tons of carbon was cycled during exhumation of deep-seated crustal rocks internal to Nuna mountain belts. Such mass transfer carbon events likely transpired in other Paleoproterozoic mountain belts with comparable million-ton graphite enrichments. These include orogens internal (Wopmay = 1.9 Ga, Foxe = 1.9 Ga, Torngat = 1.9 Ga) and external (North China = 2.0 Ga, Kimban = 1.9 Ga, Svecofennian = 1.9 Ga) to North America (Parnell and Brolly, 2021) (Fig. 4.1). The bulk of this graphite is of a similarly organic carbon sedimentary origin. These global, predominantly organic carbon, graphite occurrences coincide with, and may be causally linked to, a 200 Myr interval of enhanced carbon burial (e.g., Lomagundi-Jatuli and Shunga Events) on the planet that preceded orogenesis and assembly of the supercontinent Nuna (Fig. 4.4) (Parnell et al., 2021; Parnell and Brolly, 2021).

4.5. GRAPHITIZATION AND METALLOGENESIS

The assembly of the Nuna supercontinent led to the prolific growth of over 20 graphite-rich orogens that host 85% of the world's richest graphite deposits (> 8 wt.% C) with resources commonly exceeding the 10-million-ton level (Fig. 4.1; Schulz et al., 2017; Parnell et al. 2021). This period of supercontinent assembly was also prolific for orogenic gold (Au) depositional events (2.1-1.7 Ga) initiated during late stage orogenesis (Goldfarb et al., 2001; Lambeck et al.,

2011; Pehrsson et al., 2016) that also overlap in space and time with many late-forming graphite episodes (Gaboury et al., 2021). This association has led researchers to invoke graphite-pyrite co-precipitation as one of the principal mechanisms for inducing Au-mineralization (Hu et al., 2017).

The Trans-Hudson orogen is one of the premier Paleoproterozoic gold provinces also enriched in graphite (Goldfarb et al., 2001). The Dakota segment of the THO, for example, hosts one of the largest lode deposits (Homestake) in North America, which itself is bounded by graphite-rich stratigraphic units (Frei et al., 2009). Gold mineralization at Homestake is bracketed to 1736 ± 8 Ma by Re-Os dating of Au-bearing arsenopyrite, (Morelli et al., 2010) and coincides with numerous gold occurrences (ca. 1790-1720 Ma) in the northern extension of the THO (Manitoba-Saskatchewan segment) that are similarly hosted in brittle-ductile, sulfide-rich, shear zones (Goldfarb et al., 2001). The temporal connection between the graphitic-pyritic shear zones studied here and these orogenic gold deposits invites correlation to a shared genetic link tied to THO uplift and exhumation. Several graphite-bearing gold occurrences hosted in shear zones local to the Athabasca region (Rae and Hearne Provinces) can similarly be linked to regional-scale metallogenesis across the THO (Morelli and MacLachlan, 2012).

However, auriferous occurrences are mostly absent from pre-Athabasca Supergroup structures despite sharing commonalities (CO_2 ± CH_4 fluids; T = 200-650°C; P = 1-5 kbar) with THO orogenic gold deposits (Groves, 1993). One possible explanation for this disparity is that pre-Athabasca Basin shear zones represent the natural gold variation across the THO. Another possibility is that such structures have either had all their gold remobilized during late-forming events, with a possible example being the Cluff Lake unconformity U-deposit (Morelli and MacLachlan, 2012), and/or that any orogenic gold originally present was eroded during isostatic adjustment prior to Athabasca Basin formation with the remaining graphitic structures representing the roots of these ancient gold depositional systems. One testable solution to these speculative hypotheses would be to survey the trace elements contents of pyritic shear zones to see if they host elevated Au concentrations.

5 | Conclusion

5.1 Final Remarks and Future Considerations

This dissertation focused on (1) establishing graphite as a common mineralogical host for Re and Os and as a viable geochronometer using the Re-Os decay system (Chapter 2), (2) characterizing Os cycling in subduction zones using graphite Re-Os dating coupled with Raman thermometry and $^{13}C/^{12}C$ isotopes (Chapter 3), and (3) linking large-scale carbon cycling in Paleoproterozoic graphitic shear zones to Nuna assembly using graphite/pyrite dating in combination with monazite/zircon U-Pb dating and $^{13}C/^{12}C$ isotopic tracing (Chapter 4).

1. A suite of terrestrial and extraterrestrial graphite samples (n = 17) hosts Re concentrations at the ppb-level (0.2-1500) comparable to terrestrial sulfides, organic-rich sedimentary rocks, and hydrocarbons. X-ray diffraction crystallinity data suggest that this Re is interstitially hosted between graphene sheets within natural graphite. A sub-population of these graphites (n = 2) were selected for Re-Os dating, namely two hydrothermal graphite samples formed in lower-crustal shear zones (Wollaston-Mudjatik Transition, Canada) and tanzanite-tsavorite gemstone deposits (Merelani Hills), which yielded high-precision Re-Os dates of 1731.52 ± 7.43 Ma and 586.89 ± 2.39 Ma, respectively, that are consistent with their inferred formation ages derived from other radiometric techniques. The success of the graphite Re-Os dating method now allows for the possibility of obtaining a more robust temporal framework for other graphite-forming events. Fruitful areas of future exploration include: (1) establishing the validity of the method beyond those geological environments tested here and (2) characterizing further the residency of Re and Os in graphite.

2. Graphitization related to Franciscan subduction zone metamorphism is constrained here using a composite graphite-pyrite Re-Os date of 161.39 ± 1.50 Ma, which when combined with Raman thermometry estimates (461-506°C) and $^{13}C/^{12}C$ isotopes (-30 ‰) links graphitization to the early stages of Franciscan subduction. Initial

$^{187}Os/^{188}Os$ estimates (0.195) also suggests that radiogenic Os present in Franciscan graphite was a probable source of crustal contamination in Franciscan fore-arc mantle peridotites. These latter findings suggest that graphitic carbon is likely a major source of Os recycling in volcanic arc-type settings. Future studies looking to build upon this research should experimentally constrain the P-T conditions at which Re and Os are likely to be released from graphite during subduction zone graphitization. Such experiments can potentially be performed with a piston-cylinder apparatus with graphitic carbon or organic-rich sedimentary rock powders loaded into MgO capsules and conducted over a range of P-T conditions that simulate graphite crystallization in the Earth. An alternative (geologic) approach could instead involve sampling organic-rich sedimentary rocks exposed to regional metamorphism to see how Re and Os behave with increased P-T conditions.

3. Graphite-pyrite Re-Os dating (n = 9) and monazite/zircon U-Pb (n = 10) dating of Pre-Athabasca Supergroup shear zones (Alberta and Saskatchewan) links graphite-pyrite mineralization to crustal exhumation of the Taltson-Snowbird and Trans-Hudson orogens ca. 1.92-1.67 Ga associated with Nuna assembly. Graphite deposition occurred with a periodicity of 28.81 ± 1.79 Myr and likely involved carbon cycling on the scale of a million tons or more during this time. Carbon isotope data suggests that the bulk of this mobilized carbon is of a biogenic, organic carbon sedimentary, origin (-30 to -15‰) presumably deposited during the Lumagundi-Jatuli and Shunga Events between 2.3 and 2.0 Ga. To expand upon this research, future studies should explore further the timing of carbon cycling events in other graphite-rich Paleoproterozoic orogens.

References

Ackerman, L., Magna, T., Žák, K., Skála, R., Jonášova, S., Mizera, J., & Řanda, Z. The behavior of osmium and other siderophile elements during impacts: Insights from the Ries impact structure and central European tektites. *Geochim. Cosmochim. Acta* **210**, 59-70 (2017).

Adlakha, E. & Hattori, K. Thermotectonic events recorded by U-Pb geochronology and Zr-in-rutile thermometry of Ti oxides in basement rocks along the P2 fault, eastern Athabasca Basin, Saskatchewan, Canada. *Geol. Soc. Am. Bull.* (2021) doi: https://doi.org/10.1130/B35820.1

Aleinikoff, J. N., W. S. Schenck, M. O. Plank, L. Srogi, C. M. Fanning, S. L. Kamo, & H. Bosbyshell. Deciphering igneous and metamorphic evens in high-grade rocks of the Wilmington Complex, Delaware: Morphology, cathodoluminescence and backscattered electron zoning, and SHRIMP U-Pb geochronology of zircon and monazite. *Geol. Soc. Am. Bull.* **118**, 39–64 (2006).

Alexandre, P., Kyser, K., & Jiricka, D. Critical Geochemical and Mineralogical Factors for the Formation of Unconformity-Related Uranium Deposits: Comparison between Barren and Mineralized Systems in the Athabasca Basin, Canada. *Econ. Geol.* **104**, 413-435 (2009).

Amari, S., Anders, E., Virag, A., & Zinner, E. Interstellar graphite in meteorites. *Nature* **345**, 238-240 (1990).

Ambrosi, A., Chua, C.K., Khezri, B., Sofer, Z., Webster, R.D., & Pumera, M. Chemically reduced graphene contains inherent metallic impurities present in parent natural and synthetic graphite. *P. Natl. Acad. Sci. USA* **109**, 12899-12904 (2012).

Annesley, I.R., Madore, C., Kusmirski, R.T., & Bonli, T. Uraninite-bearing granitic pegmatite, Moore Lakes, Saskatchewan: Petrology and U-Th-Pb chemical ages; in Summary of Investigations 2000, v. 2, Saskatchewan Geological Survey, Sask. Energy Mines, Misc, Rep. 2000-4.2 (2000).

Annesley, I.R., Madore, C., and Cutler, J. Synchrotron X-ray analysis of graphite pelitic gneisses in the vicinity of unconformity-type uranium mineralization; in Summary of Investigations 2001, v. 2, Saskatchewan Geological Survey, Sask. Energy Mines, Misc. Rep. 2001-4.2 (2001).

Annesley, I.R., Madore, C., & Portella, P. Geology and thermotectonic evolution of the western margin of the Trans-Hudson Orogen: evidence from the eastern sub-Athabasca basement, Saskatchewan. *Can. J. Earth Sci* **42**, 573-597 (2005).

Ashton, K.E., Hartlaub, R.P., Heaman, L.M., Morelli, R.M., Card, C.D., Bethune, K., & Hunter, R.C. Post-Taltson sedimentary and intrusive history of the southern Rae Province along the

northern margin of the Athabasca Basin, Western Canadian Shield. *Precambr. Res.* **175**, 16-34 (2009).

Ashton, K.E., Kartlaub, R.P., Bethune, K.M., Heaman, L.M., Rayner, N., & Niebergall, G.R. New depositional age constraints for the Murmac Bay group of the southern Rae craton, Canada. *Precambr. Research* **232**, 70-88 (2013).

Baker, A.J. & Fallick, A.E. Heavy carbon in two-billion-year-old marbles from Lofoten-Vesteralen, Norway: Implications for the Precambrian carbon cycle. *Geochim. Cosmochim. Acta* **53**, 1111-1115 (1989).

Barraenechea, J.F., Luque, F.J., Millward, D., Ortega, L., Beyssac, O., & Rodas, M. Graphite morphologies from the Borrowdale deposit (NW England, UK): Raman and SIMS data. *Contrib. Min. Petrol.* **158**, 37-51 (2009).

Beyssac, O., Goeff, B., Chopin, C., & Rouzaud, J.N. Raman spectra of carbonaceous material in metasediments: a new geothermometer. *J. Metamorp. Geol.* **20**, 859-871 (2002).

Bethune, K.M., Berman, R.G., Rayner, N., & Ashton, K.E. Structural, petrological and U-Pb SHRIMP geochronological study of the western Beaverlodge domain: Implications for crustal architecture, multi-stage orogenesis and the extent of the Taltson orogen in the SW Rae craton, Canadian Shield. *Precambr. Res.* **232**, 89-118 (2013).

Birck, J.L., Barman, M.R., & Capmas, F. Re-Os Isotopic Measurements at the Femtomole Level in Natural Sample. *Geostand. Geoanal. Res.* **20**, 19-27 (1997).

Brandon, A.D., Creaser, R.A., Shirey, S.B., & Carlson, R.W. Osmium Recycling in Subduction Zones. Science **272**, 861-864 (1996).

Brett, R. & Higgins, G.T. Cliftonite: A proposed origin, and its bearing on the origin of diamonds in meteorites. *Geochim. Cosmochim. Acta* **33**, 1473-1484 (1969).

Bullen, W.D., Thomas, R.J., & Scogings, A.J. The geologic setting of industrial mineral deposits in the Natal Metamorphic Province. *S. Afr. J. Geol.* **95**, 51-50 (1992).

Buseck, P.R., & Beyssac, O. From Organic Matter to Graphite: Graphitization. *Elements* **10**, 421-426 (2014).

Cameco Corporation. Management's Discussion and Analysis. Retrieved from Cameco Corporation database on March 31, 2023, from https://cameco.com (2021).

Card., C.D. The origins of anomalously graphitic rocks and quartzite ridges in the basement to the southeastern Athabasca Basin. *Summary of Investigations, 2, Sask. Geol. Surv., Sask. Ministry of the Economy, Misc. Rep.* **2012-4.2**, 15 (2012)

Card C.D. Altered pelitic gneisses and associated ''quartz ridges'' beneath the southeastern Athabasca Basin: Alteration facies and their relationship to uranium deposits along the Wollaston-Mudjatik transition. *Summary of Investigations 2013, Volume 2:* Saskatchewan, *Canada, Sask. Geol. Surv., Sask. Ministry of the Economy, Miscellaneous Report* **2013-4.2**, 23 (2013).

Card., C.D. Distribution and significance of crystalline rocks in the Patterson Lake uranium exploration corridor of nothwest Saskatchewan. *Summary of Investigations 2017, Volume 2, Sask. Geol. Surv., Sask., Ministry of the Economy, Misc. Rep.* **2017-4.2**, 11 (2017).

Card., C.D. The Patterson Lake corridor of Saskatchewan, Canada: defining crystalline rocks in a deep-seated structure that hosts a giant, high-grade Proterozoic unconformity uranium system. *GEEA* **21**, 1 (2020).

Card, C.D., Pana, D., Portella, P., Thomas, D.J., & Annesley, I.R. Basement rocks to the Athabasca Basin, Saskatchewan and Alberta; in EXTECH IV: Geology and Uranium Exploration TECHnology of the Proterozoic Athabasca Basin, Saskatchewan and Alberta, (ed.) C.W. Jefferson and G. Delaney. *Geol. Surv. Can. Bulletin* **588**, 69-87 (2007).

Card., C.D., Bethune, K.M., Davis, J.W., Rayner, N., & Ashton, K.E. The case for a distinct Taltson orogeny: Evidence from northwest Saskatchewan, Canada. *Precambrian Res.* **225**, 245-265 (2014).

Card, C.D., Rayner, N., Pearson, G., Luo, Y., & Creaser, R. Geochronological results from the southern Athabasca Basin region, Saskatchewan; in Summary of Investigations 2018, Volume 2, Saskatchewan Geological Survey, Saskatchewan Ministry of Energy and Resources, Miscellaneous Report 2018-4.2, Paper A-4, 15p. (2018).

Card, C.D. & Heath, P. Bedrock geology of sub-Athabasca basement rocks (NTS 74H); Saskatchewan Geological Survey, Sask. Ministry of the Economy, Geoscience Map 2015-1 (2015).

Card., C.D. & Noll, J. Host-rock protoliths, pre-ore metasomatic mineral assemblages and textures, and exotic rocks in the western Athabasca Basin: ore-system controls and implications for the unconformity-related uranium model. *Summary of Investigations 2016, Volume 2, Sask. Geol. Surv., Sask. Ministry of the Economy, Misc. Rep.* **2016-4.2**, 19 (2016).

Chen, K., Walker, R.J., Rudnick, R.L., Gao, S., Gaschnig, R.M., Puchtel, I.S., Tang, M., & Hu, Z.-C. Platinum-group element abundances and Re-Os isotopic systematics of the upper continental crust through time: Evidence from glacial diamictites. *Geochim. Cosmochim. Acta* **191**, 1-16 (2016).

Clift, P. A revised budget for Cenozoic sedimentary carbon subduction. *Rev. Geophys.* **55**, 97-125 (2017).

Condie, K.C., Des Marais, D.J., & Abbott, D. Precambrian superplumes and supercontinents: a record in black shales, carbon isotopes, and paleoclimates? *Precamb. Res.* **106**, 239-260 (2001).

Condie, K.C. Preservation and Recycling of Crust during Accretionary and Collisional Phases of Proterozoic Orogens: A Bumpy Road From Nuna to Rodinia. *Geosciences* **3**, 240-261 (2013).

Cooper, F.J., Platt, J.P., & Anczkiewicz, R. Constraints on early Franciscan subduction rates from 2-D thermal modeling. Earth and Planet. Sci. Lett. **321**, 69-79 (2011).

Corrigan, D., Pehrsson, S., Wodicka, H., & Kemp, E.DE. The Paleoproterozoic Trans-Hudson Orogen: a prototype of modern accretionary processes. *Geol. Soc. London Spec. Publ.* **327**, 457-479 (2009).

Croat, T.K., Bernatowicz, T.J.,& Daulton, T.L. Presolar Graphitic Carbon Spherules: Rocks from Stars. *Elements* **10**, 441-446 (2014).

Day, J.M.D., Pearson, D.G., Macpherson, C.G., Lowry, D., & Carracedo, J. Pyroxenite-rich mantle formed by recycled oceanic lithosphere: Oxygen-osmium isotope evidence from Canary Island lavas. *Geology* **37**, 555-558 (2009).

Dobner, A., Graf, W., Hahn-Weinheimer, P., & Hirner, A. Stable carbon isotopes of graphite from Bogola Mine, Sri Lanka. *Lithos* **11**, 251-255 (1978).

Dubin, A., and Peucker-Ehrenbrink, B. The importance of organic-rich shales to the geochemical cycles of rhenium and osmium. *Chem. Geol.* **403**, 111-120 (2015).

Duke, E.F. and Rumble III, D. Textural and isotopic variations in graphite from plutonic rocks, South-Central New Hampshire. *Contrib. Min. Petrol.* **93**, 409-419 (1986).

Duke, E.F., Galbreath, K.C., Trusty, K.J. Fluid inclusion and carbon isotope studies of quartz-graphite veins, Black Hills, South Dakota, and Ruby Range, Montana. *Geochim. Cosmochim. Acta* **54**, 683-698 (1989).

Dumitru, T.A., Wakabayashi, J., Wright, J.E., & Wooden, J.L. Early Cretaceous transition from nonaccretionary behavior to strongly accretionary behavior within the Franciscan subduction complex. *Tectonics* **29**, 1-24 (2010).

Ernst, W.G. Tectonic contact between the Franciscan mélange and the Great Valley Sequence-Crustal expression of a Late Mesozoic Benioff Zone. *J. Geophys. Res.* **85**, 886-901 (1970).

Ethier, M. and Pirzada, A. Lochaber Graphite Property, Buckingham Area, Quebec, Canada. NI 43-101 Technical Report (2014).

Evans, D.A.D. & Mitchell, R.N. Assembly and breakup of the core of Paleoproterozoic-Mesoproterozoic supercontinent Nuna. *Geology* **39**, 443-446 (2011).

Feneyrol, J., Giuliani, G., Ohnenstetter, D., Le Goff, E., Malisa, E.P.J., Saul, M., Saul, E., Saul, J., & Pardieu, V. Lithostratigraphic and structural controls of 'tsavorite' deposits at Lemshuku, Merelani area, Tanzania. *C. R. Geosci.* **342**, 778-785 (2010).

Feneyrol, J., Giuliani, G., Ohnenstetter, D., Fallick, A.E., Martelat, J.E., Dubessy, J., Rollion-Bard, C., Le Goff, E., Malisa, E., Rakotondrazafy, A.F.M., Pardieu, V., Kahn, T., Ichang'I, D., Venance, E., Voarintsoa, N.R., Ranatsenho, M.M., Simonet, C., Omito, E., Nyamai, C., & Saul, M. New aspects and perspectives on tsavorite deposits. *Ore Geol. Rev.* **53**, 1-25 (2013).

Feneyrol, J., Giuliani, G., Demaiffe, D., Ohnenstetter, D., Fallick, A.E., Dubessy, J., Martelat, J.-E., Rakotondrazafy, A.F.M., Omito, E., Ichang'I, D., Nyamai, C., & Wamunya, A.W. Age and origin of the tsavorite and tanzanite mineralizing fluids in the Neoproterozoic Mozambique Metamorphic Belt. *Canad. Mineral.* **55**, 763-786 (2017).

Ferry, J.M. Petrology of graphitic sulfide-rich schists from south-central Maine: an example of desulfidation during prograde regional metamorphism. *Am. Mineral.* **66**, 908-930 (1981).

Fission Uranium Corp. Patterson Lake South, Project Overview. Retrieved from Fission Uranium Corp March 21, 2023, from https://fissionuranium.com (2022).

Ford, R.B. Occurrence and Origin of the Graphite Deposits Near Dillon, Montana. *Econ. Geol.* **49**, 31-43 (1954).

Frei, R., Dahl, P.S., Munck Frandsson, M., Apel Jenson, L. Rintza Hansen, T., Terry, M.P., Frei, K.M. Lead-isotope and trace-element geochemistry of Paleoproterozoic metasedimentary rocks in the Lead and Rochford basins (Black Hills, South Dakota, USA): Implications for genetic models, mineralization ages, and sources of leads in the Homestake gold deposit. *Precambr. Res.* **172**, 1-24 (2009).

Fröba, M., Lochte, K., & Metz, W. Xanes studies on rhenium l absorption edges of R2O7 graphite intercalation compounds and of other rhenium-oxygen compounds. *J. Phys. Chem. Solids* **57**, 635-641 (1995).

Gaboury, D. The neglected involvement of organic matter in forming large and rich hydrothermal orogenic gold deposits. *Geosciences* **11**, 344 (2021).

Galy, V., Beyssac, O., France-Lanlord, C., & Eglinton, T. Recycling of Graphite During Himalayan Erosion: A Geologic Stabilization of Carbon in the Crust. *Science* **322**, 943-945 (2008).

Gannoun, A., Burton, K.W., Parkinson, I.J., Alard, O., Schiano, P., & Thomas, L.E. The scale and origin of the osmium isotope variations in mid-ocean ridge basalts. *Earth Planet. Sci. Lett.* **259**, 541-556 (2007).

Georgiev, S., Stein, H.J., Hannah, J.L., Weiss, H.M., Bingen, B., Xu, G., Rein, E., Hatlø, V., Løseth, H., Nail, M., & Piasecki, S. Chemical signals for oxidative weathering predict Re-Os isochroneity in black shales, East Greenland. *Chem. Geol.* **324-325**, 108-121 (2012).

Goldfarb, R.J., Groves, D.I., & Gardoll, S. Orogenic gold and geologic time: a global synthesis. *Ore Geol. Rev.* **18**, 1-75 (2001).

Gong, Z., Evans, D.A.D., Youbi, N., Lahna, A.A., Söderlund, U., Malek, M.A., Wen, B., Jing, X., Ding, J., Boumedhi, M.A., & Ernst, R.E. Reorienting the West African craton in Paleoproterozoic-Mesoproterozoic supercontinent Nuna. *Geology* **49**, 1171-1176 (2021).

Grew, E.S. Carbonaceous material in some metamorphic rocks of New England and other areas. *J. Geol.* **82**, 50-73 (1974).

Groves, D.I. The crustal continuum model for late-Archean lode-gold deposits of the Yilgarn Block, Western Australia. *Miner. Deposita* **28**, 366-374 (1993).

Harper, C.T., Rayner, N., & Card, C. Preliminary U-Pb ages for Archean basement and Proterozoic intrusions from the northern Wollaston Lake area, Saskatchewan. In: summary of Investigations 2006, Volumne 2, Saskatchewan Geological Survey, Saskatchewan Industry Resources, Misc. Rep. 2006-4.2, CD-ROM, Paper A-7, 9p (2006).

Hazen, R.M. & Morrison, S. M. On the paragenetic modes of minerals: A mineral evolution perspective. *Am. Mineral.* **107**, 1262-1287 (2022).

Hiatt, E.E., Pufahl, P.K., & Edwards, C.T. Sedimentary phosphate and associated fossil bacteria in a Paleoproteroiz tidal flat in the 1.85 Ga Michigamme Formation, Michigan, USA. *Sediment. Geol.* **319**, 24-39 (2015).

Hillacre, S., Ansdell, K., & McEwan, B. Geology, structural analysis, and paragenesis of the Arrow Uranium Deposit, western Athabasca Basin, Saskatchewan, Canada: Implications for the development of the Patterson Lake Corridor. *Econ. Geol.* **116**, 285-321 (2021).

Hilton, C.D., Ash, R.D., Piccoli, P.M., Kring, D.A., McCoy, T.J., and Walker, R.J. Origin and age of metal veins in Canyon Diablo graphite nodules. *Meteorit. Planet. Sci.* **55**, 771-780 (2020).

Hnatyshin, D., Kontak, D.J., Turner, E.C., Creaser, R.A., Morden, R., & Stern, R.A. Geochronologic (Re-Os) and fluid-chemical constraints on the formation of the Mesoproterozoic-hosted Nanisivik Zn-Pb deposit, Nunavut, Canada: Evidence for early diagenetic, low-temperature conditions of formation: *Ore Geol. Rev.* **79**, 189- 217 (2016).

Hnatyshin, D., Creaser, R.A., Meffre, S., Stern, R.A., Wilkinson, J.J., & Turner, E.C. Understanding the microscale spatial distribution and mineralogical residency of Re in pyrite: Examples from carbonate-hosted Zn-Pb ores and implications for pyrite Re-Os geochronology. *Chem. Geol.* **533**, 119427 (2019).

Hoffman, P.F. United Plates of America, The Birth of a Craton: Early Proterozoic Assembly and Growth of Laurentia. *Ann. Rev. Earth Planet. Sci.* **16**, 543-603 (1988).

Hoffman, P.F. The origin of Laurentia: Rae Craton as the Backstop for Proto-Laurentian Amalgamation by Slab Suction. *Geosci. Can.* **41**, 313-320 (2014).

Hofmann, A.W., & White, W.M. Mantle plumes from ancient oceanic-crust. *Earth Planet. Sci. Lett.* **57**, 421-436 (1982).

Hu, S.-Y., Evans, K., Craw, D., Rempel, K., Grice, K. Resolving the role of carbonaceous material in gold precipitation in metasediment-hosted orogenic gold deposits. *Geology* **45**, 167-170 (2017).

IAEA. Unconformity-related Uranium Deposits. IAEA TECDOC series, ISSN 1011-4289, no. 1857, Publishing Section, Vienna (2018).

Jackson, R.A. & Montenari, M. Chapter Six – Computer modeling of zircon (ZrSiO4)-Coffinite (USiO4) solid solutions and lead incorporation: Geological implications. Stratigraphy & Timescales, *Academic Press* **4**, 217-227 (2019).

James, H.L. Iron Formation and Associated Rocks in the Iron River District, Michigan. *Geol. Soc. Am. Bull.* **62**, 251-266 (1951).

Jara, A.D, Betemariam, A., Woldetinsae, G., & Kim, J.Y. Purification, application and current market trend of natural graphite: A review. *Int. J. Min. Sci. Tech.* **29**, 671-689 (2019).

Jaszczak, J., Camberlain, S.C., & Robinson, G.W. The Graphites of New York: Scientific and Aesthetic Surprises. *Rocks and Miner.* **84**, 502-519 (2009).

Jeanneret, P., Goncalves, P., Durand, C., Poujol, M., Trap, P., Marquer, D., Quirt D. & Ledru, P. Geochronological constraints on the trans-Hundsonian tectono-metamorphic evolution of the pre-Athabasca basement within the Wollas- ton-Mudjatik Transition Zone, Saskatchewan. *Precambr. Res.* **301**, 152–178 (2017).

Jefferson C. W., Thomas D. J., Gandhi S. S., Ramaekers P., Delaney G., Brisbin D., Cutts C., Quirt D., Portella P. & Olson R. A. Unconformity- associated uranium deposits of the Athabasca Basin, Saskatchewan and Alberta. In Mineral Deposits of Canada: A Synthesis of Major Deposit-Types, District Metallogeny, the Evolution of Geological Provinces, and Exploration Methods (ed. W. D. Goodfellow). *Geol. Assoc. Can. Min. Dep. Div. Spec. Publ.* **No. 5**, 273–305 (2007).

Johnstone, D.D., Bethune, K.M., Card, C.D., & Tschirhart, V. Structural evolution and related implications for uranium mineralization in the Patterson Lake corridor, southwestern Athabasca Basin, Saskatchewan, Canada. *Geochem: Explor. Environ. Anal.* **21**, 1-27 (2021).

Kemp, D.B., Suan, G., Fantasia, A., Jin, S., & Chen, W. Global organic carbon burial during the Toarcian oceanic anoxic event: Patterns and controls. *Earth Sci. Rev.* **231**, 104086 (2022).

Kerr, W.C. The Discovery of the Phoenix Deposit: A New High-Grade, Athabasca Basin Unconformity-Type Uranium Deposit, Saskatchewan, Canada. The Challenge of Finding New Mineral Resources: Global Metallogeny, Innovative Exploration and New Discovers. *Soc. Econ. Geol.* **15**, 703-728 (2010).

Kiciński, W. & Dyjak, S. Transition metal impurities in carbon-based materials: Pitfalls, artifacts and deleterious effects. *Carbon* **168**, 748-845 (2020).

Kyser, T.K., Wilson, M.R., & Ruhrmann. Stable isotope constraints on the role of graphite in the genesis of unconformity-type uranium deposits. *Can. J. Earth Sci.* **26**, 490-498 (1989).

Lambeck, A., Mernagh, T., & Wyborn, L. (2011) Are iron-rich sedimentary rocks the key to the spike in orogenic gold mineralization in the Paleoproterozoic? *Econ. Geol.* **106**, 321-330 (2011).

Landis, C.A. Graphitization of Dispersed Carbonaceous Material in Metamorphic Rocks. *Contrib. Min. Petrol.* **30**, 34-45 (1971).

Liao, R., Li, C., Liu, H., Chen, Q., & Sun, W. Rhenium enrichment in the northwest Pacific arc. *Ore Geol. Rev.* **115**, 103176 (2019).

Li, C., Qu, W., Du, A., & Sun, W. Comprehensive study on extraction of rhenium with acetone in Re-Os isotopic dating. *Rock Mineral. Anal.* 22, 233–238 (in Chinese, with English abstract) (2009).

Liu, C., Xu, Y., & Wu, F. Limited recycling of crustal osmium in forearc mantle during slab dehydration. *Geology* **46**, 239-242 (2018).

Luque, F.J., Pasteris, J.D., Wopenka, B., Rodas, M., & Barrenechea. Natural fluid-deposited graphite: mineralogical characteristics and mechanisms of formation. *Am. J. Sci.* **298**, 471-498 (1998).

Luque, F.J., Crespo-Feo, E., Barrenechea, J.F., & Ortega, L. Carbon isotopes of graphite: Implication on fluid history. *Geosci. Front.* **3**, 197-207 (2012).

Luque, F.J., Huizenga, J-M., Crespo-Feo, E., Wada, H., Ortega, L., & Barrenechea, J.F. Vein graphite deposits: geological settings, origin, and economic significance. *Miner. Depos.* **49**, 261-277 (2013).

Martin, A.P., Condon, D.J., Prave, A.R., & Lepland. A review of temporal constraints for the Paleoproterozoic large, positive carbonate carbon isotope excursion (the Lomagundi-Jatuli Event). *Earth Sci. Rev.* **127**, 242-261 (2013).

Martz, P., Cathelineau M., Mercadier, J., Boiron, M., Jaguin, J., Tarantola, A., Demacon, M., Gerbeaud, O., Quirt, D., Doney, A. & Ledru, P. C-O-H-N fluids circulations and graphite precipitation in reactivated Hudsonian shear zones during basement uplift of the Wollaston-Mujatik Transition Zone: Example of the Cigar Lake U deposit. *Lithos* **294–295**, 222–245 (2017).

Matsuda, J.-I., Namba, M., Maruoka, T., Matsumoto, T., & Kurat, G. Primordial noble gases in graphite-metal inclusion from the Canyon Diablo IAB iron meteorite and their implications. *Meteorit. Planet. Sci.* **40**, 431-443 (2005).

McDonough, M.R. & McNicoll. V.J. U-Pb age constraints on the timing of deposition of the Waugh Lake and Burntwood (Athabasca) groups, southern Taltson magmatic zone, northeastern Alberta, in Radiogenic Age and Isotopic Studies: Reprt 10; Geological Survey of Canada, Current Research 1997-F, 101-111 (1997).

McDowell, F.W., Lehman, D.H., Gucwa, P.R., Fritz, D., & Maxwell, J.C. Glaucophane schists and ophiolites of the northern California Coast Ranges: Isotopic ages and their tectonic implications. *Geol. Soc. Am. Bull.* **95**, 1373-1382 (1984).

McKechnie, C.L., Annesley, I.R., & Ansdell, K.M. Medium- to low-pressure politic gneisses of Fraser Lakes zone B, Wollaston Domain, northern Saskatchewan, Canada: Mineral compositions, metamorphic P-T-t path, and implications for the genesis of radioactive abyssal granitic pegmatites. *Can. Mineral.* **50**, 1669-1694 (2012).

Meisel, T., Walker, R.J., Irving, A.J., & Lorand, J. Osmium isotopic compositions of mantle xenoliths: A global perspective. *Geochim. Cosmochim. Acta*, **65**, 1311-1323 (2001).

Miranda, D. A., Chaves, A.D.O., Campello, M.S., Ramos, L.L.D.M. Origin and thermometry of graphites from Itapecerica supracrustal succession of the southern Sa Francisco Craton by C isotopes, X-ray diffraction, and Raman spectroscopy. *Int. Geol. Rev.* **61**, 1864-1875 (2019).

Moles, N. R. and Boyce, A.J. Neoproterozoic microbial processes in chemical sediment diagenesis: evidence from the Aberfeldy barite deposits. SGA 15th Biennial meeting conference abstract (2019).

Montel, J.-M., Foret, S., Veschambre, M., Nicollet, C., & Provost, A. Electron microprobe dating of monazite. *Chem. Geol.* **131**, 37-53 (1996).

Morelli, R.M., Bell, C.C., Creaser, R.A., & Simonetti, A. Constraints on the genesis of gold mineralization at the Homestake Gold Deposit, Black Hills, South Dakota from rhenium-osmium sulfide geochronology. *Miner. Depos.* **45**, 461-480 (2010).

Morelli, R.M., & MacLachlan, K. Saskatchewan Gold: mineralization styles and mining history, Sask. Ministry of Energy and Resources, Rep. 262, 171 (2012).

Morrissey, L.J., Card, C.D, & Reid, A.J. Pressure-temperature-time constraints on metamorphism in the southeastern Taltson Domain, Saskatchewan, Canada. *Precambr. Res.* **373**, 106643 (2022).

Mulcahy, S.R., Starnes, J.K., Day, H.W., Coble, M.A., & Vervoort, J.D. Early Onset of Franciscan Subduction. *Tectonics* **37**, 1194-1209 (2018).

Naeser, C.W. & Saul, J.M. Fission track dating of tanzanite. *Am. Mineral.* **59**, 613-614 (1974).

O'Brien, N.R. & Slatt, R.M. Argillaceous rock atlas. *Springer-Verlag*, New York, Table 1, 124-125 (1990).

Ohtomo, Y., Kakegawa, T., Ishida, A., Nagase, T., & Rosing, M.T. Evidence for biogenic graphite in early Archean Isua metasedimentary rocks. *Nature* **7**, 25-28 (2013).

Olivier, B. The geology and petrology of the Merelani Tanzanite Deposit, NE Tanzania. Ph. D. thesis, Univ. of Stellenbosch, South Africa (2006).

Orme, D.A. & Surpless, K.D. The birth of a forearc: The basal Great Valley Group, California, USA. *Geology* **47**, 757-761 (2019).

Orrell, S.E., Bickford, M.E., Lewry, J.F. Crustal evolution and age of thermotectonic reworking in the western hinterland of the Trans-Hudson Orogen, northern Saskatchewan. *Precambr. Res.* **95**, 187-223 (1999).

Ortega, L., Millward, D., Luque, F.J., Barrenechea, J.F., Beyssac, O., Huizenga, J.-M., Rodas, M., & Clarke, S.M. The graphite deposit at Borrowdale (UK): A catastrophic mineralizing event associated with Ordovician magmatism. *Geochim. Cosmochim. Acta* **74**, 2429-2449 (2010).

Paces, J. B. & Miller, J. D. Precise U-Pb ages of Duluth Complex and related mafic intrusions, northeastern Minnesota: Geochronological insights to physical, petrogenetic, paleomagnetic, and tectonomagmatic processes associated with the 1.1 Ga Midcontinent Rift System. *J. Geophys. Res.* **98**, 13997– 14013 (1993).

Pană, D.I. Overview of the geological evolution of the Canadian Shield in the Andrew Lake area based on new field and isotope data, northeastern Alberta (NTS 74M/16). *Energy Resources Conservation Board*, ERCB/AGS Open File Report **22**, 76 (2010).

Pană, D., Creaser, R.A., Muehlenbachs, K., & Wheatley, K. Basement geology in the Alberta portion of the Athabasca Basin: context for the Maybelle River area. in EXTECH IV: Geology and Uranium Exploration TECHnology of the Proterozoic Athabasca Basin, Saskatchewan and Alberta, (ed.) C.W. Jefferson and G. Delaney. *Geol. Surv. Can. Bulletin* **588**, 135-153 (2007).

Parnell, J. & Brolly, C. Increased biomass and carbon burial 2 billion years ago triggered mountain building. *Nat. Commun. Earth Environ.* **2**, 238 (2021).

Parnell, J., Brolly, C., and Boyce, A. Graphite from Paleoproterozoic enhanced carbon burial, and its metallogenic legacy. *Geol. Mag.* **158**, 1711-1718 (2021).

Pascal, M., Ansdell, K., & Annesley, I.R. Graphite-bearing pelitic schists and their altered equivalents in the Dufferin Lake Zone, south-central Athabasca Basin, Saskatchewan: constraints on graphite formation and destruction, and implications for uranium mineralization. *Can. Min.* **54**, 1459-1491 (2016).

Paterson, S.R. & Ducea, M.N. Arc Magmatic Tempos: Gathering the Evidence. *Elements* **11**, 91-98 (2015).

Pattison, D.R.M. The fate of graphite in prograde metamorphism of pelites: An example from the Ballachulish aureole, Scotland. *Lithos* **88**, 85-99 (2005).

Pehrsson, S.J., Eglington, B.M., Evans, D.A., Huston, D., & Reddy, S.M. Metallogeny and its link to orogenic style during the Nuna supercontinent cycle. *Geol. Soc. London Spec. Publ.* **424**, 83-84 (2016).

Peterson, T.D., Scott, J.M.J., LeCheminant, A.N., Jefferson, C.W., & Pehrrson, S.J. The Kivalliq Igneous Suite: Anorogenic biomodal magmatism at 1.75 Ga in the western Churchill Province, Canada. *Precambr. Res.* **262**, 101-119 (2015).

Peucker-Ehrenbrink, B. & Ravizza, G. The marine osmium isotope record. *Terra Nova* **12**, 205-219 (2000).

Plank, T., & Manning, C.E. Subducting carbon. Nature, 574, 343-352 (2019).

Powell, J.W., Pană, D.I., Card, C.D., Potter, E.G., Tschirhart, V., and Joyce, N. New geochronological insights into the Taltson Domain of northern Alberta and Saskatchewan. Targeted Geoscience Initiative: 2017 report of activities, volume 2, (ed.) N. Rogers; Geological Survey of Canada, Open File 8373, 43-56 (2018).

Powell, J.W., Tschirhart, V., Potter, E.G., Card, C. The Clearwater Domain of northern Saskatchewan: Geophysics, geochemistry, geochronology, and potential linkages to unconformity-related uranium deposits. Geological Survey of Canada, poster (2022).

Rahl, J.M., Anderson, K.M., Brandon, M.T., & Fassoulas, C. Raman spectroscopic carbonaceous material thermometry of low-grade metamorphic rocks: Calibration and application to tectonic exhumation in Crete, Greece. *Earth Planet. Sci. Lett.* **240**, 339-354 (2005).

Raymond, L.A. What is Franciscan?: revisited. *Int. Geol. Rev.* **60**, 1968-2030 (2018).

Regis, D., Warren, C.J., Mottram, C.M., & Roberts, M.W. Using monazite and zircon petrochronology to constrain the P-T-t evolution of the middle crust in the Bhutan Himalaya. *J. Metamorp. Geol.* **34**, 617-639 (2016).

Regis, D., Pehrsson, S., Martel, E., Thiessen, E., Peterson, T., & Kellet, D. Post-1.9 Ga evolution of the south Rae craton (Northwest Territories, Canada): A Paleoproterozoic orogenic collapse system. *Precambr. Res.* **355**, 106105 (2021).

Rubin, A.E. & Ma, C. Meteoritic minerals and their origins. *Geochemistry* **77**, 325-385 (2017).

Rumble III, D., Duke, E.F., & Hoering, T.L. Hydrothermal graphite in New Hampshire: Evidence of carbon mobility during regional metamorphism. *Geology* **14**, 452-455 (1986).

Rumble, D. & Chamberlain, C.P. Graphite Vein Deposits of New Hampshire. New England Intercollegiate Geological Conference 80th Annual Meeting: Guidebook for Field Trips in Southwestern New Hampshire, Southeastern Vermont, and North-central Massachusetts, 241-245 (1988).

Rumble, D. Hydrothermal Graphitic Carbon. *Elements* **10**, 427-433 (2014).

Rutte, D., Garber, J., Kylander-Clark, A., & Renne, P.R. An Exhumation Pulse from the Nascent Franciscan Subduction Zone (California, USA). Tectonics **39**, 1-26 (2020).

Saintilan, N.J., Selby, D., Hughes, J.W., Schlatter, D., Kolb, J., & Boyce, A. Mineral separation protocol for accurate and precise rhenium-osmium (Re-Os) geochronology and sulphur isotope composition of individual sulphide species. *MethodsX* **7**, 100944 (2020).

Scharff, P., Stumpp, E., Hohne, M., & Wang, Y.X. Upon the Intercalation of Rhenium Heptoxide and Rhenium Trioxide Nitrate into Graphite. *Carbon* **29**, 595-597 (1991).

Schneider, D.A., Heizler, M.T., Bickford, M.E., Wortman, G.L., Condie, K.C., and Perilli, S. Timing constraints of orogeny to cratonization: thermochronology of the Paleoproterzoic Trans-Hudson orogen, Manitoba and Saskatchewan, Canada. *Precambr. Res.* **153**, 65-95 (2007).

Schulz, D. Monazite microstructures and their interpretation in petrochronology. *Front. Earth Sci.* **9**, 668566 (2021).

Schulz, K.J., DeYoung, J.H., Seal, R.R., II, & Bradley, D.C. Critical mineral resources of the United States – Economic and environmental geology and prospects for future supply: *U.S. Geological Survey Professional Paper* **1802**, 797 (2017).

Scibek, J. & Annesley, I.R. Permeability testing of drill core from basement rocks in the fault-hosted gryphon U deposit (Eastern Athabasca Basin, Canada): Insights into fluid-rock interactions related to deposit formation and redistribution. *Nat. Resourc. Res.* **30**, 2909-2956.

Selby, D. & Creaser, R.A. Re-Os geochronology of organic rich sediments: an evaluation of organic matter analysis methods. *Chem. Geol.* **200**, 225-240 (2003).

Shirey, S.B. & Walker, R.J. Carius Tube Digestion for Low-Blank Rhenium-Osmium Analysis. *Anal. Chem.* **67**, 2136-2114 (1995).

Silva, K.K.M.W. Mineralization and Wall-Rock Alteration at the Bogala Graphite Deposit, Bulathkohupitiya, Sri Lanka. *Econ. Geol.* **82**, 1710-1722 (1987).

Simonetti A. Heaman, L.M., Hartlaub, R.P., Creaser, R.A., MacHattiea, T.G., & Bohmb, C. U–Pb zircon dating by laser ablation-MC-ICP-MS using a new multiple ion counting Faraday collector array. *J. Anal. At. Spectrom.* **20**, 677-686 (2005).

Simonetti A. Heaman, L.M., Chacko, T., & Banerjee, N.R. In situ petrographic thin section U–Pb dating of zircon, monazite, and titanite using laser ablation–MC–ICP-MS. *Inter. J. Mass Spectrom.* **253**, 87-97 (2006).

Smoliar M. I., Walker R. J., & Morgan J. W. Re-Os ages of group IIA, IIIA, IVA, and IVB iron meteorites. *Science* **271**, 1099–1102 (1996).

Snortum, E., & Day, J.M.D. Forearc origin for the Coast Range Ophiolites inferred from osmium isotopes and highly siderophile elements. *Chem. Geol.* **550**, 1119723 (2020).

Stachel, T., & Luth, R.W. Diamond formation – Where, when and how? *Lithos* **220-223**, 200-220 (2015).

Stepanov, A.S. A review of the geochemical changes occurring during metamorphic devolatilization of metasedimentary rocks. *Chem. Geol.* **568**, 120080 (2021).

Stein, H.J. Dating and Tracing the History of Ore Formation. In: Holland, H.D. and Turekian, K.K. (eds.) *Treatise on Geochemistry*, Second Edition, **13**, 87-118. Oxford: Elsevier (2014).

Stein, H.J. & Hannah, J.L. Rhenium-Osmium Geochronology: Sulfides, Shales, Oils, and Mantle. *Encyclopedia of Scientific Dating Methods*, Edited by Rink and Thompson, Springer Reference, pp. 707-723 (2015).

Stern, R.A., Card, C.D., Pana, D., & Rayner, N. SHRIMP U-Pb ages of granitoid basement rocks of the southwestern part of the Athabasca Basin, Saskatchewan and Alberta; Radiogenic Age and Isotopic Studies: Report 16; Geological survey of Canada, Current Research 2003-F3, 20 p (2003).

Stern, R.A., Bodorkos, S., Kamo, S.L., Hickman, A.H. & Corfu, F. Measurement of SIMS Instrumental Mass Fractionation of Pb Isotopes During Zircon Dating. *Geostand. Geoanal. Res.* **33**, 145-168 (2009).

Stern, R.A, Palot M., Howell, D., Stachel, T., Pearson, D.G., Cartigny, P., & Oh, A. Methods and reference materials for SIMS diamond C- and N-isotope analysis. Canadian Centre for Isotopic Microanalysis, Research Report 14-01. Univ. of Alberta, Education and Research Archive (2014). http://hdl.handle.net/10402/era.38738.

Sun, X., Ren, Y., Sun, Z., Wang, C., and Li, Z. Geochronology and geochemical properties of the large-scale graphite mineralization associated with the Huangyangshan alkaline pluton, Eastern Junggar, Xinjiang, NW China. *Geochemistry* (2021).

Tagiri M., & Oba, T. Hydrothermal synthesis of graphite from bituminous coal at 0.5-5 kbar water vapor pressure and 300-600C, J. *Japan. Assoc. Min. Petr. Econ. Geol.* **81**, 260-271 (1986).

Tessalina, S.G., Yudovskaya, M.A., Chaplygin, I.V., Birck, J., Capmas, F. Sources of unique rhenium enrichment in fumaroles and sulphides at Kudryavy volcano *Geochim. Cosmochim. Acta* **72**, 889-909 (2008).

Toffolo, L., Tumiati, S., Villa, A., Fumagalli, P., Amalfa, A., & Miozzi, F. Experimental dissolution of carbonaceous materials in water at 1 GPa and 550C: Assessing the role of carbon forms and redox state on COH fluid production and composition during forearc subduction of organic matter. *Front. Earth Sci.* **11**, 1013014 (2023).

Toma J., Creaser R. A., & Pana D. I., 2020, High-precision Re- Os dating of Lower Jurassic shale packages from the Western Canadian Sedimentary Basin. *Palaeogeogr. Palaeoclimatol. Palaeoecol.* **560**, 110010 (2020).

Toma, J., Creaser, R.A., Card, C., Stern, R. A., Chacko, T., & Steele-McInnis, M. Re-Os Systematics and Chronology of Graphite. *Geochim. Cosmochim. Acta* **323**, 164-182 (2022).

Touret, J.L.R., Huizenga, J.M., Kehelpannala, K.V.W., & Piccoli, F. Vein-type graphite deposits in Sri Lanka: The ultimate fate of granulite fluids. *Chem. Geol.* **508**, 167-181 (2019).

Tumiati, S., Recchia, S., Remusat, L., Tiraboschi, C., Sverjensky, D.A., Manning, C.E., Vitale Brovarone, A., Boutier, A., Spanu, D., & Poli, S. Subducted organic matter buffered by

marine carbonate rules the carbon isotopic signature of arc emissions. *Nat. Commun.* **13**, 2909 (2022).

Van Acken, D., Su, W., Gao, J., & Creaser, R.A. Preservation of Re-Os isotope signatures in pyrite throughout low-T, high-P eclogite facies metamorphism. Terra Nova **26**, 402-407 (2014).

Vermeesch P. IsoplotR: A free and open toolbox for geochronology. *GSF* **9**, 1479–1493 (2018).

Wada, H., Tomita, T., Matsuura, K., Iuchi, K., Ito M, & Morikiyo, T. Graphitization of carbonaceous matter during metamorphism with references to carbonate and pelitic rocks of contact and regional metamorphisms, Japan. *Contrib. Min. Petrol.* **118**, 217-228 (1994).

Wakabayashi, J. & Dumitru, T.A. 40Ar-39Ar ages from coherent, high-pressure metamorphic rocks of the Franciscan Complex, California: Revisiting the timing of metamorphism of the world's type subduction complex. *Int. Geol. Rev.* **49**, 873-906 (2007).

Watanabe, M. & Narukawa, A. Determination of impurity elements in high purity graphite by inductively coupled plasma atomic emission spectrometry after microwave decomposition. *Analyst* **125**, 1189-1191 (2000).

Wheatley, K. & Cutts, C. Overview of the Maybelle River Uranium Mineralization, Alberta, Canada. International Symposium on Uranium Production and Raw Materials for the Nuclear Fuel Cycle: Supply and Demond, Economics, the Environment and Energy Security. Vienna, Austria, June 2005, **IAEA-CN-128/16**, 46-47 (2005).

White, R.S., McKenzie, D., & O'Nions, A.K. Oceanic crustal thickness from seismic measurements and rare earth element inversions. *J. Geophys. Res.* **97**, 19683-19715 (1992).

Wojdyr M. Fityk: a general-purpose peak fitting program. *J. Appl. Crystallogr.* **43**, 1126–1128 (2010).

Wood, R.M. The iron-rich blueschist facies minerals: I. Deerite. *Mineral. Mag.* **43**, 251-259 (1979).

Wood, RM. The Laytonville Quarry (Mendocino County California) exotic block: iron-rich blueschist-facies subduction-zone metamorphism: Mineral. Mag. **45**, 87-99 (1982).

Woodhouse, O.B., Ravizza, G., Kenison Falkner, K., Statham, P.J., & Peucker-Ehrenrink, B. Osmium in seawater: vertical profiles of concentration and isotopic composition in the eastern Pacific Ocean. *Earth Planet. Sci. Lett.* **173**, 223-233 (1999).

Worden, J.M, Cumming, G.L., Baadsgaard, H. Geochronology of host rocks and mineralization of the Midwest uranium deposit, northern Saskatchewan. In: sibbald, T.I. Petruk, W. (Eds.).

Geology of uranium deposits. *Canadian Institute of Mining and Metallurgy* **32**, 67-72 (1985).

Xiong, Y.L., and Wood, S.A. Experimental quantification of hydrothermal solubility of platinum-group elements with special reference to porphyry copper environments. *Mineral. Petrol.* **68**, 1-28 (2000).

Yeo, G.M. & Delaney, G. The Wollaston Supergroup, stratigraphy and metallogeny of a Paleoproterozoic Wilson cycle in the Trans-Hudson Orogen, Saskatchewan; in EXTECH IV: Geology and Uranium EXplortation TECHnology of the Proterozoic Athabasca Basin, Saskatchewan Alberta, (ed.) C.W. Jefferson and G. Delaney; Geological Survey of Canada, Bulletin **588**, 89-117 (2007).

Zhang, H.-F., Zhai, M.-G., Santosh, M., Wang, H.-Z., Zhao, L., & Ni, Z.-Y. Paleoproterozoic granulites from the Xinghe graphite mine, North China Craton: Geology, zircon U-Pb geochronology and implications for the timing of deformation, mineralization and metamorphism. *Ore Geol. Rev.* **63**, 478-497 (2014).

Appendix A

Supplementary Material for

Re-Os Systematics and Chronology of Graphite

Appendix A includes:

Supplementary Text

Figures A1 to A7

Tables A1-A8

References

Supplementary Text

1. Sample descriptions

1.1 Hand sample and petrographic analysis

JT20-6

JT20-6 is an augen gneiss sampled from a shear zone within the Wollaston Mudjatik Transition (sample depth = 639.6 m) and is the parental analogue to JT20-5. This mylonized rock is comprised of quartz, orthoclase, sillimanite, garnet, cordierite, and biotite with minor muscovite, graphite, pyrite, pyrrhotite, monazite, and zircon (Fig. A1a-d). Augen are made up of cordierite/orthoclase and garnet that are imbedded in a matrix of quartz, biotite, and sillimanite. The matrix itself is divided into segments of syntectonically recrystallized quartz and lineaments of cordierite and sillimanite. Garnet is preserved as severely embayed porphyroclasts that have rolled along shear foliation planes. Sillimanite also forms trails and coplanar ribbons around cordierite and garnet porphyroblasts (Fig. A1b-c). In some cases, cordierite exhibits minor sericite and pinite alteration that is indicative of metasomatic activity, which is further supported by the presence of flake graphite partially or fully replacing biotite and disseminated grains of pyrrhotite, pyrite, and chalcopyrite (Fig. A1d).
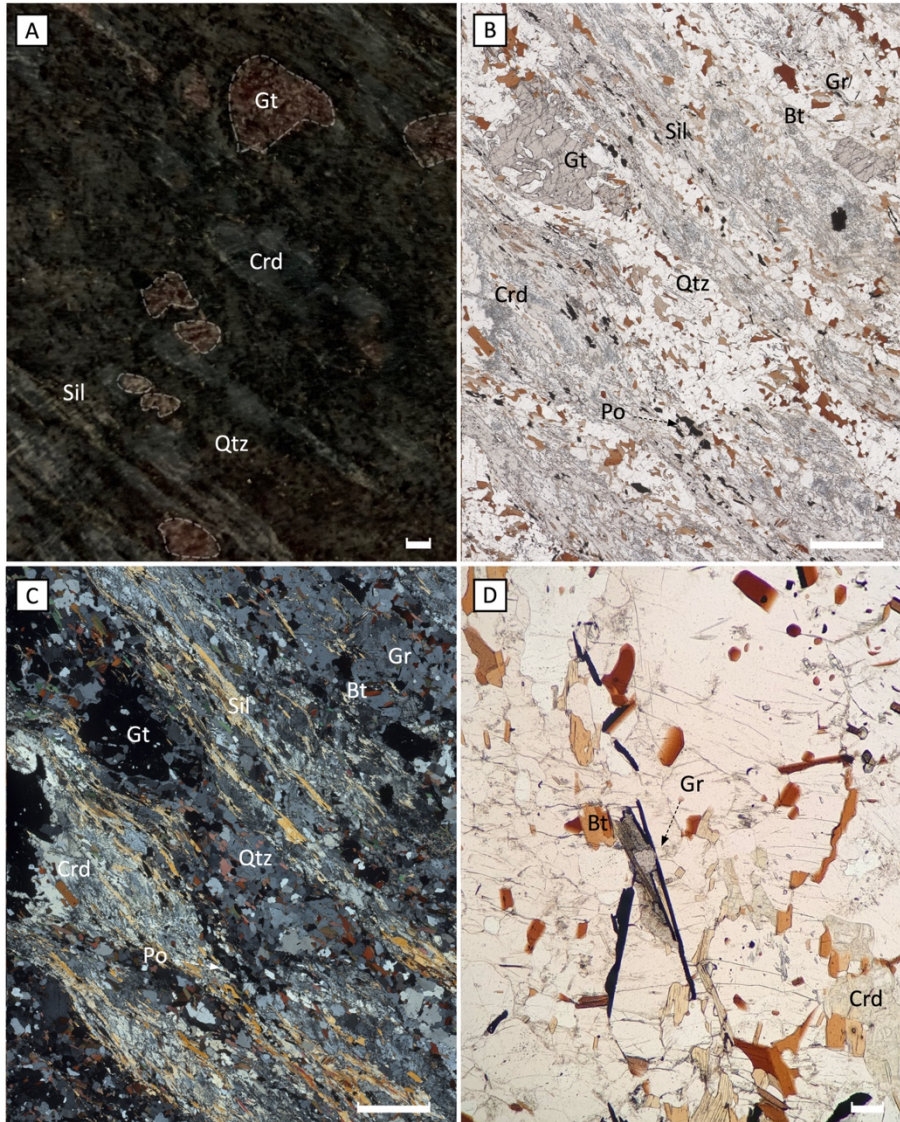
Figure A1. Photomicrographs of specimen JT20-6 (Wollaston Mudjatik Transition shear zone, SK, CA). (A) polished hand specimen depicting garnet (gt) porphyroblasts in a augen fabric, (B-C) gt, biotite (bt), quartz (qtz), cordierite (crd), sillimanite (sil), graphite (gr), and pyrrhotite (po) viewed under transmitted plane-polarized and cross-polarized light, and (D) transmitted plane-polarized light photomicrograph of graphite partially (gr_p) and full (gr_f) replacing bt. Scale bar is 200 μm.

JT20-5

Sample JT20-5 (sampled a few meters below the Phoenix deposit, SK, Canada) is the metasomatic counterpart to JT20-6 and is comprised of quartz, phlogopite, orthoclase, graphite (modal percent = 13.63%), and pyrite (modal percent = 2%) with minor garnet, sericite, and monazite (Fig. A2a-d; sample depth = 619.4 m). Extensive metasomatic alteration has replaced a lot of the precursor textures present in JT20-6. Quartz, altered orthoclase augen, and garnet porphyroblasts (reduced by 1/3 in size) are the primary relict features preserved. Sillimanite and cordierite are no longer present but instead have been replaced at the expense of biotite and sericite alteration. A large quartz vein cuts coplanar to the primary fabric, which itself is cut by a smaller (late forming) biotite-graphite-pyrite vein of the same orientation that is sequenced from core to rim into pyrite, graphite, and biotite (Fig. A2a-c). Biotite appears to serve as the primary nucleation site for graphite, which forms via partially (gr_p) or fully (gr_f) replacing biotite (Fig. A2d).
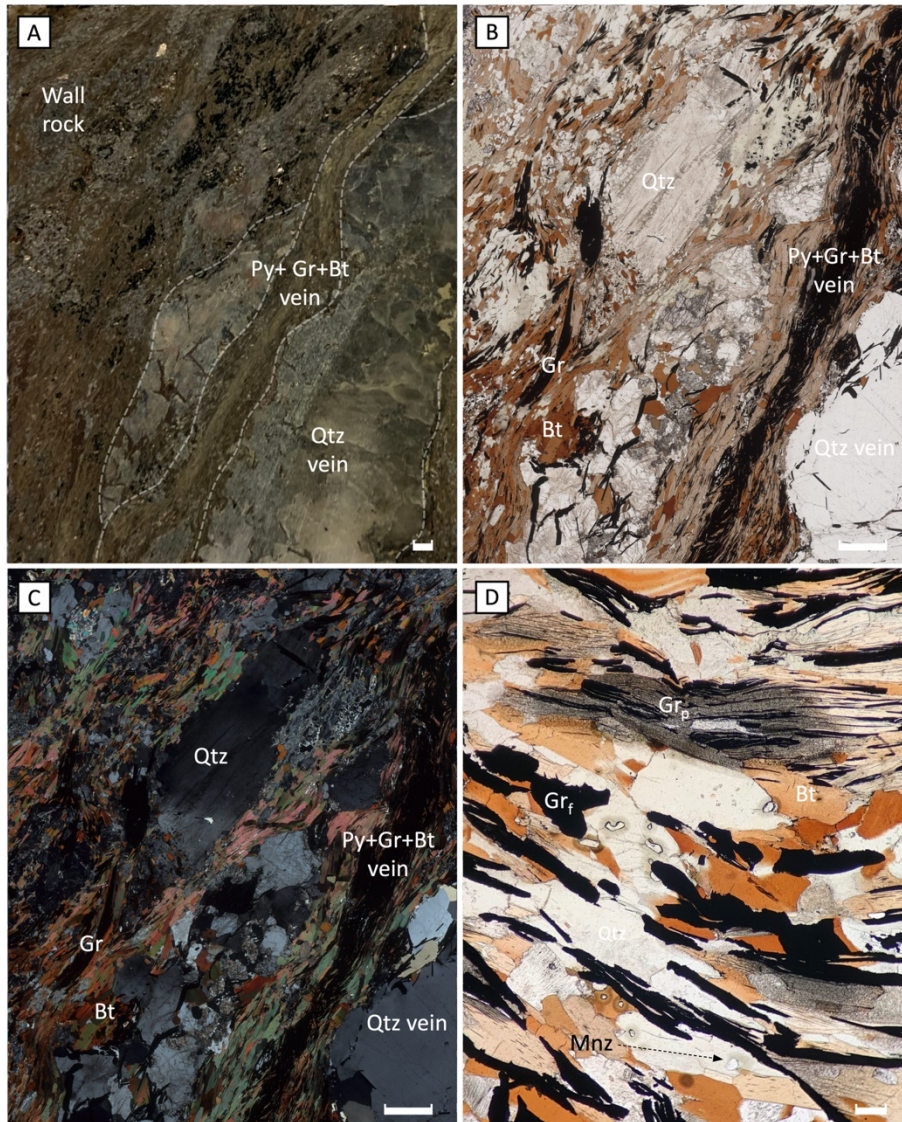
Figure A2. Photomicrographs of specimen JT20-5 (Wollaston Mudjatik Transition shear zone, SK, CA). (A) host rock cross-cut by quartz (qtz) and pyrite(py)-graphite(gr)-biotite(bt) veins, (B-C) py-gr-bt vein and contiguous wall rock viewed under transmitted plane-polarized and cross-polarized light, and (C) transmitted plane-polarized light photomicrograph of graphite partially (gr$_p$) and full (gr$_f$) replacing bt. Scale bar is 200 μm.

JT20-MH

Sample JT20-MH is a graphite-rich grossular, tsavorite, diopside, quartz, pyrite-bearing rock (Fig. A3a-d) collected from the block D mine in Merelani Hills by artisanal miners and acquired from an online mineral distributor. The face of the specimen is covered in euhedral

coarse-grained pyrite and tsavorite imbedded in a matrix of finer vein graphite (Fig. A3a). Beneath the matrix is a mix of diopside, tsavorite, quartz, graphite, and pyrite (Fig. A3b-c). Graphite morphology is distinctly flaky and commonly forms alongside pyrite (Fig. A3b-d), while diopside is present in pristine and altered forms (i.e., clays) (Fig. A3b-d). Graphite precipitation is evident along mineral grain boundaries (i.e., diopside) that resulted in minor alteration to the surrounding silicate grains (Fig. A3d).
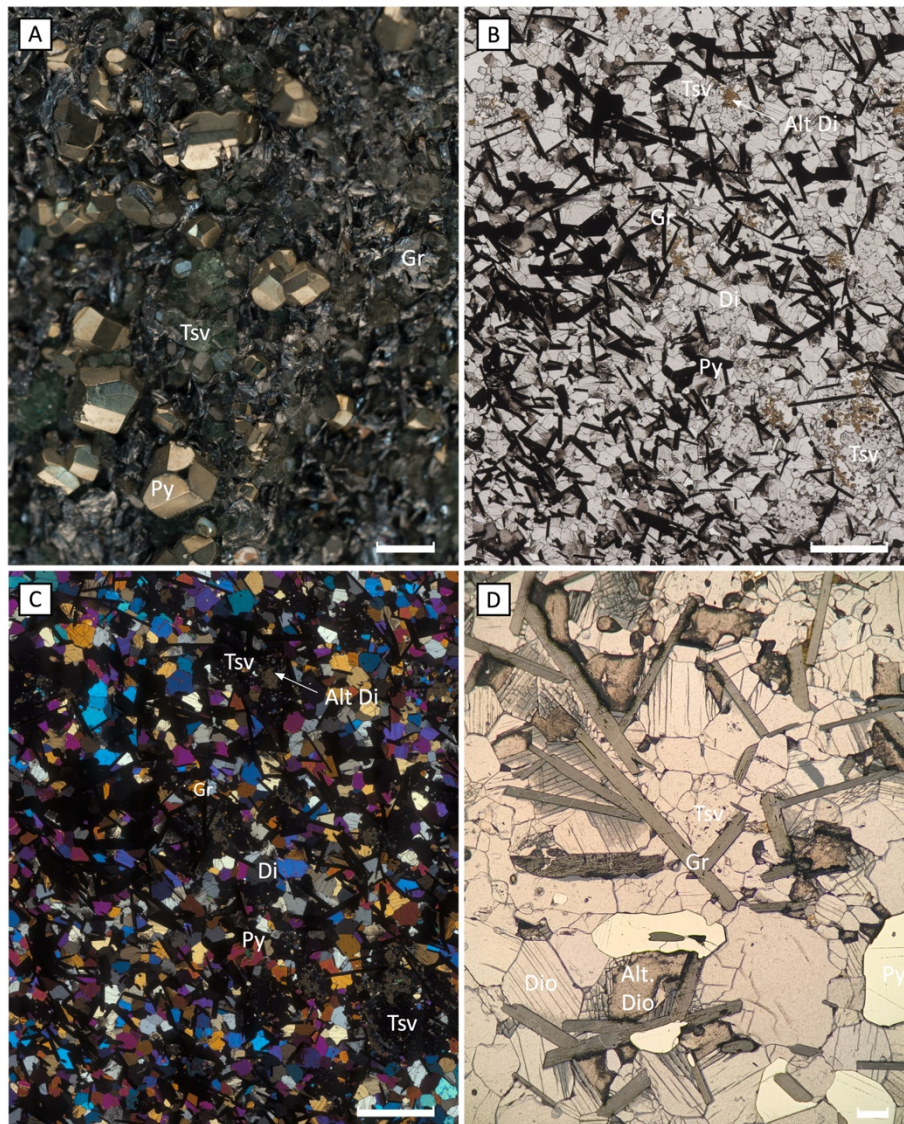
Figure A3. Photomicrographs of specimen JT20-MH (Merelani Hills, TZ). (A) hand sample depicting euhedral pyrite (py) and tsavorite (tsv) crystals imbedded in a matrix of vein graphite (gr), (B-C) py, diopside (dio), altered diopside (alt. dio), tsv, and gr viewed under transmitted plane-polarized and cross-polarized light, and (D) py, dio, alt. dio, tsv, and Gr viewed under reflected plane-polarized light. Scale bar is 200 μm.

1.2 Grain Mount Photographs

Grain mounts JT20-5 (Wollaston Mudjatik Transition shear zones, SK, CA) and JT20-MH (Merelani Hills, TZ) were used for textural analysis and modal percent estimates and are listed below in Fig. A4 & Fig. A5. Each figure depicts the mineralogical and textural variation observed between mineral separates with varying magnetic susceptibilities. This mineralogical and textural assessment also accompanied inclusion screening via SEM imaging (Fig. A6). Refer to primary text for detailed textural, mineralogical, and geochronological analysis. Raman spectra for graphite mineral separate JT20-5-NM-1.30 is depicted in Fig. A7.

A JT20-5-M-0.27   **B** JT20-5-M-0.30   **C** JT2-5-NM-0.28

D JT20-5-NM-0.30   **E** JT20-5-NM-0.40   **F** JT20-5-NM-1.30
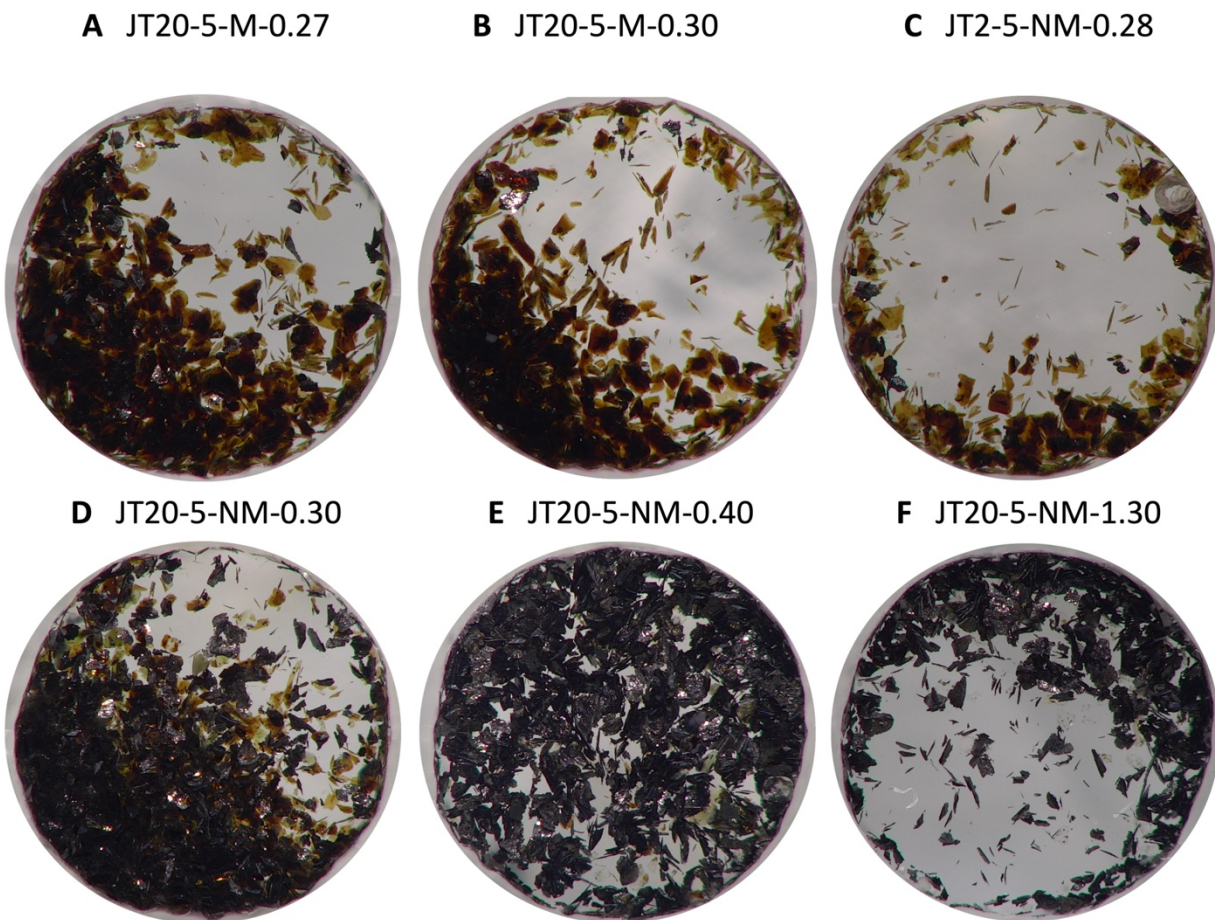
Figure A4. Photographs of mineral separates from JT20-5 (Wollaston Mudjatik Transition shear zone, SK, CA). (A-C) contain the highest concentration of biotite and partially-formed graphite. However, (A) contains 38% fully-formed graphite relative to the total graphite present, which is markedly higher than the 11% or less present in (B-C). (D) Biotite abundances decreases at the expense of increased abundances in fully-formed graphite; partially-formed

graphite is no longer present. (E-F) only fully formed graphite is present with < 10% quartz. (A-F) contain <5% pyrite. See Table A2 and *section 2.5.1* for more details.
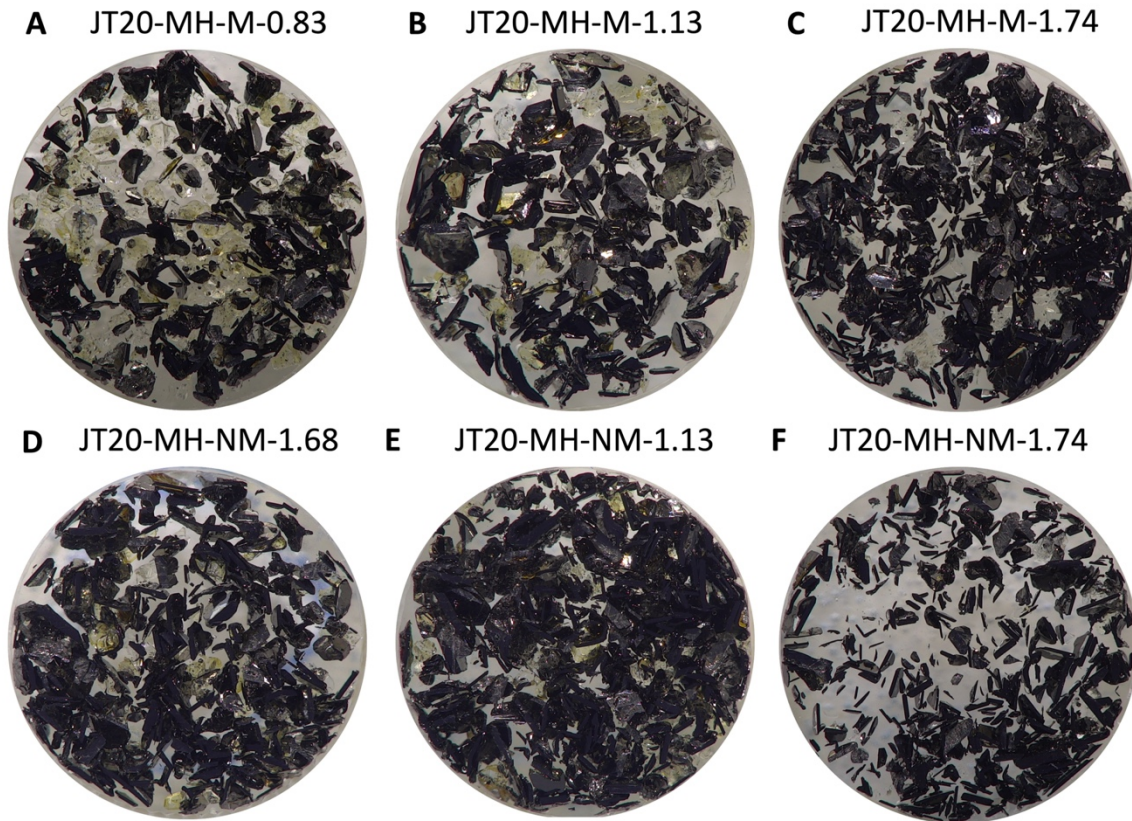
Figure A5. Photographs of mineral separates from JT20-MH (Merelani Hills, TZ). (A) contains the highest proportion of silicate phases (38%), which also appear altered and are graphite (61%) included. (B-F) silicate content contents vary between 10-16%, while graphite contents vary between 84-94%. (A-C, E-F) contain <1% pyrite. See Table A2 and *section 2.5.1* for more details.
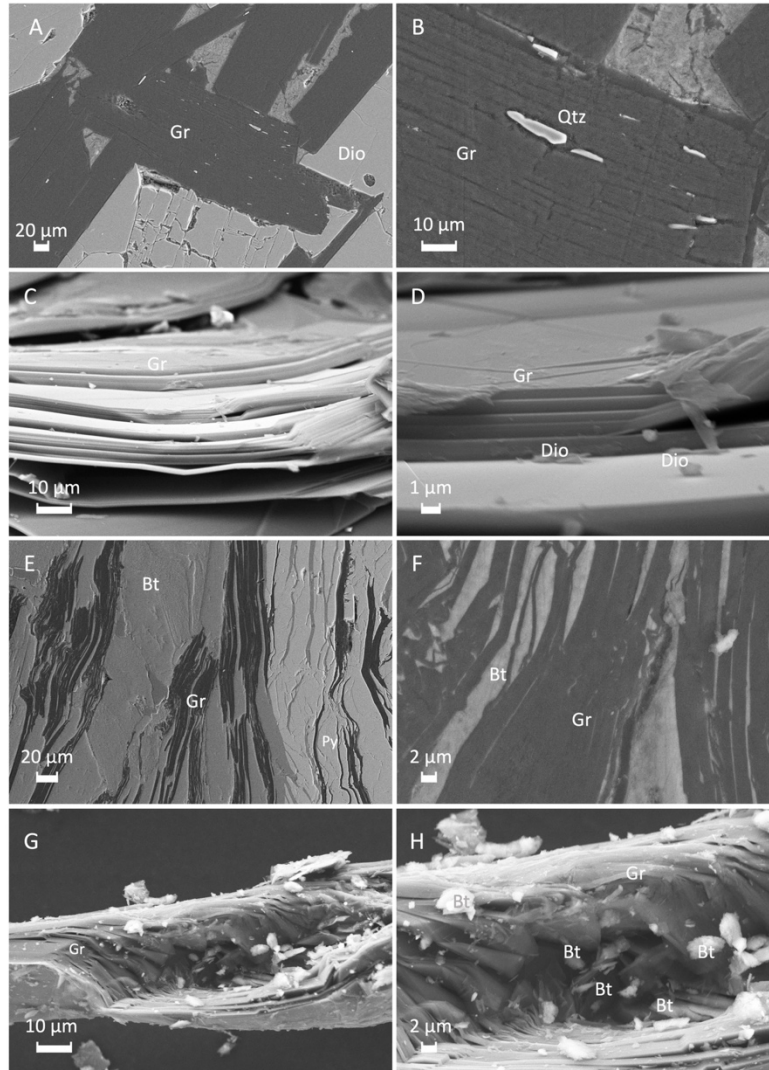
Figure A6. SEM photomicrographs of Merelani Hills (A-D) and Wollaston Mudjatik Transition (E-H) graphite. (A-B; E-F) are thin section photomicrographs, whereas (C-D; G-H) are photomicrographs of mineral separates JT20-MH-NM-1.74 and JT20-5-NM-1.3.
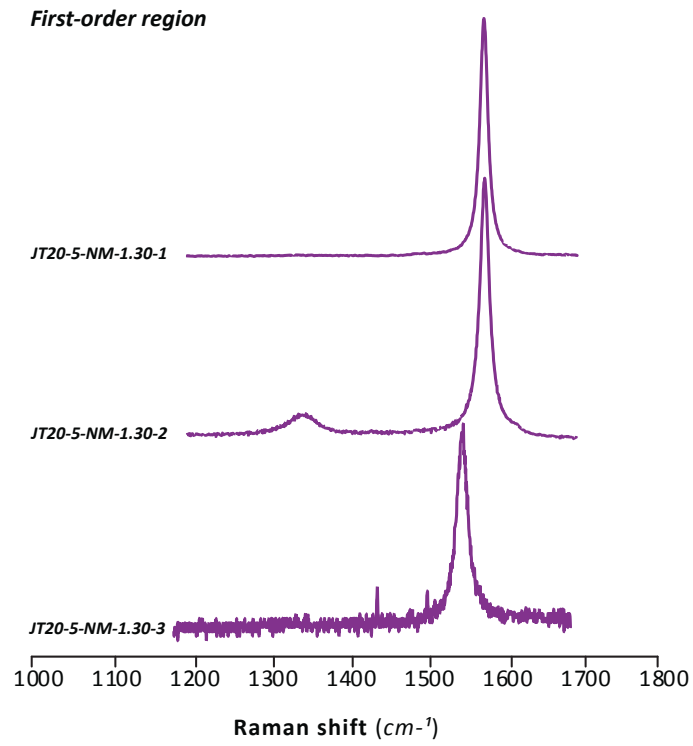
First-order region

Figure A7. First-order Raman spectra of Wollaston Mudjatik Transition graphite separates (JT20-5-NM-1.30). Refer to Table A7 for D1-band and G-band peak amplitudes.

2. Graphite sampling challenges

One of the first steps in developing a successful Re-Os research program is selecting samples that contain enough analyte (i.e., sulfide or graphite) that can be recovered to build an isochron. For a 5-point sulfide (Re = 1 ppb) isochron, this would amount to a minimum of 2 grams of sulfide (0.4 g/separate · 5 separates) but likely much more in case replicates are needed or if mineral separates must be individualized further to maximize $^{187}Re/^{188}Os$ spread. The bulk rock (e.g., 100 g metapelite with a density of 2.96 g/cm^3) itself would, therefore, need to have >2% sulfide by mode to recover >2 grams of sulfide material. In practice, the total amount of recoverable material is much less (~50%) as sample is lost during physical separation procedures (crush and sieving). These sampling concerns, however, become even more acute when considering working with graphite. Graphite, for example, has a much lower density (2.27 g/cm^3 than sulfides (4.2-6.1 g/cm^3) and hence a bulk rock will have to host >5% graphite by mode to recover an equal amount of mineral analyte (Fig. A8). This difference in volumetric proportions becomes quite apparent when comparing pure mineral separates of graphite and sulfide (e.g., arsenopyrite) of equal mass (Fig. A9) and further illustrates the unique sampling challenges imposed by the graphite Re-Os dating method. A recommended graphite Re-Os workflow is provided in Fig. A10. The modal percent graphite abundances for various samples amenable to graphite Re-Os dating are shown in Fig. A11.
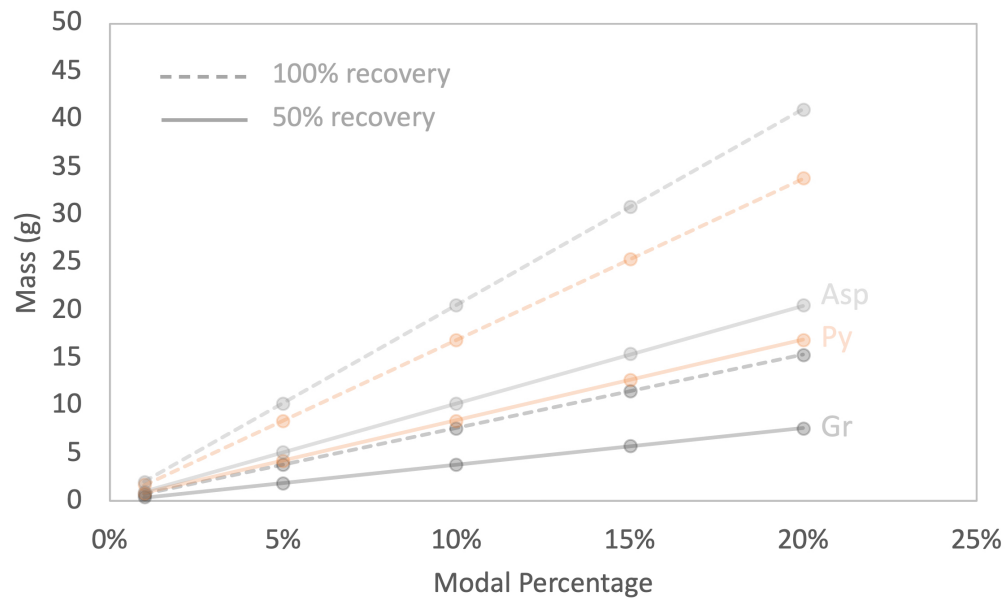
Figure A8. Mass (g) of graphite (gr), pyrite (py), and arsenopyrite (asp) recovered from a 100 g metapelite (density = 2.96 g/cm^3) sample containing 1%, 5%, 10%, 15%, and 20% gr, py, and asp by mode. Analyte recovery of 50% represents loss of sample material during physical separation (i.e., crushing and sieving).

Figure A9. Sample vials containing equal mass proportions (1.5 g) of pure graphite (A) and arsenopyrite (B) but a difference of >4 times volumetric proportions.

Graphite Re-Os Workflow

DP19-844

Lithology
Location & coordinates
Sampling depth
Geologic context

Outcrop/Drill Core Sampling

Petrographic description
Crush, mill, sieve
Frantz magnetic sep.
Spatial imaging

Sample Preparation

Carius tube digestion
Os & MD extraction
Re chromatography &
single bead

Chemical Separation

N-TIMS analysis
Data reduction
Regression analysis
(i.e., IsoplotR)

Data Acquisition and Interpretation

Figure A10. Graphite Re-Os workflow that begins with outcrop/drill core sampling followed by sample preparation, chemical separation in a clean laboratory to isolate Re and Os, and finally data acquisition by negative thermal ionization mass spectrometry (N-TIMS) and interpretation by IsoplotR. Scale bar = 1 cm.
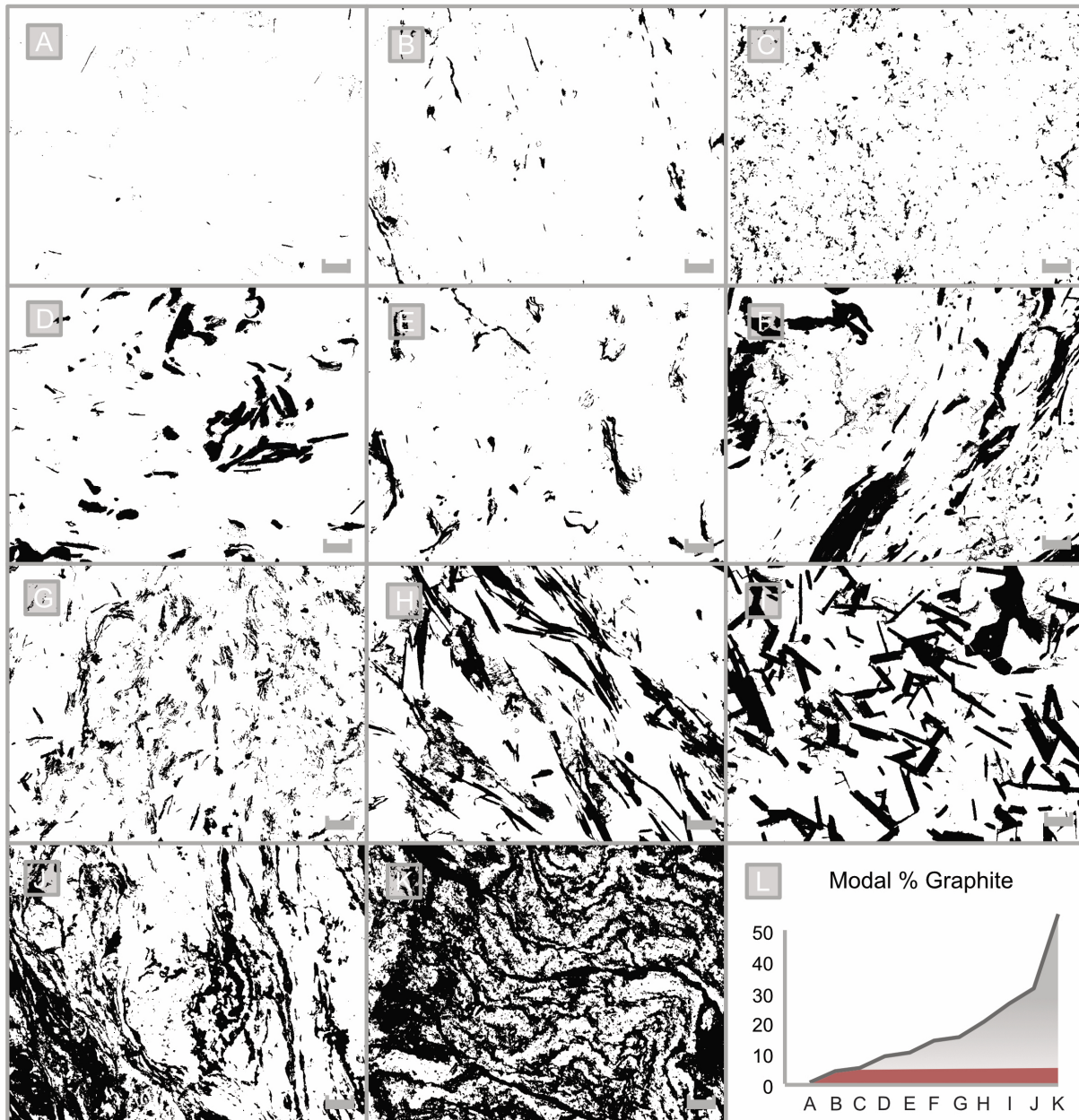
Figure A11. Thin section images processed by ImageJ that depict the modal percent abundances for hydrothermal (A-G, I-J) and metamorphic (H, K) graphite (Gr). (L) Graphical depiction of the modal percent abundances of graphite (y-axis) for each of the various samples (x-axis). A = JT20-2 (0.4 % Gr), B = DP19-843 (3.7% Gr), C = DP19-844 (5.2% Gr), D = JT20-11 (8.9% Gr), E = JT20-3 (9.7% Gr), F = JT20-5 (15.6% Gr), G = JT20-11 (14.7% Gr), H = JT20-MG (20.4% Gr), I = JT20-MH (25.9% Gr), J = PLS14-260 (30.6% Gr), K = SPXX-m6424 (54.9% Gr). Horizontal red bar in (L) defines the threshold above which graphite Re-Os dating is more likely to be feasible. Scale bar = 30 μm.

3. ^{13}C/^{12}C isotope variation in graphite mineral separates

SIMS carbon isotope analysis was performed on magnetic/non-magnetic graphite mineral separates from Merelani Hills (JT20-MH) and WMT shear zones (JT20-5) with the former yielding <1‰ variation in δ^{13}C values (-25.12 to -24.33; Fig. A12; Table A6) between graphite grains and the latter yielding a δ^{13}C variation of <5‰ (-20.86 to -16.22; Fig. A13; Table A6). In both cases, graphite carbon isotope variation failed to correlate with magnetic susceptibility and ^{187}Re/^{188}Os and ^{187}Os/^{188}Os isotopic values (not shown).
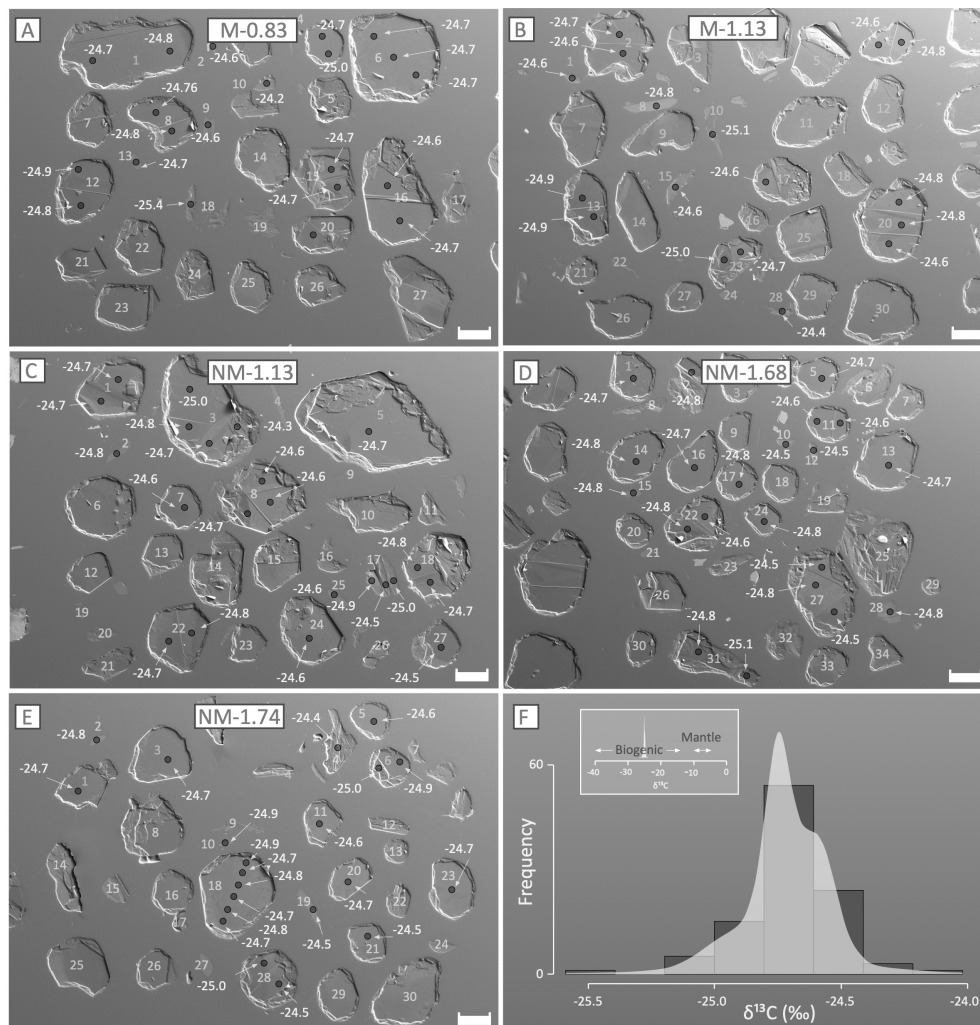
Figure A12. (A-E) SIMS δ^{13}C values of graphites from Merelanil Hills with varying magnetic susceptibilities. (F) Histogram depicting the rather homogeneous (<1‰ variation) δ^{13}C values in these graphite separates with the graphical inset illustrating the predominantly biogenic signatures preserved in Merelani Hill graphites.
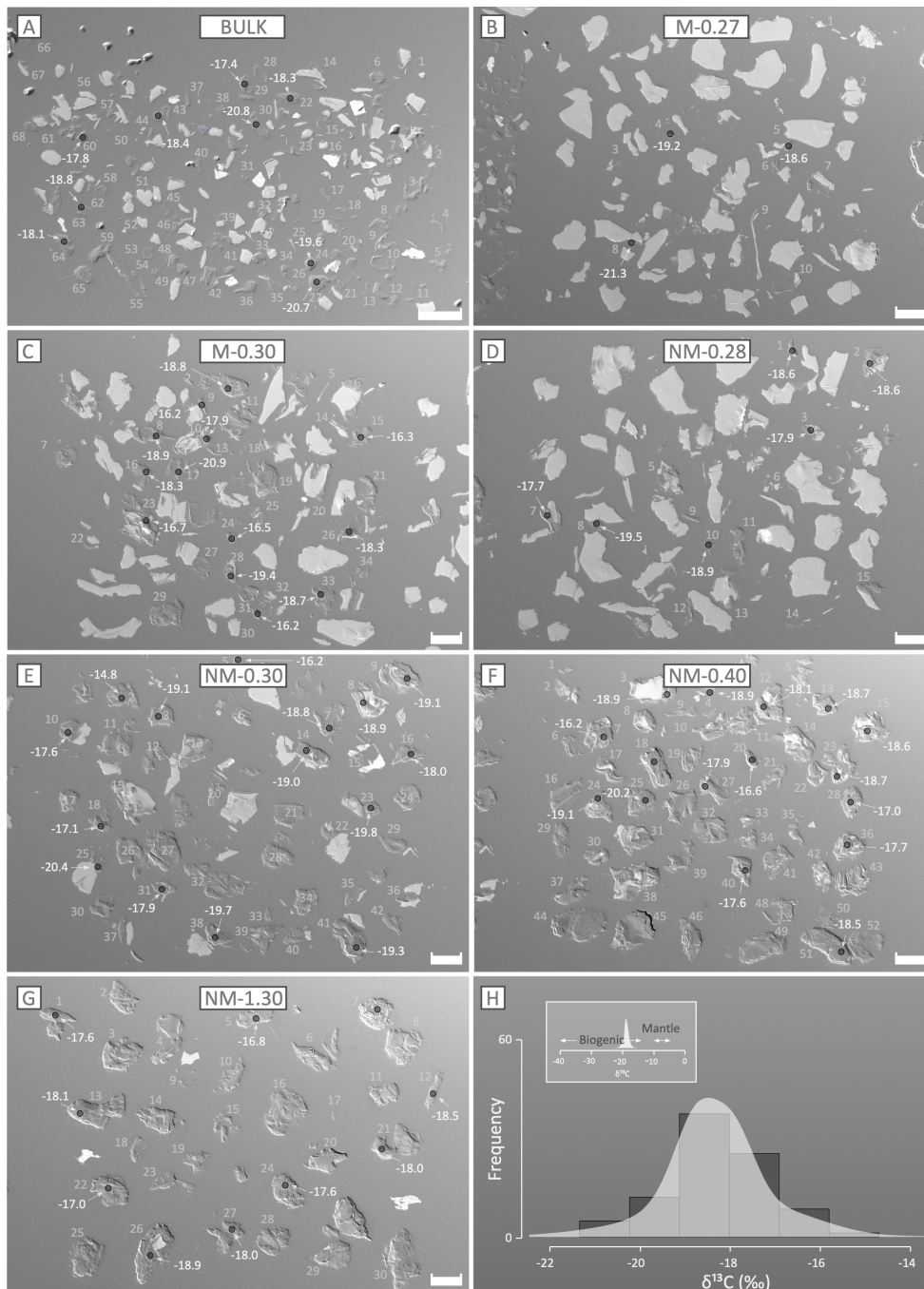
Figure A13. (A-G) SIMS δ^{13}C values of graphites from Wollaston-Mudjatik Transition (WMT) shear zones with varying magnetic susceptibilities. (h) Histogram depicting the <4‰ variation δ^{13}C values in WMT graphite separates. Graphical inset in (H) illustrates the predominantly biogenic signatures preserved in WMT graphites.

4. Merelani Hills Re-Os pyrite geochronology

Pyrite separates (Re = 18.6-21.1 ppb; Os = 4998-9092 ppt) from Merelani Hills yield $^{187}Re/^{188}Os$ and $^{187}Os/^{188}Os$ isotopic ratios that cluster around 17.58-25.25 and 1.836-1915 (Table A8), respectively, which when plotted in $^{187}Re/^{188}Os$-$^{187}Os/^{188}Os$ isotope space generated an imprecise Model 3 isochron date of 689.3 ± 87.2 (λ=120) Ma (2σ; MSWD = 18; n = 5) with an $^{187}Os/^{188}Os$ initial ratio of 1.628 ± 0.030. Age imprecision is principally caused by the lack of spread in $^{187}Re/^{188}Os$ isotope ratios. For example, plotting Merelani Hills pyrite and graphite separates together yield a far more precise Model 3 age of 588.19 ± 3.71 (λ=5.20) Ma (2σ; MSWD = 7.6; n = 5; $^{187}Os/^{188}Os$ initial ratio = 1.663 ± 0.033; Fig. A11) that agrees within uncertainty of the Merelani Hills graphite Re-Os isochron date (586.89 ± 2.39 Ma) – suggesting a coeval relationship that is supported petrographically.
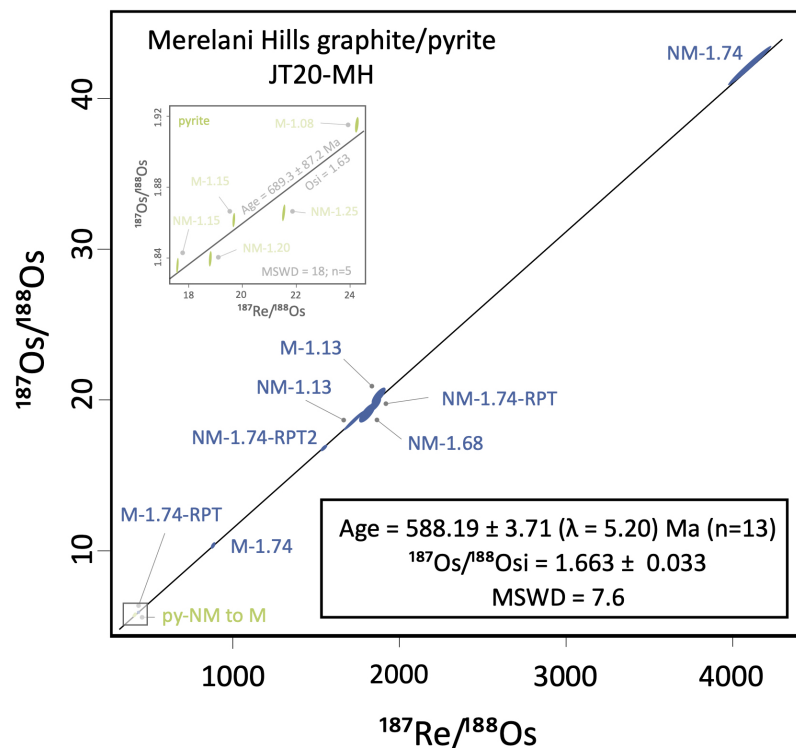
Figure A11. Merelani Hills (JT20-MH) Re-Os pyrite-graphite Model 3 isochron age generated using IsoplotR (Vermeesch, 2018). Error ellipses are reported in 2σ notation. Re-Os isochron ages were calculated using the ^{187}Re decay constant of Smoliar et al. (1996) and include decay constant uncertainties in brackets. Graphical inset depicts the imprecise Re-Os age generated using pyrite separates only. Yellow = pyrite (py) Re/Os data. Blue = graphite Re/Os data.

Table A1: Graphite Re and X-ray diffraction data

Sample	Location[a]	Type[b]	wt. (mg)	Re (ppb)	Angle	d Value (Å)	FWHM[c]	Crystallite Size D (Å)[d]	Temp (°C)[d]
JT20-05	Wallaston-Mudjatik Transition, SK, CA	HT	48.94	71.4	26.55	3.355	0.142	500	648
UNXX-BQC	Buckingham, QC, CA	HT	64.52	0.2	26.406	3.373	0.108	659	858
UNXX-BUK	Borrowdale, ENG, UK	HT	53.63	4.2	26.534	3.357	0.204	348	520
JAJXX-HB-SL-K	Khatagaha Mine, LK	HT	17.15	1.1	26.609	3.347	0.123	577	753
TCJXX-FPM-NH	Franklin Pierce Mine, NH, USA	HT	29.00	0.4	26.545	3.355	0.131	543	695
JAJ04-BLM-NH	Boston Lead Mine, NH, USA	HT	21.36	1.4	26.647	3.343	0.115	617	826
AESXX-GCM-M	Dillon, MT, USA	HT	20.96	0.5	26.543	3.355	0.107	664	900
UNXX-AN-NY	Anthony's Nose, NY, USA	HT	29.91	2.0	26.623	3.346	0.157	452	609
JAJXX-UZ-SA	Umzimkulu Quarry, SA	HT	70.55	0.2	26.566	3.353	0.120	592	768
JAJ09-LHM	Lead Hill Mine, NY, USA	HT	35.41	0.4	26.50	3.360	0.103	690	955
UNXX-TN	Aust-Agder, NO	HT	30.74	0.4	26.60	3.349	0.139	658	898
JT20-MH	Merelani Hills, Arusha, TZ	HT	51.56	38.8	26.56	3.353	0.143	497	645
TO09-BS-M	Bessie Mine, MI, USA	M	46.82	396.2	26.456	3.366	0.445	160	414
JAJXX-MG-B	Minas Gerais, BR	M	15.88	11.4	26.585	3.350	0.112	634	846
SPXX-m6423	Laytonville Quarry, CA, USA	M	49.39	1520.2	26.383	3.375	0.319	223	439
UNXX-SUK	Foss mine, SCT, UK	M	24.00	0.6	26.659	3.341	0.162	438	601
UNXX-CD-01	Canyon Diablo, AZ, USA	Mc	21.59	87.2	26.522	3.358	0.199	357	525

[a]Refer to Table S1 for complete sample description

[b]HT = hydrothermal, M = metamorphic; Mc = meteoritic

[c]Full Width at Half Maximum

[d]Calculated from Tagiri and Oba (1986) and Wada et al. (1994)

Table A2: Mineral Separate Description

Mineral Separate	Mineralogy Modal Abundance					
	Graphite$_f$[a]	Graphite$_p$[b]	Pyrite	Quartz	Silicates[c]	Biotite
JT20-MH-M-0.83	60.99	-	0.71	-	38.30	-
JT20-MH-M-1.13	89.49	-	0.67	-	9.84	-
JT20-MH-M-1.74	84.25	-	0.76	14.99	-	-
JT20-MH-NM-1.13	83.83	-	-	-	16.17	-
JT20-MH-NM-1.68	85.40	-	0.47	-	14.13	-
JT20-MH-NM-1.74	94.47	-	0.67	4.86	-	-
JT20-05-M-0.27	13.43	22.04	0.876	-	-	63.80
JT20-05-M-0.30	2.39	29.30	0.80	-	-	67.68
JT20-05-NM-0.28	3.23	27.02	0.155	-	-	69.75
JT20-05-NM-0.30	89.16	-	2.453	-	-	8.14
JT20-05-NM-0.40	88.18	-	5.017	6.69	-	-
JT20-05-NM-1.30	90.84	-	0.466	8.39	-	-

[a]Graphite$_f$ = fully formed graphite

[b]Graphite$_p$ = partially formed graphite

[c]Silicates = diopside, tsavorite, and quartz

Table A3: Re-Os graphite data

[a]Sample	wt. (mg)	Re (ppb)	±	Os (ppt)	±	^{192}Os (ppt)	^{187}Re/^{188}Os	±	^{187}Os/^{188}Os	±	rho	^{187}Os/^{188}Os$_i$
JT20-5-BULK	53.85	36.5	0.2	4639	10	1600	45.3	0.2	1.6347	0.0022	0.138	0.31
JT20-5-M-0.27	50.25	9.1	0.1	4329	12	1678	10.8	0.1	0.6274	0.0026	0.094	0.31
JT20-5-M-0.30†	51.55	6.8	0.1	2629	6	1014	13.3	0.2	0.6714	0.0018	0.059	0.28
JT20-5-NM-0.28†	45.21	6.9	0.1	2838	4	1095	12.6	0.2	0.6622	0.0010	0.041	0.29
JT20-5-NM-0.30	50.95	26.3	0.1	7550	13	2848	18.4	0.1	0.8503	0.0011	0.110	0.31
JT20-5-NM-0.40	48.94	37.5	0.2	3602	9	1173	63.6	0.3	2.1770	0.0031	0.149	0.31
JT20-5-NM-1.30	51.80	71.5	0.3	2843	25	614	231.7	1.4	7.1242	0.0575	0.445	0.34
JT20-5-NM-0.4-MQ1	37.07	22.1	0.2	3078	10	1069	41.0	0.3	1.5691	0.0046	0.135	0.37
JT20-5-NM-0.4-MQ2	20.78	21.9	0.3	2352	8	767	56.8	0.7	2.1672	0.0053	0.147	2.17
JT20-5-NM-1.30-SPT	17.72	10.6	0.3	699	5	218	96.8	3.0	2.6206	0.0211	0.257	-0.21
JT20-MH-M-0.83†	43.33	13.1	0.1	249	3	60	434.8	7.3	5.6545	0.0927	0.641	1.38
JT20-MH-M-1.13	54.01	28.5	0.1	266	6	30	1873.6	41.0	20.2781	0.5337	0.790	1.86
JT20-MH-M-1.74	44.03	35.7	0.2	456	7	81	880.6	11.5	10.3642	0.1937	0.598	1.71
JT20-MN-M-1.74 -RPT	53.72	26.2	0.1	513	4	121	432.3	3.3	5.9349	0.0405	0.602	1.68
JT20-MN-NM-1.13	56.16	17.8	0.1	170	4	21	1725.3	63.1	18.6370	0.6769	0.983	1.68
JT20-MH-NM-1.68	50.06	24.2	0.1	225	6	27	1805.5	48.7	19.1565	0.6464	0.764	1.41
JT20-MH-NM-1.74	51.56	38.5	0.2	294	6	19	4100.9	131.9	42.1781	1.3578	0.980	1.86
JT20-MH-NM-1.74-RPT	62.68	31.7	0.1	293	6	34	1851.5	32.8	19.7087	0.4576	0.716	1.51
JT20-MH-NM-1.74-RPT-2	50.61	39.3	0.2	389	5	51	1545.2	19.9	16.8297	0.2080	0.920	1.64
JT20-MH-NM-1.74-SPT	54.27	22.7	0.1	171	5	12	3708.5	174.8	37.0891	1.7973	0.959	0.63
JT20-MH-BULK-MQ1	82.40	26.1	0.1	263	4	32	1642.9	23.2	18.7461	0.3281	0.734	2.59
UNXX-BUK	53.63	4.2	0.1	89	3	26	318.3	23.8	3.1763	0.2278	0.942	0.70
SPXX-m6424	49.39	1520.2	1.7	19577	48	7645	135.1	0.5	0.5658	0.0021	0.334	0.22
TO09-BM-M	46.82	182.3	0.6	3800	24	443	819.3	3.7	19.6294	0.0676	0.636	0.49
JAJXX-MG-B	15.88	10.5	0.1	1842	6	661	31.5	0.3	1.2844	0.0045	0.264	0.13

[a]Sample nomenclature is as follows: name/location/year/sample#/magnetic/non-magnetic-current; SPT = sodium polytungstate; MQ1 = Milli-pore (18.2 MΩ) water at 23.5°C; MQ2 = Milli-pore (18.2 MΩ) water at 87.5°C
[b]Calculated from Re/Os isochron ages or inferred mineralization ages
†rejected from isochron

Table A4: Sample types and locations

Sample	Type	Origin	Host Rock	Morphology	Location	Latitude (°)	Longitude (°)	Inferred Age	Inferred Origin of C	References
JT20-05	Hydrothermal	Epigenetic	Augen gneiss (metapelites)	Flake	Southeastern Athabasca Basin, Saskatchewan, Canada	57.508349 N	105.380259 W	Paleoproterozoic (1775-1720 Ma)	assimilation of organic seds	Martz et al. (2017)
UNXX-BQC	Hydrothermal	Epigenetic	Marbles and metasediments	Cryptocrystalline and flake	Buckingham, Quebec, Canada	45.5864 N	75.4169 W	Precambrian - Grenvillian (?)	CO2 devolatilization of marble(?)	Etheir and Pirzada (2014)
UNXX-BUK	Hydrothermal	Epigenetic	Andesites	Cryptocrystalline	Plumbago Mine, Seathwaite, Borrowdale, Cumbria, England, UK	54.5130 N	3.1400 W	Ordovician (470 to 450 Ma)	assimilation of organic seds	Ortega et al. (2010)
JAJXX-HB-SL-K	Hydrothermal	Epigenetic	Granulite and ampholite faices metasediments	Flake	Khatagaha, Sri Lanka	7.8731 N	80.7718 E	Neoproterozoic (580-550 Ma)	CO2 infiltration of deep crustal carbon	Touret et al. (2019)
TCIXX-FPM-NH	Hydrothermal	Epigenetic	Syngenetic granitoids and metasediments	Cryptocrystalline	Franklin Pierce mine, Goshen, New Hampshire, USA	47.15285 N	122.4004 W	Silurian-Devonian (?)	fluid mixing during metamorphism + hydrothermal	Duke and Rumble III (1986)
JAJ04-BLM-NH	Hydrothermal	Epigenetic	Granitoids	Flake	Boston Lead mine, Little Mtn. near Mt. Kearsarge, Salisbury, New Hampshire, USA	41.94 N	72.18 W	Phanerozoic(?)	fluid mixing during metamorphism + hydrothermal (?)	Rumble III et al. (1986); Rumble and Chamberlain (1988)
AESXX-GCM-M	Hydrothermal	Epigenetic	Gneisses and pegmatites	Flake	Crystal Graphite Mine, Dillon, Beaverhead County, Montana, USA	45.10268 N	112.50587 W	Precambrian (1.85-1.60 Ga?)	CO2-CH4 infiltration; devolatilization of marble	Ford (1954) and Duke et al. (1989)
UNXX-AN-NY	Hydrothermal	Epigenetic	Marble dolomites	Cryptocrystalline	Anthony's Nose, Putnam Co., New York, USA	41.3324 N	73.9703 W	Phanerozoic(?)	CO2 devolatilization of marble(?)	Jasccak et al. (2009)
JAJXX-UZ-SA	Hydrothermal	Epigenetic	Marble dolomites	Flake	Umzimkulu Quarry, Port Shepstone, Kwazulu/Natal, South Africa	30 S	30 E	Precambrian	assimilation of organic seds (?)	Bullen et al. (1992)
JAJ09-LHM	Hydrothermal	Epigenetic	Feldspathic granitoid	Flake	Lead Hill Mine dump, Chilson Hill, Ticonderoga, Essex County, New York, USA	43.9 N	73.46667 W	Phanerozoic(?)	CO2 devolatilization of marble(?)	Jasccak et al. (2009)
UNXX-TN	Hydrothermal	Epigenetic	Gneisses and gedridites	Cryptocrystalline	Gjerstad-Tvedsetrand area, Tvedestrand, Aust-Agder, Norway	58.6223 N	8.9314 E	Precambrian (?)	carbonaceous metapelites	Touret (1968)
JT20-MH	Hydrothermal	Syngenetic/Epigenetic	Metapelites and calc-silicates	Flake	Merelani Hills, Arusha Region, Tanzania	3.554167 S	36.95 E	Neoproterozoic (630-575 Ma)	fluid deirved from carbonaceous metapelites	Feneyrol et al. (2017)
TO09-BS-M	Metamorphic	Epigenetic	Low grade massive (slickenside) graphite in slate	Cryptocrystalline	Bessie Mine, Humbold Township, Marquette Co., Michigan	46.5111 N	87.90083 W	Paleoproterozoic	carbonaceous metapelites	James (1951); Hiatt et al. (2015)
JAJXX-MG-B	Metamorphic	Sygenetic	Graphitic schist (metapelites)	Flake	Salto da Divisa, Minas Gerais, Brazil	16.0833 S	40.11667 W	Paleoproterozoic	carbonaceous metapelites	Miranda et al. (2019)
SPXX-m6423	Metamorphic	Sygenetic	Blueschists and meta-ironstones	Flake	Laytonville Quarry, Coastal Range, California, USA	39.61806 N	123.46306 W	Late Jurassic (165-150 Ma)	carbonaceous metapelites	Wood (1982); Wakabayashi (2015)
UNXX-SUK	Metamorphic	Sygenetic	Graphitic schist (metapelites)	Flake	Foss mine, SCT, UK	56.671667 N	3.926333 W	Precambrian	carbonaceous metapelites	Moles and Boyce (2019)
UNXX-CD	Meteoritic	Syngenetic	IAB iron meteorites	Cryptocrystalline	Canyon Diablo, Barringer Crater, Arizona, USA	35.0278 N	111.0222 W	Solar System Formation	condensed nebular environment	Matsuda et al. (2005) and Hilton et al. (2020)

Note: Table modified after Luque et al. (1998)

Table A5: In-situ SIMS graphite C isotope data

Spot Name	δ¹³C (VPDB)	2σ (‰) inter-session	Spot Name	δ¹³C (VPDB)	2σ (‰) inter-session
S6981B_JT20MH-1_1@1	-24.47	0.18	S6983B_JT20-5-Vr@1	-18.52	0.13
S6981B_JT20MH-1_1@2	-24.43	0.11	S6983B_JT20-5-Vr@2	-18.40	0.15
S6981B_JT20MH-1_1@3	-24.41	0.09	S6983B_JT20-5-Vr@3	-18.87	0.13
S6981B_JT20MH-1_2@1	-24.53	0.12	S6983B_JT20-5-Vr@4	-19.08	0.09
S6981B_JT20MH-1_2@2	-24.56	0.10	S6983B_JT20-5-Vr@5	-18.76	0.14
S6981B_JT20MH-1_3@1	-24.59	0.15	S6983B_JT20-5-Vr@6	-19.15	0.11
S6981B_JT20MH-1_3@2	-24.53	0.14	S6983B_JT20-5-Vr@7	-19.02	0.10
S6981B_JT20MH-1_4@1	-24.35	0.11	S6983B_JT20-5-Vr@8	-18.86	0.17
S6981B_JT20MH-1_4@2	-24.55	0.09	S6983B_JT20-5-Vr@9	-18.11	0.12
S6981B_JT20MH-1_5@1	-24.52	0.13	S6983B_JT20-5-Vr@10	-19.15	0.15
S6981B_JT20MH-1_5@2	-24.45	0.14	S6983B_JT20-5-Vr@11	-19.39	0.12
S6981B_JT20MH-1_5@3	-24.50	0.11	S6983B_JT20-5-Vr@12	-18.95	0.10
S6981B_JT20MH-1_6@1	-24.40	0.13	S6983B_JT20-5-Vr@13	-18.24	0.10
S6981B_JT20MH-1_6@2	-24.39	0.09	S6983B_JT20-5-Vr@14	-17.43	0.10
S6981B_JT20MH-1_6@3	-24.52	0.12	S6983B_JT20-5-Vr@1	-18.65	0.10
S6981B_JT20MH-1_7@1	-24.52	0.10	S6983B_JT20-5-Vr@2	-18.32	0.14
S6981B_JT20MH-1_7@2	-24.52	0.10	S6983B_JT20-5-Vr@3	-19.29	0.13
S6981B_JT20MH-1_7@3	-24.66	0.13	S6983B_JT20-5-Vr@4	-18.59	0.14
S6981B_JT20MH-1_8@1	-24.58	0.10	S6983B_JT20-5-Vr@5	-16.91	0.11
S6981B_JT20MH-1_8@2	-24.47	0.09	S6983B_JT20-5-Vr@6	-18.72	0.10
S6981B_JT20MH-1_8@3	-24.55	0.13	S6983B_JT20-5-Vr@7	-19.01	0.12
S6981B_JT20MH-1_9@1	-24.58	0.12	S6983B_JT20-5-Vr@8	-18.55	0.14
S6981B_JT20MH-1_9@2	-24.56	0.11	S6983B_JT20-5- Vc@1	-19.95	0.12
S6981B_JT20MH-1_9@3	-24.42	0.13	S6983B_JT20-5- Vc@2	-19.14	0.09
S6981B_JT20MH-1_10@1	-24.36	0.17	S6983B_JT20-5- Vc@3	-21.64	0.15
S6981B_JT20MH-1_10@2	-24.68	0.13	S6983B_JT20-5- Vc@4	-19.12	0.11
S6981B_JT20MH-1_10@3	-24.52	0.15	S6983B_JT20-5- Vc@5	-19.63	0.16
S6981B_JT20MH-1_11@1	-24.49	0.10	S6983B_JT20-5- Vc@6	-19.58	0.13
S6981B_JT20MH-1_11@2	-24.70	0.12	S6983B_JT20-5- Vc@7	-18.66	0.12
S6981B_JT20MH-1_11@3	-24.44	0.10	S6983B_JT20-5- Vc@8	-19.20	0.11
S6981C_JT20MH-1_12@1	-24.73	0.14	S6983B_JT20-5- Vc@9	-18.97	0.13
S6981C_JT20MH-1_12@2	-24.74	0.10	S6983B_JT20-5- Vc@10	-16.73	0.12
S6981C_JT20MH-1_12@3	-24.40	0.09	S6983B_JT20-5- Vc@11	-19.13	0.16
S6981C_JT20MH-1_13@1	-24.43	0.13	S6983B_JT20-5- Vc@12	-18.49	0.09
S6981C_JT20MH-1_13@2	-24.44	0.09	S6983B_JT20-5- Vc@13	-19.12	0.15
S6981C_JT20MH-1_13@3	-24.39	0.15	S6983C_JT20-5- WR3@1	-18.36	0.13
S6981C_JT20MH-1_14@1	-25.24	0.12	S6983C_JT20-5- WR3@2	-19.19	0.13
S6981C_JT20MH-1_14@2	-25.30	0.09	S6983C_JT20-5- WR3@3	-19.20	0.16
S6981C_JT20MH-1_14@3	-25.31	0.13	S6983C_JT20-5- WR3@4	-15.62	0.10
S6981C_JT20MH-1_14@4	-24.46	0.09	S6983C_JT20-5- WR3@5	-17.20	0.10
S6981C_JT20MH-1_15@1	-24.63	0.15	S6983C_JT20-5- WR3@6	-17.59	0.15
S6981C_JT20MH-1_15@2	-24.58	0.10	S6983C_JT20-5- WR3@7	-17.54	0.10
S6981C_JT20MH-1_15@3	-24.45	0.13	S6983C_JT20-5- WR3@8	-15.48	0.10
S6981C_JT20MH-1_16@1	-25.17	0.13	S6983C_JT20-5- WR3@9	-17.87	0.10
S6981C_JT20MH-1_16@2	-24.73	0.11	S6983C_JT20-5- WR3@10	-17.95	0.14
S6981C_JT20MH-1_16@3	-24.78	0.13	S6983C_JT20-5- WR3@11	-15.28	0.12
S6981C_JT20MH-1_17@1	-24.53	0.13	S6983C_JT20-5- WR3@13	-18.72	0.13
S6981C_JT20MH-1_17@2	-24.52	0.09	S6983C_JT20-5- WR3@14	-15.46	0.09
S6981C_JT20MH-1_17@3	-24.58	0.09	S6983C_JT20-5- WR3@16	-17.84	0.13
S6981C_JT20MH-1_19@1	-24.41	0.11	S6983C_JT20-5- WR3@17	-17.86	0.12
S6981C_JT20MH-1_19@2	-24.55	0.14	S6983C_JT20-5- WR3@18	-18.28	0.13
S6981C_JT20MH-1_19@3	-25.01	0.12	S6983C_JT20-5- WR3@19	-17.92	0.13
S6981C_JT20MH-1_20@1	-24.46	0.12	S6983C_JT20-5- WR3@20	-17.64	0.09
S6981C_JT20MH-1_20@2	-24.66	0.09	S6983C_JT20-5- WR3@21	-17.71	0.15
S6981C_JT20MH-1_20@3	-24.55	0.13	S6983C_JT20-5- WR3@22	-18.00	0.14
S6982B_JT20MH-2_1@1	-24.88	0.09	S6983C_JT20-5- WR3@23	-17.86	0.11
S6982B_JT20MH-2_1@2	-24.85	0.10	S6983C_JT20-5- WR3@24	-17.93	0.11
S6982B_JT20MH-2_1@3	-24.86	0.10	S6983C_JT20-5- WR3@25	-18.07	0.09
S6982B_JT20MH-2_1@4	-24.67	0.13	S6983C_JT20-5- WR3@26	-17.90	0.10
S6982B_JT20MH-2_2@1	-25.43	0.11	S6983C_JT20-5- WR3@27	-17.82	0.13
S6982B_JT20MH-2_2@2	-25.00	0.12	S6983C_JT20-5- WR3@28	-17.55	0.14
S6982B_JT20MH-2_2@3	-25.03	0.09	S6983C_JT20-5- WR3@29	-16.73	0.10
S6982B_JT20MH-2_3@1	-25.44	0.09	S6983C_JT20-5- WR3@30	-17.38	0.12
S6982B_JT20MH-2_3@2	-25.27	0.09	S6983C_JT20-5- WR3@31	-18.45	0.17
S6982B_JT20MH-2_3@3	-25.48	0.10	S6983C_JT20-5- WR3@32	-18.40	0.16
S6982B_JT20MH-2_4@1	-24.81	0.11			
S6982B_JT20MH-2_4@2	-24.73	0.11			
S6982B_JT20MH-2_4@3	-24.93	0.10			
S6982B_JT20MH-2_4@4	-24.79	0.10			
S6982B_JT20MH-2_4@5	-24.89	0.10			
S6982B_JT20MH-2_4@6	-25.12	0.13			
S6982B_JT20MH-2_4@7	-24.58	0.11			
S6982B_JT20MH-2_4@8	-24.65	0.14			
S6982B_JT20MH-2_4@9	-24.86	0.10			
S6982B_JT20MH-2_5@1	-25.14	0.12			
S6982B_JT20MH-2_5@2	-24.88	0.14			
S6982B_JT20MH-2_5@3	-25.07	0.09			
S6982B_JT20MH-2_6@1	-25.63	0.12			
S6982B_JT20MH-2_6@2	-25.35	0.13			
S6982B_JT20MH-2_6@3	-25.38	0.10			
S6982B_JT20MH-2_7@1	-25.04	0.10			
S6982B_JT20MH-2_7@2	-24.93	0.10			
S6982B_JT20MH-2_8@1	-24.62	0.09			
S6982B_JT20MH-2_8@2	-25.00	0.09			
S6982B_JT20MH-2_9@1	-24.76	0.11			
S6982B_JT20MH-2_9@2	-24.71	0.11			
S6982B_JT20MH-2_10@1	-24.62	0.12			
S6982B_JT20MH-2_10@2	-24.54	0.09			
S6982C_JT20MH-2_11@1	-25.15	0.10			
S6982C_JT20MH-2_11@2	-25.47	0.09			
S6982C_JT20MH-2_11@3	-25.23	0.11			
S6982C_JT20MH-2_12@1	-24.97	0.09			
S6982C_JT20MH-2_12@2	-24.79	0.13			
S6982C_JT20MH-2_12@3	-24.96	0.09			
S6982C_JT20MH-2_13@1	-24.59	0.09			
S6982C_JT20MH-2_13@2	-24.79	0.09			
S6982C_JT20MH-2_13@3	-25.27	0.15			
S6982C_JT20MH-2_13@4	-25.62	0.15			
S6982C_JT20MH-2_13@5	-25.60	0.09			
S6982C_JT20MH-2_14@1	-25.31	0.09			
S6982C_JT20MH-2_15@1	-25.23	0.15			
S6982C_JT20MH-2_15@2	-25.24	0.09			
S6982C_JT20MH-2_15@3	-25.22	0.11			
S6982C_JT20MH-2_16@1	-24.79	0.12			
S6982C_JT20MH-2_16@2	-25.61	0.11			
S6982C_JT20MH-2_16@3	-25.90	0.09			
S6982C_JT20MH-2_16@4	-24.81	0.11			
S6982C_JT20MH-2_17@1	-24.96	0.10			
S6982C_JT20MH-2_17@2	-25.29	0.12			
S6982C_JT20MH-2_18@1	-25.22	0.10			
S6982C_JT20MH-2_18@2	-25.22	0.11			
S6982C_JT20MH-2_19@1	-24.55	0.15			
S6982C_JT20MH-2_19@2	-24.62	0.11			

Table A6: Grain mount SIMS graphite C isotope data

Spot Name	δ¹³C (VPDB)	2σ (‰) inter-session	Spot Name	δ¹³C (VPDB)	2σ (‰) inter-session
S6981D_JT20-MH-gr-M-083_1@2	-24.83	0.14	S6983D_JT20-5-gr-bulk_27@1	-20.02	0.15
S6981D_JT20-MH-gr-M-083_2@1	-24.62	0.09	S6983D_JT20-5-gr-bulk_26@1	-19.20	0.13
S6981D_JT20-MH-gr-M-083_4@1	-24.56	0.14	S6983D_JT20-5-gr-bulk_22@1	-18.33	0.09
S6981D_JT20-MH-gr-M-083_5@1	-24.68	0.15	S6983D_JT20-5-gr-bulk_30@1	-20.81	0.15
S6981D_JT20-MH-gr-M-083_5@2	-24.99	0.12	S6983D_JT20-5-gr-bulk_64@1	-18.08	0.30
S6981D_JT20-MH-gr-M-083_6@1	-24.67	0.11	S6983D_JT20-5-gr-bulk_62@1	-18.76	0.11
S6981D_JT20-MH-gr-M-083_6@2	-24.72	0.15	S6983D_JT20-5-gr-bulk_60@1	-17.75	0.13
S6981D_JT20-MH-gr-M-083_6@3	-24.67	0.20	S6983D_JT20-5-gr-bulk_43@1	-18.43	0.14
S6981D_JT20-MH-gr-M-083_8@1	-24.76	0.09	S6983D_JT20-5-gr-bulk_39@1	-17.92	0.11
S6981D_JT20-MH-gr-M-083_8@2	-24.78	0.09	S6983D_JT20-5-gr-bulk_29@1	-17.38	0.09
S6981D_JT20-MH-gr-M-083_9@1	-24.56	0.13	S6983E_JT20-5-gr-M027_4@1	-19.20	0.13
S6981D_JT20-MH-gr-M-083_10@1	-24.19	0.10	S6983E_JT20-5-gr-M027_8@1	-21.27	0.34
S6981D_JT20-MH-gr-M-083_12@1	-24.85	0.18	S6983E_JT20-5-gr-M027_5@1	-18.60	0.28
S6981D_JT20-MH-gr-M-083_12@2	-24.78	0.11	S6983F_JT20-5-gr-M030_7@1	-18.16	0.09
S6981D_JT20-MH-gr-M-083_13@1	-24.71	0.14	S6983F_JT20-5-gr-M030_16@1	-18.33	0.10
S6981D_JT20-MH-gr-M-083_15@2	-24.73	0.11	S6983F_JT20-5-gr-M030_17@1	-20.86	0.59
S6981D_JT20-MH-gr-M-083_15@3	-24.70	0.09	S6983F_JT20-5-gr-M030_10@1	-17.94	0.58
S6981D_JT20-MH-gr-M-083_16@1	-24.56	0.13	S6983F_JT20-5-gr-M030_3@1	-18.75	0.12
S6981D_JT20-MH-gr-M-083_16@2	-24.67	0.11	S6983F_JT20-5-gr-M030_23@1	-18.72	0.11
S6981D_JT20-MH-gr-M-083_18@1	-25.40	0.13	S6983F_JT20-5-gr-M030_28@1	-19.41	0.09
S6981E_JT20-MH-gr-M113_1@1	-24.56	0.10	S6983F_JT20-5-gr-M030_33@1	-18.71	0.15
S6981E_JT20-MH-gr-M113_2@1	-24.75	0.12	S6983F_JT20-5-gr-M030_8@1	-18.89	0.13
S6981E_JT20-MH-gr-M113_2@2	-24.63	0.10	S6983F_JT20-5-gr-M030_9@1	-16.22	0.11
S6981E_JT20-MH-gr-M113_6@1	-24.60	0.13	S6983F_JT20-5-gr-M030_15@1	-16.31	0.09
S6981E_JT20-MH-gr-M113_6@2	-24.76	0.12	S6983F_JT20-5-gr-M030_26@1	-18.31	0.15
S6981E_JT20-MH-gr-M113_8@1	-24.83	0.13	S6983F_JT20-5-gr-M030_24@1	-16.46	0.55
S6981E_JT20-MH-gr-M113_10@1	-25.12	0.14	S6983F_JT20-5-gr-M030_31@1	-16.24	0.14
S6981E_JT20-MH-gr-M113_13@1	-24.88	0.11	S6983G_JT20-5-gr-NM028_2@1	-18.58	0.14
S6981E_JT20-MH-gr-M113_13@2	-24.93	0.10	S6983G_JT20-5-gr-NM028_1@1	-18.13	0.15
S6981E_JT20-MH-gr-M113_15@1	-24.61	0.15	S6983G_JT20-5-gr-NM028_3@1	-17.82	0.13
S6981E_JT20-MH-gr-M113_17@1	-24.58	0.09	S6983G_JT20-5-gr-NM028_8@1	-19.45	0.15
S6981E_JT20-MH-gr-M113_20@1	-24.75	0.13	S6983G_JT20-5-gr-NM028_7@1	-17.70	0.11
S6981E_JT20-MH-gr-M113_20@2	-24.77	0.15	S6983G_JT20-5-gr-NM028_10@1	-18.91	0.09
S6981E_JT20-MH-gr-M113_20@3	-24.64	0.14	S6983H_JT20-5-gr-NM030_1@1	-14.75	0.12
S6981E_JT20-MH-gr-M113_23@1	-24.98	0.11	S6983H_JT20-5-gr-NM030_3@1	-19.08	0.12
S6981E_JT20-MH-gr-M113_23@2	-24.74	0.09	S6983H_JT20-5-gr-NM030_14@1	-18.96	0.15
S6981E_JT20-MH-gr-M113_23@3	-24.57	0.13	S6983H_JT20-5-gr-NM030_7@1	-18.79	0.11
S6981E_JT20-MH-gr-M113_28@1	-24.41	0.12	S6983H_JT20-5-gr-NM030_8@1	-18.92	0.09
S6981F_JT20-MH-gr-NM113_1@1	-24.72	0.14	S6983H_JT20-5-gr-NM030_16@1	-18.03	0.12
S6981F_JT20-MH-gr-NM113_1@2	-24.74	0.15	S6983H_JT20-5-gr-NM030_23@1	-19.80	0.11
S6981F_JT20-MH-gr-NM113_2@1	-24.79	0.15	S6983H_JT20-5-gr-NM030_41@1	-19.28	0.12
S6981F_JT20-MH-gr-NM113_3@1	-25.01	0.09	S6983H_JT20-5-gr-NM030_38@1	-19.65	0.26
S6981F_JT20-MH-gr-NM113_3@2	-24.83	0.09	S6983H_JT20-5-gr-NM030_9@1	-19.10	0.09
S6981F_JT20-MH-gr-NM113_3@3	-24.70	0.15	S6983H_JT20-5-gr-NM030_5@1	-19.39	0.09
S6981F_JT20-MH-gr-NM113_3@4	-24.33	0.11	S6983H_JT20-5-gr-NM030_10@1	-17.58	0.11
S6981F_JT20-MH-gr-NM113_5@1	-24.73	0.13	S6983H_JT20-5-gr-NM030_18@1	-17.14	0.14
S6981F_JT20-MH-gr-NM113_7@1	-24.65	0.11	S6983H_JT20-5-gr-NM030_25@1	-20.37	0.13
S6981F_JT20-MH-gr-NM113_8@1	-24.74	0.09	S6983H_JT20-5-gr-NM030_31@1	-17.89	0.13
S6981F_JT20-MH-gr-NM113_8@2	-24.58	0.15	S6983I_JT20-5-gr-NM040_18@1	-17.88	0.09
S6981F_JT20-MH-gr-NM113_8@3	-24.60	0.11	S6983I_JT20-5-gr-NM040_20@1	-16.61	0.15
S6981F_JT20-MH-gr-NM113_17@1	-24.92	0.10	S6983I_JT20-5-gr-NM040_27@1	-17.79	0.15
S6981F_JT20-MH-gr-NM113_17@2	-24.51	0.11	S6983I_JT20-5-gr-NM040_51@2	-18.46	0.16
S6981F_JT20-MH-gr-NM113_17@3	-25.05	0.13	S6983I_JT20-5-gr-NM040_36@1	-17.71	0.11
S6981F_JT20-MH-gr-NM113_18@1	-24.77	0.12	S6983I_JT20-5-gr-NM040_28@1	-17.04	0.09
S6981F_JT20-MH-gr-NM113_18@2	-24.65	0.11	S6983I_JT20-5-gr-NM040_23@1	-18.72	0.20
S6981F_JT20-MH-gr-NM113_22@1	-24.66	0.11	S6983I_JT20-5-gr-NM040_15@1	-18.56	0.15
S6981F_JT20-MH-gr-NM113_22@2	-24.78	0.09	S6983I_JT20-5-gr-NM040_13@1	-18.67	0.17
S6981F_JT20-MH-gr-NM113_24@1	-24.57	0.09	S6983I_JT20-5-gr-NM040_12@1	-18.13	0.10
S6981F_JT20-MH-gr-NM113_25@1	-24.56	0.16	S6983I_JT20-5-gr-NM040_4@1	-18.92	0.11
S6981F_JT20-MH-gr-NM113_27@1	-25.01	0.14	S6983I_JT20-5-gr-NM040_3@1	-18.89	0.14
S6981G_JT20-MH-gr-NM168_1@1	-24.72	0.12	S6983I_JT20-5-gr-NM040_7@1	-16.15	0.27
S6981G_JT20-MH-gr-NM168_2@1	-24.76	0.11	S6983I_JT20-5-gr-NM040_25@1	-20.16	0.92
S6981G_JT20-MH-gr-NM168_5@1	-24.74	0.09	S6983I_JT20-5-gr-NM040_24@1	-19.05	0.09
S6981G_JT20-MH-gr-NM168_10@1	-24.49	0.13	S6983I_JT20-5-gr-NM040_40@1	-17.62	0.16
S6981G_JT20-MH-gr-NM168_11@1	-24.64	0.11	S6983J_JT20-5-gr-NM130_1@1	-17.61	0.14
S6981G_JT20-MH-gr-NM168_11@2	-24.61	0.13	S6983J_JT20-5-gr-NM130_5@1	-16.75	0.12
S6981G_JT20-MH-gr-NM168_12@1	-24.49	0.14	S6983J_JT20-5-gr-NM130_7@1	-17.85	0.12
S6981G_JT20-MH-gr-NM168_13@1	-24.66	0.15	S6983J_JT20-5-gr-NM130_12@1	-18.54	0.16
S6981G_JT20-MH-gr-NM168_14@1	-24.75	0.13	S6983J_JT20-5-gr-NM130_21@1	-18.02	0.28
S6981G_JT20-MH-gr-NM168_15@1	-24.79	0.16	S6983J_JT20-5-gr-NM130_26@1	-18.93	0.13
S6981G_JT20-MH-gr-NM168_16@1	-24.72	0.11	S6983J_JT20-5-gr-NM130_22@1	-17.03	0.14
S6981G_JT20-MH-gr-NM168_17@1	-24.60	0.12	S6983J_JT20-5-gr-NM130_13@1	-18.06	0.15
S6981G_JT20-MH-gr-NM168_22@1	-24.82	0.12	S6983J_JT20-5-gr-NM130_27@1	-18.04	0.20
S6981G_JT20-MH-gr-NM168_22@2	-24.64	0.09	S6983J_JT20-5-gr-NM130_24@2	-17.56	0.09
S6981G_JT20-MH-gr-NM168_24@1	-24.79	0.14			
S6981G_JT20-MH-gr-NM168_27@1	-24.51	0.12			
S6981G_JT20-MH-gr-NM168_27@2	-24.76	0.14			
S6981G_JT20-MH-gr-NM168_27@3	-24.53	0.16			
S6981G_JT20-MH-gr-NM168_28@1	-24.80	0.10			
S6981G_JT20-MH-gr-NM168_30@1	-24.79	0.09			
S6981G_JT20-MH-gr-NM168_30@2	-25.06	0.09			
S6981H_JT20-MH-gr-NM174_1@1	-24.73	0.11			
S6981H_JT20-MH-gr-NM174_2@1	-24.80	0.11			
S6981H_JT20-MH-gr-NM174_3@1	-24.74	0.12			
S6981H_JT20-MH-gr-NM174_4@1	-24.38	0.15			
S6981H_JT20-MH-gr-NM174_5@1	-24.57	0.13			
S6981H_JT20-MH-gr-NM174_6@1	-24.90	0.09			
S6981H_JT20-MH-gr-NM174_6@2	-24.96	0.12			
S6981H_JT20-MH-gr-NM174_10@1	-24.90	0.12			
S6981H_JT20-MH-gr-NM174_11@1	-24.56	0.10			
S6981H_JT20-MH-gr-NM174_18@1	-24.85	0.10			
S6981H_JT20-MH-gr-NM174_18@2	-24.74	0.10			
S6981H_JT20-MH-gr-NM174_18@3	-24.77	0.14			
S6981H_JT20-MH-gr-NM174_18@4	-24.72	0.11			
S6981H_JT20-MH-gr-NM174_18@5	-24.75	0.12			
S6981H_JT20-MH-gr-NM174_18@6	-24.66	0.09			
S6981H_JT20-MH-gr-NM174_19@1	-24.55	0.16			
S6981H_JT20-MH-gr-NM174_20@1	-24.73	0.11			
S6981H_JT20-MH-gr-NM174_21@1	-24.51	0.12			
S6981H_JT20-MH-gr-NM174_23@1	-24.66	0.11			
S6981H_JT20-MH-gr-NM174_28@1	-24.95	0.12			
S6981H_JT20-MH-gr-NM174_28@2	-24.51	0.13			

Table A7: Raman Carbonaceous Material Spectroscopy

| | Band components: peak amplitudes | | | | |
Sample	G	D1	D2	R2	[a]T(°C)
JT20-5-NM-1.30-1	1879	n.d.	n.d.	-	641.0
JT20-5-NM-1.30-2	1445	113.6	5.0	0.078	536.7
JT20-5-NM-1.30-3	83	n.d.	nd.	-	641.0

[a]Temperature of graphitization estimated from Beyssac et al. (2002)

Table A8: Merelani Hills Re-Os pyrite data

[a]Sample	Re (ppb)	±	Os (ppt)	±	^{192}Os (ppt)	^{187}Re/^{188}Os	±	^{187}Os/^{188}Os	±	rho	^{187}Os/^{188}Os$_i$[b]
JT20-MH-py-NM-1.15	18.6	0.0	6233	19	2104	17.6	0.0	1.8358	0.0044	0.455	1.66
JT20-MH-py-NM-1.20	19.9	0.1	6237	19	2105	18.8	0.1	1.8395	0.0045	0.339	1.65
JT20-MH-py-NM-1.25	21.1	0.0	5785	19	1947	21.5	0.1	1.8655	0.0049	0.440	1.65
JT20-MH-py-M-1.08	20.4	0.0	4998	15	1673	24.3	0.1	1.9152	0.0045	0.436	1.68
JT20-MH-py-M-1.15	19.8	0.0	5933	17	1998	19.7	0.0	1.8615	0.0041	0.453	1.67

[a]Sample nomenclature is as follows: name/location/year/magnetic/non-magnetic/current

[b]Calculated from Re/Os isochron ages or inferred mineralization ages

Procedural blank for analysis (n=1): Re = 0.64 pg; Os = 0.058 pg; ^{187}Os/^{188}Os = 0.342

Appendix B

Supplementary Material for

Did subducted graphite fertilize the Franciscan mantle wedge with radiogenic Os?

Appendix II includes:

Supplementary Text

Figures B1 to B7

Tables B1 to B4

Supplementary Text

1. Methods

1.1 Mineral separation for Re-Os geochronology

Rock specimen SPXX-m6424 was fragmented by hand into 1-5 mm-sized rock chips, which were then manually crushed via zirconium mortar and pestle, sieved to 70–200 μm sizes, and split into nine magnetically-distinct 100-500 mg aliquots via Frantz Isodynamic magnetic separation (current = 0.11-2.00 A and tilt = 0).

1.2 Thin section and grain mount preparation

Thin section and grain mount preparation was carried out at the University of Alberta's Thin Section Laboratory using standard abrading and polishing equipment. Mineral separates were mounted on to nine individualized 3-mm diameter discs that were epoxy sealed and polished for petrographic and micro-analysis.

1.3 Electron Microprobe Analyses

Electron microprobe analyses were performed at the University of Alberta's Electron Microprobe Laboratory. Thin section *SPXX-m6424-1* (Fig. B1) was carbon-coated and

quantitatively spot-analyzed with an energy dispersive spectrometer (EDS) housed in a JEOL 8900R.

1.4 Raman spectroscopy

Raman spectra of carbonaceous material (RSCM) was analyzed at the University of Alberta's Fluid Inclusion Laboratory using a Horiba LabRAM HR Evolution Raman microscope equipped with a green laser (532 nm wavelength), a 1800 (grooves/mm) diffraction grating, and a confocal hole size of 50 nm. RSCM was recorded over the first-order D- and G-band range (1100 to 1800 cm^{-1}) (Beyssac et al., 2002). Peak position, band area, and band width (i.e. full width at half maximum FWHM) were determined using the peak- and curve-fitting software Fityk (Wojdyr, 2010). Crystallization temperatures were estimated according to Beyssac et al. (2002).

1.5 Re-Os geochemistry

Rhenium-osmium geochemistry was performed in a class-100 clean room at the University of Alberta's Re-Os Crustal Geochronology Laboratory. Aliquots of graphite (10-30 mg) and pyrite (30 mg) were transferred to individual borosilicate glass Carius tubes along with a known amount of ^{185}Re-^{190}Os tracer solution (UA3) and an 8 mL 1:1 mixture of 4 N H_2SO_4 and 4 N CrO_3-H_2SO_4 (0.5 g CrO3 per 1mL of 4 N H_2SO_4) and a 3:1 mixture of concentrated purged-distilled nitric acid and concentrated TMG hydrochloric acid (inverse aqua regia), respectively. This was immediately followed by cryogenic freezing (-116 ˚C) via ethanol-dry ice bath. Carius tubes housing graphite and pyrite were then sealed with a blow torch and spike-sample equilibrated at 240˚C for 72 hours and 220 ˚C for 24 hours, respectively.

Post-digested sample Carius tubes were frozen prior to opening and then processed via chloroform solvent extraction performed in triplicate (3.5-mL CHCl$_3$/extraction) to isolate Os followed by Os purification via microdistillation (Birck et al., 1997). Chromic-sulfuric solutions were then processed via acetone solvent extraction performed in duplicate (7.5-mL (CH$_3$)$_2$CO/extraction) to isolate Re and involved sample-solution mixtures containing 2-mL of chromic-sulfuric solution and ~7-mL of pre-cleaned concentrated (~17 N) NaOH. Rhenium was

then purified using anion exchange chromatography. Aqua regia solutions were processed using anion exchange chromatography and anion exchange single bead to separate and purify Re, respectively (Hnatyshin et al., 2016).

Purified Re and Os was loaded onto Ni and Pt filaments, respectively, and coated with $Ba(NO_3)_2$ and $Ba(OH)_2$ salts. Rhenium and osmium isotope measurements were made on a Thermo Scientific Triton Thermal Mass Spectrometer in negative polarity mode (N-TIMS) using static Faraday collectors and secondary electron multipliers. Instrument performance was monitored over a two-month period using in-house laboratory standard AB2, which yielded $^{187}Os/^{188}Os$ and $^{185}Re/^{187}Re$ ratios of 0.10680 ± 0.00018 and 0.59769 ± 0.00096 (1σ). Post-analysis data reduction included mass bias corrections, isobaric oxide corrections, blank corrections, and spike-sample unmixing (isotope dilution). Average Re and Os chromic-sulfuric acid procedural blank concentrations were 8.8 ± 6.8 pg (n = 3) and 0.2 ± 0.08 pg (n = 33) with a $^{187}Os/^{188}Os$ ratio of 0.33 ± 0.25, respectively. Average Re and Os inverse aqua-regia acid procedural blank concentrations were 1.1 ± 0.7 pg (n = 3) and 0.07 ± 0.03 pg (n = 3) with a $^{187}Os/^{188}Os$ ratio of 0.33 ± 0.07, respectively. A model 1 Re-Os isochron age (probability of fit = 0.95) was generated in IsoplotR (Vermeesch, 2018) using a ^{187}Re decay constant (1.666e11.a-1 ± 0.31%) of Smoliar et al. (1996).

2. Results

2.1 Thin section descriptions

Specimen *SPXX-m6424* is a blueschist facies graphitic iron-rich metapelite with an anthracitic appearance (Fig. B1a) identical in description to Wood's (1982) "stilpnomelane ironstones" preserved in the Laytonville Quarry exotic block. Stilpnomelane bow-tie clusters ($\leq$ 50 mm long), radial deerite (needles $\leq$ 500 μm long and 20 μm across), and cubic pyrite porphyroblasts ($\leq$ 25 mm in diameter) are embedded in a quartz-graphite-rich (~ 50% graphite by mode) groundmass (Fig. B1 and B2). The quartz groundmass is peppered with micron-sized graphite inclusions and interleaved with rhythmically folded graphite bands (Fig. B1b-d). Corroded pyrite porphyroblasts (Fig. B2b-e) show evidence of overprinting preexisting graphitic

fabric (Fig. B2c). Notably, concentric pyrite overgrowth displaced graphite into orientations that mimic successive stages of crystal growth (Fig. B2d). Coarse-grained quartz developed in pressure shadows adjacent to pyrite (Fig B2b/e) and is notably absent of graphitic carbon inclusions. This latter observation implies that the pyrite porphyroblasts are indeed a (prograde) metamorphic feature rather than a (relict) syndepositional feature. Pyrite ± chalcopyrite and sphalerite occur elsewhere as micron-sized anhedral (fragmented/corroded) crystals hosted within or surrounded by graphitic fabric. Stilpnomelane bow-ties commonly overprint preexisting graphitic fabric and display secondary oxidation (Fig. B1b). Titanite occurs as disarticulated anhedral fragments cored with deerite, whereas barite veins crosscut earlier formed graphite and stilpnomelane.
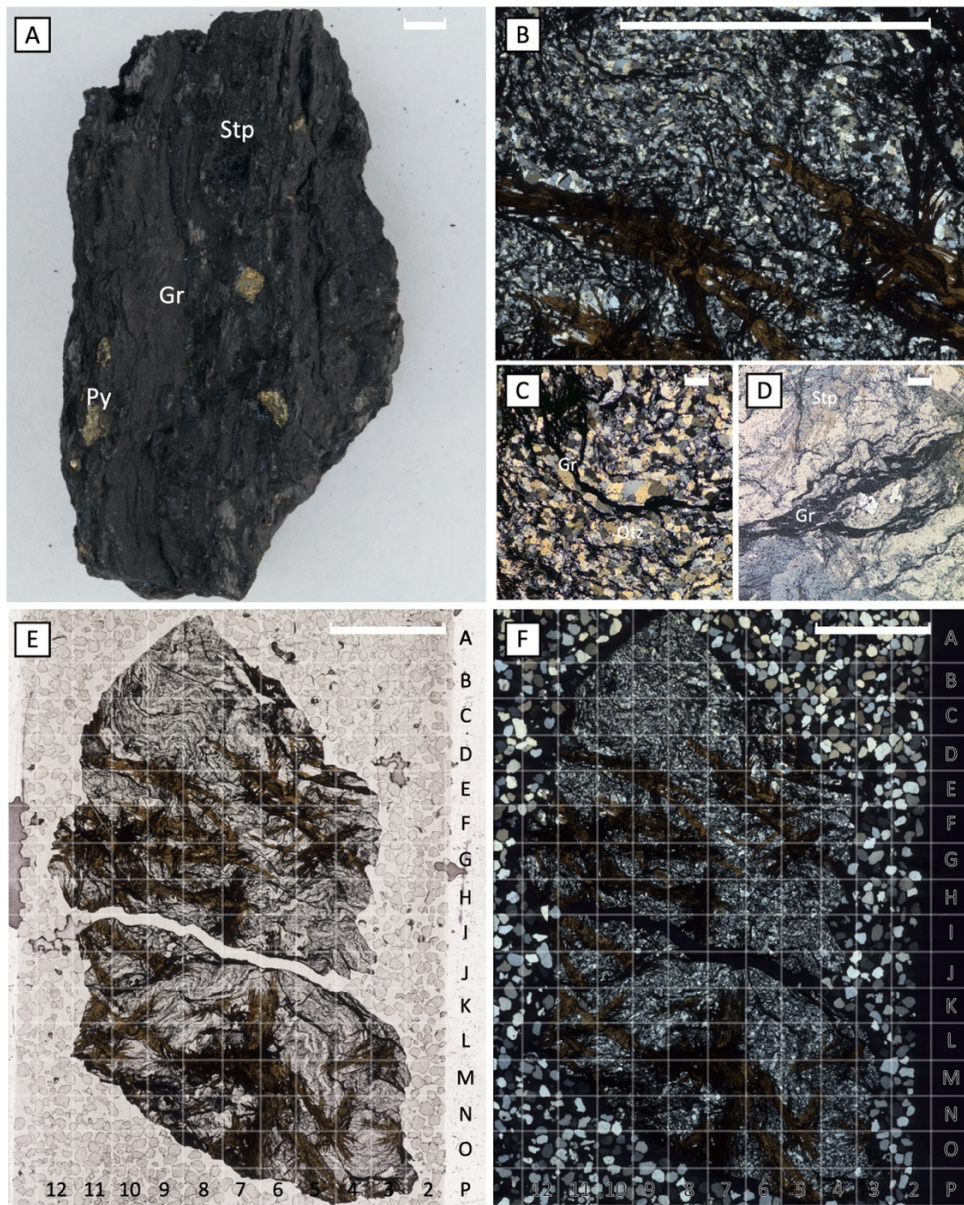
Figure B1. (A) Hand sample specimen *SPXX-m6424* showing pyrite (py) and stilpnomelane (stp) porphyroblasts embedded in a matrix of graphite (gr) and quartz (qtz). (B-C) partially oxidized stp bowtie clusters, complexly folded gr bands, and recrystallized qtz viewed under transmitted cross polarized light. (D) gr viewed under reflected plane-polarized light. (E-F) number/letter grid for microprobe spot analyses. Scale bar: (A-B/E-F) = 500 mm; (C-D) = 20 μm
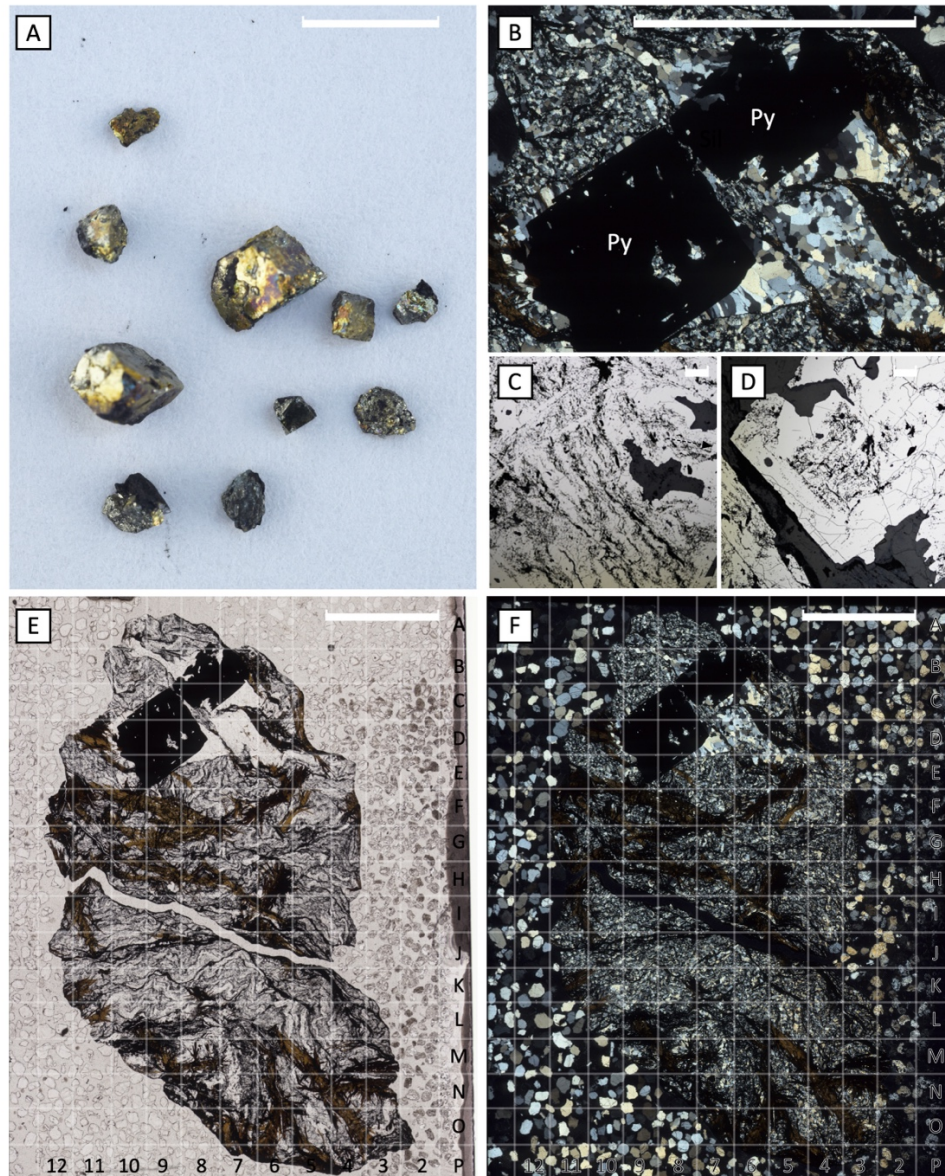
Figure B2. (A) Pyrite (py) porphyroblasts sampled from specimen *SPXX-m6424* for Re-Os geochronology. (B) Euhedral py porphyroblasts with quartz (qtz) pressure shadows viewed under transmitted cross-polarized light, (C-D) gr inclusions within py cubes, (E-F) Thin section scans showing macro-scale textural features viewed under transmitted plane- and cross-polarized light. Scale bar: (A-B/E-F) = 500 mm; (C-D) = 20 μm.

2.2 Grain mount mineralogy

Magnetic mineral separates (current < 0.49 A) of *SPXX-m6424* are primarily comprised of stilpnomelane grains at 73 to 98%, followed by graphite grains at 1 to 26%, and finally quartz

grains at < 1% (Table B2). However, the bulk of the stilpnomelane grains host inclusions of graphite (60 to 92% of stilpnomelane grains), quartz (11 to 38% of stilpnomelane grains), and pyrite-chalcopyrite (2 to 8% of stilpnomelane grains). Conversely, non-magnetic mineral separates (current > 0.49 A) of *SPXX-m6424* are dominated by quartz and graphite grains at 49 to 71% and 25 to 50%, respectively (Table B2). And 30 to 61% and <1% of these non-magnetic quartz grains host graphite and pyrite-chalcopyrite inclusions, respectively. Deerite, barite, titanite, fluorapatite, allanite, and sphalerite contribute <1% of the total grains in magnetic and non-magnetic separates.

2.3 Stilpnomelane and deerite mineralogy

Microprobe analyses of thin section *SPXX-m6424-1* (Fig. B1) identified quartz, stilpnomelane, deerite, and titanite (Fig. 3; Table B4). Stilpnomelane contained 45.2-46.8 wt.% SiO_2, 5.1-5.7 wt.% Al_2O_3, 0.4-0.9 wt.% V_2O_3, 0.1-0.3 wt.% Cr_2O_3, 30.6-31.7 wt.% FeO, 4.9-5.2 wt.% MnO, 1.5-1.7 wt.% MgO, and 0.7-1.5 wt.% K_2O. MnO and MgO contents correspond to 13 cation % Mn^{2+} and 7-8 cation % Mg^{2+}, respectively, per total R^{2+}-R^{3+} cations. Stilpnomelane MnO and MgO contents reported here are analogous to other low-Mg bearing stilpnomelane reported by Wood (1982) (Fig. B4a). The structural formula for stilpnomelane in *SPXX-m6424-1* is calculated based on 15 octahedral and tetrahedral cations and 27 anions (O, OH, F, and Cl) and is reported here as $(K_{0.22})(Fe_{4.56}Mn_{0.75}Mg_{0.40}V_{0.07}Cr_{0.02})_6(Si_{8.07}Al_{0.93})_9(O,OH)_{27}(H_2O)_{2.78}$. However, petrographic inspection of *SPXX-m6424* reveals partial stilpnomelane oxidation (Fig. B1b), and thus a ferristilpnomelane species with equal parts ferrous and ferric iron is assumed with a revised structural formula corresponding to $(K_{0.22})(Fe^{2+}_{2.28}Fe^{3+}_{2.28}Mn_{0.75}Mg_{0.40}V_{0.07}Cr_{0.02})_6(Si_{8.07}Al_{0.93})_9(O,OH)_{27}(H_2O)_{2.78}$. Deerite contained 33.7-34.3 wt.% SiO_2, 3.3-5.5 wt.% TiO_2, 0.1-0.3 wt.% Al_2O_3, 5.4-7.8 wt.% V_2O_3, 0.1-0.8 wt.% Cr_2O_3, 42.3-44.9 wt.% FeO, 3.6-4.0 wt.% MnO, 0.1-0.2 wt.% MgO, and 0.1-1.4 wt.% CaO. These V_2O_3 contents exceed all other values reported for deerite in the literature (Fig. B4b) and correspond to 29-37 cation % V^{3+} per total R^{3+} cations. Deerite MnO contents, in turn, correspond to 9-10 cation % Mn^{2+} per total R^{2+} cations. The structural formula for deerite in *SPXX-m6424-1* is calculated based on the empirical formula of

15 cation and 25 anions sites and is reported here as $(Fe^{2+}_{5.19}Mn_{0.58}Mg_{0.05}Ca_{0.03})_6$

$(Fe^{3+}_{1.38}V_{0.95}Ti_{0.56}Cr_{0.07}Al_{0.04})_3Si_{6.08}O_{20}(OH)_5$.
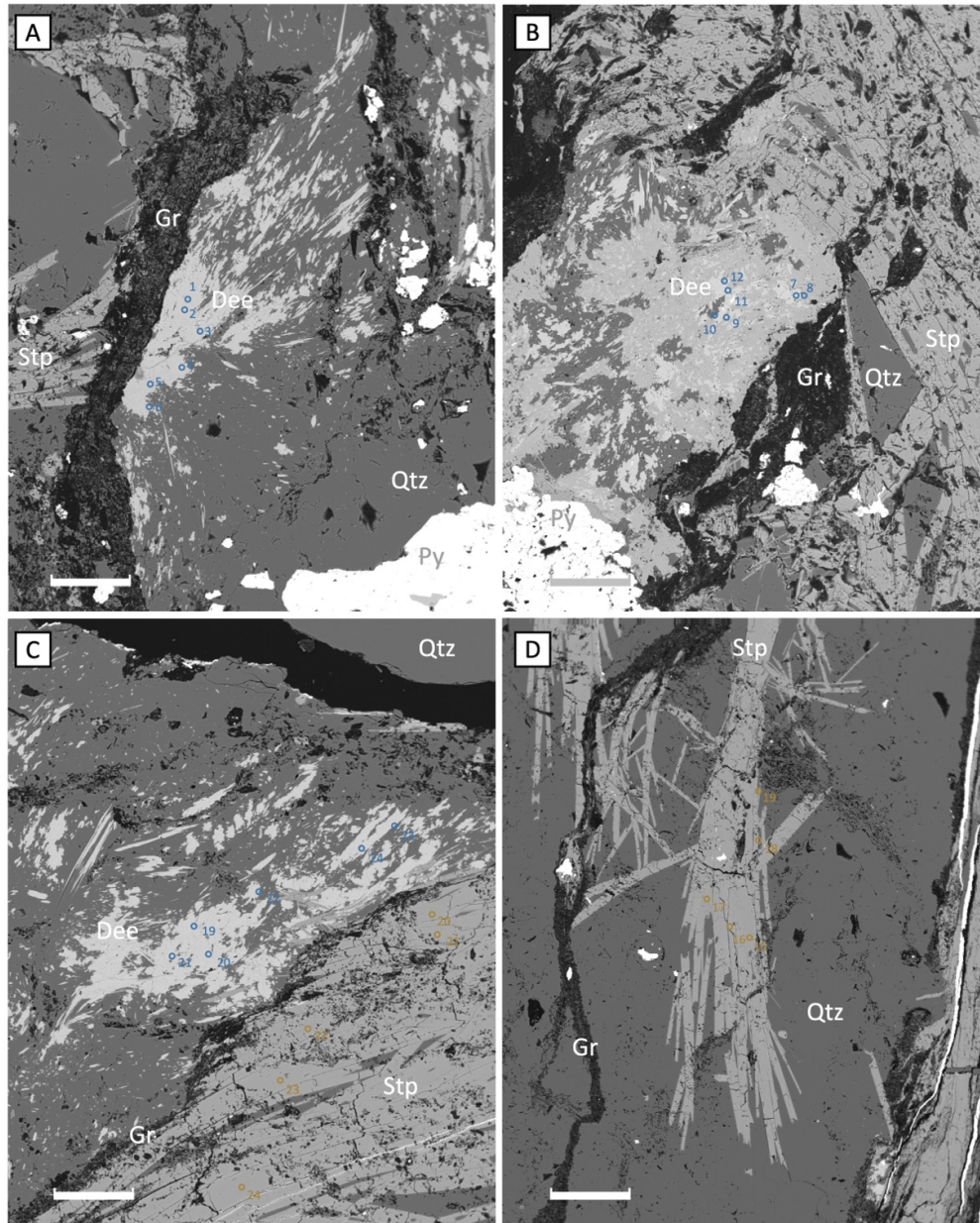
Figure B3. (A-D) BSE images depicting microprobe spot analyses of deerite (dee) and stilpnomelane (stp). (A-F) correspond to grid locations O7, O8, C11, and E4-F4, respectively, in Fig. B1F/E. Blue text = deerite. Green text = stilpnomelane. Abbreviations: py = pyrite, gr = graphite, and qtz = quartz. Scale bar = 140 μm.
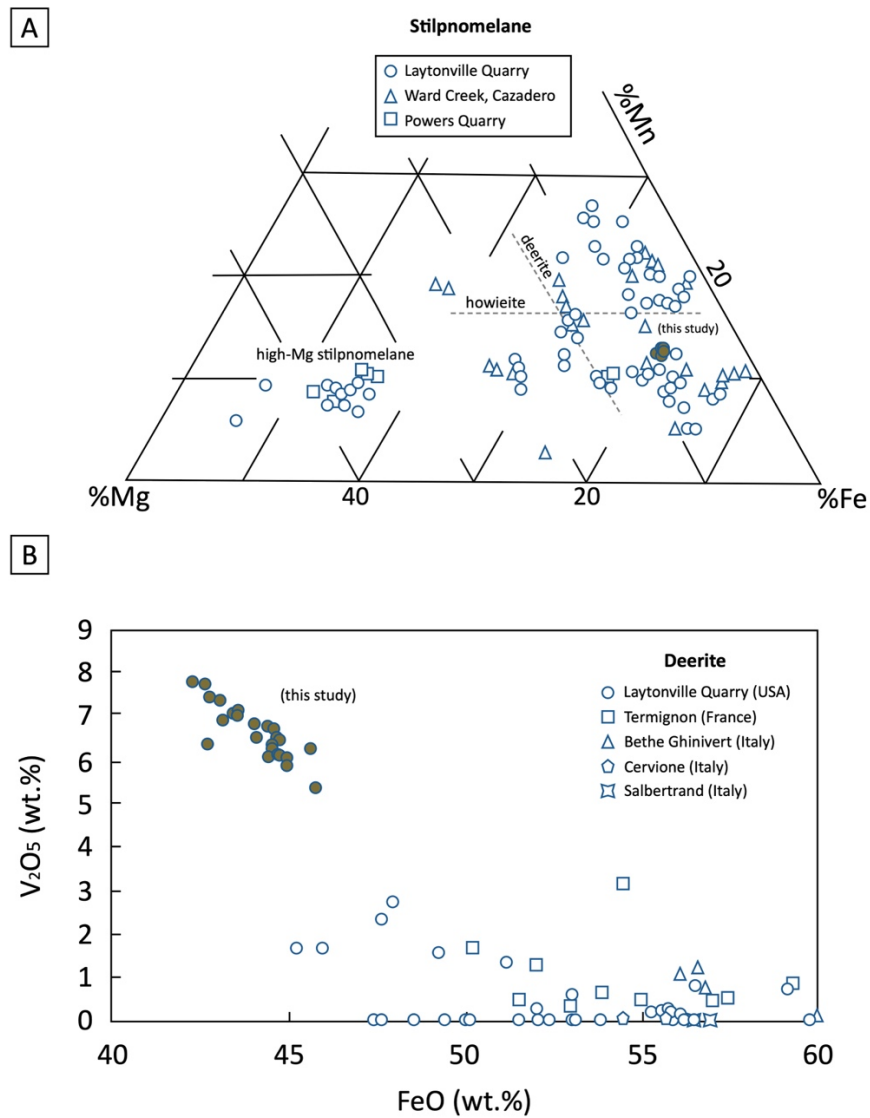
Figure B4. (A) Ternary diagram showing the variation of Mn-Mg-Fe (wt.%) content in stilpnomelane from localities in California, USA. (B) FeO and V_2O_5 (wt.%) content in stilpnomelane from localities in the USA, France, and Italy. Data in (A) and (B) sourced from Wood (1979, 1982).

2.4 $^{13}C/^{12}C$ isotopes

Carbon isotope ($^{13}C/^{12}C$) analysis of Laytonville graphite (n = 6) yielded $\delta^{13}C$ values (-34.4‰ to -26.4‰; Table B2) consistent with a sedimentary organic carbon source ($\delta^{13}C$ = ~ -20‰).

3. Interpretation

3.1 Mineral Paragenesis

The inferred protolith of the Laytonville metapelites are East Pacific Rise spreading ridge sediment interstratified with organic-rich layers and overlying mid-ocean ridge basalts. According to Wood (1982), Laytonville metapelites (formerly described as "meta-ironstones") record a complex history of subduction metamorphism that resulted in multiple paragenetic stages of mineral growth and replacement. The first stage involved early prograde development of aegirine and garnet followed by secondary mineral growth of deerite and zussmanite through late-forming hydration reactions (Wood, 1982) (Fig. B5). Graphitization and pyrite (± chalcopyrite and sphalerite) recrystallization similarly preceded retrogression (Fig. B5). Deerite growth was accompanied by quartz recrystallization (Fig. B5). Hydration continued at lower pressure conditions with the formation of howieite, stilpnomelane, riebeckite, and a more manganous variety of zussmanite (Wood, 1982) (Fig. B5). During this second hydrous event, stilpnomelane formed a "late-stage bloom" replacing earlier forming garnet and amphibole (Wood, 1982). Stilpnomelane overgrew pre-existing graphite at this time and was subsequently oxidized to the ferristilpnomelane species (Fig. B5). A final hydrous mineral growth event resulted in barite, ekmanite, and minnesotaite formation (Wood, 1982) (Fig. B5).
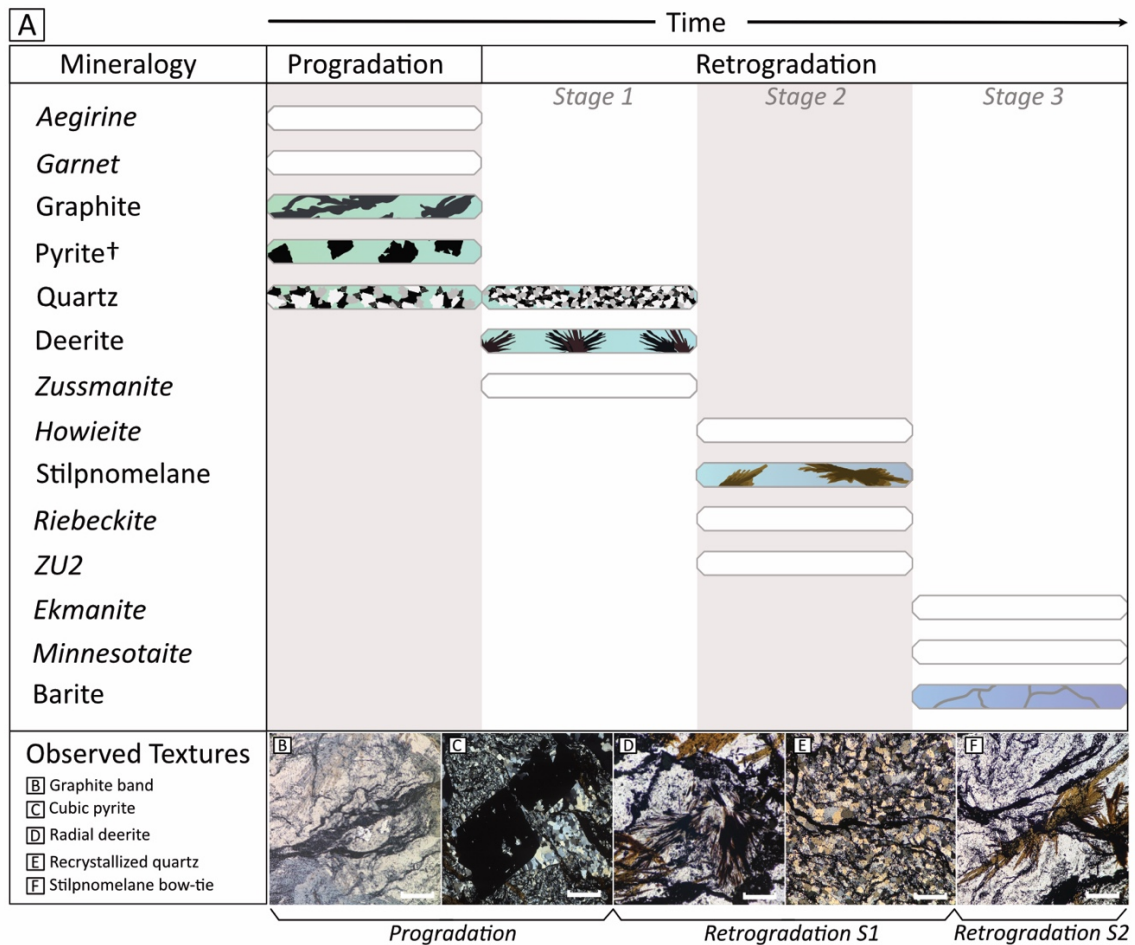
Figure B5. (A) Paragenetic sequence of prograde and retrograde mineral growth during Franciscan subduction and exhumation. (B-F) Thin section photomicrographs depicting textural evidence of progradation (B-C) and retrogradation (D-F) viewed under reflected (B) and transmitted light (C-F). Scale bar = 20 μm. †Includes chalcopyrite and sphalerite.

3.2 Graphite Re-Os systematics

Graphite Re-Os systematics for *SPXX-m6424* are strongly controlled by bulk mineralogy. Mineral separates, for example, with high magnetic susceptibility (<1.00 A) are dominated by polymineralic phases (stilpnomelane, deerite, graphite, and quartz) and yield Re/Os ratios that deviate from a well-defined isochron produced from mineral separates with low magnetic susceptibilities (≥1.00 A) and more monomineralic phases (graphite and quartz). Presumably,

the anisochroneity in these former mineral separates is tied to the presence of late-forming iron silicates, notably stilpnomelane, that commonly include graphite grains and show evidence of secondary oxidation (*see section B2.1 and B2.3*). Stilpnomelane oxidation plausibly accounts for the difference in $^{187}Os/^{188}Osi$ values observed in high (0.13 and 0.29) and low (0.19) magnetic susceptibility mineral separates. The $^{187}Os/^{188}Osi$ values observed in isochronous mineral separates is similarly replicated in individually analyzed pyrite porphyroblasts (0.19) and provide support for this interpretation. There is also a clear deviation from the regression line in mineral separates with higher modal percentage of silicates (stilpnomelane ± deerite ± quartz) with graphite inclusions (Fig. B6).
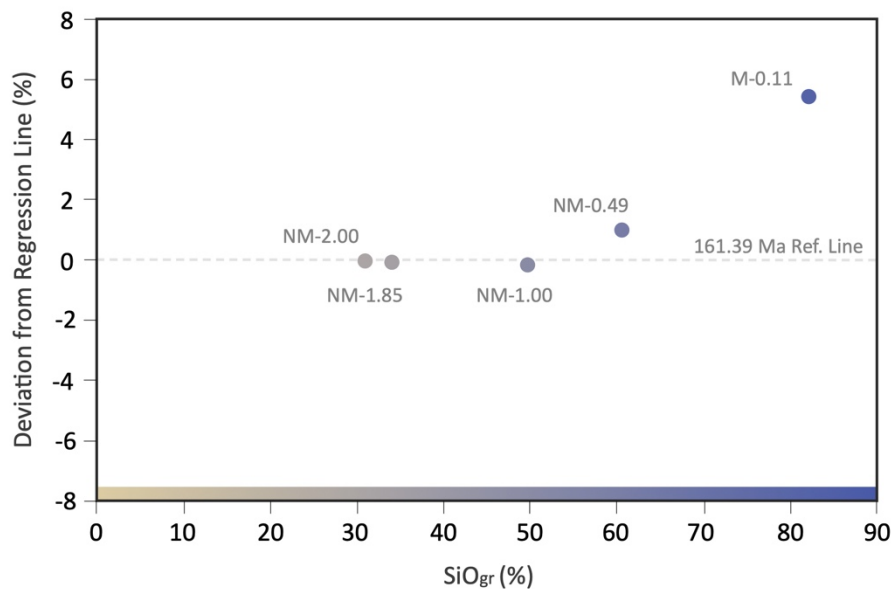
Figure B6. Mineral separate modal percentage (SiO$_{gr}$) data plotted against deviation in Re/Os model ages from a regression line defined at 161.39 Ma with an $^{187}Os/^{188}Osi$ value of 0.193. Mineral separates with >50% SiO$_{gr}$ deviate from the regression line and contain more stilpnomelane and deerite than mineral separates with <50% SiO$_{gr}$. SiO$_{gr}$ = silicates with graphite inclusions.
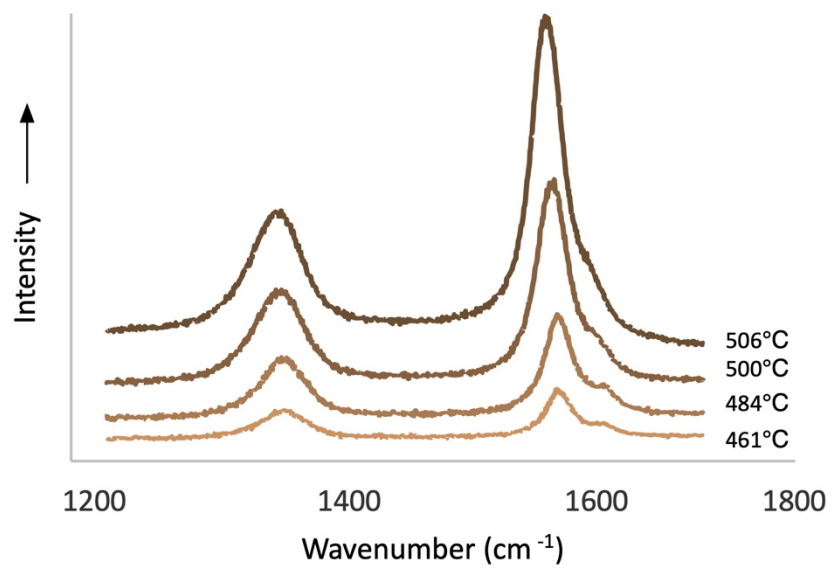
Figure B7. First-order Raman spectra of Laytonville Quarry graphite separate SPXX-m6424-NM-2.00. Refer to Table A2 for D1-band and G-band peak amplitudes.

4. Modelling global Os fluxes in subduction zones

The global Os flux from subducted sedimentary carbon (C_{org}) was calculated using a global subducted C_{org} flux of $1.1 \cdot 10^{13}$ g/yr (Clift et al., 2017) and an average TOC of 2.69 wt.% (O'Brien and Slatt, 1990) and an average Os concentration of 586 pg/g (Dubin and Peucker-Ehrenbrik, 2015) in shales. The amount of radiogenic Os entering subduction zones from C_{org} was calculated from an $^{187}Os/^{188}Os$ ratio of ~1.0 that was assumed to be inherited from modern-day seawater at the time of deposition and the ^{187}Os atom percentage calculated therefrom (Woodhouse et al., 1999).

Conversely, the global Os flux from oceanic crust was modelled by first calculating the global flux of oceanic crust being subducted annually. Here, we assumed that the annual production of new mid-ocean ridge basalt (MORB) is balanced by the consumption of older MORB at subduction zones. Assuming a MORB production rate of 3 km^2/yr (Hofmann and White, 1982), an average oceanic crustal thickness of 7 km (White et al., 1992), and MORB density of 3.3 g/cm^3 yields an annual MORB consumption rate of $6.93 \cdot 10^{13}$ g/yr. The total Os flux from subducted oceanic crust was then calculated from the global flux of subducted oceanic crust and MORB with an average Os value of 8 ppt and $^{187}Os/^{188}Os$ ratio of 0.133 (Gannoun et al., 2007).

For the quantity of Os released from graphite in a block of Laytonville quarry rock, we assumed a block 1km x 1km x 10m containing 24 wt. % graphite (density 2.27 g/cm^3) having the maximum [Os] of 85 ppb. This contains 0.58g Os with $^{187}Os/^{188}Os$ = 0.1953, which if mixed with 1 km^3 peridotite (density 3.2g/cm^3) containing 0.15 ppb Os with $^{187}Os/^{188}Os$ = 0.129, yields a mixed product with $^{187}Os/^{188}Os$ = 0.164 as shown in Figure 3.3. Using an average [Os] graphite value (33.1 ppb Os), in contrast, yields a mixed mantle with $^{187}Os/^{188}Os$ = 0.150 when using the same model parameters.

Table B1: Re-Os graphite and pyrite data for SPXX-m6424

[a]Sample	Re (ppb)	±	Os (ppt)	±	192Os (ppt)	^{187}Re/^{188}Os	±	^{187}Os/^{188}Os	±	rho	^{187}Os/^{188}Os$_i$[b]
Whole rock	515.5	1.7	19979	29	7812	131.3	0.4	0.5559	0.0008	0.182	0.20
M-0.11†	345.0	1.1	11168	16	4318	159.0	0.5	0.6469	0.0008	0.197	0.21
M-0.49†	560.3	1.9	21018	47	8209	135.8	0.5	0.5648	0.0018	0.191	0.20
NM-1.00	2412.6	8.0	85858	124	33465	143.4	0.5	0.5811	0.0008	0.179	0.19
NM-1.85	820.5	2.7	31529	43	12334	132.3	0.4	0.5516	0.0007	0.183	0.19
NM-2.00	741.5	2.5	28900	59	11313	130.4	0.5	0.5466	0.0016	0.150	0.19
py-1	198.5	0.9	6813	10	2651	149.0	0.7	0.5968	0.0008	0.135	0.19
py-2	225.1	0.8	5950	12	2279	196.5	0.7	0.7244	0.0015	0.322	0.19

aSample nomenclature is as follows: name/location/year/sample#/magnetic/non-magnetic-current

bCalculated from Re/Os isochron ages or inferred mineralization ages

†rejected from isochron *(refer to supplementary text for details)*

Table B2: Graphite C isotopes

Sample	$\delta^{13}C_{VPDB}$(‰)	±[a]
Whole rock	-26.4	
M-0.11	-30.9	
M-0.49	-34.4	<0.2‰
NM-1.00	-30.2	
NM-1.85	-30.3	
NM-2.00	-30.0	

a2s sd

Table B3: Raman Spectroscopy of carbonaceous material for SPXX-m6424

	D1				G				D2							
Sample	Peak Height	Peak Center	FWHM	Area	Peak Height	Peak Center	FWHM	Area	Peak Height	Peak Center	FWHM	Area	R1	R2	[a]T(°C)	[b]T(°C)
NM-2.0-1	63.61	1338.17	46.05	3859.72	194.69	1565.25	28.88	7408.62	32.89	1603.51	21.52	932.472	0.33	0.32	500	478
NM-2.0-2	12.11	1340.47	40.35	643.834	25.19	1569.24	30.13	1000.01	6.25	1606.47	21.51	177.251	0.48	0.35	484	476
NM-2.0-3	18.59	1341.46	41.22	1009.66	55.07	1566.7	28.02	2033.31	9.82	1600.56	21.94	283.809	0.34	0.30	506	495
NM-2.0-4	9.41	1350.65	45.11	559.583	23.25	1577.72	26.28	805.109	4.57	1606.95	3.37	20.3029	0.40	0.40	461	403

aTemperature estimated from Beyssac et al. (2002)

bTemperature estimated from Rahl et al. (2005)

Table B4: Description of mineral separates

Mineral Separate	Modal Abundance			
	Graphite[a]	Stilpnomelane	Quartz	SiO$_{Gr}$[b]
M5-0.11	0.60	16.11	0.00	82.08
M0-0.49	24.88	3.00	12.08	60.63
NM0-1.00	28.23	0.20	20.97	49.60
NM0-1.85	51.25	0.10	14.64	33.94
NM0-2.00	50.05	0.10	18.68	30.88

aGraphite = grains with ≥50% surface area of graphite

bSiO$_{Gr}$ = silicates with graphite inlcusions

Table B5: Microprobe Analysis for SPXX-m6424

No.	1	2	3	4	5	6	7	8	9	10	11	12	13	14	15	16	17	18	19	20	21	22	23	24	Average	Standard Dev
Ref. Location[a]	O7	O7	O7	O7	O7	O7	O7	O8	O8	O8	O8	O8	H7	H7	H7	H7	E4	E4	C11	C11	C11	C11	C11	C11		
Mineral	Deerite	Deerite	Deerite	Deerite	Deerite	Deerite	Deerite	Deerite	Deerite	Deerite	Deerite	Deerite	Deerite	Deerite	Deerite	Deerite	Deerite	Deerite	Deerite	Deerite	Deerite	Deerite	Deerite	Deerite		
SiO2	34.07	34.09	34.17	34.20	34.02	33.77	33.94	34.19	33.68	34.09	34.17	33.73	34.24	34.30	33.98	34.14	34.28	34.34	34.10	34.18	34.31	34.27	34.20	34.28	34.11	0.18
TiO2	3.75	4.80	4.18	4.94	4.09	4.44	4.60	4.03	5.48	4.36	4.11	3.60	3.89	4.22	3.44	3.34	4.29	4.31	3.93	4.62	4.60	3.85	4.34	3.34	4.19	0.52
ZnO	0.04	0.00	0.03	0.04	0.03	0.15	0.03	0.06	0.00	0.08	0.04	0.04	0.06	0.04	0.04	0.00	0.00	0.00	0.04	0.04	0.00	0.00	0.03	0.04	0.03	0.02
Al2O3	0.21	0.13	0.15	0.12	0.16	0.15	0.19	0.27	0.17	0.16	0.19	0.22	0.25	0.18	0.19	0.17	0.16	0.14	0.15	0.12	0.13	0.18	0.15	0.18	0.17	0.04
V2O3	6.29	7.79	7.16	7.82	6.73	6.94	6.10	6.07	6.37	5.89	6.29	6.13	5.39	6.14	6.80	6.55	7.09	6.54	6.85	7.47	7.40	6.38	7.05	6.49	6.66	0.61
Cr2O3	0.08	0.68	0.61	0.75	0.27	0.58	0.25	0.10	0.41	0.21	0.51	0.53	0.30	0.47	0.67	0.79	0.78	0.57	0.56	0.59	0.61	0.11	0.52	0.65	0.48	0.22
FeO	45.59	42.60	43.55	42.26	44.57	43.12	44.41	44.94	42.68	44.93	44.50	44.72	45.74	44.66	44.39	44.63	43.41	44.08	44.01	42.73	43.03	44.52	43.54	44.71	44.06	0.96
MnO	3.86	3.72	3.90	3.78	3.83	3.74	3.93	3.89	3.62	3.86	3.80	3.87	4.05	4.04	3.91	3.86	3.75	3.73	3.98	3.85	3.80	3.82	3.90	3.87	3.85	0.10
MgO	0.15	0.20	0.20	0.17	0.21	0.20	0.18	0.18	0.16	0.18	0.18	0.17	0.19	0.18	0.18	0.19	0.16	0.17	0.17	0.19	0.19	0.17	0.14	0.16	0.18	0.02
CaO	0.00	0.03	0.05	0.03	0.04	0.03	0.30	0.25	1.42	0.34	0.42	0.23	0.00	0.00	0.02	0.02	0.02	0.00	0.02	0.02	0.02	0.00	0.01	0.00	0.14	0.30
Na2O	0.00	0.00	0.00	0.00	0.04	0.00	0.00	0.00	0.00	0.00	0.00	0.03	0.00	0.00	0.00	0.00	0.00	0.00	0.00	0.00	0.00	0.00	0.00	0.00	0.00	0.01
K2O	0.00	0.02	0.00	0.02	0.02	0.00	0.00	0.00	0.01	0.00	0.00	0.05	0.01	0.00	0.00	0.00	0.00	0.00	0.00	0.00	0.00	0.00	0.00	0.00	0.01	0.01
P2O5	0.00	0.00	0.00	0.00	0.00	0.00	0.00	0.00	0.00	0.00	0.00	0.00	0.00	0.00	0.00	0.00	0.00	0.00	0.00	0.00	0.00	0.00	0.00	0.00	0.00	0.00
O	0.72	0.30	0.47	0.24	0.61	0.51	0.59	0.65	0.46	0.64	0.59	0.79	0.73	0.55	0.68	0.67	0.41	0.47	0.57	0.35	0.33	0.61	0.44	0.66	0.54	0.15
H2O	4.25	4.26	4.26	4.27	4.25	4.27	4.26	4.26	4.27	4.25	4.26	4.26	4.25	4.25	4.26	4.26	4.26	4.26	4.26	4.27	4.26	4.27	4.26	4.26	4.26	0.01
TOTAL	99.01	98.62	98.73	98.64	98.87	97.78	98.78	98.89	98.73	98.99	99.06	98.34	99.13	99.03	98.56	98.62	98.61	98.61	98.64	98.43	98.68	98.18	98.58	98.64	98.67	0.30
Si apfu	6.068	6.075	6.088	6.091	6.061	6.062	6.048	6.087	5.989	6.067	6.074	6.038	6.089	6.101	6.069	6.093	6.110	6.122	6.083	6.100	6.109	6.132	6.102	6.117	6.082	0.031
Ti apfu	0.502	0.643	0.560	0.662	0.548	0.600	0.616	0.540	0.733	0.583	0.549	0.484	0.521	0.564	0.462	0.449	0.575	0.578	0.527	0.621	0.616	0.517	0.583	0.448	0.562	0.069
Zn apfu	0.005	0.000	0.005	0.006	0.004	0.004	0.004	0.007	0.000	0.010	0.005	0.006	0.008	0.005	0.005	0.000	0.000	0.000	0.006	0.005	0.000	0.000	0.004	0.006	0.004	0.003
Al apfu	0.045	0.027	0.032	0.026	0.034	0.032	0.039	0.056	0.036	0.033	0.039	0.047	0.052	0.038	0.039	0.036	0.034	0.030	0.031	0.025	0.026	0.038	0.031	0.039	0.036	0.008
V apfu	0.897	1.113	1.023	1.117	0.961	0.998	0.872	0.867	0.909	0.840	0.897	0.880	0.769	0.876	0.974	0.937	1.013	0.935	0.980	1.056	0.916	1.008	0.928	0.951		
Cr apfu	0.011	0.096	0.086	0.106	0.037	0.082	0.035	0.014	0.058	0.029	0.072	0.075	0.042	0.066	0.095	0.111	0.110	0.080	0.078	0.084	0.086	0.016	0.073	0.092	0.068	0.031
Fe apfu	6.790	6.348	6.488	6.296	6.641	6.474	6.620	6.690	6.348	6.687	6.615	6.693	6.802	6.644	6.631	6.661	6.470	6.571	6.566	6.378	6.408	6.663	6.497	6.672	6.569	0.141
Mn apfu	0.582	0.561	0.588	0.570	0.578	0.569	0.594	0.586	0.545	0.582	0.572	0.587	0.609	0.608	0.592	0.584	0.566	0.562	0.601	0.582	0.573	0.578	0.589	0.585	0.581	0.015
Mg apfu	0.040	0.053	0.053	0.045	0.055	0.053	0.047	0.048	0.042	0.048	0.049	0.045	0.051	0.049	0.051	0.043	0.046	0.046	0.049	0.051	0.045	0.038	0.043	0.047		0.004
Ca apfu	0.000	0.006	0.009	0.005	0.008	0.006	0.058	0.048	0.270	0.065	0.080	0.043	0.000	0.000	0.004	0.004	0.004	0.000	0.005	0.004	0.004	0.000	0.002	0.000	0.026	0.057
Na apfu	0.000	0.000	0.000	0.000	0.013	0.000	0.000	0.000	0.000	0.000	0.000	0.011	0.000	0.000	0.000	0.000	0.000	0.000	0.000	0.000	0.000	0.000	0.000	0.000	0.001	0.003
K apfu	0.000	0.004	0.000	0.004	0.003	0.000	0.000	0.000	0.002	0.000	0.000	0.012	0.002	0.000	0.000	0.000	0.000	0.000	0.000	0.000	0.000	0.000	0.000	0.000	0.001	0.003
P apfu	0.000	0.000	0.000	0.000	0.000	0.000	0.000	0.000	0.000	0.000	0.000	0.000	0.000	0.000	0.000	0.000	0.000	0.000	0.000	0.000	0.000	0.000	0.000	0.000	0.000	0.000
O apfu	25.000	25.000	25.000	25.000	25.000	25.000	25.000	25.000	25.000	25.000	25.000	25.000	25.000	25.000	25.000	25.000	25.000	25.000	25.000	25.000	25.000	25.000	25.000	25.000	25.000	0.000
H apfu	5.048	5.068	5.062	5.068	5.056	5.112	5.061	5.055	5.062	5.050	5.046	5.083	5.042	5.047	5.071	5.067	5.067	5.067	5.067	5.079	5.065	5.091	5.071	5.068	5.066	0.015
Si - P	14.940	14.926	14.928	14.928	14.943	14.880	14.943	14.933	14.932	14.944	14.952	14.910	14.956	14.920	14.926	14.925	14.924	14.923	14.917	14.929	14.905	14.927	14.930	14.929		

Structural Form $(Fe^{3+}_{1.19}Mn_{0.58}Mg_{0.05}Ca_{0.03})_6(Fe^{3+}_{1.38}Al_{0.04}V_{0.95}Cr_{0.07}Ti_{0.56})_5Si_{6.08}O_{25}(OH)_5$

No.	1	2	3	4	5	6	Average	Standard Dev	1	2	3	4	5	6	7	8	9	10	11	12	13	14	15	16	17	18
Ref. Location[a]	O7	O7	O7	O7	O7	O7			O7	N9	N9	N9	H7	H7	H7	H7	E4	E4	E4	E4	E4-F4	E4-F4	E4-F4	E4-F4	E4-F4	E4-F4
Mineral	quartz	quartz	quartz	quartz	quartz	quartz			stilpnomelane	stilpnomelane	stilpnomelane	stilpnomelane	stilpnomelane	stilpnomelane	stilpnomelane	stilpnomelane	stilpnomelane	stilpnomelane	stilpnomelane	stilpnomelane	stilpnomelane	stilpnomelane	stilpnomelane	stilpnomelane	stilpnomelane	stilpnomelane
SiO2	101.29	100.98	101.25	100.10	99.99	99.68	99.92	0.22	46.52	46.15	46.46	46.51	45.54	44.99	45.99	46.37	46.29	46.73	45.96	45.88	45.28	45.51	45.71	46.48	46.54	45.48
TiO2	0.00	0.00	0.00	0.00	0.00	0.00	0.00	0.00	0.00	0.00	0.00	0.00	0.00	0.03	0.00	0.00	0.00	0.00	0.04	0.02	0.00	0.00	0.00	0.00	0.00	0.00
ZnO	0.00	0.00	0.00	0.00	0.00	0.00	0.00	0.00	0.00	0.00	0.00	0.00	0.00	0.00	0.00	0.00	0.00	0.00	0.00	0.00	0.00	0.00	0.00	0.00	0.00	0.00
Al2O3	0.00	0.00	0.00	0.00	0.00	0.00	0.00	0.00	5.26	5.31	5.65	5.38	5.29	5.29	5.07	5.47	5.48	5.52	5.72	5.42	5.52	5.59	5.60	5.45	5.51	5.44
V2O3	0.00	0.00	0.00	0.00	0.00	0.00	0.00	0.00	0.39	0.59	0.34	0.38	0.41	0.52	0.56	0.53	0.42	0.40	0.67	0.47	0.73	0.87	0.33	0.30	0.40	0.52
Cr2O3	0.00	0.00	0.00	0.00	0.00	0.00	0.00	0.00	0.15	0.25	0.03	0.06	0.17	0.20	0.22	0.16	0.16	0.08	0.29	0.14	0.15	0.11	0.04	0.00	0.00	0.00
FeO	0.14	0.13	0.17	0.05	0.08	0.12	0.08	0.04	30.82	31.14	31.68	31.53	31.11	31.39	31.35	31.73	31.24	31.62	30.52	30.37	30.52	30.41	30.88	31.63	31.68	30.78
MnO	0.00	0.00	0.00	0.00	0.02	0.00	0.01	0.01	4.95	4.99	5.17	5.16	4.92	5.00	5.05	5.20	5.14	5.07	4.89	5.03	4.91	5.13	5.19	4.91	4.98	
MgO	0.00	0.00	0.00	0.00	0.00	0.00	0.00	0.00	1.53	1.58	1.50	1.55	1.72	1.54	1.54	1.51	1.60	1.59	1.47	1.50	1.48	1.45	1.51	1.53	1.64	1.57
CaO	0.00	0.01	0.00	0.00	0.00	0.00	0.00	0.00	0.00	0.00	0.00	0.00	0.00	0.00	0.00	0.01	0.00	0.02	0.00	0.00	0.02	0.00	0.00	0.00	0.00	0.00
Na2O	0.00	0.00	0.00	0.00	0.00	0.00	0.00	0.00	0.00	0.04	0.10	0.00	0.12	0.07	0.09	0.05	0.04	0.00	0.06	0.00	0.00	0.00	0.00	0.00	0.00	0.03
K2O	0.01	0.00	0.01	0.00	0.00	0.00	0.00	0.00	0.89	1.08	0.96	1.04	1.04	1.13	1.08	0.92	0.95	0.85	1.11	1.20	1.36	1.45	0.83	0.93	1.02	0.94
P2O5	0.00	0.00	0.00	0.00	0.00	0.00	0.00	0.00	0.00	0.00	0.00	0.00	0.00	0.03	0.00	0.00	0.00	0.00	0.00	0.00	0.00	0.00	0.00	0.00	0.00	0.00
O	0.00	0.00	0.00	0.00	0.00	0.00	0.00	0.00	0.00	0.00	0.00	0.00	0.00	0.00	0.00	0.00	0.00	0.00	0.00	0.00	0.00	0.00	0.00	0.00	0.00	0.00
H2O	0.00	0.00	0.00	0.00	0.00	0.00	0.00	0.00	7.90	7.86	7.86	7.86	7.86	7.83	7.85	7.85	7.87	7.87	7.88	7.90	7.86	7.87	7.89	7.86	7.87	7.88
TOTAL	101.44	101.12	101.43	100.15	100.09	99.80	100.01	0.19	98.47	99.11	99.65	99.59	98.16	97.79	98.98	99.79	99.06	99.82	98.81	97.79	97.93	98.17	97.92	99.37	99.65	97.69
Si apfu	0.999	0.999	0.998	0.999	0.999	0.999	1.00	0.00	8.513	8.421	8.447	8.457	8.359	8.304	8.407	8.436	8.444	8.486	8.393	8.431	8.324	8.348	8.402	8.469	8.459	8.374
Ti apfu	0.000	0.000	0.000	0.000	0.000	0.000	0.00	0.00	0.000	0.000	0.000	0.000	0.000	0.004	0.000	0.000	0.000	0.000	0.006	0.003	0.000	0.000	0.000	0.000	0.000	0.000
Zn apfu	0.000	0.000	0.000	0.000	0.000	0.000	0.00	0.00	0.000	0.000	0.000	0.000	0.000	0.000	0.000	0.000	0.000	0.000	0.000	0.000	0.000	0.000	0.000	0.000	0.000	0.000
Al apfu	0.000	0.000	0.000	0.000	0.000	0.000	0.00	0.00	1.134	1.142	1.210	1.152	1.144	1.102	1.140	1.172	1.179	1.181	1.231	1.174	1.196	1.209	1.214	1.170	1.180	1.181
V apfu	0.000	0.000	0.000	0.000	0.000	0.000	0.00	0.00	0.057	0.086	0.050	0.056	0.061	0.077	0.082	0.077	0.062	0.059	0.098	0.069	0.108	0.127	0.049	0.043	0.058	0.077
Cr apfu	0.000	0.000	0.000	0.000	0.000	0.000	0.00	0.00	0.022	0.035	0.005	0.009	0.025	0.029	0.032	0.023	0.023	0.011	0.042	0.020	0.021	0.016	0.005	0.000	0.012	0.010
Fe apfu	0.001	0.001	0.001	0.000	0.001	0.001	0.00	0.00	4.716	4.751	4.816	4.795	4.775	4.844	4.792	4.827	4.765	4.802	4.661	4.668	4.692	4.665	4.747	4.820	4.816	4.739
Mn apfu	0.000	0.000	0.000	0.000	0.000	0.000	0.00	0.00	0.768	0.771	0.797	0.795	0.765	0.782	0.782	0.802	0.781	0.791	0.784	0.761	0.783	0.763	0.799	0.801	0.755	0.776
Mg apfu	0.000	0.000	0.000	0.000	0.000	0.000	0.00	0.00	0.418	0.429	0.407	0.419	0.470	0.423	0.419	0.408	0.434	0.431	0.400	0.411	0.407	0.397	0.415	0.415	0.443	0.430
Ca apfu	0.000	0.000	0.000	0.000	0.000	0.000	0.00	0.00	0.000	0.000	0.000	0.000	0.000	0.000	0.000	0.000	0.000	0.004	0.000	0.000	0.004	0.000	0.000	0.000	0.000	0.000
Na apfu	0.000	0.000	0.000	0.000	0.000	0.000	0.00	0.00	0.000	0.013	0.035	0.000	0.041	0.026	0.033	0.019	0.013	0.000	0.022	0.000	0.000	0.000	0.000	0.000	0.000	0.010
K apfu	0.000	0.000	0.000	0.000	0.000	0.000	0.00	0.00	0.209	0.252	0.224	0.241	0.244	0.266	0.252	0.214	0.221	0.196	0.258	0.282	0.319	0.339	0.194	0.217	0.236	0.221
P apfu	0.000	0.000	0.000	0.000	0.000	0.000	0.00	0.00	0.000	0.000	0.000	0.000	0.000	0.000	0.000	0.000	0.000	0.000	0.000	0.000	0.000	0.000	0.000	0.000	0.000	0.000
O apfu	1.998	1.999	1.998	2.000	1.999	1.999	2.00	0.00	29.688	29.632	29.704	29.665	29.528	29.444	29.615	29.697	29.676	29.747	29.584	29.511	29.542	29.603	29.587	29.700		29.555
H apfu	0.000	0.000	0.000	0.000	0.000	0.000	0.00	0.00	9.647	9.568	9.533	9.530	9.625	9.635	9.571	9.521	9.581	9.534	9.601	9.679	9.637	9.626	9.672	9.557	9.537	9.680
Si - P	1.000	1.000	0.999	0.999	1.000	1.000	1.00	0.00	15.873	15.930	15.956	15.965	15.873	15.830	15.864								15.819	15.850	15.864	15.825	15.935	15.959	15.818

Structural Form (quartz): SiO_2

Structural Form (stilpnomelane): $(K_{0.22})(Fe^{3+}_{2.28}Mn_{1.5}Mg_{0.46}V_{0.07}Cr_{0.02})_4(Si_{8.07}Al_{0.93})_8(O,OH)_{27}(H2O)_{2.76}$

No.	19	20	21	22	23	24	Average	Standard Dev	1	2	3	Average	Standard Deviation
Ref. Location[a]	E4-F4	C11	C11	C11	C11	C11			O8	O8	O8		
Mineral	stilpnomelane	stilpnomelane	stilpnomelane	stilpnomelane	stilpnomelane	stilpnomelane			titanite	titanite	titanite		
SiO2	45.57	45.78	46.05	45.88	45.81	45.78	45.97	0.45	30.61	31.04	30.87	30.84	0.22
TiO2	0.00	0.00	0.00	0.03	0.00	0.01	0.01		36.47	33.15	33.95	34.52	1.73
ZnO	0.00	0.00	0.00	0.02	0.00	0.00	0.00	0.01	0.00	0.00	0.00	0.00	0.00
Al2O3	5.34	5.40	5.43	5.44	5.60	5.39	5.44	0.14	0.20	0.28	0.41	0.30	0.11
V2O3	0.44	0.50	0.40	0.50	0.41	0.48	0.48	0.13	2.04	2.93	2.95	2.64	0.52
Cr2O3	0.14	0.17	0.16	0.17	0.07	0.07	0.13	0.07	0.26	0.47	0.31	0.35	0.11
FeO	30.59	30.88	31.25	30.98	31.13	30.80	31.08	0.43	0.30	3.12	2.03	1.82	1.42
MnO	5.08	5.05	5.05	5.13	5.18	5.10	5.06	0.10	0.09	0.36	0.24	0.23	0.14
MgO	1.53	1.50	1.57	1.51	1.57	1.56	1.54	0.06	0.00	0.00	0.00	0.00	0.00
CaO	0.00	0.00	0.00	0.00	0.02	0.00	0.00	0.01	28.81	26.31	27.94	27.69	1.27
Na2O	0.00	0.00	0.00	0.06	0.00	0.00	0.03	0.04	0.04	0.03	0.07	0.05	0.02
K2O	1.07	0.78	0.87	0.93	0.65	0.81	1.00	0.18	0.00	0.05	0.06	0.04	0.03
P2O5	0.00	0.00	0.00	0.00	0.00	0.00	0.00	0.00	0.00	0.00	0.00	0.00	0.00
O	0.00	0.00	0.00	0.00	0.00	0.00	0.00		0.00	0.00	0.00	0.00	0.00
H2O	7.88	7.89	7.87	7.87	7.88	7.89	7.87	0.02	0.00	0.00	0.00	0.00	0.00
TOTAL	97.64	97.95	98.65	98.46	98.47	97.88	98.62	0.74	97.82	97.74	98.83	98.46	0.63
Si apfu	8.390	8.419	8.430	8.409	8.398	8.418	8.41	0.05	1.005	1.032	1.012	1.02	0.01
Ti apfu	0.000	0.000	0.000	0.000	0.005	0.000	0.00		0.900	0.829	0.837	0.86	0.04
Zn apfu	0.000	0.000	0.000	0.003	0.000	0.000	0.00		0.000	0.000	0.000	0.00	0.00
Al apfu	1.160	1.170	1.171	1.176	1.209	1.169	1.17	0.03	0.008	0.011	0.016	0.01	0.00
V apfu	0.065	0.074	0.059	0.073	0.060	0.070	0.07	0.02	0.054	0.078	0.077	0.07	0.01
Cr apfu	0.021	0.025	0.023	0.022	0.024	0.010	0.02	0.01	0.007	0.012	0.008	0.01	0.00
Fe apfu	4.711	4.750	4.785	4.748	4.773	4.737	4.76	0.05	0.008	0.087	0.056	0.05	0.04
Mn apfu	0.792	0.787	0.782	0.796	0.804	0.795	0.78	0.01	0.002	0.010	0.007	0.01	0.00
Mg apfu	0.420	0.412	0.429	0.411	0.428	0.429	0.42	0.02	0.000	0.000	0.000	0.00	0.00
Ca apfu	0.000	0.000	0.000	0.000	0.004	0.000	0.00		1.013	0.937	0.981	0.98	0.04
Na apfu	0.000	0.000	0.000	0.020	0.000	0.000	0.01	0.01	0.002	0.002	0.004	0.00	0.00
K apfu	0.251	0.183	0.202	0.217	0.151	0.191	0.23	0.04	0.000	0.000	0.000	0.00	0.00
P apfu	0.000	0.000	0.000	0.000	0.000	0.000	0.00		0.000	0.000	0.002	0.00	0.00
O apfu	29.549	29.628	29.649	29.615	29.657	29.610	29.62	0.07	4.938	4.913	4.900	4.92	0.02
H apfu	9.677	9.676	9.615	9.625	9.636	9.677	9.61	0.05	0.000	0.000	0.000	0.00	0.00
Si - P	15.810	15.820	15.881	15.872	15.836	15.819	15.89	0.05	2.999	2.999	3.000	3.00	0.00

Structural Form (stilpnomelane): $(K_{0.22})(Fe^{3+}_{2.28}Mn_{0.78}Mg_{0.40}V_{0.07}Cr_{0.02})_4(Si_{8.24}Al_{0.93})_8(O,OH)_{27}(H2O)_{2.76}$

Structural Form (titanite): $Ca_{0.93}Ti_{0.86}V_{0.07}Cr_{0.02}Fe_{0.05}Al_{0.02}Mn_{0.01}Si_{1.02}O_{4.92}$

aRefer to Fig.51e/f for reference grid
bStructural formula caluated from average apfu values

Appendix C

Supplementary Material for

Carbon cycling in Paleoproterozoic shear zones

in Northern Saskatchewan linked to Nuna assembly

Table of Contents

Other Supplementary Materials for this manuscript includes the following:

Tables C1-C5

C1 Summary of Pre-Athabasca Supergroup Geology

C1-1.1 Regional Geology

The Athabasca Basin is a sequence of Paleoproterozoic to Mesoproterozoic-aged (ca. 1.71-1.50 Ga) sedimentary units located in northern Saskatchewan and Alberta (Fig. C1) that is host to and/or contiguous with some of the highest-grade unconformity uranium deposits (ca. 1.6-1.4 Ga) in the world (Jefferson et al., 2007; Jeanneret et al., 2017). Unconformably beneath the Athabasca Supergroup is the Western Churchill Province of the Canadian Shield, which is bifurcated into the Rae (west) and Hearne (east) Provinces by the Snowbird Tectonic Zone (Hoffman, 1989). The Rae and Hearne Craton are in turn divided into a handful of Mesoarchean to Paleoproterozoic lithotectonic blocks that host several regional-scale structures and mylonitic belts that serve as the foci for many Athabasca uranium deposits (Card et al. 2007; Jefferson et al., 2007).

The Taltson Domain forms the western margin of the Rae Craton and consists of basement gneiss (ca. 3.2-2.14 Ga) and supracrustal successions (ca. 2.13-1.97 Ga) intruded by I- and S-type granites emplaced during continental arc magmatism (ca. 2.01-1.97 Ga) and Taltson orogenesis (ca. 1.94-1.92 Ga), respectively (Card et al., 2014). Thermotectonism imprinted a regional (S1-S2) gneiss fabric (greenschist- to granulite-facies) and isoclinal folding across the Taltson domain. Snowbird orogenesis (ca. 1.91-1.90 Ga) from Rae-Hearne collision resulted in further deformation (F3), upright folding, and shearing accompanied by retrograde amphibolite facies metamorphism (Morrissey et al. 2022). Clearwater granitic plutons were emplaced in the SE section of the Taltson Domain by ca. 1.85-1.82 Ga and overlap with a regional brittle reactivation event tied to far-field stresses of the Trans-Hudson orogeny (ca. 1.85-1.80 Ga) (Johnstone et al., 2021; Morrissey et al., 2022).

The Mudjatik and Wollaston Domain form a suite of Archean basement and Paleoproterozoic supracrustal rocks belonging to the Hearne Craton that were compressed into a NE-trending fold-thrust belt during Trans-Hudson orogeny (ca. 1.87-1.76 Ga). This resulted in polyphase deformation, metamorphism, and magmatism across both lithostructural units.

The Wollaston Domain consists largely of supracrustal Paleoproterozoic sedimentary rocks of the Wollaston Supergroup that were deposited along a passive margin between ca. 2.10-1.85 Ga (Jeanneret et al., 2017 and references therein). Sediment deposition was followed by burial (depth = 35 km; T = 750-825 ℃) and regionally metamorphism (ca. 1.84-1.83 Ga), nappe stacking, and under-thrusting resulting from Hearne-Superior collision. The Mudjatik Domain is in turn comprised of older Archean basement (2.78-2.60 Ga) sourced from recycled continental crust and minor supracrustal successions (Orrell et al., 1999) orientated into NE-trending thrust stacking wedge generated alongside Wollaston deformation (Jeanneret et al., 2017). Regional metamorphism was followed by exhumation and isothermal decompression (ca. 1.81-1.77 Ga) in a sinistral transpressional tectonic regime that produced the Wollaston-Mudjatik Transition Zone structural corridor.
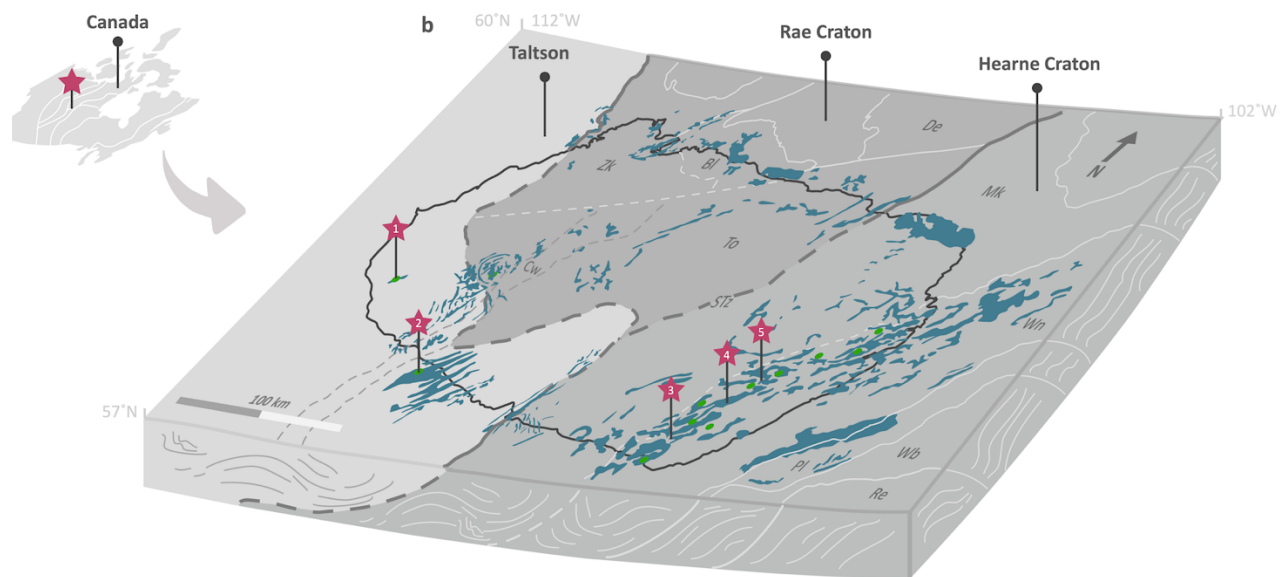
Figure C1. (a-b) Locations for drill core (red star) sampled from subsurface Precambrian basement rock in northern Alberta and Saskatchewan, Canada. (a) Sampling location relative to major lithotectonic blocks (white outlines) in Canada. (b) Graphitic-pyritic shear zones sampled (red star) in Rae (1 = Maybelle River; 2 = Patterson Lake South) and Hearne (3 = Key Lake; 4 = Christie Lake; 5 = Phoenix Deposit) basement. Blue areas = graphitic-pyritic zones inferred from EM conductors/drill core; orange dots = major U-deposits; black line = perimeter of the Athabasca Basin; dashed lines = inferred tectonic boundaries. Abbreviations: Cw = Clearwater; Zk = Zemlak, Bl = Beaverlodge, De = Dodge, To = Tantato, Mk = Mudjatik, Wn = Wollaston, STz = Snowbird Tectonic Zone; py = pyrite, gr = graphite, bt = biotite.

C1-2 Local Geology

C1-2.1 Maybelle River Shear zone

The Maybelle River shear zone is a northerly trending subvertical to vertical mylonitic belt consisting of schist and gneiss assemblages belonging to the Taltson Domain (Panǎ et al., 2007; Fig. C1). Deformation has produced an array of granitic protomylonite, mylonite, and brecciated lithologies formed under varying rheological conditions that grade with depth into brittle, brittle-ductile, and ductile regimes. Low-grade mineral assemblages (biotite, sericite, and chlorite) overprint high-grade mineral assemblages (garnet, spinel, sillimanite, and cordierite) within mylonite zones, whereas hematite-rich and clay-rich portions predominate near the basal Athabasca Supergroup contact (Panǎ et al., 2007). Basal clastics of the Athabasca Supergroup in turn host disseminated to high-grade (up to 21% U_3O_8) uranium ore within brittle fractures generated during post-Athabasca shear zone reactivation (Wheatley and Cutts, 2005).

C1-2.2 Patterson Lake Corridor

The Patterson Lake Corridor is a northeast to southwest trending high-strain zone located within the Taltson domain and is surrounded by an assortment of igneous protoliths metamorphosed to upper amphibolite to granulite facies conditions (Card, 2017; Fig. C1). Igneous assemblages are dominated by orthogneiss and metasomatized granitoids/tonalitic gneiss and lesser amounts of metamorphosed ultrabasic rocks, alkaline intrusives, carbonatite-like rocks, anatectic pegmatites, and migmatites (Card and Noll, 2016; Card et al., 2018). High-strain zones are defined by ductile (mylonites, phyllonites) to brittle lithologies (brittle fault rocks, incohesive fault breccias, cataclasites, and fault gouge) overprinted by alteration assemblages of biotite, white, mica (sericite), chlorite, hematite, and iron sulfides (Hillacre et al., 2021). Pre-Athabasca paleoweathering has bleached the upper section of the basement in contact with basal Athabasca Supergroup sedimentary units. Post-Athabasca brittle reactivation resulted in further metasomatism and brittle fracturing of basal Athabasca Supergroup sediment.

C1-S2.3 Wollaston-Mudjatik Transition Zone

The Wollaston-Mudjatik Transition Zone is a structural corridor located within the Wollaston and Mudjatik Domains (Fig. C1) that is host to a series of brittle faults spatially linked with major Athabasca uranium deposits in the area (e.g., McArthur River Phoenix, Cigar Lake). The WMTZ is characterized by felsic to tonalitic gneisses (ca. 2.73-2.70 Ga), Neoarchean granites (2.64-2.58 Ga), Paleoproterozoic supracrustal Wollaston Group sediments (ca. 2.10-1.85 Ga), and THO intrusives (ca. 1.85-1.81 Ga) deformed under high-strain conditions (Jeanneret et al., 2017). This has resulted in an assortment of ductile to brittle lithologies that follow similar depth profiles and alteration sequences (e.g., biotite, sericite, chlorite, hematite, graphite, and iron sulfides) observed elsewhere in other high-strain zones such as in the Patterson Lake Corridor and Maybelle River shear zone of the Taltson Domain.

C2 Geochronology (Re-Os and U-Pb) for Pre-Athabasca graphitic-pyritic shear zones

C2-1 Overview

Rock specimens (n = 10) were collected from drill core sampled from government core facilities (Mineral Core Research Facility in Edmonton, AB and Subsurface Geological Laboratory in Regina, SK) and/or gifted from industry collaborators (e.g., Fission Uranium Corp.). The sampling program focused on Pre-Athabasca Supergroup structures (i.e., graphitic-pyritic shear zones in Rae and Hearne basement) spatially associated with major Athabasca unconformity uranium deposits (e.g., Maybelle River Deposit, Triple R Deposit, and Phoenix Deposit) in northern Alberta and Saskatchewan, Canada (Fig. C1). From west to east, these include graphitic-pyritic mylonite/metapelite and gneiss units in Maybelle River (drill holes = MR-68 and MR-120), Patterson Lake South (drill holes = PLS14-133 and PLS14-260), and Wollaston-Mudjatik Transition (WMT) shear zones (drill holes = WR-440, GRL-133A, and CB95-057A) (Fig C2; Table C1). All Re-Os and U-Pb isotope data is reported in Tables C2 and C3. Modal abundances for mineral separates used for Re-Os dating are reported in Table C5.
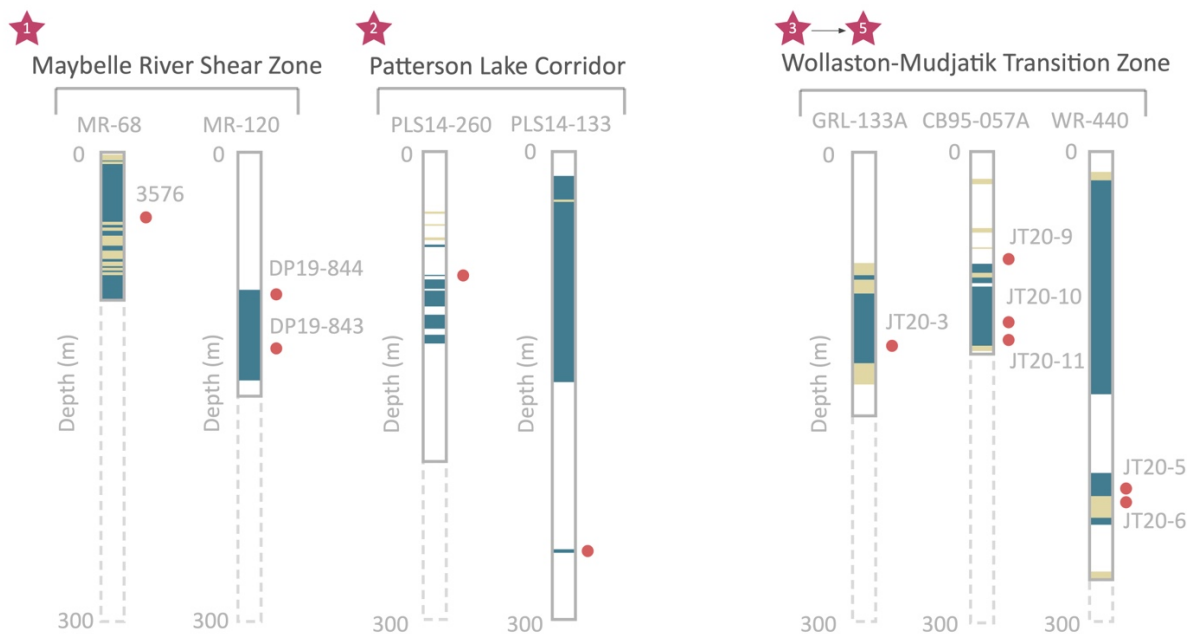
Figure C2. Drill holes intersecting Precambrian basement rock in northern Alberta and Saskatchewan, Canada. Drill core sampling depths (red circle) below unconformity (0 m) shown relative to graphitic/pyritic (blue) and pegmatitc (beige) zones. Refer to Fig. C1 for drill hole locations.

C2-2 Maybelle River Shear Zones, Taltson Basement, Western Athabasca Basin

C2-2.1 Drill hole MR-68
Sample number: 3576
Location: 58.30° N, 110.69° W
Re-Os pyrite age: 1906 ± 16.6 Ma (n =5)

Drill hole MR-68 is located 12.2 km NE of the Maybelle River Deposit (U_3O_8 grade = 5-20 wt.%) and insects Taltson basement rock at 379.6 m below surface (Wheatley and Cutts, 2005). Several 10 m intervals of strongly chloritized graphitic-pyritic gneisses were intersected in the basement. These occur as either mylonized or fault brecciated/gouged metapelites containing trace-10% graphite and 1-5% disseminated (cubic) pyrite. Massive graphite (>10%) is localized to several <5m intervals and occurs along shear planes and slickensides in fault brecciated regions with localized graphite/pyrite veining throughout. Core specimen 3576 was sampled from a chloritized mylonitic unit (41.8 m below the unconformity) containing disseminated graphite/pyrite (Fig. C2). Pyrite separates from this sample (3576-py) yield a Model 1 Re-Os isochron date of 1905.6 ± 11.6 Ma (2σ; MSWD = 0.65; n = 5; λ = 16.6 Ma) with $^{187}Os/^{188}Os$ initial ratio 0.77 ± 0.076 (Fig. C3).
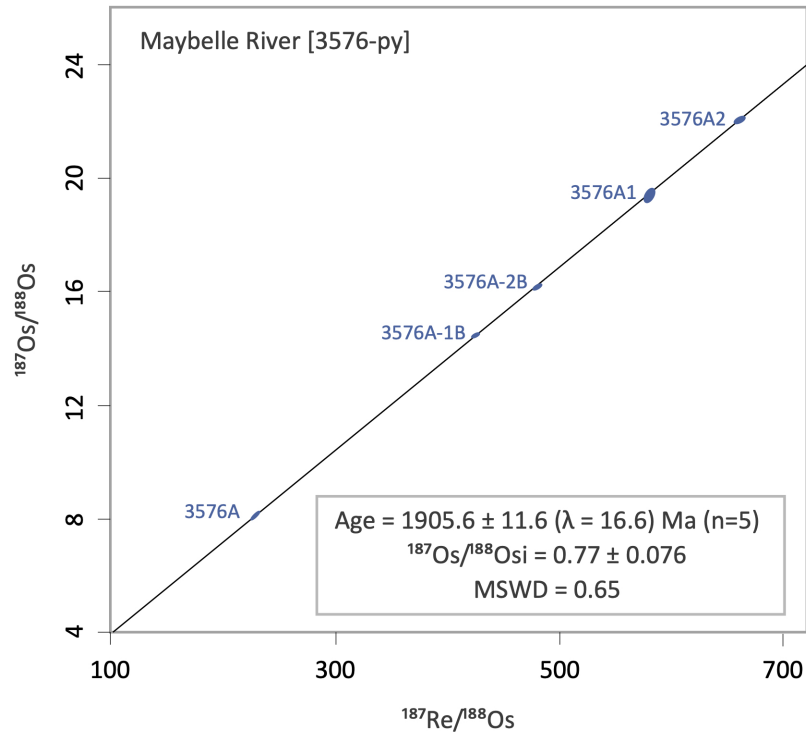
Figure C3. Re-Os pyrite Re-Os isochron date calculated in IsoplotR (Vermeesch, 2018) using the [187]Re decay constant (λ = 1.666·10[-11] ± 0.31%) of Smoliar et al. (1996) with systematic uncertainties (λ) shown in brackets. Error ellipses are reported in 2σ notation with a probability of fit >0.15. Abbreviations: py = pyrite.

C2-2.2 Drill hole MR-120
Sample number: DP19-844
Location: 58.20° N, 110.66° W
Re-Os pyrite-graphite age: 1918.33 ± 18 (n = 9)
In-situ U-Pb monazite age: 1897.05 ± 8.18 Ma (n =6)

Drill hole MR-120 is located 440 m NE of the Maybelle River Deposit (U_3O_8 grade = 5-20 wt.%) and intersects Taltson basement rock at 198.6 m below surface (Wheatley and Cutts, 2005). Mylonized granodiorite and silicified granodiorite gneiss units crosscut by a carbonate-bearing dykes and veins were intersected prior to the appearance of a 58.1 m interval of graphitic protocataclasites. This brittle-ductile interval contains unstructured granodiorite and pelitic gneiss along with mylonitic graphitic protolith. Brittle reactivation and subsequent fluid remobilization are inferred from graphite, sulfides, and quartz veins that run parallel and/or

oblique to shearing. Core sample DP19-844 was sub-sampled from a graphitic (modal percent = 5.24%) pelitic gneiss unit (89.2 m below the unconformity) within this shear zone (Fig. C2/C4).

Figure C4. Photographs (A) and thin section scans (B) of drill core DP19-844. (A) Mylonitic pelite containing disseminated pyrite. A thin veneer of slickenside (sooty) graphite is visible at the base of the core. (B) Transmitted light photomicrograph depicting euhedral pyrite porphyroblasts (≤1 mm diameter) embedded in a pelitic matrix containing 5% metamorphic graphite. Scale bar: 0.5 cm.

Pyrite mineral separates (n = 8) combined with bulk graphite (n = 1) from this core (DP19-844-py-gr) yield a Model 3 Re-Os isochron date of 1918.33 ± 18.0 Ma (2σ; MSWD = 5.8; n = 9) with $^{187}Os/^{188}Os$ initial ratios of 0.773 ± 0.028 (Fig. C5). Any anisochroneity present in the isochron cannot be linked to pyrite purity levels since both magnetic and nonmagnetic mineral separates exhibit minor deviations from the regression line. Any scatter is thus inferred to be geological (Fig. C5).
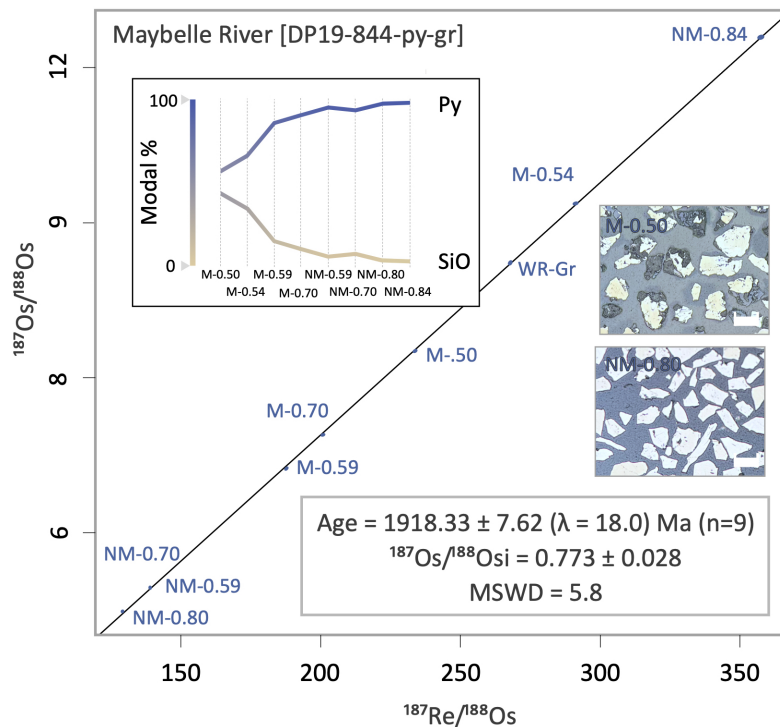
Figure C5. Re-Os pyrite- graphite isochron date calculated in IsoplotR (Vermeesch, 2018) using the [187]Re decay constant ($\lambda = 1.666 \cdot 10^{-11} \pm 0.31\%$) of Smoliar et al. (1996) with systematic uncertainties (λ) shown in brackets. Error ellipses are reported in 2σ notation with a probability of fit of 0.15. Graphical insets (a-c) depict mineral modal percentages per datapoint, whereas reflected light photomicrographs (a-c) show mineralogy/textures for datapoints with endmember (high and low) magnetic susceptibilities. Abbreviations: py = pyrite, SiO = silicates. Scale bar = 200 μm.

Monazite and zircon occur as anhedral grains (10-40 μm) within a metasomatized pelitic matrix in DP19-844. Most monazite grains are heavily corroded by adjacent sulfide (pyrite) phases. Six analyses of a single well-preserved monazite (Mnz-1) yield a weighted mean [207]Pb/[206]Pb date of 1897.05 ± 8.18 Ma (MSWD = 1.59) while X-ray mapping revealed Y zonation within zircon grains despite there being a statistically uniform U-Pb age population among spot analyses (Fig. C6). Two analyses of a single hydrothermal zircon (Zr-1) yield [207]Pb/[206]Pb dates of 1353 ± 11 Ma and 1469 ± 11 Ma (Table C4).
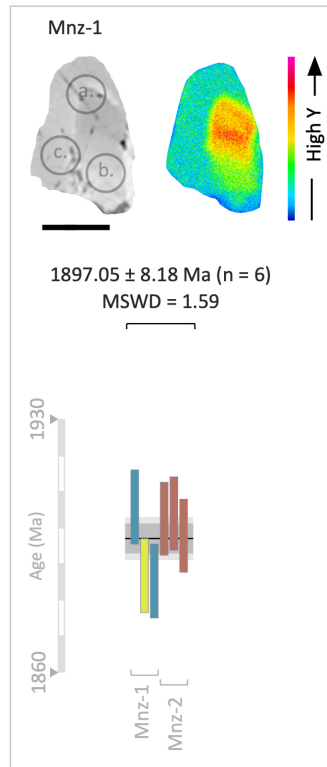
Figure C6. In-situ U-Pb monazite [207]Pb/[206]Pb weighted mean age for sample DP19-844. Errors are reported in 2σ notation. BSE images of monazite grains with laser ablation spot analyses and WDS yttrium element map. Scale bar = 20 μm.

C2-2.3 Drill hole MR-120
Sample number: DP19-843
Location: 58.20° N, 110.66° W
Re-Os pyrite age: 1807.58 ± 17.6 (n = 6)
Re-Os graphite age: 1783.16 ± 18.0 (n = 4/5)
In-situ U-Pb monazite age: 1924.37 ± 7.02 Ma (n =12/13)
In-situ U-Pb zircon age: 1908.05 ± 10.6 Ma (n =3)

Drill hole MR-120 is located 440 m NE of the Maybelle River Deposit (U_3O_8 grade = 5-20 wt.%) and intersects Taltson basement rock at 198.6 m below surface (Wheatley and Cutts, 2005). Core sample DP19-843 was sub-sampled from a mylonite unit (126.0 m below the unconformity) in the brittle-ductile regime that contains remobilized graphite and pyrite (Fig. C2/C7a). A 1-cm wide pyrite vein crosscuts DP19-843, which also bears several natural fractures

that are filled with bitumen residue. The groundmass is heavily altered to sericite and is facture-filled with several generations of quartz (Fig. C7b). Graphite (modal percent = 3.67%) contours the grain boundaries, microfractures, and foliation of altered silicate and sulfide (sphalerite) grains, whereas pyrite is present as disseminated subhedral to euhedral masses.

Figure S7. Photographs (A) and thin section scans (B) of drill core DP19-843. Mylonite crosscut by a ca. 1 cm wide pyrite vein. (B) 3.8% secondary (hydrothermal) graphite precipitated along mylonitic fabric. Scale bar: 0.5 cm

Hydrothermal pyrite and graphite mineral separates from samples DP19-843-py and DP19-843-gr yielded two statistically unresolvable Model 1 Re-Os isochron dates of 1807.58 ± 11.56 Ma (2σ; MSWD = 0.73; n = 6) and 1783.16 ± 12.39 1 Ma (2σ; MSWD = 0.48; n = 4) with uniform $^{187}Os/^{188}Os$ initial ratios of 0.724 ± 0.054 and 0.721 ± 0.035, respectively (Fig. C8/C9). This age discrepancy implies that graphite remobilization post-dates pyrite mineralization, which is supported by a pyrite-rich (33.16%) mineral separate (M-1.94) in sample DP19-843-gr that exhibits a -1.29% deviation from the isochron slope defined by graphites (Fig. C9). In

contrast, silicate impurities are present in the mineral separates of both samples and are thus assumed to have negligible influence over the Re/Os systematics (Fig. C8/C9).
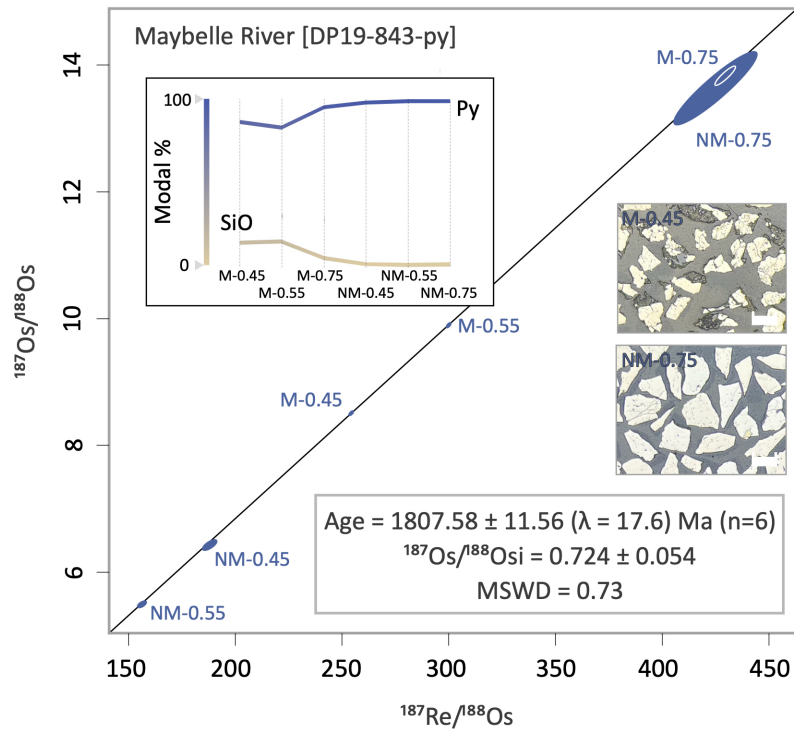
Figure C8. Re-Os pyrite isochron date calculated in IsoplotR (Vermeesch, 2018) using the [187]Re decay constant (λ = 1.666·10⁻¹¹ ± 0.31%) of Smoliar et al. (1996) with systematic uncertainties (λ) shown in brackets. Error ellipses are reported in 2σ notation with a probability of fit of 0.15. Graphical insets depict mineral modal percentages per datapoint, whereas reflected light photomicrographs show mineralogy/textures for datapoints with endmember (high and low) magnetic susceptibilities. Abbreviations: py = pyrite, SiO = silicates. Scale bar = 200 μm.
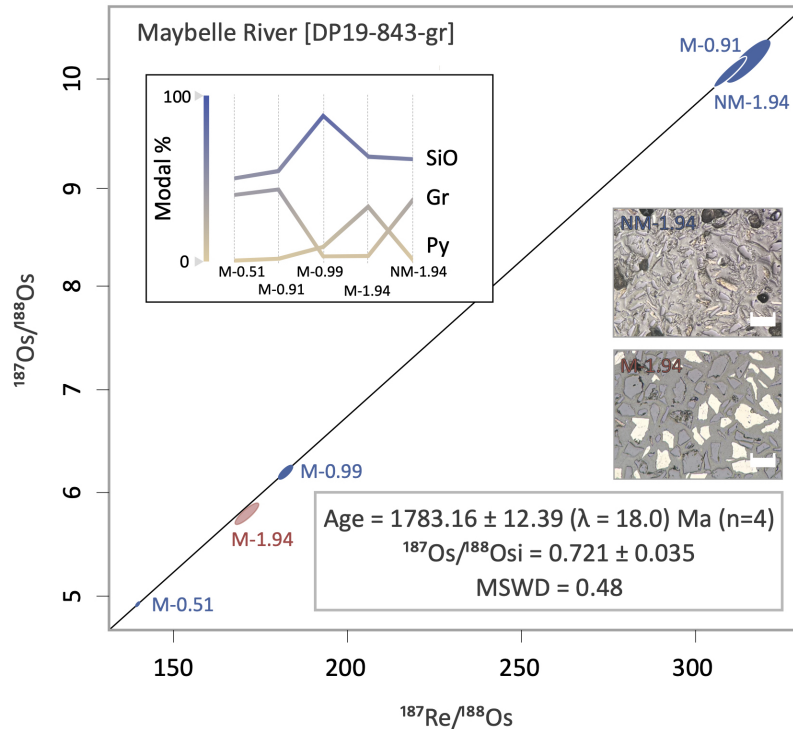
Figure C9. Re-Os graphite isochron date calculated in IsoplotR (Vermeesch, 2018) using the [187]Re decay constant (λ = 1.666·10[-11] ± 0.31%) of Smoliar et al. (1996) with systematic uncertainties (λ) shown in brackets. Error ellipses are reported in 2σ notation with a probability of fit of 0.15. Graphical insets depict mineral modal percentages per datapoint, whereas reflected light photomicrographs show mineralogy/textures for datapoints with endmember (high and low) magnetic susceptibilities. Abbreviations: py = pyrite, SiO = silicates, gr = graphite. Scale bar = 200 μm.

Monazite and zircon occur as anhedral grains (10-100 μm) within a metasomatized mylonite matrix. Several monazites are heavily corroded by contiguous sulfide (pyrite ± chalcopyrite) phases. Twelve out of thirteen analyses of three monazite grains (Mnz-1 to Mnz-3) yield a weighted mean $^{207}Pb/^{206}Pb$ age of 1924.37 ± 7.02 Ma (MSWD = 1.4) (Fig. C10). X-ray mapping of monazite revealed Y (± Ce and Th) zonation (but not U) despite there being no observable $^{207}Pb/^{206}Pb$ age differences (Fig. C10). Three analyses of a single zircon (Zr-1) yield a weighted mean $^{207}Pb/^{206}Pb$ age of 1908.05 ± 10.6 Ma (MSWD = 0.21) (Fig. C10).
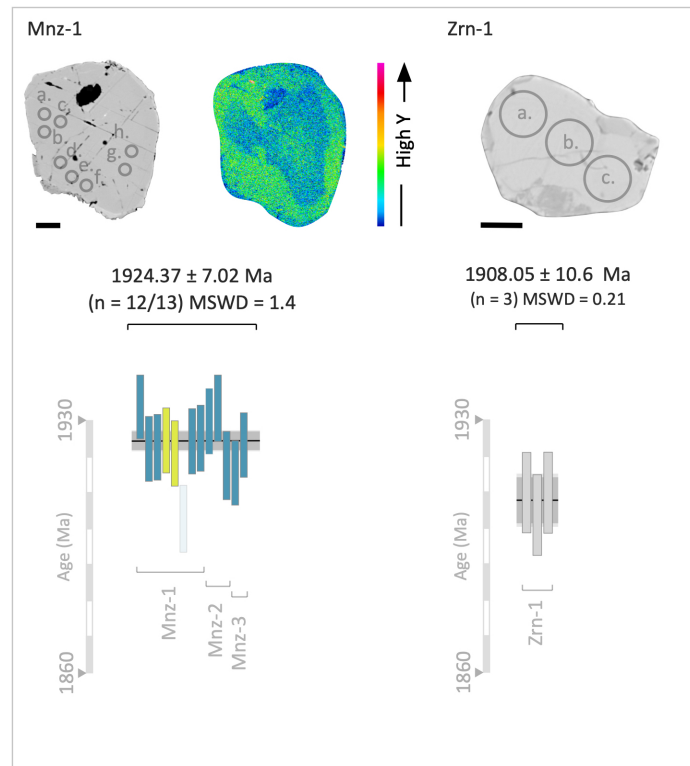
Figure C10. U-Pb monazite and zircon ^{207}Pb/^{206}Pb weighted mean ages for sample DP19-843 (Maybelle River). Errors are reported in 2σ notation. Rejected outliers shown in translucent light grey. BSE images of zircon and monazite grains with laser ablation spot analyses and EDS yttrium element map for monazite. Scale bar = 20 μm.

C2-3 Patterson Lake South Shear Zones, Taltson Basement, Southwestern Athabasca Basin

C2-3.1 Drill hole PLS14-133
Sample number: PLS14-133-316
Location: 57.63° N, 109.36° W
Re-Os pyrite age: 1939.88 ± 19.00 Ma (n =8)

Drill hole PLS14-133 is located within the perimeter of the Triple R Uranium Deposit (U_3O_8 grade = 2.18 wt.%) at Patterson Lake South (Fig. C2) and intersects Taltson basement rock 50.0 m below surface (Fission Uranium Corp, 2022). Lithology intersected at this location include ~150 m of graphitic (± garnet) gneiss and ~150 m of quartz-feldspar-biotite-garnet gneiss. Core specimen PLS14-133-316 was sampled from a pyrite-bearing gneissic unit (266.0 m below the unconformity) and exhibits evidence of sericite alteration and quartz and pyrite veining (Fig. C11). Anhedral to euhedral pyrite is common throughout the hand specimen and forms the dominant mineral phase at 80% by volume.
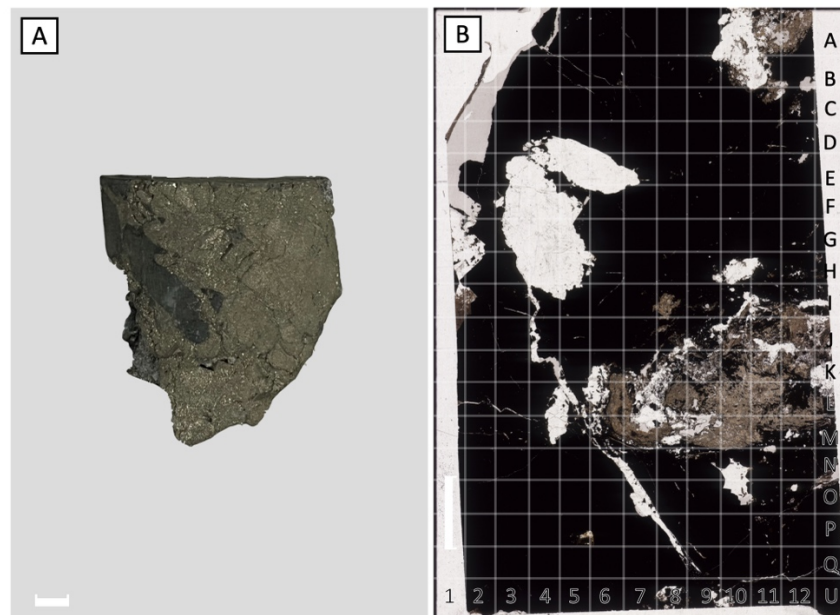
Figure C11. Photograph (A) and thin section scan (B) of drill core PLS14-133-360. (a) Coarse-grained massive pyrite. (B) Transmitted-light photomicrograph depicting pyrite (black) and silicate groundmass. Scale bar: 0.5 cm.

Pyrite mineral separates for sample PLS14-133-py yield a Model 3 Re-Os isochron date of 1939.88 ± 12.65 Ma (2σ; MSWD = 3.1; n = 8) with $^{187}Os/^{188}Os$ initial ratios of 1.955 ± 0.084 (Fig. C12).
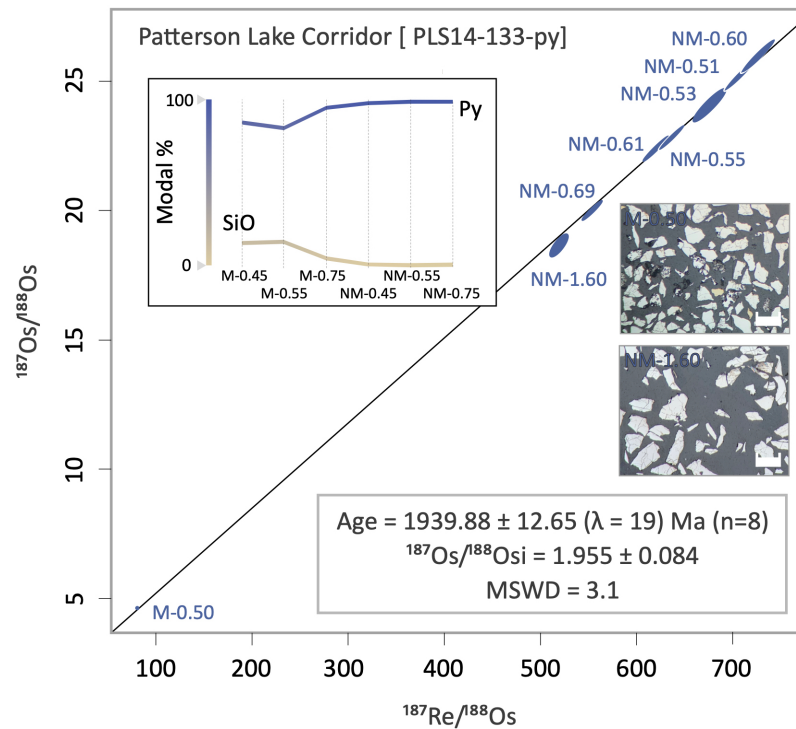
Figure C12. Re-Os graphite isochron date calculated in IsoplotR (Vermeesch, 2018) using the ^{187}Re decay constant (λ = 1.666·10^{-11} ± 0.31%) of Smoliar et al. (1996) with systematic uncertainties (λ) shown in brackets. Error ellipses are reported in 2σ notation with a probability of fit of 0.15. Graphical insets depict mineral modal percentages per datapoint, whereas reflected light photomicrographs show mineralogy/textures for datapoints with endmember (high and low) magnetic susceptibilities. Abbreviations: py = pyrite, SiO = silicates. Scale bar = 200 μm.

C2-3.2 Drill hole PLS14-260
Sample number: PLS14-260-97.5
Location: 57.56° N, 109.13° W
Re-Os pyrite-graphite age: 1883.19 ± 14.31 Ma (n =8)
In-situ U-Pb zircon age: 1902.73 ± 8.31 (n = 7)

Drill hole PLS14-260 is located 2.0 km SE of the Triple R Uranium Deposit (U_3O_8 grade = 2.18 wt.%) at Patterson Lake South and intersects Taltson basement rock 11.68 m below surface (Fission Uranium Corp., 2022). Lithology intersected at this location includes anatectic pegmatites, graphitic-sulfidic pelitic gneisses (22 m), and orthogneisses. Core specimen PLS14-260 was sampled from a graphitic-sulfidic pelitic gneiss units 85.6 m below the unconformity. This metapelitic contains a heavily altered groundmass dominated by chlorite and sericite. Secondary graphite (modal percent = 15.30%) and pyrite (modal percent = 15.30%) are present as anastomosing vein networks parallel to the rock fabric. The co-precipitation of graphite (flaky) and pyrite (cubic) is evidenced through the interfingering of graphite-pyrite veins. Molybdenite is present at the trace-level (<1 modal %) alongside the boundaries of a few graphite and pyrite grains.
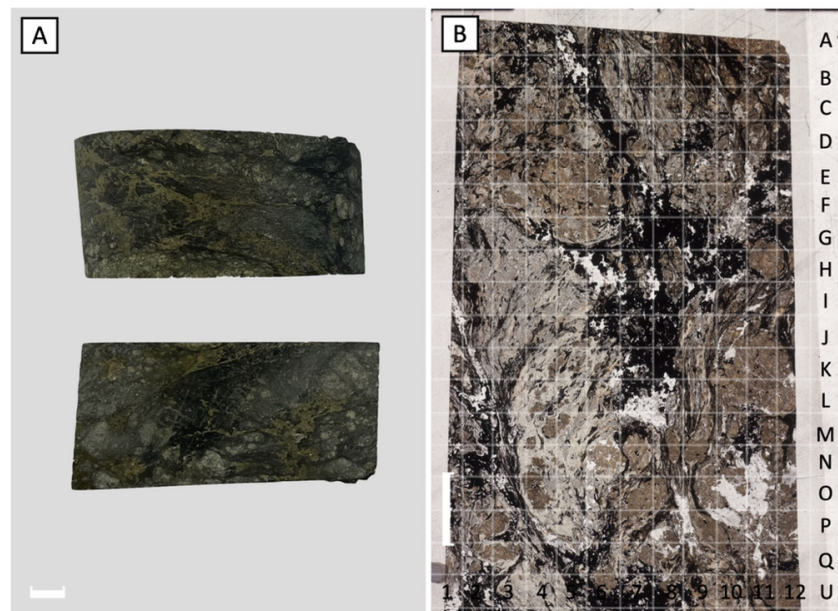
Figure C13. Photograph (A) and thin section scan (B) of drill core PLS14-260-97.5. (A) Chloritized metapelite crosscut by pyrite/graphite veins. (B) Transmitted-light photomicrograph depicting pyrite/graphite (black) and silicate groundmass. Scale bar: 0.5 cm.

Pyrite mineral separates combined with bulk graphite from sample PLS14-260-py-gr yield a Model 3 Re-Os isochron date of 1883.19 ± 3.69 Ma (2σ; MSWD = 2.6; n = 8) with an $^{187}Os/^{188}Os$ initial ratio of 0.5812 ± 0.017 (Fig. C14). Silicate impurities present in the magnetic and non-magnetic mineral fractions of this sample implies negligible influence over the Re/Os systematics (Fig. C14).
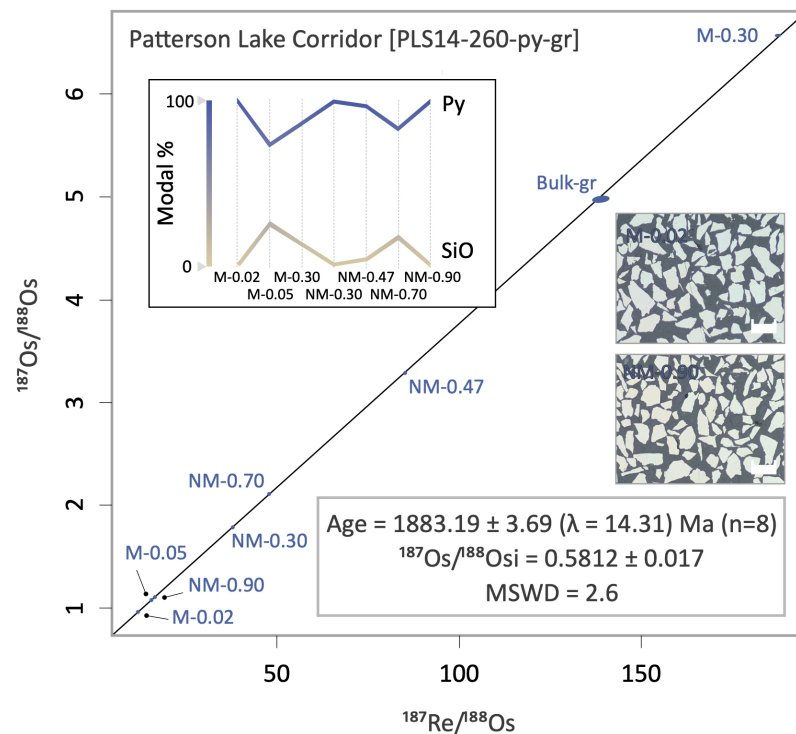
Figure C14. Re-Os graphite isochron date calculated in IsoplotR (Vermeesch, 2018) using the ^{187}Re decay constant (λ = 1.666·10^{-11} ± 0.31%) of Smoliar et al. (1996) with systematic uncertainties (λ) shown in brackets. Error ellipses are reported in 2σ notation with a probability of fit of 0.15. Graphical insets depict mineral modal percentages per datapoint, whereas reflected light photomicrographs show mineralogy/textures for datapoints with endmember (high and low) magnetic susceptibilities. Abbreviations: py = pyrite, SiO = silicates. Scale bar = 200 μm.

Zircon occurs as subhedral to anhedral grains (10-60 μm) in matrix. Seven analyses of a single zircon grain (Zrn-1) yield a weighted mean ^{207}Pb/^{206}Pb date of 1902.73 ± 8.31 Ma (MSWD = 1.75) (Fig. C15).
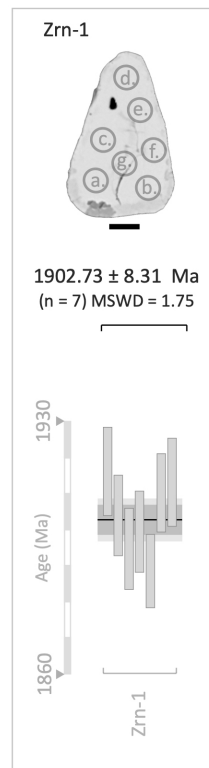
Figure C15. U-Pb zircon ^{207}Pb/^{206}Pb weighted mean ages for sample PLS14-260-97.5 (Patterson Lake South). Errors are reported in 2σ notation. Scale bar = 20 μm.

C2-4 Wollaston-Mudjatik Shear Zones, Hearne Basement, Eastern Athabasca Basin

C2-4.1 Drill hole GRL-133A
Sample number: JT20-3
Location: 57.36° N, 105.55° W
Re-Os graphite age: 1703.24 ± 8.64 Ma (n = 5)
In-situ U-Pb Monazite age: 1784.31 ± 9.52 Ma (n =7)

Drill hole GRL-133A is located 18.0 km NE of the Key Lake mine (U_3O_8 grade = 2.0 wt.%) and intersects WMTZ basement rock at 218.8 m below surface. Basement lithology includes several 3-10 m graphite-rich intervals containing brecciated pegmatites, quartzofeldspathic rocks, and pseudopelites crosscut and fracture-filled by graphite and pyrite veins that attest to widespread late-forming metasomatism. This sooty and flaky graphite follows the contorted foliation of some sheared protoliths and replaces the primary textures in others. Core specimen JT20-3 was sampled from a heavily metasomatized section (130.2 m below the unconformity) of the brittle-ductile regime. Feldspars in the specimen's groundmass appear microfractured and altered to sericite, which in turn forms the nucleation site for much of the replacive (flake) graphite (modal percent = 9.71%). Sulfides, primarily pyrite ± chalcopyrite and sphalerite, are present as fractured euhedral to anhedral masses that crosscut the groundmass.
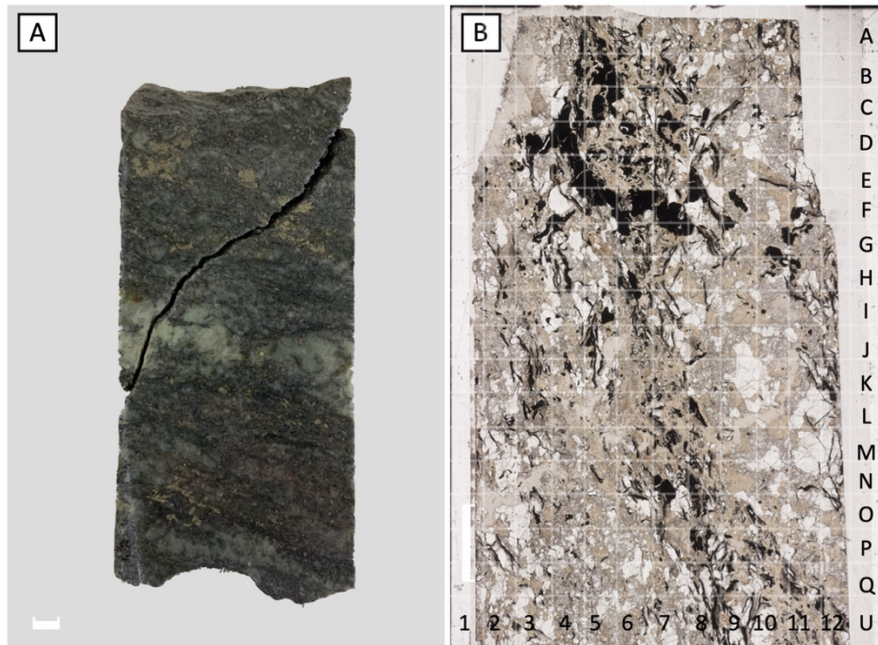
Figure C16. Photograph (A) and thin section scan (B) of drill core JT20-3. (A) Metasomatized orthogneiss crosscut by pyrite/graphite veins. (B) Transmitted-light photomicrograph depicting pyrite/graphite vein (black) around silicate groundmass. Scale bar: 0.5 cm.

Hydrothermal graphite mineral separates (n =3) for sample JT20-3-gr yielded Re-Os modal ages of 1594.34 ± 9.13 Ma (2σ with λ), 1703.24 ± 8.64 Ma (2σ with λ), and 1658.38 ± 6.53 (2σ with λ) Ma that are indicative of isotopic disequilibrium between graphites. Thus, the Re-Os modal age of 1703.24 ± 8.64 Ma is considered the best estimate for graphite formation in sample JT20-3-gr.

Monazite occurs as subhedral to anhedral grains (20-150 µm) in matrix and as inclusions in biotite in JT20-3. Seventeen analyses of two monazite grains (Mnz-1 to Mnz-2) yield a weighted mean $^{207}Pb/^{206}Pb$ date of 1784.31 ± 9.52 Ma (MSWD = 7.46) and X-ray maps of Y display low to high values within this uniform age population (Fig. C17).
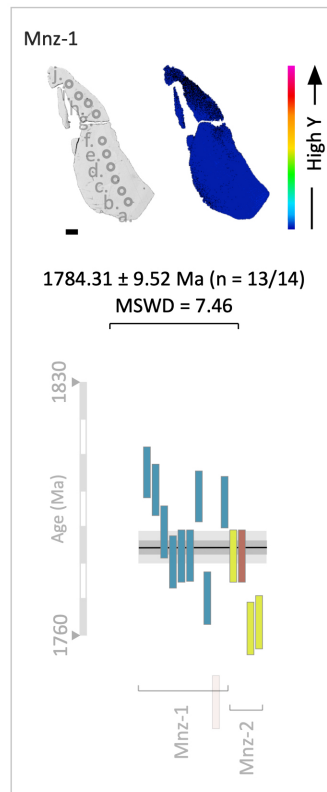
Figure C17. U-Pb monazite ^{207}Pb/^{206}Pb weighted mean ages for sample JT20-3 (Wollaston-Mudjatik Transition Shear Zones – Key Lake). Errors are reported in 2σ notation. Rejected outliers shown in translucent light grey. BSE images of zircon and monazite grains with laser ablation spot analyses and WDS yttrium element map for monazite. Scale bar = 20 μm.

C2-4.2 Drill hole WR-440
Sample number: JT20-5
Location: 57.51° N, 105.38° W
In-situ U-Pb monazite age: 1812.46 ± 6.83 Ma (n =25) and 1779.69 ± 7.23 Ma (n =9)

Drill hole WR-440 is located within the perimeter of the Phoenix Deposit (U_3O_8 grade = 1.06-62.6 wt.%) and intersects WMTZ basement rock at 403.55 m below surface (Kerr, 2010). Many basement lithologies (augen gneisses, metapelites, and pegmatites) intersected by this drill hole are sheared and fractured from being in the brittle-ductile regime. Late forming metasomatism has silicified, graphitized, and pyritized most of the original protolith. Graphite and pyrite are present along foliations and fault planes in folded and sheared gneisses and vein-fill the fractures in brecciated units. Core specimen JT20-5 was sampled from a section of

metasomatized augen gneiss (215.45 m below the unconformity) and contains graphites (modal percent = 13.63%) that are principally flaky and replace earlier formed biotite/chlorite (Toma et al., 2022). Previous Re-Os dating of these graphites constrains graphite mineralization to 1731.52 ± 12.71 Ma (Toma et al., 2022).
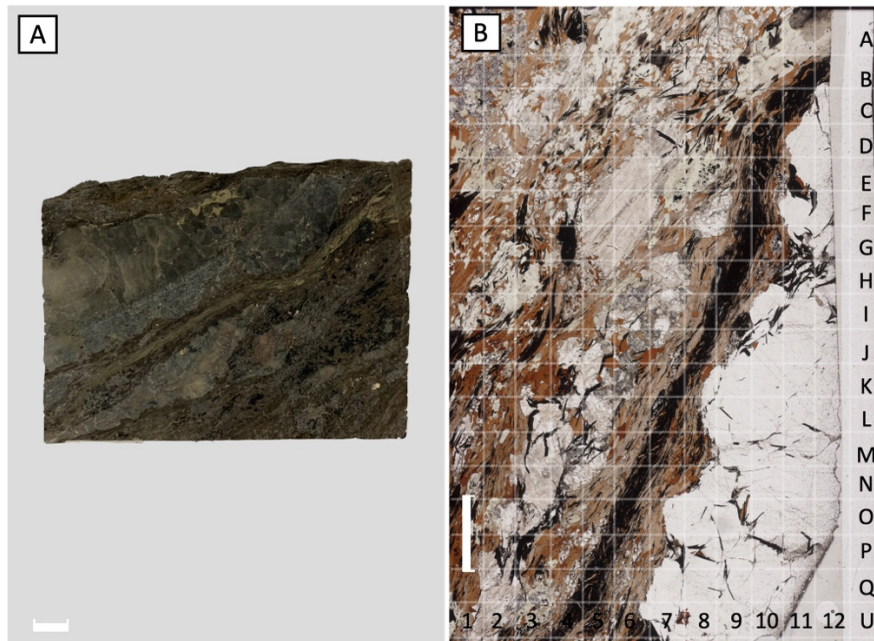
Figure C18. Photograph (A) and thin section scan (B) of drill core JT20-5. (A) Metasomatized augen gneiss crosscut by pyrite/graphite veins. (B) Transmitted-light photomicrograph depicting pyrite/graphite vein (black) around silicate groundmass and quartz vein. Scale bar: 0.5 cm.

Monazite occurs as subhedral to anhedral grains (20-150 μm) in matrix and as inclusions in biotite and chlorite in JT20-5. Twenty-five out of thirty-four (25/34) analyses of eight monazite grains (Mnz-1 to Mnz-8) yield a weighted mean ^{207}Pb/^{206}Pb age of 1812.46 ± 6.83 Ma (MSWD = 1.8), whereas nine out of thirty-four (9/34) analyses of seven monazite grains (Mnz-1 to Mnz-5 and Mnz-7 to Mnz-8) yield a weighted mean ^{207}Pb/^{206}Pb age of 1779.69 ± 7.23 Ma (MSWD = 2.6) (Fig. C19). Both monazite age populations display qualitatively high and low Y values (Fig. C19).
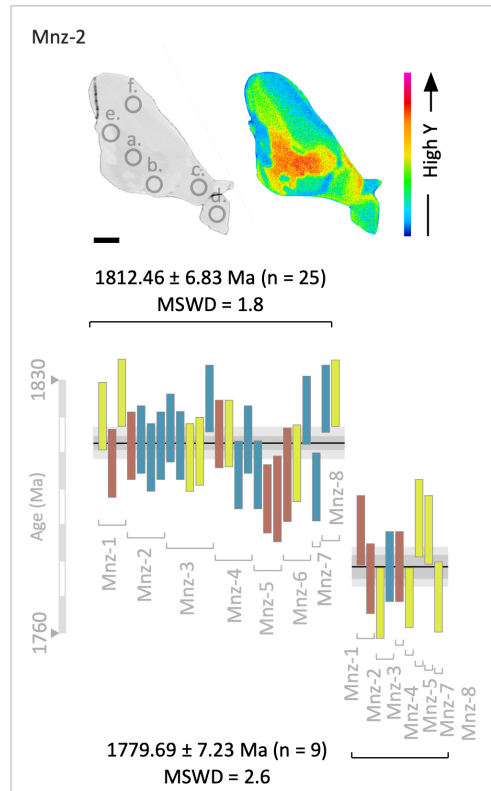
Figure C19. U-Pb monazite ^{207}Pb/^{206}Pb weighted mean ages for sample JT20-5 (Wollaston-Mudjatik Transition Shear Zones – Phoenix Deposit). Errors are reported in 2σ notation. BSE images of zircon and monazite grains with laser ablation spot analyses and WDS yttrium element map for monazite. Scale bar = 20 μm.

C2-4.3 Drill hole CB95-057A
Sample number: JT20-9
Location: 57.84° N, 109.90° W
In-situ U-Pb monazite age: 1794.32 ± 6.64 Ma (n =28) and 1763.39 ± 11.6Ma (n =3)

Drill hole CB95-057A is located 23.75 km SW of the McArthur River deposit (U_3O_8 grade = 6.89 wt.%) and intersects WMTZ basement rock at 447.3 below surface (Cameco, 2021). Much of the basement intersected here (orthogneisses, amphibolites, psammopelites) has been metasomatized following shearing and brittle faulting. Anastomosing biotite- and quartz-rich zones are commonly associated with graphite and pyrite veins. Graphite is common up to

2-5% in these regions. Core specimens JT20-9 (Fig. C20) was subsampled from an orthogneiss unit (71.9 m below the unconformity) with minor metasomatism. whereas specimens JT20-10 (94.5 m below the unconformity) and JT20-11(122.4 m below the unconformity) were sampled from heavily/moderately metasomatized intervals rich in pyrite and graphite, respectively. Flake graphites in these metasomatized regions appear to be replacing phyllosilicates such as biotite and sericite.

Figure C20. Photograph (A) and thin section scans (B-C) of drill core JT20-9 (Christie Lake). (A) Orthogneiss. (b-c) Transmitted-light photomicrograph depicting orothgneiss dominated by feldspars, quartz, and biotite. Scale bar: 0.5 cm.

Monazite occurs as subhedral to anhedral grains (20-150 µm) within matrix and as inclusions in biotite in sample JT20-9. Twenty-eight out of thirty-one (28/31) analyses of six monazite grains (Mnz-1 to Mnz-6) yield a weighted mean ^{207}Pb/^{206}Pb age of 1794.34 ± 6.64 Ma (MSWD = 1.05), whereas three out of thirty-one (3/31) analyses of two monazite grains (Mnz-1 and Mnz-3) yield a weighted mean ^{207}Pb/^{206}Pb age of 1763.39 ± 11.6 Ma (MSWD = 1.23) (Fig. C21). Both monazite age populations display qualitatively high and low Y (± Ce and Th) values (Fig. C21).
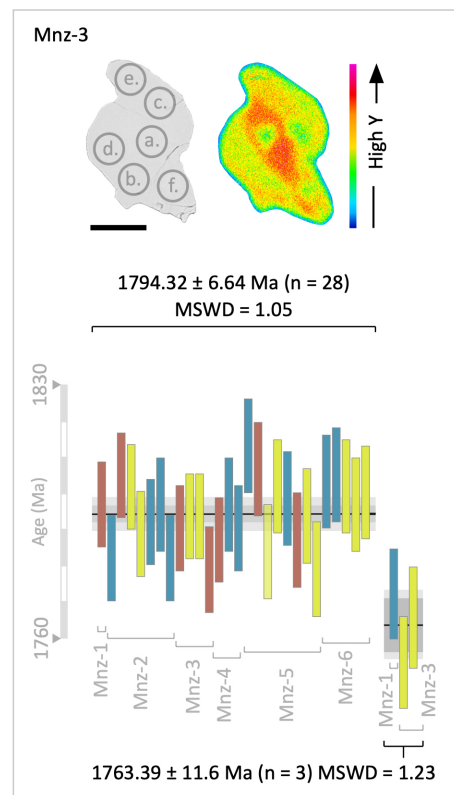
Figure C21. U-Pb monazite ^{207}Pb/^{206}Pb weighted mean ages for sample JT20-9 (Wollaston-Mudjatik Transition Shear Zones – Christie Lake). Errors are reported in 2σ notation. BSE images of zircon and monazite grains with laser ablation spot analyses and WDS yttrium element map for monazite. Scale bar = 20 µm.

C2-4.4 Drill hole CB95-057A
Sample number: JT20-10
Location: 57.84° N, 109.90° W
Re-Os pyrite age: 1749.18.4 ± 22.5 Ma (n = 7)

Drill hole CB95-057A is located 23.75 km SW of the McArthur River deposit (U_3O_8 grade = 6.89 wt.%) and intersects WMTZ basement rock at 447.3 below surface (Cameco, 2021). Core specimen JT20-10 (Fig. C22) was sampled 94.5 m below the unconformity in heavily metasomatized interval rich in pyrite and graphite.
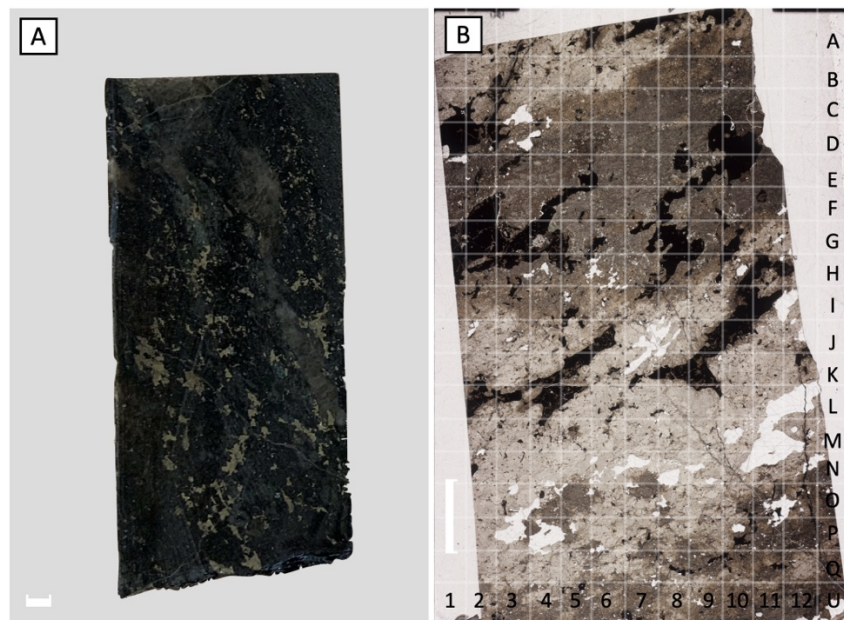
Figure C22. Photograph (A) and thin section scan (B) of drill core JT20-10 (Christie Lake). (A) Metasomatized gneiss crosscut by pyrite/graphite and quartz veins. (B) Transmitted-light photomicrograph depicting pyrite ± graphite (black) around heavily altered groundmass and quartz vein. Scale bar: 0.5 cm.

Pyrite mineral separates from sample JT10-py yield a Model 3 Re-Os isochron date of 1749.18.4 ± 18.4 Ma (2σ; MSWD = 28; n = 7) and ^{187}Os/^{188}Os initial ratios of 22.89 ± 2.37 Ma (Fig. C23).
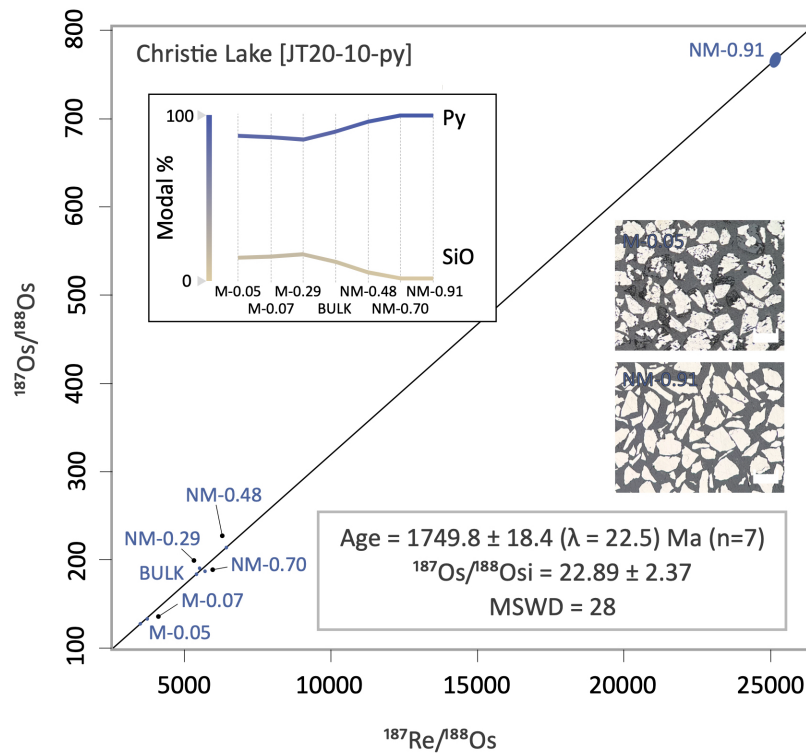
Figure C23. Re-Os pyrite isochron date calculated in IsoplotR (Vermeesch, 2018) using the ^{187}Re decay constant (λ = 1.666·10^{-11} ± 0.31%) of Smoliar et al. (1996) with systematic uncertainties (λ) shown in brackets. Error ellipses are reported in 2σ notation with a probability of fit of 0.15. Graphical insets depict mineral modal percentages per datapoint, whereas reflected light photomicrographs show mineralogy/textures for datapoints with endmember (high and low) magnetic susceptibilities. Abbreviations: py = pyrite, SiO = silicates. Scale bar = 200 μm.

C2-4.5 Drill hole CB95-057A
Sample number: JT20-11
Location: 57.84° N, 109.90° W
Re-Os graphite age: 1681.3 ± 24.2 Ma (n = 5)
In-situ U-Pb monazite age: 1800.06 ± 6.80 Ma (n =17)

Drill hole CB95-057A is located 23.75 km SW of the McArthur River deposit (U_3O_8 grade = 6.89 wt.%) and intersects WMTZ basement rock at 447.3 below surface (Cameco, 2021). Core specimens JT20-11 (Fig. C24) was sampled 122.4 m below the unconformity from a moderately metasomatized interval rich in pyrite and graphite. Flake graphites (modal percent = 8.86%) in this metasomatized region appear to be replacing phyllosilicates such as biotite and sericite.
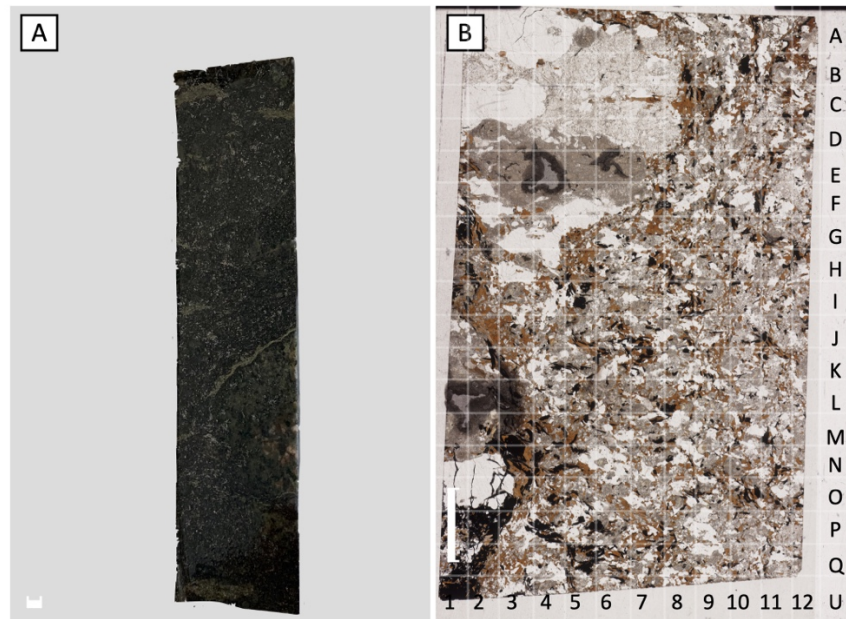
Figure C24. Photograph (A) and thin section scan (B) of drill core JT20-11 (Christie Lake). (A) Metasomatized orthogneiss crosscut by pyrite/graphite veins. (B) Transmitted-light photomicrograph depicting pyrite/graphite (black) around a silicate groundmass of alkali feldspar, quartz, plagioclase, biotite, and sericite. Pyrite and graphite occur at around 5 and 10 modal percent. Scale bar: 0.5 cm.

Graphite mineral separates for sample JT20-11-gr yield a Model 3 Re-Os isochron date of 1681.3 ± 17.1 Ma (2σ; MSWD = 3.8; n = 5) and an $^{187}Os/^{188}Os$ initial ratio of -0.0012 ± 0.138 (Fig. C25).
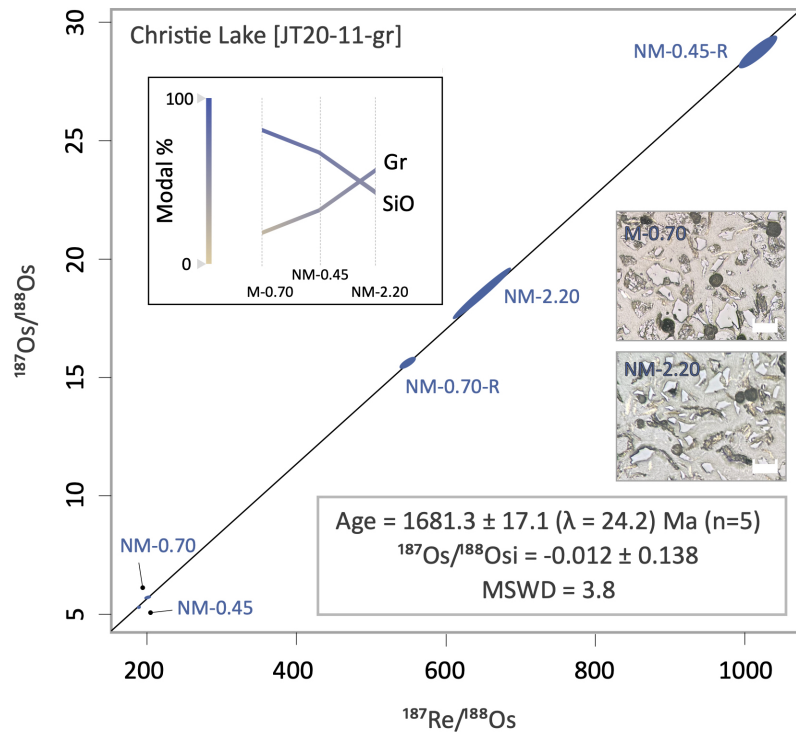
Figure C25. Re-Os graphite isochron date calculated in IsoplotR (Vermeesch, 2018) using the [187]Re decay constant (λ = 1.666·10[-11] ± 0.31%) of Smoliar et al. (1996) with systematic uncertainties (λ) shown in brackets. Error ellipses are reported in 2σ notation with a probability of fit of 0.15. Graphical insets depict mineral modal percentages per datapoint, whereas reflected light photomicrographs show mineralogy/textures for datapoints with endmember (high and low) magnetic susceptibilities. Abbreviations: py = pyrite, SiO = silicates. Scale bar = 200 μm.

Monazite occurs as subhedral to anhedral grains (20-150 μm) in a metasomatized pelitic matrix and as inclusions in biotite. Seventeen analyses of three monazite grains (Mnz-1 to Mnz-3) yield a weighted mean [207]Pb/[206]Pb date of 1800.06 ± 6.80 Ma (MSWD = 0.40) with X-ray maps of Y (± Ce and Th) displaying medium to high values within this uniform age population (Fig. C26).
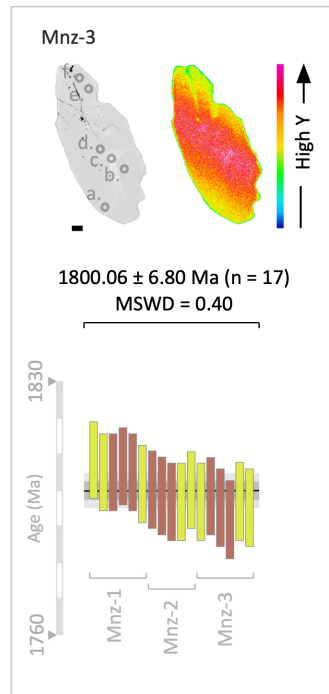
Figure C26. U-Pb monazite ^{207}Pb/^{206}Pb weighted mean ages for sample JT20-11 (Wollaston-Mudjatik Transition Shear Zones – Christie Lake). Errors are reported in 2σ notation. BSE images of zircon and monazite grains with laser ablation spot analyses and WDS yttrium element map for monazite. Scale bar = 20 μm.

C3 Bulk carbon isotopes for Pre-Athabasca graphitic-pyritic shear zones

   Carbon isotope ($^{13}C/^{12}C$) analysis of Taltson (n = 5) and WMTZ (n = 2) graphites yielded $\delta^{13}C$ values that ranged from -26.10‰ to -20.90‰ and -28.30‰ to -25.20‰, respectively (Table C4). These values are comparable to bulk carbon isotopes from shear zone graphites ($\delta^{13}C_{avg}$ = -23.31 ‰; n = 44) located elsewhere in Taltson and WMTZ basement rocks and confirms that the graphitic carbon in pre-Athabasca shear zones is dominated by an isotopically light carbon signature indicative of a biological rather than abiological origin (Fig. C27; Table C4).
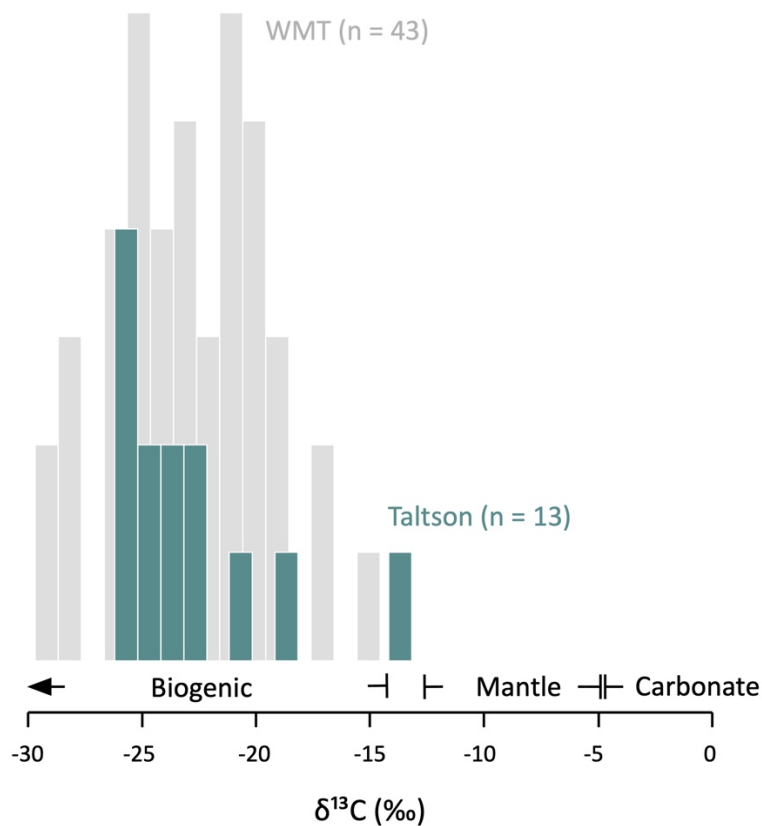
Figure C27. Compilation of all Taltson and WMT graphite carbon isotopic values reported in $\delta^{13}C$ notation.

C4 Hydrothermal graphite replacive textures

Hydrothermal graphite in pre-Athabasca Supergroup structures show petrographic evidence of nucleating and replacing phyllosilicates (sericite, biotite, chlorite). Presumably these replacive textures formed as basement lithologies were exhumed into the brittle-ductile zone and infiltrated with fluids that lead to biotization and seritization that was followed by graphite replacement (Fig. C28 and Fig. C29).
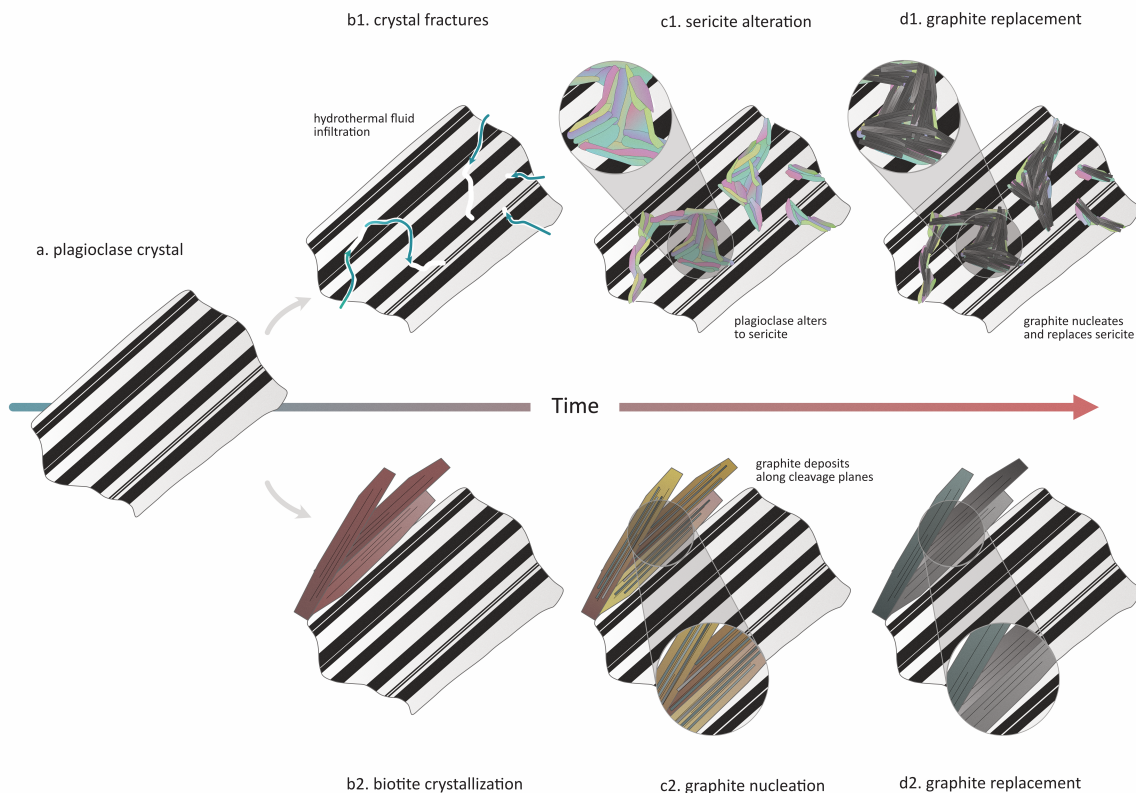
Figure C28. Replacive textures of hydrothermal flake graphite observed in pre-Athabasca Supergroup structures. Hydrothermal flake graphite nucleates along cleavage planes of phyllosilicates and replaces them thereafter as pristine feldspar crystals (a) become fractured and altered to sericite (b1-d1) and/or are deposited with hydrothermal biotite ± chlorite (b2-d2).
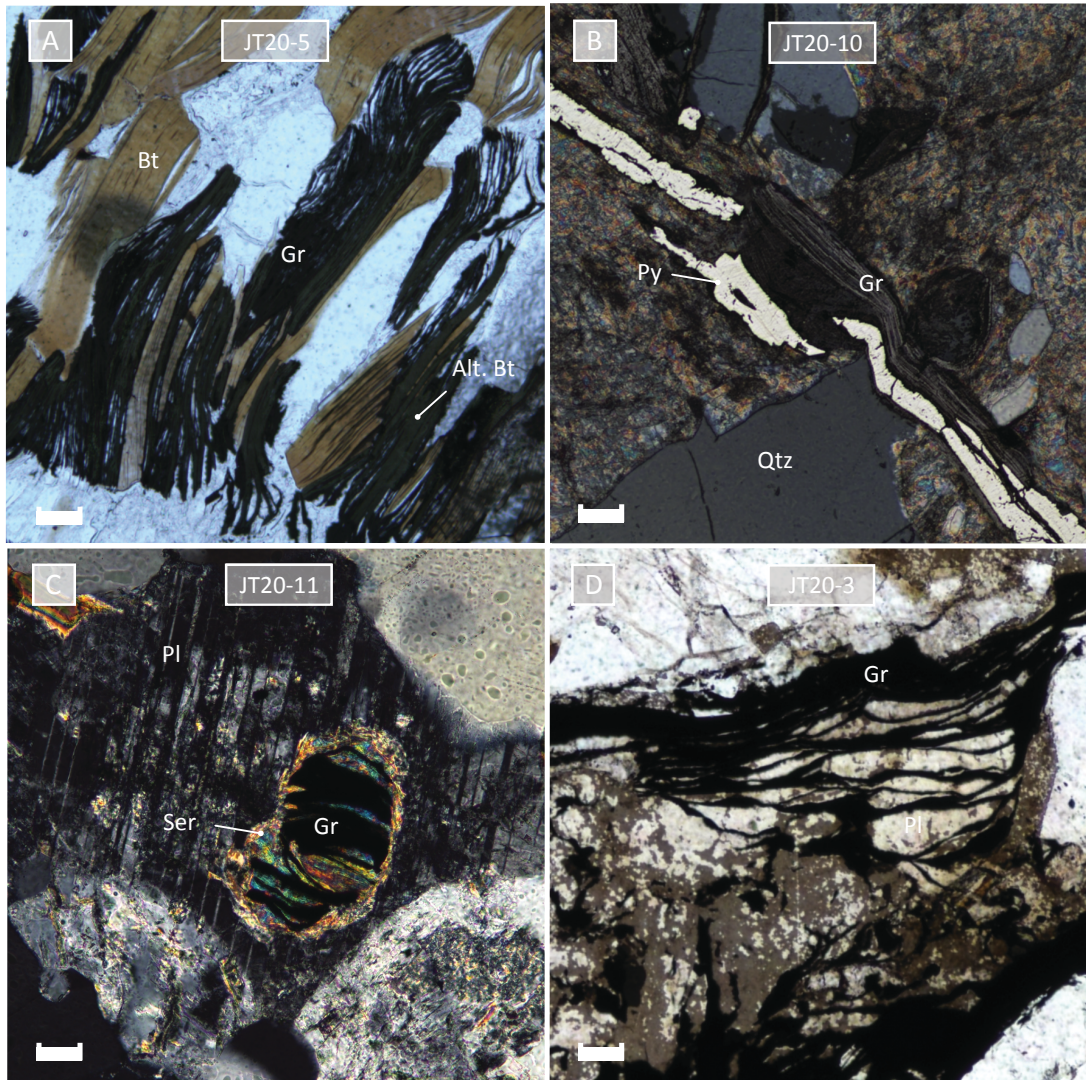
Figure C29. Replacive textures (A-D) of hydrothermal flake graphite observed in pre-Athabasca Supergroup structures. Hydrothermal flake graphite nucleates along cleavage planes of phyllosilicates and replaces them thereafter as pristine feldspar crystals (A-B) are deposited with hydrothermal biotite ± chlorite or (C-D) become fractured and altered to sericite. A & D = transmitted plane-polarized light, B = reflected plane-polarized light, and C = transmitted cross-polarized light photomicrograph. Abbreviations: Bt = biotite, Gr, graphite, Alt = altered, Qtz = quartz, Ser = sericite, Pl = plagioclase, py = pyrite. Scale bar = 100 µm.

Table C1: Sample information

Sample	Drillcore	Location	Depth below surface (m)	Latitude (N)	Longitude (W)	Domain	Lithology	Nearest U-deposit
DP19-843	MR-120	Maybelle River	326.0	58.20	-110.66	Taltson	Graphitic mylonite	Maybelle River (440 m NE)
DP19-844	MR-120	Maybelle River	289.2	58.20	-110.66	Taltson	Graphitic pelite/mylonite	Maybelle River (440 m NE)
3576	MR-68	Maybelle River	421.4	58.30	-110.69	Taltson	Graphitic pelite/mylonite	Maybelle River (12.2 km NE)
PLS14-260	PLS14-260	Patterson Lake South	97.5	57.56	-109.13	Taltson	Graphitic pelite	Triple R (in perimeter)
PLS14-133	PLS14-133	Patterson Lake South	316.0	57.63	-109.36	Taltson	Graphitic pelite	Triple R (2.0 km SE)
JT20-03	GRL-133A	Key Lake	350.0	57.36	-105.55	WMTZ	Graphitic pelite	Key Lake (18.0 km NE)
JT20-05	WR-440	Phoenix Deposit	619.4	57.51	-105.38	WMTZ	Graphitic gneiss	Phoenix (in perimeter)
JT20-06	WR-440	Phoenix Deposit	639.6	57.51	-105.38	WMTZ	Augen gneiss	Phoenix (in perimeter)
JT20-09	CB95-057A	Christie Lake	517.6	57.84	-104.90	WMTZ	Monzogranite	McArthur River (23.8 km SW)
JT20-10	CB95-057A	Christie Lake	541.4	57.84	-104.90	WMTZ	Graphitic orthogneiss	McArthur River (23.8 km SW)
JT20-11	CB95-057A	Christie Lake	569.7	57.84	-104.90	WMTZ	Graphitic orthogneiss	McArthur River (23.8 km SW)

Abbreviations: WMTZ = Wollaston-Mudjatik Transition Zone

Table C2: Re-Os graphite and pyrite data

[a]Sample	Mineral	Re (ppb)	±	Os (ppt)	±	^{192}Os (ppt)	^{187}Re/^{188}Os	±	^{187}Os/^{188}Os	±	rho
DP19-844-M-0.50	Pyrite	67.7	0.2	2890	12	576	233.8	0.7	8.3492	0.0148	0.327
DP19-844-M-0.69	Pyrite	51.7	0.1	2487	9	548	187.7	0.5	6.8312	0.0109	0.277
DP19-844-NM-0.69	Pyrite	49.4	0.1	2865	11	707	139.0	0.4	5.2888	0.0095	0.260
DP19-844-NM-0.80	Pyrite	58.5	0.2	3566	12	901	129.2	0.4	4.9886	0.0075	0.246
DP19-844-M-0.54	Pyrite	89.3	0.2	3429	15	610	291.3	0.9	10.2512	0.0198	0.354
DP19-844-M-0.70	Pyrite	58.1	0.2	2697	10	576	200.7	0.6	7.2697	0.0112	0.281
DP19-844-NM-0.70	Pyrite	46.8	0.1	2715	10	669	139.0	0.4	5.3000	0.0103	0.319
DP19-844-NM-0.84	Pyrite	153.8	0.4	5391	26	856	357.5	1.0	12.3910	0.0263	0.302
DP19-844-WR	Graphite	31.1	0.1	1242	6	231	267.8	0.6	9.4829	0.0245	0.433
3576A	Pyrite	15.3	0.1	656	6	132	229.8	2.8	8.1815	0.0984	0.915
3576A1	Pyrite	51.7	0.2	1063	15	177	580.3	3.8	19.4648	0.2069	0.392
3576A2	Pyrite	58.3	0.2	1645	7	176	660.6	3.5	22.0889	0.0976	0.557
3576A-1B	Pyrite	37.3	0.1	1217	6	174	425.6	2.7	14.5353	0.0868	0.674
3576A-2B	Pyrite	43.1	0.2	1339	6	178	480.5	2.9	16.2398	0.0836	0.710
DP19-843-T1-NM-0.75	Pyrite	0.8	0.0	24	1	4	425.0	20.0	13.6324	0.5968	0.922
DP19-843-T1-M-0.75	Pyrite	3.3	0.0	104	1	15	429.6	4.9	13.8375	0.1500	0.896
DP19-843-T2-NM-0.55	Pyrite	1.4	0.0	71	1	17	156.2	2.2	5.4923	0.0536	0.653
DP19-843-T2-M-0.55	Pyrite	8.5	0.0	310	2	56	299.9	1.2	9.8952	0.0413	0.675
DP19-843-T3-NM-0.45	Pyrite	1.1	0.0	53	1	12	188.0	3.4	6.4289	0.0871	0.724
DP19-843-T3-M-0.45	Pyrite	5.6	0.0	222	1	44	254.3	1.2	8.5089	0.0362	0.726
DP19-843-M-0.51	Graphite	15.1	0.0	845	5	215	139.8	0.6	4.9268	0.0202	0.657
DP19-843-M-0.91	Graphite	34.5	0.2	1220	19	218	315.1	6.2	10.1687	0.2124	0.858
DP19-843-M-0.99	Graphite	9.7	0.1	461	4	106	182.2	2.0	6.2004	0.0666	0.779
DP19-843-M-1.94	Graphite+pyrite	8.9	0.1	437	5	104	171.2	3.5	5.7955	0.1027	0.846
DP19-843-NM-1.94	Graphite	12.5	0.1	446	6	80	309.8	5.0	10.0682	0.1556	0.937
PLS14-260-NM-0.30	Pyrite	27.1	0.1	4180	10	1418	37.9	0.1	1.7877	0.0028	0.253
PLS14-260-NM-0.47	Pyrite	22.1	0.1	1763	6	515	85.2	0.3	3.2898	0.0075	0.235
PLS14-260-NM-0.70	Pyrite	17.2	0.1	2171	6	712	47.9	0.2	2.1113	0.0039	0.190
PLS14-260-NM-0.90	Pyrite	6.1	0.0	1988	4	728	16.6	0.0	1.1084	0.0018	0.249
PLS14-260-M-0.02	Pyrite	7.7	0.0	3414	7	1271	12.0	0.0	0.9657	0.0016	0.239
PLS14-260-M-0.05	Pyrite	9.7	0.0	3349	7	1230	15.6	0.0	1.0807	0.0017	0.247
PLS14-260-M-0.30	Pyrite	125.1	0.3	5924	21	1329	187.3	0.5	6.5713	0.0101	0.241
PLS14-260-gr-BULK	Graphite	24.7	0.4	1401	9	354	138.8	2.3	4.9786	0.0297	0.347
PLS14-133-NM-0.51	Pyrite	1.1	0.0	33	1	3	708	17.6	25.3	0.6419	0.9657
PLS14-133-NM-0.53	Pyrite	1.2	0.0	34	1	3	676	17.3	24.1	0.6689	0.9120
PLS14-133-NM-0.55	Pyrite	1.2	0.0	37	1	4	636	13.2	22.8	0.4852	0.9586
PLS14-133-NM-0.60	Pyrite	1.3	0.0	37	1	4	725	17.6	25.9	0.6410	0.9697
PLS14-133-NM-0.61	Pyrite	1.2	0.0	36	1	4	620	13.7	22.4	0.5012	0.9704
PLS14-133-NM-0.69	Pyrite	1.2	0.0	38	1	4	553	10.4	20.0	0.3875	0.9502
PLS14-133-NM-1.60	Pyrite	1.2	0.0	39	1	5	519	9.9	18.7	0.4572	0.7623
PLS14-133-M-0.50	Pyrite	4.2	0.0	402	2	104	81	0.3	4.6	0.0142	0.3867
JT20-10-py-BULK	Pyrite	105.1	0.5	2327	26	39	5417.9	44.0	183.2548	1.4296	0.725
JT20-10-M--py-0.05	Pyrite	79.5	0.4	1923	26	45	3508.2	27.5	127.5208	1.1998	0.562
JT20-10-M--py-0.07	Pyrite	84.7	0.4	1999	18	45	3738.6	20.3	132.8961	0.6276	0.371
JT20-10-NM--py-0.29	Pyrite	105.3	0.5	2367	22	38	5531.1	31.0	190.3015	0.9857	0.397
JT20-10-NM--py-0.48	Pyrite	128.6	0.6	2779	31	40	6436.3	39.1	213.8376	1.4557	0.411
JT20-10-NM--py-0.70	Pyrite	104.9	0.5	2247	21	37	5709.7	32.1	187.0198	0.9841	0.396
JT20-10-NM--py-0.91	Pyrite	348.3	1.6	6741	102	28	25147.4	182.0	766.9194	7.9492	0.433
JT20-11-M-0.7	Graphite	2.1	0.0	99	2	26	166.3	6.1	4.6894	0.1461	0.844
JT20-11-M-0.7-RPT	Graphite	4.4	0.0	117	3	16	555.6	21.7	15.7407	0.6067	0.979
JT20-11-M-0.7-RPT2	Graphite	4.0	0.0	166	2	40	202.4	4.0	5.7433	0.1024	0.883
JT20-11-NM-0.45	Graphite	6.8	0.0	289	3	71	190.4	2.3	5.3199	0.0562	0.859
JT20-11-NM-0.45-RPT	Graphite	3.0	0.0	88	2	15	381.7	20.4	10.4654	0.5416	0.963

[a]Sample	Mineral	Re (ppb)	± 2σ	^{187}Re (ppb)	±	^{187}Os (ppb)	± 2σ	Total Common Os (pg)	[b]Model Ages (Ma)	± 2σ with λ (Ma)
JT20-3-NM-1.7	Graphite	69.26	0.28	43.54	0.18	1.1622	0.0030	1.72	1581.38	9.13
JT20-3-NM-1.84	Graphite	203.17	0.77	127.70	0.49	3.6613	0.0041	1.17	1696.74	8.62
JT20-3-NM-2.00	Graphite	137.45	0.26	86.39	0.16	2.4090	0.0036	1.80	1650.83	6.53

[a]Sample nomenclature is as follows: name-year-sample#-magnetic/non-magnetic-current

Table C3: LA-ICPSMS U-Pb data

			ratios									apparent ages (Ma)										
Sample	Mineral	Grid Zone	$^{206}Pb/^{204}Pb$ cps	$^{204}Pb/^{206}Pb$ cps	$^{207}Pb/^{206}Pb$	2 s	$^{207}Pb/^{235}U$	2 s	$^{206}Pb/^{238}U$	2 s	r	$^{207}Pb/^{206}Pb$	2 s	$^{207}Pb/^{235}U$	2 s	$^{206}Pb/^{238}U$	2 s	% disc.	$^{238}U/^{206}Pb$	2 s	$^{207}Pb/^{206}Pb$	2 s
44069-1	Monazite	NA	222869	28	0.0559	0.0005	0.51	0.01	0.066	0.001	0.910	450	19	420	7	415	8	8.4	15.04	0.29	0.0559	0.0005
44069-2	Monazite	NA	182445	33	0.0561	0.0005	0.51	0.01	0.066	0.001	0.898	455	21	420	7	414	8	10.1	15.09	0.29	0.0561	0.0005
44069-3	Monazite	NA	119530	37	0.0564	0.0009	0.51	0.01	0.066	0.001	0.778	470	35	422	9	413	8	13.8	15.12	0.30	0.0564	0.0009
44069-4	Monazite	NA	130063	16	0.0554	0.0009	0.51	0.01	0.066	0.001	0.783	428	34	416	8	414	8	3.3	15.08	0.29	0.0554	0.0009
44069-1	Monazite	NA	106677	18	0.0564	0.0008	0.50	0.01	0.067	0.001	0.802	468	30	428	8	421	7	11.2	14.83	0.27	0.0564	0.0008
44069-2	Monazite	NA	119345	20	0.0555	0.0007	0.50	0.01	0.065	0.001	0.833	432	26	412	7	408	7	5.8	15.30	0.27	0.0555	0.0007
44069-3	Monazite	NA	168100	45	0.0567	0.0007	0.51	0.01	0.065	0.001	0.825	479	27	417	7	406	7	18.0	15.39	0.28	0.0567	0.0007
44069-4	Monazite	NA	124353	31	0.0547	0.0006	0.49	0.01	0.065	0.001	0.846	402	25	408	7	409	7	-1.7	15.28	0.28	0.0547	0.0006
44069-1	Monazite	NA	199655	65	0.0573	0.0007	0.53	0.01	0.067	0.001	0.830	503	26	432	8	419	7	19.9	14.88	0.26	0.0573	0.0007
44069-2	Monazite	NA	124856	87	0.0579	0.0009	0.54	0.01	0.068	0.001	0.757	527	34	438	9	421	7	25.0	14.80	0.27	0.0579	0.0009
44069-3	Monazite	NA	174160	36	0.0570	0.0008	0.53	0.01	0.067	0.001	0.784	493	32	431	8	419	7	17.6	14.88	0.27	0.0570	0.0008
44069-4	Monazite	NA	242843	12	0.0538	0.0006	0.49	0.01	0.066	0.001	0.842	365	26	405	7	412	7	-11.5	15.15	0.27	0.0538	0.0006
JT20-5-mnz-1a	Monazite	A6	734502	23	0.1113	0.0008	4.73	0.10	0.308	0.006	0.944	1821	12	1772	17	1732	29	5.1	3.24	0.06	0.1113	0.0008
JT20-5-mnz-1b	Monazite	A6	607760	12	0.1094	0.0008	4.59	0.09	0.305	0.006	0.940	1790	13	1748	17	1714	29	4.4	3.28	0.06	0.1094	0.0008
JT20-5-mnz-1c	Monazite	A6	687440	17	0.1086	0.0008	4.55	0.09	0.304	0.006	0.941	1776	13	1741	17	1713	29	3.7	3.29	0.06	0.1086	0.0008
JT20-5-mnz-1d	Monazite	A6	969646	12	0.1105	0.0008	4.81	0.10	0.316	0.006	0.941	1807	12	1787	17	1770	30	2.1	3.17	0.06	0.1105	0.0008
JT20-5-mnz-1e	Monazite	A6	760620	40	0.1117	0.0008	4.98	0.10	0.323	0.006	0.941	1827	13	1816	17	1807	31	1.1	3.09	0.06	0.1117	0.0008
JT20-5-mnz-2a	Monazite	C2	822500	29	0.1108	0.0008	4.72	0.10	0.309	0.006	0.948	1813	12	1770	18	1736	31	4.4	3.24	0.07	0.1108	0.0008
JT20-5-mnz-2b	Monazite	C2	553554	17	0.1109	0.0008	4.78	0.10	0.313	0.006	0.948	1815	13	1782	18	1755	32	3.4	3.20	0.07	0.1109	0.0008
JT20-5-mnz-2c	Monazite	C2	522626	23	0.1082	0.0008	4.42	0.09	0.297	0.006	0.942	1770	13	1717	17	1674	29	5.7	3.37	0.07	0.1082	0.0008
JT20-5-mnz-2d	Monazite	C2	357624	15	0.1088	0.0008	4.51	0.10	0.301	0.006	0.942	1780	13	1733	18	1696	30	4.9	3.32	0.07	0.1088	0.0008
JT20-5-mnz-2e	Monazite	C2	1258501	38	0.1106	0.0008	4.64	0.10	0.304	0.006	0.949	1810	12	1756	18	1712	31	5.7	3.29	0.07	0.1106	0.0008
JT20-5-mzn-2f	Monazite	C2	319527	27	0.1108	0.0008	4.62	0.10	0.302	0.006	0.947	1813	13	1753	18	1703	31	6.4	3.31	0.07	0.1108	0.0008
JT20-5-mnz-3a	Monazite	C9	682232	17	0.1088	0.0008	4.68	0.10	0.312	0.006	0.941	1779	13	1764	17	1753	30	1.5	3.20	0.06	0.1088	0.0008
JT20-5-mnz-3b	Monazite	C9	497507	16	0.1111	0.0008	4.70	0.10	0.307	0.006	0.948	1818	13	1767	18	1725	31	5.4	3.26	0.07	0.1111	0.0008
JT20-5-mnz-3c	Monazite	C9	531905	17	0.1108	0.0008	4.83	0.10	0.316	0.007	0.948	1813	12	1789	18	1770	32	2.4	3.16	0.07	0.1108	0.0008
JT20-5-mnz-3d	Monazite	C9	650623	25	0.1106	0.0008	4.80	0.11	0.315	0.007	0.954	1809	13	1786	19	1767	34	2.4	3.17	0.07	0.1106	0.0008
JT20-5-mnz-3e	Monazite	C9	730419	23	0.1107	0.0008	4.77	0.11	0.313	0.007	0.955	1811	13	1780	20	1755	34	3.2	3.20	0.07	0.1107	0.0008
JT20-5-mnz-3f	Monazite	C9	236212	26	0.1116	0.0008	4.84	0.12	0.314	0.007	0.954	1826	13	1791	20	1762	35	3.6	3.18	0.07	0.1116	0.0008
JT20-5-mnz-4a	Monazite	D9	1158306	14	0.1110	0.0008	4.78	0.11	0.312	0.007	0.952	1817	12	1782	19	1753	32	3.7	3.20	0.07	0.1110	0.0008
JT20-5-mnz-4b	Monazite	D9	382969	38	0.1110	0.0008	4.65	0.10	0.304	0.006	0.940	1815	13	1758	17	1712	30	6.0	3.29	0.07	0.1110	0.0008
JT20-5-mnz-4c	Monazite	D9	730683	22	0.1103	0.0008	4.74	0.10	0.312	0.006	0.946	1805	12	1775	18	1750	31	3.1	3.21	0.06	0.1103	0.0008
JT20-5-mnz-4d	Monazite	D9	607281	34	0.1083	0.0007	4.49	0.10	0.301	0.006	0.946	1770	13	1730	18	1697	30	4.3	3.32	0.07	0.1083	0.0007
JT20-5-mnz-4e	Monazite	D9	699098	24	0.1109	0.0008	4.67	0.10	0.306	0.006	0.944	1815	13	1763	18	1719	30	5.6	3.27	0.07	0.1109	0.0008
JT20-5-mnz-5a	Monazite	E9	224734	24	0.1103	0.0008	4.74	0.10	0.312	0.006	0.943	1804	13	1775	18	1750	32	3.1	3.21	0.07	0.1103	0.0008
JT20-5-mnz-5b	Monazite	E9	621552	31	0.1099	0.0008	4.79	0.10	0.316	0.006	0.944	1798	13	1783	18	1771	31	1.5	3.16	0.06	0.1099	0.0008
JT20-5-mnz-5c	Monazite	E9	722798	23	0.1096	0.0009	4.76	0.12	0.315	0.007	0.940	1793	15	1778	21	1765	36	1.6	3.17	0.07	0.1096	0.0009
JT20-5-mnz-5d	Monazite	E9	303478	19	0.1099	0.0010	4.80	0.11	0.317	0.007	0.922	1798	16	1784	19	1773	32	1.4	3.16	0.07	0.1099	0.0010
JT20-5-mnz-6a	Monazite	E5	165619	24	0.1103	0.0011	4.66	0.10	0.307	0.006	0.894	1804	18	1760	18	1724	29	4.6	3.26	0.06	0.1103	0.0011
JT20-5-mnz-6b	Monazite	E5	145257	27	0.1105	0.0009	4.51	0.10	0.296	0.006	0.924	1807	15	1733	17	1673	29	8.0	3.37	0.07	0.1105	0.0009
JT20-5-mnz-6c	Monazite	E5	295810	20	0.1114	0.0008	4.58	0.09	0.298	0.006	0.937	1823	13	1745	17	1682	28	8.3	3.35	0.06	0.1114	0.0008
JT20-5-mnz-7a	Monazite	L2	521292	8	0.1101	0.0008	4.56	0.09	0.300	0.006	0.938	1802	13	1741	17	1692	28	6.5	3.33	0.06	0.1101	0.0008
JT20-5-mnz-7b	Monazite	L2	711204	16	0.1094	0.0008	4.59	0.09	0.305	0.006	0.942	1789	13	1748	17	1714	29	4.4	3.28	0.06	0.1094	0.0008
JT20-5-mnz-8a	Monazite	L2	371499	25	0.1116	0.0008	4.74	0.10	0.308	0.006	0.933	1826	14	1774	17	1731	30	5.4	3.25	0.06	0.1116	0.0008
JT20-5-mnz-8b	Monazite	L2	505520	22	0.1083	0.0008	4.62	0.10	0.309	0.006	0.942	1771	13	1753	17	1738	30	1.9	3.23	0.06	0.1083	0.0008
JT20-5-mnz-8c	Monazite	L2	375936	31	0.1117	0.0008	4.49	0.09	0.292	0.006	0.942	1827	12	1729	17	1649	28	10.8	3.43	0.07	0.1117	0.0008
JT20-9-mnz-1a	Monazite	E6	1396432	11	0.1099	0.0010	4.69	0.10	0.310	0.006	0.899	1797	17	1765	18	1739	29	3.4	3.23	0.06	0.1099	0.0010
JT20-9-mnz-1b	Monazite	E6	694133	24	0.1084	0.0010	4.44	0.09	0.297	0.005	0.885	1773	17	1721	17	1679	27	5.6	3.36	0.06	0.1084	0.0010
JT20-9-mnz-2a	Monazite	J7	1022083	11	0.1090	0.0010	4.57	0.10	0.304	0.006	0.895	1782	17	1743	18	1712	29	4.1	3.29	0.06	0.1090	0.0010
JT20-9-mnz-2b	Monazite	J7	1321386	9	0.1104	0.0010	4.67	0.10	0.308	0.006	0.889	1806	17	1789	17	1775	28	1.7	3.15	0.06	0.1104	0.0010
JT20-9-mnz-2c	Monazite	J7	1000251	4	0.1102	0.0010	4.67	0.10	0.308	0.006	0.888	1803	17	1762	17	1729	28	4.3	3.15	0.06	0.1102	0.0010
JT20-9-mnz-2d	Monazite	J7	2200281	13	0.1094	0.0010	4.57	0.09	0.303	0.006	0.890	1789	17	1744	17	1708	27	4.9	3.30	0.06	0.1094	0.0010
JT20-9-mnz-2e	Monazite	J7	2298655	7	0.1096	0.0010	4.58	0.10	0.309	0.006	0.898	1793	17	1763	18	1738	29	3.2	3.23	0.06	0.1096	0.0010
JT20-9-mnz-2f	Monazite	J7	1074425	40	0.1099	0.0011	4.61	0.09	0.304	0.006	0.885	1797	17	1751	17	1713	27	4.9	3.29	0.06	0.1099	0.0011
JT20-9-mnz-2g	Monazite	J7	1482827	16	0.1090	0.0010	4.58	0.10	0.305	0.006	0.894	1783	17	1746	17	1715	28	4.0	3.28	0.06	0.1090	0.0010
JT20-9-mnz-3a	Monazite	O9	1825395	11	0.1095	0.0010	4.69	0.10	0.311	0.006	0.893	1792	17	1765	17	1744	28	2.8	3.22	0.06	0.1095	0.0010
JT20-9-mnz-3b	Monazite	O9	1153206	20	0.1073	0.0010	4.58	0.10	0.310	0.006	0.898	1754	17	1745	18	1738	29	0.9	3.23	0.06	0.1073	0.0010
JT20-9-mnz-3c	Monazite	O9	1118881	17	0.1097	0.0010	4.81	0.11	0.318	0.007	0.916	1795	17	1787	20	1781	33	0.8	3.14	0.07	0.1097	0.0010
JT20-9-mnz-3d	Monazite	O9	901442	8	0.1080	0.0011	4.63	0.11	0.311	0.006	0.900	1766	18	1755	19	1746	31	1.1	3.21	0.07	0.1080	0.0011
JT20-9-mnz-3e	Monazite	O9	1144090	20	0.1097	0.0011	4.85	0.11	0.321	0.006	0.900	1794	17	1793	18	1793	31	0.1	3.12	0.06	0.1097	0.0011
JT20-9-mnz-3f	Monazite	O9	873477	9	0.1088	0.0010	4.72	0.10	0.315	0.006	0.898	1779	17	1771	18	1764	30	0.9	3.18	0.06	0.1088	0.0010
JT20-9-mnz-4a	Monazite	O9	1552504	10	0.1093	0.0010	4.67	0.10	0.310	0.006	0.892	1787	17	1762	17	1742	28	2.6	3.22	0.06	0.1093	0.0010
JT20-9-mnz-4b	Monazite	O9	493172	11	0.1099	0.0011	4.83	0.10	0.319	0.006	0.895	1798	17	1791	18	1786	30	0.7	3.13	0.06	0.1099	0.0011
JT20-9-mnz-4c	Monazite	O9	833084	7	0.1095	0.0010	4.91	0.11	0.325	0.007	0.913	1792	17	1804	19	1815	33	-1.3	3.08	0.07	0.1095	0.0010
JT20-9-2-mnz-5a	Monazite	A10	2298742	48	0.1109	0.0011	4.87	0.10	0.319	0.006	0.882	1814	18	1798	18	1785	29	1.6	3.13	0.06	0.1109	0.0011
JT20-9-2-mnz-5b	Monazite	A10	1880648	59	0.1105	0.0011	4.91	0.11	0.322	0.006	0.892	1808	18	1804	19	1802	31	0.4	3.10	0.06	0.1105	0.0011
JT20-9-2-mzn-5c	Monazite	A10	1491653	49	0.1091	0.0011	4.66	0.10	0.310	0.006	0.876	1785	18	1761	17	1741	28	2.5	3.23	0.06	0.1091	0.0011
JT20-9-2-mnz-5d	Monazite	A10	1982592	93	0.1102	0.0011	4.83	0.10	0.318	0.006	0.882	1803	18	1790	18	1779	29	1.3	3.15	0.06	0.1102	0.0011
JT20-9-2-mnz-5e	Monazite	A10	1982670	58	0.1100	0.0011	4.81	0.10	0.317	0.006	0.873	1800	18	1787	17	1777	28	1.3	3.15	0.06	0.1100	0.0011
JT20-9-2-mnz-5f	Monazite	A10	1850811	18	0.1093	0.0011	4.82	0.10	0.320	0.006	0.876	1787	18	1788	17	1790	29	-0.2	3.12	0.06	0.1093	0.0011
JT20-9-2-mnz-5g	Monazite	A10	1169210	20	0.1097	0.0011	4.75	0.11	0.315	0.006	0.883	1794	19	1777	18	1763	30	1.7	3.18	0.06	0.1097	0.0011
JT20-9-2-mnz-5h	Monazite	A10	1017858	15	0.1088	0.0011	4.77	0.10	0.318	0.006	0.874	1780	18	1779	17	1780	28	0.0	3.15	0.06	0.1088	0.0011
JT20-9-2-mnz-6a	Monazite	A10	2852234	50	0.1103	0.0011	4.81	0.11	0.316	0.006	0.895	1805	18	1786	19	1770	31	2.0	3.16	0.06	0.1103	0.0011
JT20-9-2-mnz-6b	Monazite	A10	1583273	53	0.1104	0.0011	4.96	0.11	0.326	0.006	0.889	1805	18	1813	19	1820	31	-0.8	3.07	0.06	0.1104	0.0011
JT20-9-2-mnz-6c	Monazite	A10	2707768	45	0.1102	0.0011	4.83	0.11	0.318	0.007	0.903	1802	18	1790	20	1781	33	1.2	3.14	0.07	0.1102	0.0011
JT20-9-2-mnz-6d	Monazite	A10	1904842	24	0.1099	0.0011	4.82	0.14	0.318	0.009	0.936	1797	18	1788	24	1782	42	0.9	3.14	0.08	0.1099	0.0011
JT20-9-2-mnz-6e	Monazite	A10	2470264	31	0.1101	0.0011	4.85	0.12	0.319	0.007	0.905	1801	18	1793	20	1787	34	0.8	3.13	0.07	0.1101	0.0011
JT20-3-mnz-1a	Monazite	E2	1173243	32	0.1104	0.0006	4.660	0.117	0.306	0.007	0.973	1805	11	1760	21	1723	37	4.8	3.264	0.080	0.1104	0.0006
JT20-3-mnz-1b	Monazite	E2	3822803	34	0.1101	0.0006	4.655	0.118	0.307	0.008	0.975	1800	10	1759	21	1725	37	4.3	3.258	0.081	0.1101	0.0006
JT20-3-mnz-1c	Monazite	E2	3441312	95	0.1094	0.0006	4.698	0.117	0.312	0.008	0.972	1789	11	1767	21	1749	38	2.3	3.209	0.078	0.1094	0.0006
JT20-3-mnz-1d	Monazite	E2	3461338	33	0.1089	0.0006	4.706	0.117	0.314	0.008	0.974	1781	10	1768	21	1759	37	1.3	3.188	0.077	0.1089	0.0006
JT20-3-mnz-1e	Monazite	E2	2319915	28	0.1090	0.0006	4.712	0.118	0.314	0.008	0.973	1783	10	1769	21	1758	37	1.4	3.189	0.078	0.1090	0.0006
JT20-3-mnz-1f	Monazite	E2	2626456	23	0.1090	0.0006	4.723	0.119	0.314	0.008	0.974	1782	10	1771	21	1763	38	1.1	3.180	0.078	0.1090	0.0006
JT20-3-mnz-1g	Monazite	E2	4259426	34	0.1100	0.0006	4.822	0.119	0.318	0.008	0.973	1799	10	1789	21	1781	37	1.0	3.143	0.076	0.1100	0.0006
JT20-3-mnz-1h	Monazite	E2	3255211	19	0.1083	0.0006	4.656	0.118	0.312	0.008	0.974	1770	10	1759	21	1751	38	1.1	3.205	0.079	0.1083	0.0006
JT20-3-mnz-1i	Monazite	E2	3374782	22	0.1066	0.0006	4.542	0.114	0.309	0.008	0.974	1743	10	1739	21	1736	37	0.4	3.236	0.079	0.1066	0.0006
JT20-3-mnz-1j	Monazite	E2	3277300	65	0.1099	0.0006	5.069	0.126	0.335	0.008	0.973	1798	10	1831	21	1861	39	-3.4	2.989	0.072	0.1099	0.0006
JT20-3-mnz-2a	Monazite	J12	2995607	60	0.1090	0.0006	4.934	0.124	0.329	0.008	0.974	1782	10	1808	21	1831	39	-2.7	3.044	0.075	0.1090	0.0006
JT20-3-mnz-2b	Monazite	J12	3486942	46	0.1090	0.0006	4.934	0.123	0.329	0.008	0.974	1782	10	1808	21	1831	38	-2.7	3.044	0.074	0.1090	0.0006
JT20-3-mnz-2c	Monazite	J12	3635559	53	0.1078	0.0006	4.822	0.121	0.323	0.008	0.974	1763	10	1789	21	1805	38	-2.3	3.094	0.075	0.1078	0.0006
JT20-3-mnz-2d	Monazite	J12	3544671	54	0.1079	0.0006	4.849	0.122	0.326	0.008	0.974	1764	10	1793	21	1819	39	-3.0	3.067	0.075	0.1079	0.0006
JT20-11-mnz-1a	Monazite	D8	1934697	26	0.1106	0.0009	4.726	0.119	0.310	0.007	0.949	1810	14	1772	21	1741	36	3.96	3.226	0.077	0.1106	0.0009
JT20-11-mnz-1b	Monazite	D8	2451945	21	0.1104	0.0009	4.738	0.119	0.311	0.007	0.949	1806	14	1774	21	1748	36	3.32	3.211	0.077	0.1104	0.0009
JT20-11-mnz-1c	Monazite	D8	2775717	31	0.1104	0.0009	4.829	0.122	0.317	0.008	0.950	1806	14	1790	21	1777	37	1.65	3.151	0.075	0.1104	0.0009
JT20-11-mnz-1d	Monazite	D8	2108036	34	0.1105	0.0009	4.835	0.121	0.318	0.008	0.949	1808	14	1791	21	1778	37	1.68	3.149	0.075	0.1105	0.0009
JT20-11-mnz-1e	Monazite	D8	2454962	69	0.1104	0.0009	4.855	0.121	0.319	0.008	0.949	1805	14	1794	21	1786	37	1.11	3.133	0.074	0.1104	0.0009
JT20-11-mnz-1f	Monazite	D8	2315079	98	0.1102	0.0009	4.884	0.122	0.322	0.008	0.947	1803	15	1800	21	1798	37	0.29	3.109	0.074	0.1102	0.0009
JT20-11-mnz-2a	Monazite	Q9	2081904	59	0.1101	0.0009	4.716	0.118	0.311	0.007	0.949	1801	14	1770	21	1745	36	3.20	3.217	0.076	0.1101	0.0009
JT20-11-mnz-2b	Monazite	Q9	2447681	68	0.1100	0.0009	4.781	0.120	0.315	0.008	0.950	1799	14	1782	21	1767	37	1.82	3.171	0.076	0.1100	0.0009
JT20-11-mnz-2c	Monazite	Q9	2446353	39	0.1099	0.0009	4.762	0.120	0.314	0.008	0.950	1797	14	1778	21	1763	37	1.97	3.180	0.076	0.1099	0.0009
JT20-11-mnz-2d	Monazite	Q9	2380353	25	0.1099	0.0009	4.767	0.119	0.315	0.007	0.948	1798	14	1779	21	1764	36	1.95	3.178	0.075	0.1099	0.0009
JT20-11-mnz-2e	Monazite	Q9	2385791	12	0.1101	0.0009	4.742	0.118	0.313	0.007	0.948	1800	14	1775	21	1754	36	2.65	3.198	0.076	0.1101	0.0009
JT20-11-mnz-2f	Monazite	Q9	2394083	7	0.1099	0.0009	4.769	0.119	0.315	0.007	0.949	1797	14	1779	21	1765	36	1.80	3.175	0.075	0.1099	0.0009
JT20-11-mnz-3b	Monazite	P7	1811555	35	0.1100	0.0009	4.701	0.119	0.310	0.007	0.949	1800	14	1767	21	1741	36	3.42	3.226	0.077	0.1100	0.0009
JT20-11-mnz-3c	Monazite	P7	2158493	59	0.1098	0.0009	4.702	0.118	0.311	0.008	0.951	1796	14	1768	21	1745	37	2.92	3.217	0.078	0.1098	0.0009
JT20-11-mnz-3d	Monazite	P7	2538801	47	0.1096	0.0009	4.746	0.119	0.314	0.008	0.948	1793	14	1775	21	1761	37	1.76	3.182	0.075	0.1096	0.0009
JT20-11-mnz-3e	Monazite	P7	2414771	30	0.1099	0.0009	4.619	0.116	0.305	0.007	0.949	1797	14	1753	21	1716	36	4.72	3.278	0.078	0.1099	0.0009
JT20-11-mnz-3f	Monazite	P7	2773911	38	0.1098	0.0009	4.651	0.116	0.307	0.007	0.949	1796	14	1758	21	1728	36	3.91	3.253	0.077	0.1098	0.0009
DP19-844-mnz-1a	Monazite	R7	1018018	86	0.1167	0.0009	5.638	0.151	0.350	0.009	0.954	1907	14	1922	23	1937	43	-1.55	2.8535	0.0730	0.1167	0.0009
DP19-844-mnz-1b	Monazite	R7	3404422	55	0.1155	0.0009	5.575	0.151	0.350	0.009	0.959	1888	14	1912	23	1935	43	-2.46	2.8556	0.0743	0.1155	0.0009
DP19-844-mnz-1c	Monazite	R7	2575594	84	0.1154	0.0009	5.524	0.149	0.347	0.009	0.959	1886	14	1903	23	1919	43	-1.76	2.8836	0.0747	0.1154	0.0009
DP19-844-mnz-2a	Monazite	P6	3221439	48	0.1165	0.0009	5.676	0.151	0.353	0.009	0.957	1903	14	1928	23	1951	43	-2.46	2.8290	0.0722	0.1165	0.0009
DP19-844-mnz-2b	Monazite	P6	3087723	113	0.1166	0.0009	5.656	0.153	0.352	0.009	0.958	1904	14	1925	23	1945	43	-2.10	2.8398	0.0735	0.1166	0.0009
DP19-844-mnz-2c	Monazite	P6	2814605	7	0.1162	0.0009	5.627	0.153	0.351	0.009	0.958	1898	14	1920	23	1942	43	-2.25	2.8450	0.0739	0.1162	0.0009
DP19-843-mnz-1a	Monazite	C9	1467304	63	0.1189	0.0009	5.650	0.112	0.345	0.006	0.926	1939	13	1924	17	1910	30	1.529	2.900	0.053	0.1189	0.0009
DP19-843-mnz-1b	Monazite	C9	1394558	12	0.1178	0.0009	5.648	0.111	0.348	0.006	0.929	1923	13	1923	17	1924	30	-0.032	2.875	0.053	0.1178	0.0009
DP19-843-mnz-1c	Monazite	C9	1411335	7	0.1175	0.0009	5.705	0.115	0.352	0.007	0.932	1919	13	1932	17	1945	31	-1.361	2.839	0.053	0.1175	0.0009
DP19-843-mnz-1d	Monazite	C9	1150680	19	0.1179	0.0009	5.654	0.111	0.348	0.006	0.926	1925	13	1924	17	1924	30	0.055	2.875	0.052	0.1179	0.0009
DP19-843-mnz-1e	Monazite	C9	1156999	10	0.1177	0.0009	5.637	0.114	0.348	0.007	0.932	1921	13	1922	17	1923	31	-0.073	2.877	0.054	0.1177	0.0009
DP19-843-mnz-1f	Monazite	C9	1163671	30	0.1170	0.0009	5.349	0.127	0.332	0.007	0.950	1911	13	1877	20	1847	36	3.471	3.014	0.068	0.1170	0.0009
DP19-843-mnz-1g	Monazite	C9	1285993	32	0.1178	0.0009	5.669	0.110	0.349	0.006	0.928	1922	13	1927	17	1931	30	-0.454	2.863	0.051	0.1178	0.0009
DP19-843-mnz-1h	Monazite	C9	1289511	21	0.1177	0.0009	5.701	0.115	0.352	0.007	0.933	1921	13	1931	17	1942	31	-1.085	2.844	0.053	0.1177	0.0009
DP19-843-mnz-2a	Monazite	H4	657080	29	0.1185	0.0009	5.628	0.130	0.345	0.007	0.947	1933	13	1920	20	1909	36	1.234	2.901	0.063	0.1185	0.0009
DP19-843-mnz-2b	Monazite	H4	769302	18	0.1187	0.0009	5.680	0.130	0.347	0.008	0.946	1937	13	1927	20	1918	36	0.988	2.886	0.063	0.1187	0.0009
DP19-843-mnz-2c	Monazite	H4	680997	7	0.1176	0.0009	5.567	0.127	0.343	0.008	0.953	1921	13	1911	20	1903	38	0.940	2.912	0.068	0.1176	0.0009
DP19-843-mnz-3a	Monazite	D7	492662	2	0.1178	0.0009	5.513	0.110	0.340	0.006	0.922	1923	14	1903	17	1885	30	2.008	2.944	0.054	0.1178	0.0009
DP19-843-mnz-3b	Monazite	D7	452079	14	0.1184	0.0009	5.558	0.108	0.340	0.006	0.922	1933	13	1910	17	1888	30	2.315	2.937	0.053	0.1184	0.0009
DP19-843-mnz-4a	Monazite	G4	821339	57	0.1198	0.0009	5.717	0.121	0.346	0.007	0.924	1953	14	1934	18	1917	33	1.907	2.888	0.057	0.1198	0.0009
DP19-843-mnz-4b	Monazite	G4	680058	79	0.1198	0.0010	5.638	0.126	0.342	0.007	0.924	1953	15	1922	19	1894	34	3.111	2.928	0.061	0.1198	0.0010
DP19-843-zrn-1a	Zircon	K3	690141	18	0.1170	0.0010	5.621	0.139	0.349	0.009	0.953	1911	15	1919	21	1928	45	-0.869	2.869	0.077	0.1170	0.0010
DP19-843-zrn-1b	Zircon	K3	633133	19	0.1166	0.0010	5.225	0.139	0.325	0.009	0.948	1905	15	1857	22	1814	45	5.013	3.076	0.077	0.1166	0.0010
DP19-843-zrn-1c	Zircon	K3	601480	22	0.1170	0.0010	5.553	0.157	0.344	0.009	0.953	1912	15	1909	24	1907	44	0.233	2.905	0.078	0.1170	0.0010
DP19-843-zrn-2a	Zircon	U9	354489	15	0.1510	0.0013	8.692	0.266	0.418	0.012	0.959	2357	15	2306	28	2250	56	4.783	2.394	0.070	0.1510	0.0013
DP19-843-zrn-2b	Zircon	U9	383332	20	0.1502	0.0013	8.108	0.265	0.392	0.012	0.967	2348	14	2243	29	2131	57	10.197	2.553	0.081	0.1502	0.0013
DP19-843-zrn-2c	Zircon	U9	344017	13	0.1478	0.0014	8.131	0.258	0.399	0.010	0.938	2321	16	2246	24	2165	46	7.225	2.506	0.063	0.1478	0.0014
DP19-843-zrn-2d	Zircon	U9	305049	11	0.1508	0.0013	8.325	0.226	0.401	0.010	0.948	2355	15	2267	24	2172	47	8.396	2.496	0.064	0.1508	0.0013
DP19-843-zrn-3a	Zircon	A7	519595	21	0.1588	0.0015	8.471	0.290	0.387	0.013	0.964	2443	15	2283	31	2110	59	15.788	2.583	0.085	0.1588	0.0015
DP19-843-zrn-3b	Zircon	A7	1022827	34	0.1341	0.0012	5.576	0.218	0.302	0.011	0.974	2153	15	1912	33	1699	57	26.683	3.315	0.126	0.1341	0.0012
DP19-843-zrn-3c	Zircon	A7	1063610	41	0.1339	0.0016	4.131	0.121	0.224	0.006	0.909	2150	21	1660	24	1302	31	65.148	4.468	0.118	0.1339	0.0016
DP19-843-zrn-4a	Zircon	D3	703866	10	0.1208	0.0011	5.471	0.160	0.329	0.009	0.947	1968	17	1896	25	1832	44	7.442	3.043	0.084	0.1208	0.0011
DP19-843-zrn-4b	Zircon	D3	954415	41	0.1101	0.0013	3.771	0.154	0.248	0.010	0.928	1802	21	1587	32	1430	50	25.975	4.025	0.157	0.1101	0.0013
DP19-843-zrn-5a	Zircon	N5	529173	44	0.1252	0.0011	5.275	0.150	0.306	0.008	0.952	2031	15	1865	24	1720	41	18.122	3.271	0.088	0.1252	0.0011
DP19-843-zrn-5b	Zircon	N5	659523	30	0.1231	0.0012	5.429	0.221	0.320	0.013	0.978	2001	15	1889	34	1790	62	11.794	3.124	0.124	0.1231	0.0012
PLS14-260-2-zrn-1a	Zircon	I2	343812	20	0.1174	0.0011	5.638	0.138	0.348	0.008	0.917	1917	17	1922	21	1927	40	-0.52	2.870	0.064	0.1174	0.0011
PLS14-260-2-zrn-1b	Zircon	I2	350940	19	0.1166	0.0010	5.611	0.122	0.349	0.007	0.926	1905	16	1918	19	1931	33	-1.34	2.864	0.057	0.1166	0.0010
PLS14-260-2-zrn-1c	Zircon	I2	384258	35	0.1160	0.0010	5.538	0.116	0.346	0.007	0.909	1896	16	1907	18	1917	32	-1.08	2.888	0.055	0.1160	0.0010
PLS14-260-2-zrn-1d	Zircon	I2	341614	11	0.1163	0.0010	5.584	0.113	0.348	0.006	0.909	1901	15	1914	17	1926	30	-1.34	2.871	0.053	0.1163	0.0010
PLS14-260-2-zrn-1e	Zircon	I2	384798	86	0.1156	0.0009	5.492	0.135	0.345	0.008	0.944	1890	15	1899	21	1909	38	-1.02	2.901	0.068	0.1156	0.0009
PLS14-260-2-zrn-1f	Zircon	I2	354847	30	0.1170	0.0010	5.608	0.147	0.348	0.009	0.947	1910	15	1917	22	1924	41	-0.74	2.875	0.071	0.1170	0.0010
PLS14-260-2-zrn-1g	Zircon	I2	256342	74	0.1172	0.0011	5.138	0.091	0.318	0.005	0.840	1914	17	1842	15	1781	23	7.49	3.143	0.047	0.1172	0.0011

Table C4: C isotope data

Sample	$\delta^{13}C_{VPDB}$(‰)	2s (‰)
DP19-843-M	-26.10	< 0.2
DP19-843-NM	-25.90	< 0.2
DP19-844	-23.60	< 0.2
PLS14-133	-20.90	< 0.2
PLS14-260	-23.00	< 0.2
JT20-3-NM	-28.30	< 0.2
JT20-11	-25.20	< 0.2
JT20-5-VC-min	-21.64	< 0.2
JT20-5-VR-min	-19.15	< 0.2
JT20-5-WR-min	-19.20	< 0.2
JT20-5-VC-max	-16.75	< 0.2
JT20-5-VR-max	-16.91	< 0.2
JT20-5-WR-max	-15.28	< 0.2

Note: JT20-5 are minmum and maximum C isotope data sourced from Toma et al. (2022)

Table C5: Modal abundances for Re/Os mineral separates

Sample	Min. Sep.	Pyrite (%)	SiO (%)	Graphite (%)	Bornite (%)	Chalcopyrite (%)	Total
DP19-844-py	M-0.50	56.54	43.46	0.00	0.00	0.00	100
DP19-844-py	M-0.54	66.05	33.95	0.00	0.00	0.00	100
DP19-844-py	M-0.59	85.65	14.35	0.00	0.00	0.00	100
DP19-844-py	M-0.70	90.60	9.40	0.00	0.00	0.00	100
DP19-844-py	NM-0.59	95.15	4.85	0.00	0.00	0.00	100
DP19-844-py	NM-0.70	93.42	6.58	0.00	0.00	0.00	100
DP19-844-py	NM-0.84	97.83	2.17	0.00	0.00	0.00	100
DP19-843-py	T3-M-0.45	86.45	13.55	0.00	0.00	0.00	100
DP19-843-py	T2-M-0.55	83.06	14.66	0.00	0.00	2.28	100
DP19-843-py	T1-M-0.75	95.36	4.64	0.00	0.00	0.00	100
DP19-843-py	T3-NM-0.45	98.20	0.90	0.00	0.00	0.90	100
DP19-843-py	T2-NM-0.55	98.88	0.19	0.00	0.00	0.94	100
DP19-843-py	T1-NM-0.75	98.95	0.84	0.00	0.00	0.21	100
DP19-843-gr	M-0.51	0.52	50.00	40.00	0.00	0.00	91
DP19-843-gr	M-0.91	1.60	54.76	43.64	0.00	0.21	100
DP19-843-gr	M-0.99	8.76	88.02	3.23	0.00	0.00	100
DP19-843-gr	M-1.94	33.16	63.50	3.34	0.00	0.00	100
DP19-843-gr	NM-1.94	1.25	61.83	36.92	0.00	0.00	100
PLS14-260-2-py	M-0.02	99.66	0.00	0.00	0.00	0.00	100
PLS14-260-2-py	M-0.05	73.16	24.97	1.71	0.00	0.00	100
PLS14-260-2-py	M-0.30	86.07	12.95	1.15	0	0	100
PLS14-260-2-py	NM-0.30	99.26	0.62	0.00	0.00	0.12	100
PLS14-260-2-py	NM-0.47	96.42	3.58	0.00	0.00	0.00	100
PLS14-260-2-py	NM-0.70	82.92	17.08	0.00	0.00	0.00	100
PLS14-260-2-py	NM-0.90	99.57	0.43	0.00	0.00	0.00	100
PLS14-133	M-0.50	97.00	3.00	0.00	0.00	0.00	100
PLS14-133	NM-0.51	84.00	15.00	0.00	0.00	1.00	100
PLS14-133	NM-0.53	99.50	0.50	0.00	0.00	0.00	100
PLS14-133	NM-0.55	99.50	0.50	0.00	0.00	0.00	100
PLS14-133	NM-0.60	99.50	0.50	0.00	0.00	0.00	100
PLS14-133	NM-0.61	99.50	0.50	0.00	0.00	0.00	100
PLS14-133	NM-0.69	99.50	0.50	0.00	0.00	0.00	100
PLS14-133	NM-1.60	99.50	0.50	0.00	0.00	0.00	100
JT20-10-py	Bulk	89.19	10.81	0.00	0.00	0.00	100
JT20-10-py	M-0.05	86.70	13.30	0.00	0.00	0.00	100
JT20-10-py	M-0.07	85.88	13.94	0.00	0.00	0.00	100
JT20-10-py	NM-0.29	84.49	15.51	0.00	0.00	0.00	100
JT20-10-py	NM-0.48	95.34	4.66	0.00	0.00	0.00	100
JT20-10-py	NM-0.70	99.00	1.00	0.00	0.00	0.00	100
JT20-11-gr	M-0.70	0.78	80.62	18.86	0.00	0.00	100
JT20-11-gr	NM-0.45	0.35	67.48	32.17	0.00	0.00	100
JT20-11-gr	NM-2.20	0.00	43.54	56.46	0.00	0.00	100
JT20-3-gr	NM-1.74	0.00	16.18	83.82	0.00	0.00	100
JT20-3-gr	NM-1.86	0.00	20.14	79.86	0.00	0.00	100
JT20-3-gr	NM-2.00	0.00	2.66	97.34	0.00	0.00	100

Abbreviations: py = pyrite; gr = graphite